THE UNIVERSITY
OF ADELAIDE
AUSTRALIA

Fluorescence-Based Chemical Sensing Using Suspended-Core Microstructured Optical Fibres

by

Stephen Christopher Warren-Smith

A thesis submitted for the degree of
Doctor of Philosophy

in the

Faculty of Science
School of Chemistry & Physics

October 2010

To Anna, Joey, Emily, Aaron, Ellie, Declan,
Orlando, Noah, and Ruby

Choose your road.
Ride it well.

Alastair Humphreys

Contents

Abstract ix

Declaration x

Acknowledgements xi

Publications Contained Within Thesis xiv

Other Publications xv

Conference Presentations During Candidature xvi

List of Figures xviii

Abbreviations xxi

I Introduction 1

1 Motivation and Thesis Structure 3
1.1 Motivation . . . 4
1.2 Project Aims . . . 5
1.3 Thesis Structure . . . 7

2 Review of Optical Fibre Chemical Sensing 11
2.1 Introduction . . . 12
2.2 Classification of Optical Fibre Chemical Sensors and Chapter Overview . 13
2.3 Extrinsic Sensors . . . 14
2.3.1 Basic Optical Fibre Sensing . . . 14
2.3.2 Distal End Sensing . . . 16
2.4 Intrinsic Sensors . . . 19
2.4.1 Evanescent Field Sensing . . . 19
2.4.2 Grating Sensors . . . 20
2.4.3 Surface Plasmon Resonance Sensing . . . 21
2.4.4 Surface Enhanced Raman Spectroscopy . . . 22

2.4.5 Interferometric Sensors . . . 23
2.5 Evanescent Field Sensing . . . 23
2.5.1 Concepts . . . 23
2.5.2 Multi Mode Fibres . . . 24
2.5.3 Single Mode Fibres . . . 27
2.5.4 Microstructured Optical Fibres . . . 30
2.6 Coatings for Indicator Immobilisation . . . 38
2.6.1 Polymer Coatings . . . 39
2.6.2 Sol-Gel Coatings . . . 39
2.6.3 Surface Attachment - Silanisation . . . 40
2.6.4 Surface Attachment - Polyelectrolytes . . . 41
2.6.5 Discussion . . . 41
2.7 Distributed Sensing . . . 41
2.7.1 Optical Time Domain Reflectometry . . . 42
2.7.2 Distributed Moisture Sensing . . . 43
2.7.3 Fluorescence-Based Distributed Sensing . . . 43
2.8 Corrosion Sensing . . . 44
2.8.1 Direct Spectroscopic Analysis . . . 45
2.8.2 Metal-Clad Fibres . . . 45
2.8.3 Long Period Gratings . . . 46
2.8.4 Fluorescence Measurements . . . 47
2.9 Discussion and Relevance to Project . . . 48

II Thesis Body **51**

3 Fluorescence Sensing Theory **53**
3.1 Theory Overview and Motivation . . . 54
3.2 Fluorescence Capture Fraction: Fundamental Mode Analysis . . . 58
3.2.1 P1 Publication Overview . . . 58
3.2.2 P1 Statement of Contribution . . . 60
3.3 Fluorescence Capture Fraction: Backwards Fluorescence Capture . . . 73
3.3.1 P2 Publication Overview . . . 73
3.3.2 P2 Statement of Contribution . . . 73
3.4 Fluorescence Capture Fraction: Exposed-Core Fibre . . . 78
3.4.1 P3 Publication Overview . . . 78
3.4.2 P3 Statement of Contribution . . . 80
3.5 Fluorescence Capture Fraction: Higher Order Modes and Experiment . . . 94
3.5.1 P4 Publication Overview . . . 94
3.5.2 P4 Statement of Contribution . . . 96
3.6 Fluorescence Capture Fraction: Thin-Layer Sensing . . . 110
3.6.1 P5 Publication Overview . . . 110
3.6.2 P5 Statement of Contribution . . . 112
3.7 Discussion and Conclusions . . . 124

4 Optical Fibre Fabrication and Characterisation **127**
4.1 Fabrication Overview and Motivation . . . 128

4.2 Suspended Optical Nanowires . . . 136
4.2.1 P6 Publication Overview . . . 136
4.2.2 P6 Statement of Contribution . . . 138
4.3 Exposed-Core Fibres . . . 152
4.3.1 P7 Publication Overview . . . 152
4.3.2 P7 Statement of Contribution . . . 154
4.3.3 Wedged-Jacket Extrusion . . . 166
4.4 Distributed Sensing using Exposed-Core Fibres . . . 173
4.4.1 P8 Publication Overview . . . 173
4.4.2 P8 Statement of Contribution . . . 174
4.4.3 Distributed Sensing: Extending the Range . . . 179
4.5 Discussion and Conclusions . . . 181

5 Corrosion Sensing Application 183
5.1 Chapter Overview . . . 184
5.1.1 Approach . . . 184
5.1.2 Choice of Organic Fluorophore . . . 186
5.2 Characterisation of Lumogallion . . . 189
5.2.1 Sample Preparation . . . 189
5.2.2 Absorption Measurements . . . 189
5.2.3 Fluorescence Measurements . . . 190
5.3 Exposed-Core Fibre Solution Measurements . . . 193
5.4 Porous Polymer Coating . . . 196
5.4.1 Overview . . . 196
5.4.2 Material Preparation . . . 197
5.4.3 Dip Coated Fibre Experiments . . . 197
5.4.4 Lap Joint Experiments . . . 201
5.4.5 Discussion and Conclusions . . . 204
5.5 Polyelectrolyte Attachment . . . 206
5.5.1 Concepts . . . 206
5.5.2 Compound Characterisation . . . 207
5.5.3 Glass Slide Experiments . . . 210
5.5.4 Microstructured Optical Fibre Experiments . . . 213
5.6 Discussion and Conclusions . . . 216

6 Conclusions and Future Work 219

A Fluorescence Capture Fraction Derivation 225
A.1 Power Propagation in the Fibre . . . 225
A.2 An Expression for the Captured Fluorescence . . . 227
A.3 Calculating the Power Density Function . . . 229
A.4 Calculating the Fluorescence Capture Fraction . . . 231
A.5 Variations of the Fluorescence Capture Fraction Equations . . . 233

B Coupling Efficiency Derivation 237
B.1 Free Space Coupling . . . 238

B.2 Numerical Modelling of Free Space Coupling into Optical Nanowires . . . 244
B.3 Coupling Between Two Waveguides . . . 246
B.4 Coupling Equations used in [P3] . . . 248

C W-fibre Confinement Loss **251**
C.1 TE Modes . . . 253
C.2 TM Modes . . . 257
C.3 Hybrid (HE) Modes . . . 258
C.4 Implementation of Confinement Loss Theory . . . 261

D Aluminium Ion Sensing Publication **263**
D.1 Statement of Contribution . . . 263

Bibliography **269**

Errata

Stephen Warren-Smith

December 2010

Chapter 1, Section 1.2, Page 6: For a scale reference, the optical fibre outer diameters in Fig. 1.1 are 160 μm.

Chapter 2, Section 2.5.4, Page 32: "Fibre Bragg Gratings" should be "Long Period Gratings", in relation to Ref. [87].

Chapter 2, Section 2.5.4, Page 36, Line 4 from below: "Fig. 2.15(b, c))" and "Fig. 2.15(d, e))" should be swapped.

Chapter 3, Section 3.6.1, Page 112, Lines 5-6: The statement "that this was the first experimental example of internal surface functionalisation with fluorophores and the technique has since evolved, such as that used in Chapter 5" is incorrect as this has previously been achieved in Refs. [87, 152].

Chapter 5, Section 5.2.3, Page 192: The smallest y-axis tick should be "1" instead of "0".

Appendix B, Section B.3, Pages 246-248: In Eqs. B.29 to B.39 there should be a prime above the electric and magnetic fields on the right hand side of the equations to separate them from fields on the left hand side as these fields are in two different waveguides. That is, there should be a prime above fields that have a ν subscript.

Response to general examiner remarks

1. The soft glass fibres fabricated and used in this project were generally not coated. While fragility was an issue, it was still possible to re-spool and handle the fibres. Note that the fibres were lead-silicate glass, which is less fragile than most other soft glasses. Practical applications would require the fibre to be coated.

2. For most of the exposed-core fibres in this project air holes had formed between the cane and jacket during drawing, such as seen in Fig. 5.11. This resulted from an imperfect fit between the cane and jacket, and the inability to apply a vacuum to the wedged jacket during drawing for the exposed-core fibre. However, the presence of these holes had no detrimental effect on the performance of the fibre as they are sufficiently far from the guided modes of the core.

3. Photobleaching is recognised as a significant problem for organic fluorophore-based sensing. As shown in [P1], the effect of photobleaching is to reduce the fluorescence intensity by an order of magnitude over several minutes. Note that a major contributing factor is the small volume used, and thus the small number of molecules that are located within the optical fibre. For the experiment on page 163 a larger volume size was used and thus photobleaching was not a significant problem for the time frames used.

THE UNIVERSITY OF ADELAIDE

Abstract

Faculty of Science
School of Chemistry & Physics

Doctor of Philosophy

by Stephen Christopher Warren-Smith

This thesis contains a study on the fluorescence based chemical sensing properties of microstructured optical fibres. Specifically, suspended core optical micro/nano-wires, including those with the core partially exposed along their length, are studied both theoretically and experimentally. Comparisons are made between these exposed-core and enclosed-core optical fibres in terms of their fluorescence sensing performance, fabrication, and function. The application of corrosion sensing of aluminium alloys was the primary motivator for this project and methods for achieving this are presented. However, the findings presented in this thesis could be extended to many other biological and chemical applications.

Chapter 1 outlines the motivation of the work and the structure of the thesis. Chapter 2 reviews the state of the art for optical fibre chemical sensing. In Chapter 3 a theoretical model is derived and used to predict the fluorescence capture of high index contrast small-core fibres using vectorial solutions to Maxwell's equations. This model is subsequently used to compare exposed-core and enclosed-core fibres, where distinct advantages are found for liquid-immersed exposed-core fibres due to their asymmetric refractive index profile. In Chapter 4 the fabrication of both enclosed and exposed suspended-core fibres are demonstrated using the extrusion technique for soft-glass preform development. It is then confirmed experimentally that advantages of using exposed-core fibres include the ability to perform real time and distributed fluorescence based sensing. In Chapter 5 two methods of sensitising these fibres for corrosion sensing of aluminium alloys are investigated. Both methods use a fluorescence based indicator molecule for aluminium ions, which is either embedded into a porous polymer coating or chemically attached via polyelectrolytes.

Declaration

I confirm that this work contains no material which has been accepted for the award of any other degree or diploma in any university or other tertiary institution to Stephen Warren-Smith and, to the best of my knowledge and belief, contains no material previously published or written by another person, except where due reference has been made in the text.

I give consent to this copy of my thesis when deposited in the University Library, being made available for loan and photocopying, subject to the provisions of the Copyright Act 1968.

The author acknowledges that copyright of published works contained within this thesis (listed on pages xiv and xv) resides with the copyright holder(s) of those works.

I also give permission for the digital version of my thesis to be made available on the web, via the University's digital research repository, the Library catalogue, the Australasian Digital Theses Program (ADTP) and also through web search engines, unless permission has been granted by the University to restrict access for a period of time.

Signed: _____

Date: _____

Acknowledgements

I have many people to acknowledge for their contribution and support throughout my PhD experience both professionally and personally. Due to the collaborative nature of this project it is impossible to acknowledge everyone who contributed in some way to this thesis. I hope the following does some justice to the efforts of those who supported me and that those who are not specifically acknowledged are already aware of my appreciation.

First acknowledgements must go to my supervisors, Tanya Monro, Heike Ebendorff-Heidepriem, and Shahraam Afshar. The results of this thesis would not have been possible without their support and guidance. Tanya's enthusiasm and ability to find solutions to all aspects of physics research make her a fantastic supervisor and a great role model for a young scientist. Heike's approach to science is to be envied, she has an understanding of the fibre fabrication process that is inspiring, making her an excellent supervisor for a project such as this. I thank Shahraam for sharing the fluorescence sensing theory journey with me. Indeed, Shahraam's enthusiam and skills in theoretical physics have constantly been pivotal in producing the final results that appear in this thesis.

I would like to acknowledge the optics and photonics research group as a whole. In particular, those associated with the soft-glass optical fibre fabrication. It is not possible for an individual PhD student to work on a project such as this without significant infrastructure and personnel already in place. Tanya's original decision to start a soft-glass optical fibre group at the University of Adelaide has been greatly beneficial to me personally, as was the support of others who encouraged her to come here such as the Defence Science and Technology Organisation (DSTO). I also thank the many people who have been involved in starting and running this group such as Heike Ebendorff-Heideprie and Roger Moore.

I would like to acknowledge the many other people at the University of Adelaide who also contributed to this project in one way or another. I would like to thank Roger Moore for drawing the fibres that are presented in this thesis. I have been privileged to have a technician with over 20 years experience drawing my fibres that, due to their unique design, were not a simple task. I thank the other technical staff that were always willing to assist with practical aspects of this project. This includes Adrian Selby, Alastair Dowler, Trevor Waterhouse, and Blair Middlemiss. I thank Herbert Foo for helping me with hydrofluoric acid (HF) etching experiments, FTIR-ATR measurements, and general discussions on the chemical aspects of this project. Kevin Kuan for general support in chemistry. Markus Pietsch for starting work on the chemical synthesis of a derivative

of lumogallion that was used in this project, Sabrina Heng for continuing and finishing this work, and Andrew Abell for encouraging this work to be done in his lab. Alexandre Francois for instruction on the use of polyelectrolytes for surface funtionalisation. Erik Schartner for many useful and critical discussions on my project, and the sharing of ideas and work due to our closely related projects. Dominic Murphy and Florian Englich for purchasing some of the optical equipment used in the later experiments of this project. John Terlet and other staff at Adelaide Micrscopy who made it possible to perform scanning electron microscope (SEM) imaging of optical fibres at their very convenient on-campus location. Peter Hoffman who collaborated in the biosensing project that resulted in one of the publications in this thesis. Olivia Towers and Sara Boffa who constantly helped to take the pain out of university administration and beaurocracy.

One of the strengths and most enjoyable aspects of this PhD has been the collaboration with not only many different people but also organisations. This has allowed many things to be achieved that otherwise could not have been possible had I been working in isolation.

I would like to thank Claire Davis, Silvia Tejedor, and Grant McAdam from DSTO for providing funding for this project, their many useful conversations on my work, and allowing me to perform experiments in their labs. In particular, I acknowledge the DSTO Corporate Initiative on Smart Materials and Structures for sponsorship of this program of research. I would like to thank Elena Sinchenko and Paul Stoddart from Swinburne University with whom I performed distributed sensing measurements using my fibres, which lead to a publication contained within this thesis. I acknowledge Christopher Gibson from Flinders University for assisting me with atomic force microscopy images that appear in this thesis. Also, Milena Ginic-Markovic from Flinders University for assisting Herbert Foo and myself with fourier-transform infra-red (FTIR) spectroscopy: attenuated total reflectance (ATR) measurements that unfortunately do not appear in this thesis.

On the personal side, there are many people, both friends and family, who I would like to thank for their continued friendship and support over the last few years. There are too many to name everyone here, but particular thanks to my friends since childhood, Richard Harvey, Brett Thredgold, Tristan Williamson, Michael Sawyer, Adam Hennessy, and Cathryn Matto. Thanks to the many other friends I have made over recent years, in particular, Adam Kilpatrick, Michael Oermann, Jeffrey Newman, Katrina Newman, Michael Woodward, Hannah Laven, Erik Schartner, Herbert Foo, and Faisal Amir.

Special thanks to Mum and Dad for their love, support, and encouragement not just during my PhD but for the last 25 years. Thanks to my step-mum, Suzanne. Thanks to my grandpa. Thanks to my brothers and sisters, Anna, Joey, Emily, Aaron, Ellie, and

Declan, and to my nephews and niece, Orlando, Noah, and Ruby. I sincerely wish the best for you all.

Publications Contained Within Thesis

P1. S. Afshar V., S. C. Warren-Smith, and T. M. Monro, "Enhancement of fluorescence-based sensing using microstructured optical fibres," *Optics Express* **15**, 17891-17901 (2007).

P2. S. Afshar V., Y. Ruan, S. C. Warren-Smith, and T. M. Monro, "Enhanced fluorescence sensing using microstructured optical fibers; a comparison of forward and backward collection modes," *Optics Letters* **33**, 1473-1475 (2008).

P3. S. C. Warren-Smith, S. Afshar V., and T.M. Monro, "Theoretical study of liquid-immersed exposed-core microstructured optical fibres for sensing," *Optics Express* **16**, 9034-9045 (2008).

P4. S. C. Warren-Smith, S. Afshar V., and T.M. Monro, "Fluorescence-based sensing with optical nanowires: a generalized model and experimental validation," *Optics Express* **18**, 9474-9485 (2010).

P5. Y. Ruan, T. C. Foo, S. C. Warren-Smith, P. Hoffmann, R. C. Moore, H. Ebendorff-Heidepriem, and T. M. Monro, "Antibody immobilization within glass microstructured fibers: a route to sensitive and selective biosensors," *Optics Express* **16**, 18514-18523 (2008).

P6. H. Ebendorff-Heidepriem, S. C. Warren-Smith, and T. M. Monro, "Suspended nanowires: fabrication, design and characterization of fibers with nanoscale cores," *Optics Express* **17**, 2646-2657 (2009).

P7. S. C. Warren-Smith, H. Ebendorff-Heidepriem, T. C. Foo, R. Moore, C. Davis, and T. M. Monro, "Exposed-core microstructured optical fibers for real-time fluorescence sensing," *Optics Express* **17**, 18533-18542 (2009).

P8. S. C. Warren-Smith, E. Sinchenko, P. R. Stoddart, and T. M. Monro, "Distributed fluorescence sensing using exposed-core microstructured optical fiber," *Photonics Technology Letters* **22**, 1385-1387 (2010).

These publications are included within the main body of this thesis. When referred to in the text the reference number is prefixed by a 'P'. For example, the first publication in this list is referred to as [P1].

Other Publications

The following paper was prepared after Chapter 5 was drafted and thus is included in Appendix D.

1. S. C. Warren-Smith, S. Heng, H. Ebendorff-Heidepriem, A. D. Abell, T. M. Monro, "Fluorescence-based aluminum ion sensing using a surface functionalized microstructured optical fiber," to be submitted to the *Journal of the American Chemical Society*.

The following papers, which are not included in this thesis, have been submitted for publication.

2. T. M. Monro, S. C. Warren-Smith, E. P. Schartner, A. Franois, S. Heng, H. Ebendorff-Heidepriem, S. Afshar V., "Sensing with suspended-core optical fibers," accepted for publication in *Optical Fiber Technology*.

3. T. Palmisano, F. Prudenzano, S. C. Warren-Smith, T. M. Monro, "Design of exposed-core fiber for methadone monitoring in biological fluids," submitted to the *Journal of Non-Crystalline Solids*.

Conference Presentations During Candidature

1. S. C. Warren-Smith, S. Afshar V., and T. M. Monro, "Highly-efficient fluorescence sensing using microstructured optical fibres; side-access and thin-layer configurations," *19th International Conference on Optical Fibre Sensing (OFS)*, Perth, Australia (April 2008).

2. S. Afshar V., Y. Ruan, S. C. Warren-Smith, H. Ebendorff-Heidepriem, and T. M. Monro, "Highly-efficient fluorescence sensing using microstructured optical fibres; general model and experiment," *19th International Conference on Optical Fibre Sensing (OFS)*, Perth, Australia (April 2008).

3. S. C. Warren-Smith, H. Ebendorff-Heidepriem, S. Afshar V., G. McAdam, C. Davis, and T. M. Monro, "Corrosion sensing of aluminium alloys using exposed-core microstructured optical fibres," *2nd Asia-Pacific Workshop on Structural Health Monitoring*, Melbourne, Australia (December 2008).

4. S. C. Warren-Smith, H. Ebendorff-Heidepriem, and T. M. Monro, "Suspended optical nanowires for sensing applications," *18th Australian Institute of Physics (AIP) Congress*, Adelaide, Australia (December 2008).

5. H. Ebendorff-Heidepriem, S. C. Warren-Smith, and T. M. Monro, "Fabrication of suspended nanowire optical fibres," *18th Australian Institute of Physics (AIP) Congress*, Adelaide, Australia (December 2008).

6. S. C. Warren-Smith, H. Ebendorff-Heidepriem, T. C. Foo, R. C. Moore and C. E. Davis, and T. M. Monro, "Exposed-core microstructured fibres for real-time fluorescence sensing," *20th International Conference on Optical Fibre Sensors (OFS)*, Edinburgh, United Kingdom (October 2009).

7. E. P. Schartner, R. T. White, S. C. Warren-Smith, and T. M. Monro, "Practical sensitive fluorescence sensing with microstructured fibres," *20th International Conference on Optical Fibre Sensors (OFS)*, Edinburgh, United Kingdom (October 2009).

8. Y. Ruan, H. Ebendorff-Heidepriem, S. Afshar V., S. C. Warren-Smith, and T. M. Monro, "Advances in chemical and biological sensing using emerging soft glass optical fibers," *Frontiers in Optics*, San Jose, United States of America (October 2009).

9. S. C. Warren-Smith, E. Sinchenko, P. R. Stoddart, C. E. Davis and T. M. Monro, "Distributed fluorescence sensing with exposed-core microstructured optical fibres," *34th Australian Conference on Optical Fibre Technology (ACOFT)*, Adelaide, Australia (December 2009).

10. H. Ebendorff-Heidepriem, S. Afshar V., S. C. Warren-Smith, W. Q. Zhang, Y. Ruan, S. Atakaramians and T. M. Monro, "Fibres with subwavelength features: fabrication and novel guidance properties," 3*4th Australian Conference on Optical Fibre Technology (ACOFT)*, Adelaide, Australia (December 2009).

List of Figures

1.1 Suspended-core microstructured optical fibre . . . 6

2.1 Extrinsic optical fibre sensor . . . 14
2.2 Multiplexed optical fibre sensing . . . 15
2.3 Bifurcated optical fibre sensors and fibre bundle . . . 17
2.4 Double clad microstructured optical fibre . . . 18
2.5 Long period grating optical fibre sensor . . . 21
2.6 Evanescent field . . . 24
2.7 U-shaped fibre sensor . . . 27
2.8 D-shaped fibre sensor . . . 28
2.9 Tapered fibre sensor . . . 29
2.10 Optical nanowires . . . 29
2.11 Microstructured optical fibres . . . 30
2.12 Microstructured optical fibre concept . . . 31
2.13 Suspended optical nanowires . . . 34
2.14 Schematic of a side access MOF . . . 36
2.15 Images of side access MOFs . . . 37
2.16 Attachment of proteins via silanisation . . . 40
2.17 Example of an OTDR trace for distributed sensing . . . 42
2.18 Distributed moisture sensor . . . 43
2.19 Evanescent-field corrosion sensing using a fluorescent indicator . . . 47

3.1 Fluorescence sensing concept . . . 54
3.2 Chapter 3 flowchart . . . 57

4.1 Chapter 4 flowchart . . . 129
4.2 Suspended-core fibre fabrication . . . 131
4.3 F2 glass billet . . . 132
4.4 Exposed-core fibre fabrication . . . 132
4.5 Extrusion machine . . . 134
4.6 Soft glass drawing tower . . . 135
4.7 Schematic diagram of extrusion bending . . . 167
4.8 Bent wedged jacket . . . 167
4.9 Guiding pole for straight extrusions . . . 168
4.10 Straight wedged-jacket preforms . . . 168
4.11 Square wedged jacket . . . 170
4.12 45^o wedged-jacket . . . 171
4.13 Channeled wedged-jacket . . . 171

4.14 D-shaped wedged-jacket . . . 172
4.15 Distributed sensing range . . . 181

5.1 Chapter 5 flowchart . . . 185
5.2 Lumogallion as a fluorescent indicator for aluminium . . . 187
5.3 Lumogallion absorption . . . 190
5.4 Experimental setup for fluorescence measurements using cuvettes . . . 191
5.5 Lumogallion fluorescence response to aluminium - spectra . . . 192
5.6 Lumogallion fluorescence response to aluminium - linear . . . 192
5.7 Lumogallion fluorescence using exposed-core fibre: setup . . . 193
5.8 Lumogallion fluorescence using exposed-core fibre: results . . . 195
5.9 Polymer dip coated F2 and silica bare fibres . . . 198
5.10 Polymer dip coated F2 bare fibres . . . 198
5.11 Polymer dip coated exposed-core fibres . . . 199
5.12 Polymer dip coated fibres: fluorescence response to aluminium . . . 200
5.13 Lap joint image: without aluminium plate . . . 202
5.14 Salt spray chamber . . . 203
5.15 Lap joint image: with aluminium plates . . . 203
5.16 Lap joint fibres: fluorescence response to aluminium . . . 204
5.17 Polyelectrolyte attachment to glass . . . 206
5.18 Derivative of lumogallion . . . 207
5.19 Lumogallion derivative absorption . . . 208
5.20 Lumogallion derivative fluorescence response to aluminium - spectra . . . 208
5.21 Lumogallion derivative fluorescence response to aluminium - linear . . . 209
5.22 Teflon bath and rack used for coating glass slides . . . 210
5.23 Glass slide attachment fluorescence results . . . 212
5.24 Inflated suspended-core fibre SEM . . . 214
5.25 Pressure filling setup for MOFs . . . 214
5.26 Suspended-core fibre attachment results . . . 215

B.1 Free space coupling . . . 238
B.2 Coupling efficiency definitions . . . 245

C.1 W-fibre profile . . . 251

Abbreviations

8-HQ	8-**H**ydroxy**q**uinoline
AFM	**A**tomic **F**orce **M**icroscopy
BF	**B**are **F**ibre
CCD	**C**harge **C**oupled **D**evice
CE	**C**oupling **E**fficiency
CL	**C**onfinement **L**oss
CW	**C**onitinuous **W**ave
DMSO	**D**i**m**ethyl **S**ulf**o**xide
DNA	**D**eoxyribo**n**ucleic **A**cid
EDC	1-**E**thyl-3-(3-**D**imethylaminopropyl)**C**arbodiimide
ELISA	**E**nzyme **L**inked **I**mmuno**s**orbent **A**ssay
F2	Lead-Silicate Glass ($n \approx 1.62$)
FBG	**F**ibre **B**ragg **G**rating
FCF	**F**luorescence **C**apture **F**raction
FEM	**F**inite **E**lement **M**odelling
GMBS	N-γ-Maleimidobutyryloxy Succinimide Ester
HF	**H**ydro**f**luoric acid
ID	**I**nner **D**iameter
IR	**I**nfra **R**ed
JASR	**J**acketed **A**ir **S**uspended **R**od
LIT	**L**iquid **I**nterface **T**ransmission
LLF1	Lead-Silicate Glass ($n \approx 1.55$)
LLJ	**L**ong **L**ap **J**oint
LP	**L**ong **P**ass
LPG	**L**ong **P**eriod **G**rating

MDS	**M**ercaptomethyl**d**imethylethoxy**s**ilane
MMF	**M**ulti **M**ode **F**ibre
MOF	**M**icrostructured **O**ptical **F**ibre
MTS	3-**M**ercaptopropyl**t**rimethoxy**s**ilane
Nd:YAG	**N**eo**d**ymium-doped **Y**ttrium **A**luminium **G**arnet
NHS	**N**-**H**ydroxy**s**uccinimide
NOI	**N**ormalised **O**verlap **I**ntegral
OD	**O**uter **D**iameter
OSA	**O**ptical **S**pectrum **A**nalyser
OTDR	**O**ptical **T**ime **D**omain **R**eflectometry
PAH	**P**oly(**A**llylamine **H**ydrochloride)
PBG	**P**hotonic **B**and**g**ap
PF	**P**ower **F**raction
PML	**P**erfectly **M**atched **L**ayer
PMMA	**P**oly(**m**ethyl **m**eth**a**crylate)
PMT	**P**hoto **M**ultiplier **T**ube
PU	**P**oly **U**rethane
PVA	**P**oly**v**inyl**a**lcohol
SEM	**S**canning **E**lectron **M**icroscope
SERS	**S**urface **E**nhanced **R**aman **S**pectroscopy
SF57	Lead-Silicate Glass ($n \approx 1.85$)
SLJ	**S**hort **L**ap **J**oint
SMF	**S**ingle **M**ode **F**ibre
SPR	**S**urface **P**lasmon **R**esonance
UV	**U**ltra **V**iolet
WW	**W**agon **W**heel Fibre (Enclosed suspended-core MOF)

Part I

Introduction

Chapter 1

Motivation and Thesis Structure

In science one tries to tell people,
in such a way as to be understood by everyone,
something that no one ever knew before.
But in poetry, it's the exact opposite.

Paul Dirac

1.1 Motivation

The field of optical fibre sensing has received great interest over the last 30 years [1–3]. Strain and temperature sensors using fibre Bragg gratings are commercially available, along with optical fibre gyroscopes and other physical sensors [1]. Of increasing interest is the field of chemical and biological sensing, which has traditionally made use of evanescent field sensing such as through absorption and fluorescence [3, 4]. Sensors utilising alternative transduction mechanisms have been developed, such as surface plasmon resonance [5] and surface enhanced Raman spectroscopy [6], but because of the versatility and sensitivity of fluorescence-based sensing [7] it was the focus of this project. In particular, fluorescence-based sensing can be used effectively for corrosion sensing [8], which was the application that motivated this project. In fluorescence-based sensing the analyte can either be fluorescent or an indicator can be used where its fluorescence intensity is dependent on the analyte concentration [7]. Evanescent coupling of the fluorescence emission into the guided modes of the fibre thus allows a measurement of the analyte. High sensitivity is possible due to fluorescence emission generally being greater than other mechanisms such as Raman scattering, and versatility and selectivity can be achieved through appropriate choice of an indicator [4].

Along with an increase in chemical and biological sensing applications using optical fibres, over the last 10 years there has also been a dramatic increase in the range of optical fibre geometries that have been studied. Conventional step-index fibres have been modified by tapering [4] or with D-shaped designs [9] in attempts to gain greater access to the guided optical field. A more intricate concept has been the microstructured optical fibre (MOF), which contains a pattern of air holes that run along its length [10]. The design flexibility of microstructured fibres allows greater control over the optical properties, which for sensing applications is usually exploited by increasing the fraction of the optical field that interacts with the analyte [11, 12].

Despite the potential of microstructured fibres to deliver highly sensitive measurements and the wealth of published examples (see Sec. 2.5.4), there has been relatively little detailed theoretical investigation into the mechanisms of fluorescence-based sensing using MOFs. While it is generally understood that higher evanescent fields and numerical apertures are beneficial, it is unknown how current theoretical models for conventional

step-index fibres [13–20] behave when high index contrasts are present and when operating in the single (or few) mode regime, as is often the case for microstructured optical fibres. There has also been a dearth of experiments that verify current theoretical models. One of the aims of this project was thus to develop a theoretical model and perform subsequent experiments for fluorescence sensing with MOFs.

In addition to the above theoretical questions, there are also several practical challenges associated with using microstructured optical fibres for chemical and biological sensing applications. Firstly, it is necessary to develop a method for fabricating these structures, which can become increasingly difficult as the fibre's features increase in complexity or reduce in size. A method for fabricating fibres with small (nanoscale) dimensions is presented in [P6] of this thesis, which was led by Heike Ebendorff-Heidepriem.

Other challenges stem from the fact that the analyte must infiltrate the holes of the MOF in order to interact with the evanescent field. This can be readily achieved with either diffusion of gases or capillary forces for liquids but results in a time delay for measurements and prevents distributed measurements from being possible. The question is thus how to modify an MOF structure so that the core can be exposed to the external environment along the length of the fibre thus allowing real-time and distributed sensing to be achieved. In this project an exposed-core MOF has been designed, fabricated, and investigated theoretically and experimentally.

Finally, an ongoing problem for all forms of optical fibre chemical and biological sensing is how to make the sensor sensitive to the analyte of interest if the analyte has no intrinsic optical fingerprint in the transmission window of the optical fibre materials. The particular application investigated in this project was the sensing of corrosion, and several methods for achieving this have been studied in this thesis.

1.2 Project Aims

The aims of this project were to answer the questions above with particular emphasis given to the suspended-core design of microstructured optical fibre shown in Fig. 1.1(a, b). As will be seen in the literature that follows, this design has several advantages such as simple filling characteristics and a high percentage of optical power in the evanescent field if the core is fabricated small enough. Another aim of this project was to modify

the design such that the core is partially exposed along its length as shown in Fig. 1.1(c). This exposed-core fibre design can potentially solve the problems of slow filling speeds and inability to perform distributed sensing using traditional enclosed MOFs.

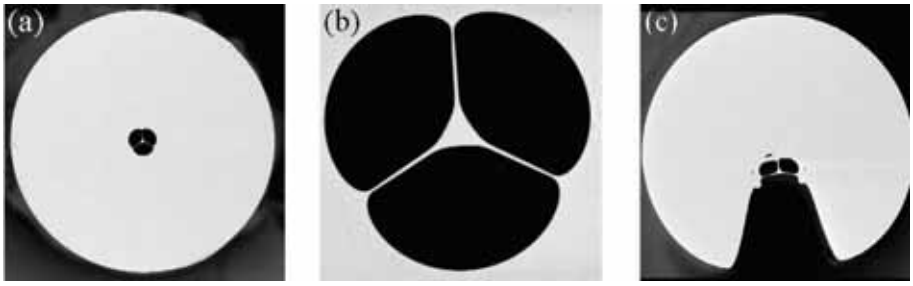

FIGURE 1.1: Enclosed (a, b) and exposed (c) suspended-core microstructured optical fibre.

Specifically, the aims of this project are to:

1. Construct a general theoretical model that is capable of quantifying the performance of evanescent field fluorescence sensing using microstructured optical fibres.
2. Use this model to optimise the geometry and materials of suspended-core MOFs, for both enclosed-core and exposed-core variants.
3. Fabricate suspended-core fibres and use these to test the fluorescence capture theory.
4. Design and fabricate an exposed-core MOF.
5. Demonstrate that the exposed-core MOF can be used for real-time and distributed fluorescence sensing.
6. Investigate methods for sensitising the surface of MOFs (and glass surfaces in general) for the particular application of aluminium ion sensing, and thus corrosion sensing of aluminium alloys.

Corrosion sensing (described in more detail in Sec. 2.8 and Chapter 5) was the application that motivated this project, and it highlights the importance of the advantages that come with using fluorescence sensing in conjunction with exposed-core MOFs. Firstly, corrosion by-products such as aluminium ions do not have distinct fingerprints at optical wavelengths and thus fluorescent indicator methods can provide a transduction mechanism. Also, high sensitivity, which can be achieved by using MOFs, is desired so

that corrosion can be detected early and thus safety can be improved and repair costs minimised. Finally, distributed sensing, such as using time-domain methods, is highly desirable for corrosion sensing as corrosion events are generally not uniform across an entire structure. That said, the fibre designs and surface sensitisation methods developed in this project are directly applicable to practically any other chemical analyte, provided a suitable indicator can be found. This includes, but is not limited to, pH, cations, anions, gases such as hydrogen and methane, humidity, and organic molecules [4].

1.3 Thesis Structure

This thesis is primarily comprised of the eight publications listed on page 9. Most of these publications are interconnected, such as with fibre fabrication required in order to perform certain experiments or theory dictating desired fibre dimensions. The flowchart on page 10 conveys how these publications relate to each other, and also places in context the additional chapters and appendices.

Chapter 3 (black) contains theoretical derivations and modelling, and experimental results that were performed specifically for comparison with theory. [P1, P2] contain the development of the fluorescence capture theory, with a full derivation given in Appendix A. This theory is then extended for the case of exposed-core MOFs [P3], inclusion of higher order modes [P4], and thin layer sensing [P5]. Coupling between filled and unfilled regions of fibre is also included in [P3] and a derivation of the equations used to calculate this is given in Appendix B. Confinement loss of small-core MOFs is added to the theory in [P4] and a derivation of the equations used to calculate this is given in Appendix C.

Chapter 4 (orange) contains details of the methods used to fabricate the enclosed suspended-core [P6] and exposed-core [P7] MOFs, in addition to characterisation of their transmission and fluorescence sensing properties. In particular, experiments were performed to demonstrate that exposed-core fibres can be used for real-time [P7] and distributed [P8] sensing. The enclosed suspended-core fibres fabricated in [P6] were also used for experiments in [P2, P4, P5] for testing several theoretical predictions.

Chapter 5 (blue), which does not contain any publications, investigates two methods for sensitising the fibres fabricated in [P6, P7] for the application of aluminium ion sensing, and thus corrosion sensing of aluminium alloys. As indicated in the flowchart, Chapter 5 and [P8] together demonstrate significant progress towards accomplishing the ultimate, but challenging, goal of distributed corrosion sensing using exposed-core microstructured optical fibres.

Flowchart showing the links between chapters, publications, and appendices

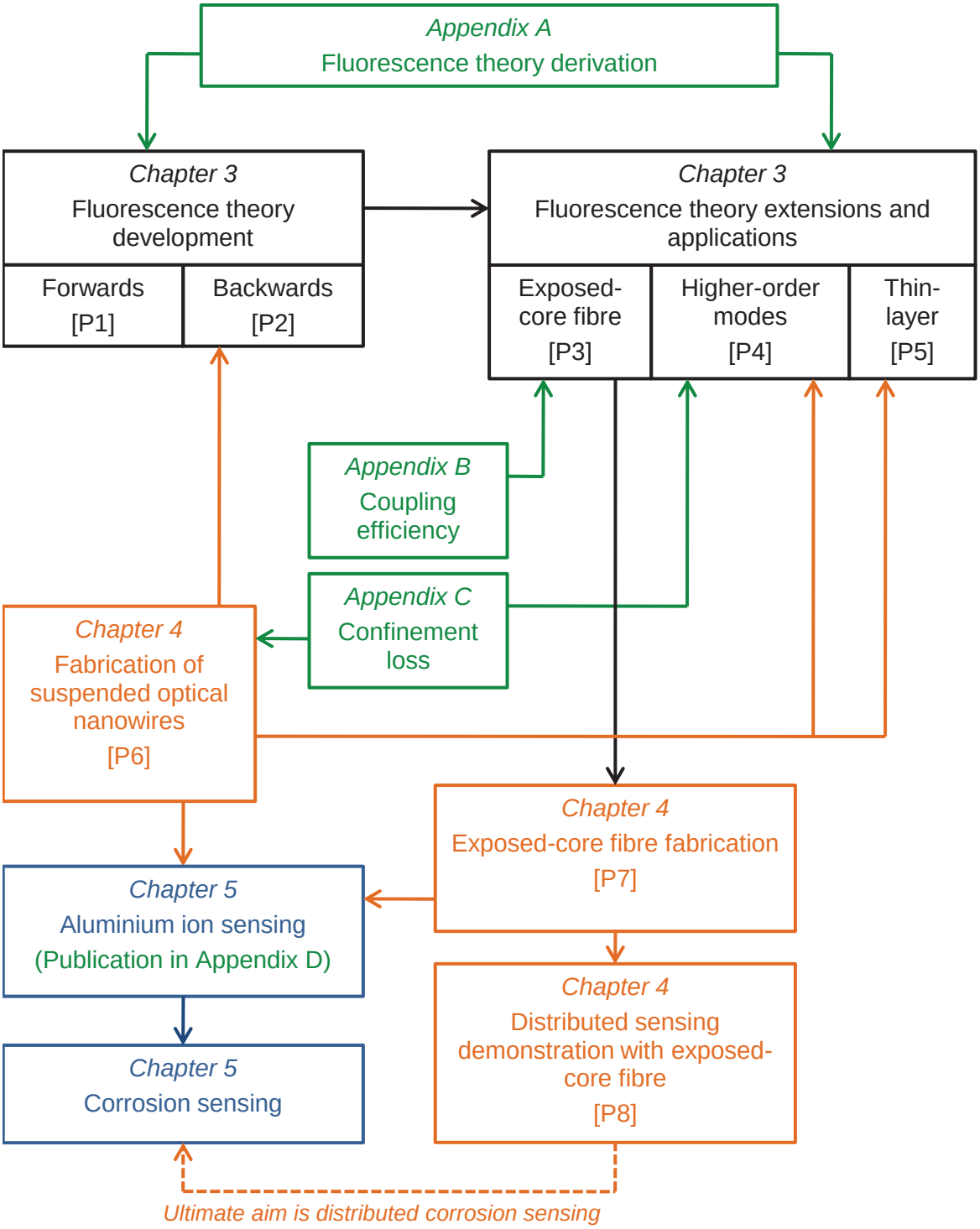

Chapter 2

Review of Optical Fibre Chemical Sensing

A man ceases to be a beginner in any given science and becomes a master in that science when he has learned that he is going to be a beginner all his life.

Robin G. Collingwood

We shall not cease from exploration,
And the end of all our exploring
Will be to arrive where we started,
And to know the place for the first time.

T. S. Eliot

2.1 Introduction

Optical fibres can be used for a wide variety of sensing applications such as gyroscopes [2], pressure sensing [2], strain and temperature sensing [21], and chemical and biological sensing [4, 7]. Many advantages of using optical fibres for sensing have been quoted and these include [4, 7]:

- Optical fibres are small, light weight and flexible, allowing them to be located in inaccessible regions in a non-destructive manner. This can allow fibres to be permanently imbedded into structures and allow continuous monitoring without any need to dismantle the structure.
- Optical fibres can be used for distributed sensing. By using optical time domain reflectometry or similar radar-type methods, optical fibre sensors can make measurements that are correlated with position along the fibre.
- Optical fibre sensors can be wavelength division multiplexed, allowing several different parameters to be measured simultaneously.
- Depending on the application and method used optical fibre sensor designs can offer highly sensitive measurements.
- Optical fibres are resistant to electromagnetic interference.
- Optical fibres do not carry currents and are thus safe for use in explosive or flammable environments.

Of course, challenges associated with using optical fibres for sensing have also been identified, such as [1]:

- Creating low-loss fibres, particularly after a transduction mechanism is added.
- Creating good detection systems, which is relevant for any optical fibre application including sensing.
- Finding an appropriate transduction mechanism that operates in the high transmission window of optical fibres, which generally lies within visible and near-infrared wavelengths. Alternatively, this can be solved by using stronger excitation

sources and better optical detection methods, or fabricating fibres from materials with different transmission windows.

- For evanescent field based sensors, designing a fibre that has sufficient optical field interaction with the analyte. As will be seen in this review, this issue has lead to many different designs of optical fibre.
- Economics. To be commerically successful the final sensor must either be cost competitive with alternative sensors or have a strong functional advantage, such as those outlined above.

The aim of this literature survey is to present an overview of work in the literature for chemical sensing using optical fibres, with a particular emphasis on fluorescence methods and corrosion sensing. Much of the review focusses on the optical fibre design, such as methods used to gain (greater) access to the optical field. Also considered are methods for distributed sensing and methods for sensitising fibres using various coatings.

2.2 Classification of Optical Fibre Chemical Sensors and Chapter Overview

There are several methods for classifying optical fibre chemical sensors [7]. One classification is to separate intrinsic and extrinsic sensors. For extrinsic sensors the optical fibre simply acts as a method of sending and receiving optical signals whereas an intrinsic sensor is such that the optical fibre itself is used to construct the sensor, in addition to carrying optical information. Another form of classification is to define direct and indirect sensors. Direct sensors use the interaction of the light carried by the fibre with the analyte of interest, such as absorption, fluorescence, or Raman emission, while indirect sensors require some form of additional transduction mechanism such as an indicator molecule. Optical fibre chemical sensors can also be classified according to the type of light modulation that is used to make the measurements, this can be amplitude, wavelength, phase, polarisation, or time [7].

In this review optical fibre chemical sensors are broadly separated into intrinsic and extrinsic sensors, with the other classifications discussed within. It should be noted that the subclassifications within these categories are not exclusive, that is, the mechanisms

discussed within the extrinsic sensors can generally be used in an intrinsic sensing configuration and vice versa. However, the inclusions in each section generally indicate the more commonly used approaches for that particular configuration.

Some simple extrinsic optical fibre sensors will be discussed first in Sec. 2.3, followed by intrinsic sensors in Sec. 2.4. Several types of intrinsic sensors are discussed such as grating and surface plasmon resonance sensors. However, the sensing mechanism ultimately chosen for this project was evanescent field based sensing and this is discussed in detail Sec. 2.5, with a particular emphasis on microstructured optical fibres and optical nanowires. The subsequent section discusses some of the methods currently available for sensitising evanescent field sensors for chemical sensing (Sec. 2.6). Next, a review on distributed chemical sensing (Sec. 2.7) and corrosion sensing (Sec. 2.8) is given, followed by a discussion on how this review relates specifically to the work contained within this thesis.

2.3 Extrinsic Sensors

2.3.1 Basic Optical Fibre Sensing

The simplest use of an optical fibre for chemical sensing it to use it as means of carrying light to and from the sensing environment. In this way, the interaction between the electromagnetic field and the analyte such as scattering, absorption, or fluorescence occurs at a location physically separate from the fibre. As seen in Fig. 2.1, this type of sensor can consist of an input fibre that carries an excitation signal to the region of interest, the light then transmits through this region, and a second fibre captures and carries the optical output to a detector [3].

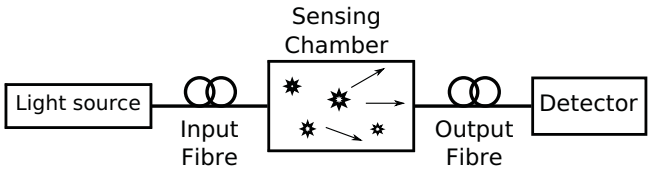

FIGURE 2.1: Extrinsic optical fibre sensor where the measured optical intensity is inversely proportional to the scattering or absorbing material.

This design of sensor has been commonly demonstrated for the detection of gases, methane in particular, using absorption spectra in the near infrared [22–24]. Interest in this area has been generated due to the desire to have a safe sensor for explosive and flammable gases, which can be provided by optical fibres as they do not carry currents and can have their source and detection units located up to several kilometres away from the sensing location [23]. However, an evident difficulty with using optical fibres for methane detection is that the absorption lines in the transmission window of silica are approximately 200 times weaker than in the mid-infrared [23]. To overcome this problem signal processing techniques have been developed such as the use of a distributed feedback laser for frequency modulated spectroscopy [22].

Using optical fibres in the way described above does not allow for truly distributed sensing. However, work has been done to create a multi-point sensor that allows for quasi distributed sensing. The aim is to place sensors at different locations but only using one optical source, and if possible, only one detection device. Culshaw *et al.* proposed three different approaches for multipoint sensing, which are shown in Fig. 2.2 [23].

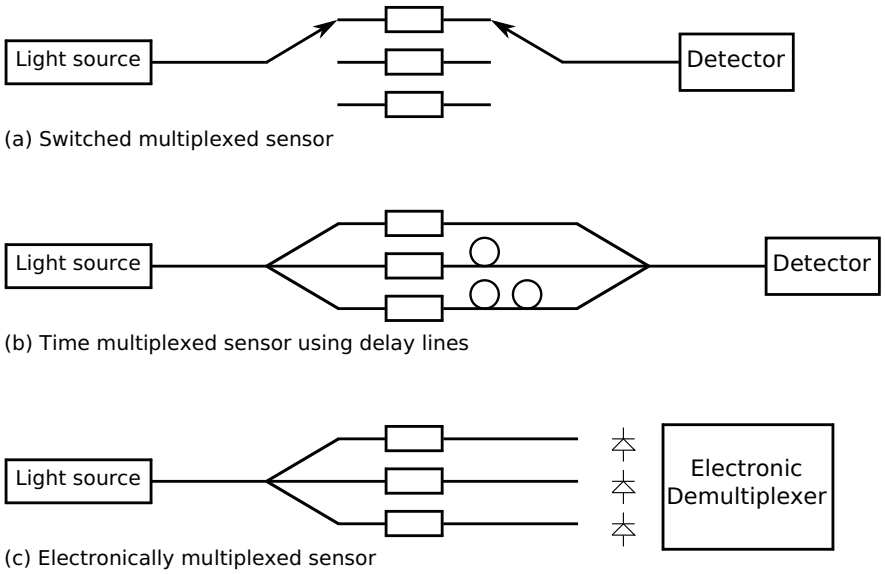

FIGURE 2.2: Three methods for multiplexing extrinsic optical fibre sensors [23]. (a) A switch can be used to connect to the different sensors. (b) Time domain multiplexing using optical delay lines. (c) Electronically multiplexed.

In Fig. 2.2(a) an optical switch is used to swap between the different sensing channels, which has the benefit of using only one source and detector but requires the use of an expensive optical switch. Figure 2.2(b) shows how an optical switch can be avoided

by using optical delay lines to separate the signals from each channel. However, due to the excessive amount of optical fibres that would be required for the system in Fig. 2.2(b) the authors decided that the system shown in Fig. 2.2(c) would be the most cost effective approach where the data from each sensor element is separated using an electronic demultiplexer [23]. These designs of quasi-distributed sensing can in principle be applied to any design of optical sensor and should be kept in mind when considering fibre sensors that do not intrinsically have fully distributed sensing potential.

2.3.2 Distal End Sensing

The use of the distal end of a fibre for the sensing of chemicals has been widely used due the simplicity of the design. The demonstrated applications for distal end sensing are varied and examples include the sensing of gases, pharmaceuticals, pH, and corrosion.

Concepts

Distal end sensing is similar to that discussed in Sec. 2.3.1, but with the subtle differences that the sensing occurs close to the fibre's distal end and usually the same fibre is used to supply the source light and collect the resultant signal. This is achieved with either a bifurcated fibre [8] or a fibre bundle [25] as shown in Fig. 2.3. The sensing systems discussed in this section also differ from the systems described in Sec. 2.3.1 because an indicator is often located at the distal end of the fibre, thus they are indirect sensors. This indicator produces a measurable optical signal when in the presence of the desired analyte such as by producing or quenching fluorescence, or altering its absorption spectrum. Also important is the need for a permeable matrix to support both the analyte and the indicator. The selection of indicator and carrier matrix is specific for the particular sensing application. A few case by case examples are given below with more detail described later, in Sec. 2.6.

Chemical Sensing Examples

Wolfbeis *et al.* demonstrated the use of distal end sensing with the simultaneous measurement of oxygen and carbon dioxide using fluorescent indicators [26]. Two separate gas permeable layers were deposited onto the fibre tip, one that fluoresces in the presence

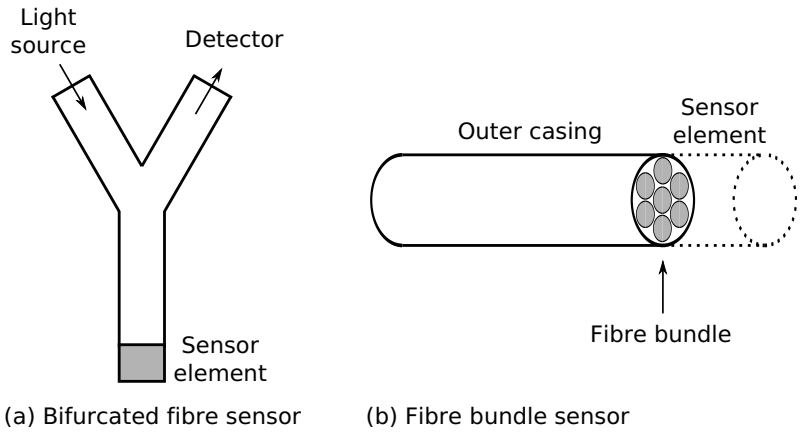

FIGURE 2.3: (a) Bifurcated optical fibre sensors. (b) Optical fibre bundle.

of oxygen and the other for carbon dioxide. The materials were chosen because their excitation could occur at the same wavelength but the fluorescence emissions were separate. Hence, two chemicals could be measured separately and simultaneously but only one optical source was required, thereby demonstrating the possibility of multiplexed fibre sensors.

The development of indicators has meant that distal-end fibre sensing is not limited to the measurement of gases. For example, Zhang *et al.* successfully developed a mercury ion sensor based on the fluorescence quenching of a porphyrin dimer [27]. Two significant results were obtained in this study, the first being that the sensor was selective to mercury ions over many other transition metals, which can prevent the false positive detection of mercury. Also, the sensor demonstrated good reversibility when washed and re-exposed to mercury ions. Another example of using fluorescence quenching was demonstrated by Wen-xu *et al.* [28]. In this study a sol-gel was used to attach a fluorescent chemical to the distal end of a fibre whose fluorescence was quenched proportional to the concentration of Adriamycin, which is a drug used for cancer chemotherapy. This method was shown to be successful in the measurement of Adriamycin *in-vivo*, that is, in the blood system of an animal.

One of the early demonstrations of using an optical fibre for the sensing of pH was achieved by Peterson *et al.* in 1980 [25]. The design of this sensor was to place two fibres into a plastic tube that was packed with phenol red, a pH indicator, allowing one to supply the light and the other to collect the scattered reflection. The tube located at the distal end of the fibres also contained polystyrene microspheres that allowed for

greater light scattering, increasing the efficiency of the light collection. This sensor was then used to correctly measure the pH of blood samples in the range of 7.0 to 7.4.

Double-Clad Fibres for Two Photon Fluorescence Sensing

In general, distal-end fibre sensing uses the same optical fibre to supply the source signal and collect the resultant optical signal. Furthermore, because the interaction occurs at the tip of the fibre there are generally no special features that direct the optical signal back into the fibre other than the intrinsic collection properties of the fibre, which are generally quite poor using standard fibres [29]. For single photon fluorescence the simplest optimisation is to increase the numerical aperture and core diameter of the fibre to increase the collection angle and area, such as by using multi-mode fibres. However, two photon fluorescence is a nonlinear interaction and thus high peak intensity for the excitation is desired [30], which can be achieved by using single mode fibres.

A proposed solution to this trade-off problem is to make use of a double clad optical fibre, which can be an all-solid design, or a more intricate design as shown in Fig. 2.4 [29, 30]. This design of microstructured optical fibre (MOF, see Sec. 2.5.4) allows the inner core to be excited at high intensity. The outer cladding is then a collector of the return optical signal, such as fluorescence, with higher collection efficiency than if collecting with only the inner core. Using MOFs is particularly advantageous due to the high numerical aperture that is possible using air and glass refractive indices, thus providing a greater acceptance angle for collecting the signal. Myaing *et al.* found that the collection efficiency improved by approximately nine times compared with a conventional single mode fibre [29].

FIGURE 2.4: Double clad microstructured optical fibres used to enhanced the collection numerical aperture. Images from Ref. [29] (a) and Ref. [30] (b).

Konorov *et al.* noted that this design can also be useful for (linear) single-photon fluorescence if high precision positioning of the excitation beam is desired [30], which could have applications in fluorescence imaging.

Discussion

The use of distal end sensing has been demonstrated for many applications, some of which are discussed above, such as the sensing of pH, gases, pharmaceuticals, and corrosion. The advantage of this design is in its simplicity where only a single bifurcated fibre is needed for the measurement in addition to an indictor attached to the end of the fibre. A disadvantage of this design is the low efficiency with which the optical signal is collected by the fibre. This design also does not make use of the long interaction lengths that can be achieved using optical fibre and distributed sensing cannot be performed, which is desirable in many applications such as corrosion monitoring [8]. Thus, while distal end, and more generally extrinsic, optical fibre sensors can be implemented for many applications, it is intrinsic sensors that utilise some of the more unique advantages of optical fibres as will now be seen.

2.4 Intrinsic Sensors

2.4.1 Evanescent Field Sensing

A conventional optical fibre operates on the principle of total internal reflection. However, not all of the propagating light is bound to the core as a small fraction propagates in the cladding, which is known as the evanescent field [31]. By allowing an analyte to come into contact with the evanescent field any traditional spectroscopic measurement can be performed such as absorption spectroscopy or fluorescence measurements.

Evanescent field sensing is possibly the most commonly studied method for optical fibre chemical sensing. Due to its versatility, sensitivity, and ability to be used for distributed sensing it has been chosen as the sensing mechanism to be studied in this project. Therefore, it is discussed in detail in Sec. 2.5, after discussion on some of the alternative intrinsic sensing configurations.

2.4.2 Grating Sensors

Fibre gratings can be classified into two categories, fibre Bragg gratings (FBG) and long period gratings (LPGs). Both types of gratings consist of a periodic variation in refractive index along the fibre axis that couples light out of the forward propagating core-guided mode(s) [2].

A fibre Bragg grating has a periodic variation in refractive index such that phase matching of the forward propagating mode causes a particular wavelength to reflect into the backward propagating mode(s) [2]. This creates a characteristic minimum at a wavelength (Bragg wavelength) given by

$$\lambda_B = 2n_{eff}\Lambda, \tag{2.1}$$

where λ_B is the reflected Bragg wavelength, n_{eff} is the effective index of the core guided mode, and Λ is the grating period [2]. Alternatively, LPGs have grating periods in the order of millimeters, which couple light from the core guided modes into the cladding modes [2].

Bragg gratings are generally used to create temperature and strain sensors using the dependence of refractive index on temperature and grating period on strain [2]. When considering chemical sensing, the concept of measuring strain using a FBG has been studied for the purpose of corrosion sensing [32–35]. In this design a section of an FBG was prestrained and then coated with the metal of interest [34]. Before corrosion occurs there are two distinct Bragg wavelengths corresponding to the prestrained and unstrained sections of grating. When corrosion occurs the strain is released and only one Bragg wavelength remains. The advantage of using this technique is that the measurement is not dependant on parameters such as light intensity or temperature [32].

Chemical sensors usually make use of long period gratings (LPGs) because they couple the forward propagating mode into cladding modes as shown in Fig. 2.5 [1, 21, 36, 37]. The wavelength of light that is coupled into the cladding is dependant on the refractive index of the cladding itself. As the cladding light is generally attenuated quickly, a characteristic minimum which is dependent on the refractive index of the cladding materials can be measured at the fibre output [38].

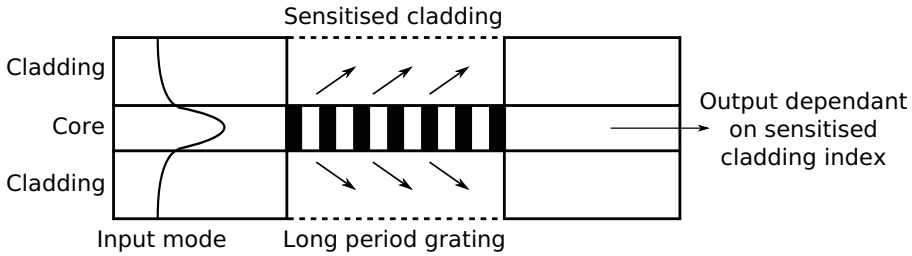

FIGURE 2.5: Long period grating optical fibre sensor.

Examples of using LPGs for chemical sensing include work done by Allsop *et al.* where organic aromatic compounds were detected in a paraffin solution. This design was able to detect changes in concentration of approximately 0.04% [38]. DeLisa *et al.* also successfully used an LPG for the measurement of antibodies [37].

It should also be noted that grating sensors can be used for both time domain distributed sensing (Sec. 2.7) and wavelength division quasi-distributed sensing [39]. For example, a 64 element quasi-distributed fibre Bragg grating sensor system has been demonstrated using wavelength division multiplexing [2]. As will be seen in Sec. 2.8.3, LPGs have been studied for the purpose of corrosion sensing and can be considered an alternative to the evanescent field sensors developed in this project. The primary motivation for evanescent field sensing over LPG sensors is that continuous distributed sensing is possible, and more direct measurements can be made such as the measurement of aluminium ions from corrosion of aluminium alloys [8].

2.4.3 Surface Plasmon Resonance Sensing

Surface plasmon resonance (SPR) sensors make use of the sensitive resonance properties between a dielectric and thin metal coatings. Surface plasmon resonance forms by excitation of a surface mode at the boundary between a dielectric, such as an optical fibre, and a metal [40]. This excitation occurs for a resonance wavelength and is strongly dependant on the angle of incidence, the metal thickness, and the external refractive index [41]. SPR is used with optical fibres by coating the core of a fibre with a metal film and then observing the resonance wavelength in the transmission spectrum [41]. Chemical sensors make use of the dependence of the resonant wavelength on the external refractive index. For example, Jorgenson *et al.* demonstrated the use of SPR in an optical fibre chemical sensor [41]. In this research a thin layer of silver (550 Å) was deposited onto the core of a single-mode fibre. The results showed a non-linear correlation between the

refractive index of the analyte (varied fructose solutions) with the resonance wavelength. It is unlikely though that SPR sensors could be used for sensing chemicals that do not induce a significant change in the refractive index, such as low concentrations of metals ions, unless an additional transduction mechanism is designed.

Recent work has seen an interest in using this concept with microstructured optical fibres and optical nanowires (see Sec. 2.5.4), with the promise of higher sensitivity [42–47]. A difficulty with using microstructured optical fibres for SPR is that most metal deposition techniques cannot be used in the confined space of the fibre holes. A method for avoiding this problem was demonstrated using a side access (exposed-core) MOF [47] (see Sec. 2.5.4). This allowed for deposition by sputtering into the open region of the fibre, unlike other proposed methods that involved passing fluids though the holes of the fibre [45]. While MOFs can provide higher sensitivity, a direct result is that metal coated MOFs generally have large optical loss due to a greater interaction between the optical field and the highly attenuating metal. Loss predictions are in the order of at least several few dB/cm away from the resonance, and up to 250 dB/cm at resonance [44, 45]. Clearly MOF based SPR sensors are not particularly amenable to distributed sensing, but are nevertheless a promising design for highly sensitive refractive index point sensing.

2.4.4 Surface Enhanced Raman Spectroscopy

Raman spectroscopy is a useful tool for chemical and biological sensing as the analyte generally has a fingerprint that can allow for selective detection without the need for labelling or an indicator [48]. Optical fibres have been demonstrated as useful devices for Raman-based sensing both in intrinsic and extrinsic configurations. For example, Pristinski *et al.* have shown that microstructured optical fibres can be used for intrinsic Raman sensing when the air holes are filled with acetonitrile [49]. However, a more sensitive and commonly used approach is to further process the fibre so that surface enhanced Raman spectroscopy (SERS) can be used [6, 48, 50–52]. SERS is achieved by coating metal particles onto either the optical fibre tip or along the length of the fibre. The metal particles serve to increase the electric field and thus increase the Raman interaction. Examples include using a chemically etched tip of a conventional fibre [50], a chemically etched fibre bundle [51, 52], and along the length of different microstructured optical fibres [48].

SERS is not commonly used for the sensing of metal ions and would thus seem an unlikely candidate for aluminium ion or corrosion sensing, though some examples do exist, such as the indirect measurement of copper ions via an interaction with 4-Mercaptopyridine [53]. SERS also suffers from the fact that the metal coatings, as is the case with surface plasmon resonance sensors, increase the optical loss [6] and thus SERS sensors are best suited to applications where specificity is required, rather than, say, distributed sensing.

2.4.5 Interferometric Sensors

Interferometric sensors make use of the phase information present within an electromagnetic wave. Here the interference between a reference beam and a sensing beam reveal information on the refractive index of the analyte, which can be correlated with concentration [7]. These sensors make use of any of the common configurations used for free-space optics, that is, the Fabry Perot, the Michelson, the Mach-Zehnder, and the Young configurations [7]. Advantages of this method, over say intensity based sensors, is that the measurement is not affected by variations in system power, and compensation for variations due to temperature can be made via the reference arm. As with SPR and Raman sensing, these sensors can be used for any application where a transduction mechanism between the analyte and the refractive index can be made, but the concept generally cannot be used for distributed sensing.

2.5 Evanescent Field Sensing

2.5.1 Concepts

The evanescent field is a wave property of the electromagnetic propagation that is derived by solving Maxwell's equations [54]. The evanescent field decays exponentially out from the core and extends to a distance approximately equal to the wavelength of the propagating light as shown in Fig. 2.6 [55]. Note that the fraction of guided light that propagates within the evanescent field is sometimes referred to as the power fraction (PF) [54].

The principle of evanescent field sensing is to allow an interaction between the evanescent field and the analyte so that spectroscopic measurements can be utilised to detect and

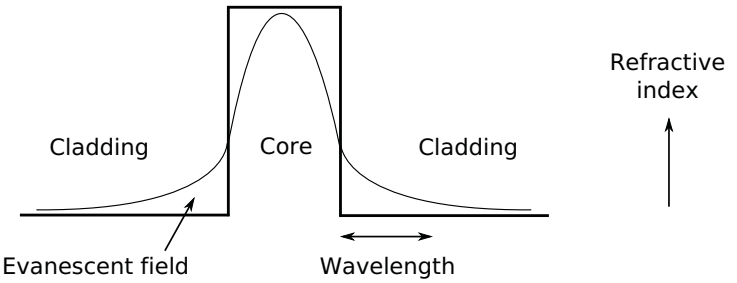

FIGURE 2.6: Evanescent field of a step-index optical fibre, which extends a distance of approximately the wavelength of the propagating light into the cladding.

measure the desired chemical [55]. Spectroscopy can be used to measure an intrinsic property of the analyte, such as its optical absorption spectrum or fluorescence emission. Commonly though, as with extrinsic sensors (Sec. 2.3), an indicator dye is used as a transduction mechanism as the analyte often does not have suitable spectroscopic properties within the transmission window of conventional optical fibre materials [7]. This indicator dye can operate through a change in its absorption and/or fluorescence properties. Much of the challenge is to immobilise these indicator dyes onto the optical fibre surface and some of the methods used to achieve this will be discussed in Sec. 2.6.

The type of fibre used for evanescent field sensing can broadly be categorised into two groups; multi-mode fibres (MMF) and single mode fibres (SMF). Multi-mode fibres are generally less sensitive compared to single-mode fibres due to the evanescent field percentage being inversely proportional to the optical fibre V-number, and thus the number of supported modes [56]. However, the core diameter of multi-mode fibres are more practical to handle as they can be in the order of 100 μm or greater, whereas the core diameter of single-mode fibres need to be much smaller. While the outer diameter of the fibre is dictated by the cladding diameter, not the core diameter, for an evanescent field sensor the core must be exposed to the external environment at least partially, and thus single mode fibre sensors are generally more fragile.

2.5.2 Multi Mode Fibres

Unclad Bare Fibres

The simplest method for using the evanescent field for chemical sensing is to use an unstructured glass (or polymer) fibre which can either be fabricated as such or produced by removing the cladding of a conventional step-index fibre. The whole unstructured

(or bare) fibre forms the core and is placed into an analyte, where the analyte, or the solution it is dissolved in, acts as the cladding.

Bunimovich *et al.* demonstrated infrared spectroscopic measurement of gas partial pressure using an unclad multi-mode fibre [57]. The sensor was successful at both detecting the gases and also at quantitatively measuring their concentration by use of the Beer-Lambert law, although with limited accuracy. Likewise Potyrailo *et al.* demonstrated the ability to use fibre optics for near-ultraviolet spectroscopic measurements of ozone [58]. In this study an unclad fibre was compared with a plastic-clad fibre with selective permeability. It was concluded that the permeable cladding is a superior design compared to the bare unclad fibre due to its ability to protect the surface of the core, preventing surface contamination and subsequent signal loss.

The use of permeable coatings doped with indicators has been studied extensively for evanescent field sensors in order to increase the sensor versatility and sensitivity. For example, the cladding can be replaced with a permeable coating such as the polymers polyvinylalcohol (PVA) [59] and polymethyl methacrylate (PMMA) [31], or sol-gel [60]. These coatings can then be doped with indicators for the particular chemical of interest. For example, a pH sensor can be constructed by doping the coating with pH sensitive chromoionophores such as methyl red and thymol blue [31]. Absorption measurements are then used to detect and measure the pH of the surrounding environment. This process has also been used for the detection of other complex chemicals such as proteins [60].

The above examples were based on absorption measurements, but other mechanisms are of course possible. Xu *et al.* demonstrated the use of evanescent-wave scattering for the measurement of atmospheric relative humidity when using a porous sol-gel coating [55]. A more common approach is to use fluorescent indicators [7]. Lieberman *et al.* fabricated an oxygen sensor by doping the cladding with an organic fluorescent indicator dye [61]. The fibre was side illuminated so that a small fraction of the fluorescence was captured by the guided modes of the fibre. When in the presence of oxygen the fluorescence reduced depending on the oxygen concentration, hence allowing for quantitative measurements of the oxygen concentration. A key aspect is the amount of the fluorescence which is captured by the guided modes. This value is stated as being strongly dependant on the fibre's V-number and was approximately 0.02% for the particular fibre used in this

study as calculated using the work of Marcuse [17]. The experimental results showed a slightly larger value for the capture efficiency than the theoretical prediction for unknown reasons. Regardless, the amount of captured fluorescence possible is quite small and hence attempts have been made to increase the capture efficiency. For example, Kao *et al.* modelled and tested the use of a thin, high refractive index sol-gel core coating to increase the collection efficiency of an evanescent-field sensor [14]. Both theoretical studies and experiments confirmed this method and showed that there is an optimal choice of refractive index and width of the sol-gel coating for maximum fluorescence capture.

Optimising Multi-Mode Evanescent Field Sensing

The sensitivity of a multi-mode evanescent field sensor is generally quite poor due to the evanescent field percentage being inversely proportional to the optical fibre V-number, and thus the number of supported modes [56], but it can be optimised by varying the optical fibre properties and the launch conditions. For a multi-mode optical fibre the penetration depth, d_p, of the evanescent field is given by [62]:

$$d_p = \frac{\lambda}{2\pi n_1 (sin^2\theta - sin^2\theta_c)^{1/2}}, \tag{2.2}$$

where λ is the free space wavelength, n_1 is the refractive index of the core, and θ_c is the critical angle of the fibre. As shown by Eq. 2.2, the sensitivity can be improved by exciting rays that are close to the critical angle of the fibre. This can be achieved by modifying the launch optics such as by spatially filtering the input beam [63]. Another method is to use a U-shaped fibre, which allows propagating rays to approach the critical angle of the sensing region if the sensing part of the fibre is bent. This has been demonstrated by Gupta *et al.* where a fibre with a phenol red doped PMMA coating was used to measure humidity as shown in Fig. 2.7 [64]. It was shown that by decreasing the bending radius of the U-shaped fibre the sensitivity of the sensor was increased. For example, the sensitivity can be increased by a factor of 20 by reducing the bending radius from 3.80 mm to 2.45 mm. Similar results were produced by Khijwania *et al.*, who compared the U-shaped fibre with straight conventional unclad fibres [62].

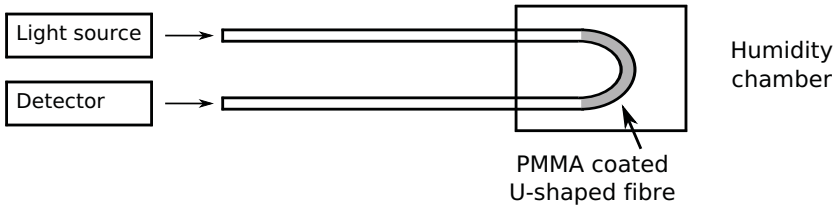

FIGURE 2.7: U-shaped fibre sensor for enhanced evanescent field sensing, in this case for humidity sensing.

2.5.3 Single Mode Fibres

The alternative to multimode fibre sensing is the use of single mode fibres, which can generally provide a significantly higher overlap of the evanescent field with the analyte. As stated previously, the sensitivity of evanescent field sensors is inversely proportional to the fibre's V-number, which is given by [54]:

$$V = \frac{2\pi a}{\lambda}\sqrt{n_{core}^2 - n_{clad}^2}, \tag{2.3}$$

where a is the core radius, λ is the free space wavelength, n_{core} is the refractive index of the core, and n_{clad} is the refractive index of the cladding.

Thus, the most sensitive fibre design is to use a single-mode fibre, where the V-number is less than 2.405 [54]. The challenge is to design a fibre that is simultaneously single-moded, allows the optical field access to the external environment, and is practical to handle. The later point is particularly challenging, given that the core diameter generally needs to be extremely small whilst having the core at least partially exposed to the external environment. For example, evaluating Eq. 2.3 shows that an air-clad silica fibre requires the core diameter to be smaller than 320 nm to be single mode at a wavelength of 600 nm. For this reason single-mode evanescent field sensors generally require special fabrication and packaging techniques in order to make them practical to handle, such as the fabrication of D-shape fibres (Sec. 2.5.3) or tapered fibres (Sec. 2.5.3). Of increasing interest are microstructured optical fibres, that can have small features over long lengths while still being practical to handle, and these will be discussed in the next section (Sec. 2.5.4).

D-Shaped Fibres

Rather than removing the entire cladding of an optical fibre, which can reduce the fibre's durability, a different method is to use a D-shaped fibre. A D-shaped fibre has a section of the cladding absent such that the core is close to the external environment on one side as shown in Fig 2.8 [9]. A fraction of the evanescent field can then interact with the surrounding environment in the region of the missing cladding. Stewart *et al.* carried out extensive work on this type of sensor for the purpose of methane sensing, with a simplified version of the experimental setup shown in Fig. 2.8 [9]. It was noted that this design has the advantage of having potential in a distributed scheme and it was also a single mode fibre offering greater sensitivity and stability over previously used fibres. However, there were also several weaknesses pointed out for this design including the still poor overlap between the optical field and the surrounding environment ($\approx 0.1\%$), difficulty in splicing to standard fibre, and low commercial availability.

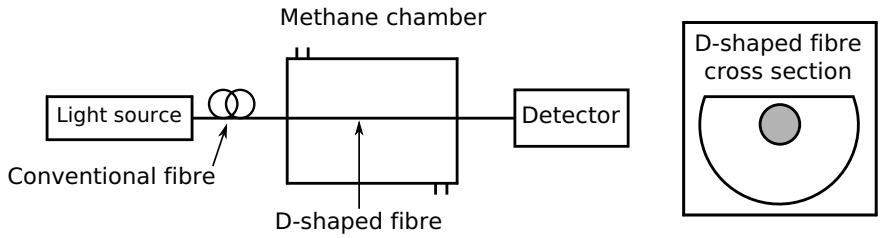

FIGURE 2.8: D-shaped fibre sensor for evanescent field gas (methane) sensing.

Tapered Fibres and Optical Nanowires

Another method to increase the proportion of optical field within the sensing region is to taper the fibre. A fibre taper is fabricated from a conventional fibre by applying tension with the application of heat such as from a CO_2 laser [65]. The effect of this is to produce a thin section of the fibre as shown in Fig. 2.9 where the indicated parameters (a-d) can be varied via fabrication in order to optimise the performance of the sensor [66]. This allows for a highly sensitive tapered region, which can potentially be small enough to be single moded, while being directly connected to a large diameter multi-mode fibre for more practical coupling and handling.

Extending from the concept of tapered fibre sensors is the use of nanowires. Recent sensing research involving nanowires has included using materials such as metals, metal

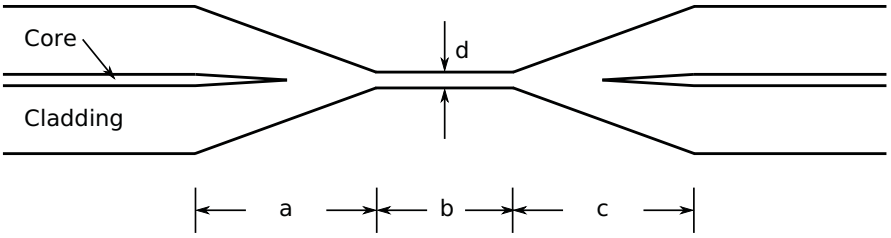

FIGURE 2.9: Diagram of a fibre taper and the key geometrical features.

oxides, polymers, silicon, and silica [67–73]. Of particular interest to this review is the use of silica nanowires because a nanowire is essentially an optical fibre with much smaller dimensions, such as widths as small as 50 nm [73]. Images of optical nanowires fabricated by Tong *et al.* are shown in Fig. 2.10 [73]. The main benefit is that a large portion of the optical energy propagates externally to the nanowire, that is, it has a large evanescent field. Lou *et al.* reported that theoretically the evanescent field can make up between 20% and 100% of the total propagating energy and thus allows for greater interaction with the surrounding environment compared with other evanescent field based sensors [70]. However, the main disadvantage with the use of optical nanowires is that the length of a fabricated nanowire is generally quite small, typically smaller than one millimetre [67] due to the loss and the fragility of a long nanowire, and also the fabrication technique which is often by tapering standard fibre. Consequently, despite the promise of high sensitivity, traditional optical nanowires negate two of the most commonly stated advantages of using fibre optics for sensing being long interaction lengths and the ability to do distributed sensing.

NOTE:
This figure is included on page 29
of the print copy of the thesis held in
the University of Adelaide Library.

FIGURE 2.10: Optical nanowires fabricated by Tong *et al.*. Images from Ref. [73].

It will thus be shown in the next section that a compromise between the sensitivity and accessability (to the analyte) of a optical nanowire and the physical robustness of a multi-mode fibre is the use of a microstructured optical fibre.

2.5.4 Microstructured Optical Fibres

With the emergence of microstructured optical fibre technology there has been increased interest in using these fibres for sensing applications. MOFs generally consist of a single glass material with an arrangement of holes that run along the fibre's length [10], as shown in the examples in Fig. 2.11. Through appropriate choice of holes and material the fibre's optical properties can be tailored to suit the application [74]. The common approach to sensing is to fill the holes of the fibres with the material of interest and the design of the MOF is used to optimise the optical field overlap with the analyte.

NOTE:
These figures are included on page 30 of the print copy of the thesis held in the University of Adelaide Library.

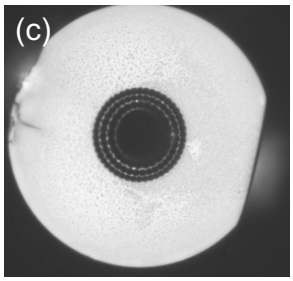

FIGURE 2.11: Example microstructured optical fibres. Images from Ref. [75] (a), Ref. [76] (b) and Ref. [10] (c) . (a, b) are index guiding fibres and (c) is a photonic bandgap guiding fibre.

Concepts

There are two distinct mechanisms for which light can be guided in MOFs; these are known as index guiding and photonic bandgap guiding [10]. Index guiding optical fibres operate by a form of total internal reflection comparable to the manner in which conventional core-clad fibres operate. To obtain the index contrast required to guide light the average index of the cladding, $n_{cladding}$ (often called the effective cladding index, see below), must be lower than that of the core, $n_{material}$ [10]. This is achieved by having air holes in the cladding with a solid core. A simplified one-dimensional example is given in Fig. 2.12, where an index contrast exists between the cladding and the core.

A useful model for guidance in a step-index fibre is to consider the effective cladding index of the fundamental space filling mode (FSM), which is defined as the fundamental mode of the infinite MOF cladding if the core is absent, and fills the role of the cladding index as if the fibre were a conventional step-index fibre [77]. The guided modes of the fibre then propagate with an effective index that lies between the cladding effective index and the material index of the core [77].

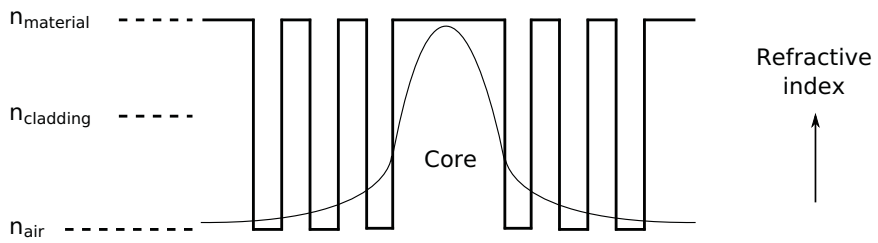

FIGURE 2.12: Refractive index cross section of an index-guiding microstructured optical fibre showing that the core index is greater than the average cladding index thus allowing total internal reflection.

Photonic bandgap fibres have their cladding consist of a period arrangement of air holes for which light cannot propagate for a particular range of frequencies due to interference effects. Introducing a defect into this pattern then produces a core. Light can be guided along this core by virtue of the fact that the light cannot propagate in the surrounding material and is thus confined to the defect [10, 74, 78].

To use MOFs for sensing the holes of the fibre are filled with the analyte of interest so that the portion of optical power that propagates in the holes can interact with the filling material [79]. When considering index guiding MOFs this is referred to as evanescent sensing because the evanescent field exists in the cladding holes. However, when considering filled photonic bandgap fibres the material can be placed in the central hole and is thus not an evanescent field effect but nevertheless allows the analyte to interact with the propagating optical field.

An MOF based sensor can then be used to make any of the traditional spectroscopic measurements that are used in other optical fibre sensor designs with the most common being absorption [80] and fluorescence [81] based measurements, provided the fibre can support the wavelength(s) of light required. Analogous to conventional fibre evanescent-wave sensors, the primary issue is the amount of optical energy that can be made to interact with the analyte material. This is the key advantage of using MOFs, with examples of potential power fractions (power of optical energy in the holes) including 40% for index-guiding MOFs [82] (Sec. 2.5.4) and 98% for photonic bandgap MOFs [83] (Sec. 2.5.4).

Index Guiding

Monro *et al.* studied the use of index-guiding MOFs for sensing purposes by theoretically determining the power fractions that can be achieved [79]. The results showed that power fractions greater than 35% can be achieved. The results also demonstrated that longer wavelengths and larger relative hole diameters were preferable when trying to increase the power fraction. Similar results were also obtained by Hoo *et al.* [84].

Gas absorption spectroscopy has been demonstrated using filled MOFs [80, 84, 85]. Hoo *et al.* filled an MOF with acetylene gas via diffusion and successfully measured its absorption lines in the range of 1520 nm to 1542 nm [80]. By comparing their results with an absorption cell the power fraction was estimated to be 6%, approximately 50 times greater than for the D-shaped fibre. Similarly, Pickrell *et al.* fabricated a random-hole MOF for the absorption measurement of acetylene [85]. The fabrication process involved placing gas producing particles in the glass which expand during the drawing process. This method is simpler than traditional MOF fabrication techniques such as capillary stacking or extrusion [74] but does not allow for much control over the optical properties of the fibre. Pickrell *et al.* also identified that a limitation of using gas filled MOFs is the time of filling the fibre, which could be improved by using larger holes or increasing the gas temperature [85].

Sensing with MOFs is not limited to chemical gas sensing. Jensen *et al.* experimentally demonstrated that an index-guiding MOF could be used for absorption measurements of biomolecules in aqueous solutions [86]. In this experiment DNA molecules were labelled with Cy5 and the absorption spectrum was successfully measured in the region from 500 nm to 800 nm. Extending on this work, Jensen *et al.* used a Cy3 coated polymer MOF to selectively measure the presence of particular antibodies [81]. That is, only the antibody of interest formed a fluorophore with Cy3 and could hence produce fluorescence. In this experiment the fluorescence was excited with side illuminated light with the fluorescence then captured by the guided modes of the fibre and measured at the fibre's output. The results showed the expected fluorescence spectrum for concentrations as low as 80 nM, noting that the sample volumes used were as low as 27 μL. Rindorf *et al.* have also studied the ability to use a fibre Bragg grating (FBG) within an MOF for sensing applications [87]. In this research the FBG was able to indicate the thickness of a thin biofilm on the surface of the MOF holes by measuring the resonant Bragg wavelength.

Suspended-Core Fibres

A subset of index guiding MOFs is the suspended core fibre shown in Fig. 2.13 [82, 88–91]. As was discussed in Chapter 1, this design of fibre is the focus of this project, along with the exposed-core design.

It has been proposed that this structure is an ideal evanescent field sensor as it is as practically close to an air suspended rod as possible, which can have large evanescent fields [79, 82]. Zhu *et al.* theoretically predicted power fractions as great as 29% at a wavelength of 1500 nm with sufficiently small confinement loss [82], which is significantly larger than the 0.1-0.1% quoted for D-shaped fibres [9]. Likewise, Webb *et al.* performed theoretical calculations and found comparable values for the power fraction, and that smaller core sizes could achieve power fractions of almost arbitrary value [90]. A fibre of this design was subsequently fabricated using a drilled preform technique, filled with acetylene, and the expected absorption spectrum recorded [90]. These results all consider the benefits of using suspended core fibres for absorption spectroscopy of gases. The purpose of this thesis is to demonstrate the benifits of using these fibres for liquid-based fluorescence sensing both theoretically and experimentally.

A significant reason for this structure being ideal for sensing purposes is that is does not require selective filling of holes and that the large hole sizes allow for faster filling for liquids or gases compared with more traditional MOFs, particularly if inflated during fibre drawing [91, 92]. If the core diameter is made sufficiently small it can essentially be considered an optical nanowire but in a configuration that allows it to be handled practically. Fabrication of these fibres has been demonstrated with core diameters as small as 800 nm from silica [89], 480 nm from tellurite [91], and 450 nm from bismuth [93]. It will be shown in [P6] in this thesis that suspended-core fibres made from lead-silicate glass can be made with core diameters as small as 400 nm.

A modification of the suspended-core fibre is the exposed-core fibre where one of the MOF holes have been made open to the external environment, these fibres will be discussed shortly.

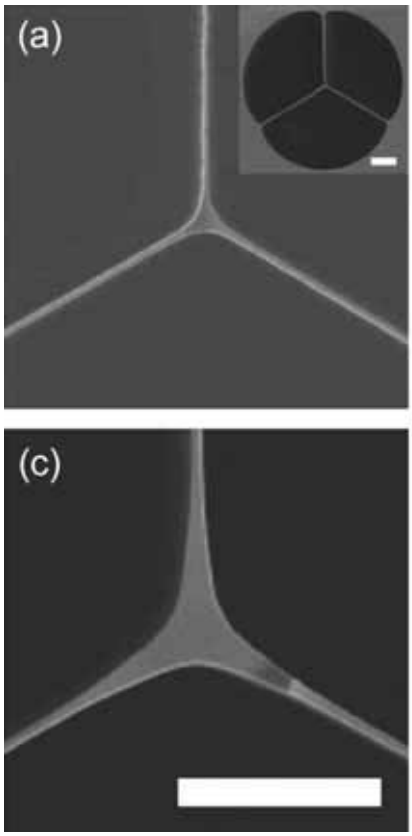

FIGURE 2.13: Suspended optical nanowires. Images from Ref. [89] (a, c) and Ref. [91] (b, d). White scale bars are 10 μm (a, c) and 4 μm (d).

Photonic Bandgap

As with index-guiding MOFs, photonic bandgap (PBG) MOFs have been studied with particular reference to gas sensing. The reasons for studying gas sensing rather than liquid-based sensing is much more apparent for bandgap fibres because the refractive index of the filling material significantly affects what wavelengths can propagate in the fibre [94]. For gases this is not a problem because they have approximately the same refractive index as air, but liquid filling the fibre's holes will dramatically change the fibre's optical characteristics [94].

Laegsgaard *et al.* calculated the power fractions that could be obtained for PBG fibres [83]. For the designs studied, between 2% and 9% of the propagating power travelled in the glass of the fibre, where the remaining power could be exploited for chemical sensing. Gas sensing was then demonstrated by Ritari *et al.* where a PBG fibre was filled with acetylene gas and absorption measurements were made [95]. To demonstrate

the high sensitivity of using PGB fibres the absorption spectra of the weakly absorbing gases methane and ammonia were obtained.

Work has also been done in the field of liquid filled PBG fibres because of the effects filling has on the propagation characteristics of the fibre [96–98]. Cox *et al.* considered the effects of filling all the holes of a PBG fibre with water [97]. Theoretical results showed that filling the holes shifts the transmission region to shorter wavelengths, given by a simple scaling rule, and experimental results confirmed this effect. This can thus be used as a refractive index sensor [96, 97]. Liquid filling of PBG fibres can also be used to create temperature sensors via a liquid's refractive index dependence on temperature, and this has been demonstrate for high-index liquids [98] and liquid crystals [99].

Index Guiding Liquid-Core Fibres

Research has been done on filling only the core of PBG fibres with liquids [100, 101]. This converts the fibre into an index guiding fibre because the refractive index of the filling liquid is greater than the effective index of the air-hole cladding. Consequently, the bandgap effect is no longer present and hence there are no longer issues with propagating at the correct wavelength, and this also results in the majority of the optical field propagating within the liquid. While this design allows for nearly a 100% optical field overlap with the analyte the difficulty lies in that selective filling into the core must be achieved, which generally involves post-processing of the fibre. As with liquid-filled PBGs, there are also issues with ensuring that the ends of the fibre do not contain air bubbles, which can be solved by having the fibre fully immersed [97] or by plugging the ends of the fibre [101].

Exposed-Core Fibres

An important consideration for filled MOF sensors is the rate at which the fibre can be filled. For gas filled fibres the holes are filled via diffusion [84] and liquid filled fibres are generally filled via capillary forces as governed by Navier-Stokes equations [86], although filing rates are generally approximated with simpler capillary theory [102]. It is possible to improve the filling rates by increasing the gas temperature or by applying an external pressure. For example, Jensen *et al.* reduced the filling time for a 20 cm length of

fibre from 10 minutes to 4 minutes by applying a 200 kPa external pressure [86]. An alternative solution to this problem is the exposed-core fibre, where one of the MOF holes is made open to the external environment along the length of the fibre. This allows the fibre to be filled near instantaneously, and also allows for the possibility of distributed sensing using an MOF.

When considering only filling speed, the optimum solution would be to have the MOF holes open continuously along the fibre length. However, having the holes open only at discreet locations would nevertheless assist in improving filling speed, and could have beneficial practical benefits over a continuously open fibre depending on the application. An example of such a device is to create periodic openings along the length of the fibre as suggesting by Hoo *et al.* in 2003 and shown in Fig. 2.14 [84].

FIGURE 2.14: (a) One quarter cross section of an MOF with a side opening. (b) An MOF with periodic openings for faster gas diffusion into the holes. Images from Ref. [84].

An implementation of this idea was tested by Cordeiro *et al.* where side-holes were formed in the side of both solid core and hollow core MOFs [76]. The side-holes were created by first fusing the fibre holes at each end using an electrical arc, another arc was then used at locations along the fibre where the sudden pressure increase blew open a side-hole (Fig. 2.15(a)). It was shown that this method could either be used to fill approximately 30% of the holes of an index-guiding MOF or to selectively fill the core of a hollow-core PBG fibre. However, the presence of these side-holes lead to large propagation losses and significantly scattered the core guided optical mode into the cladding. Cleaner fabrication techniques have since been developed, which include the use of a focused ion beam [103, 104] (Fig. 2.15(b, c)) and femtosecond laser micromachining [105–107] (Fig. 2.15(d, e)). These methods allow short sections of fibre to be exposed, in the order of tens of microns long, with negligible insertion loss. Cox *et al.* subsequently demonstrated that long lengths of exposed-core polymer fibre can

be fabricated by creating an opening at the preform stage of the fibre fabrication, such as by drilling holes into the cladding of a polymer MOF preform [108] (Fig. 2.15(f, g)).

In this project, glass continuously exposed suspended-core fibres have been fabricated and tested for real-time and distributed fluorescence sensing (Chapter 4). In principle, the use of glass allows lower loss fibres to be fabricated than if made from polymer, making it more suitable for distributed sensing.

NOTE:
These figures are included on page 37 of the print copy of the thesis held in the University of Adelaide Library.

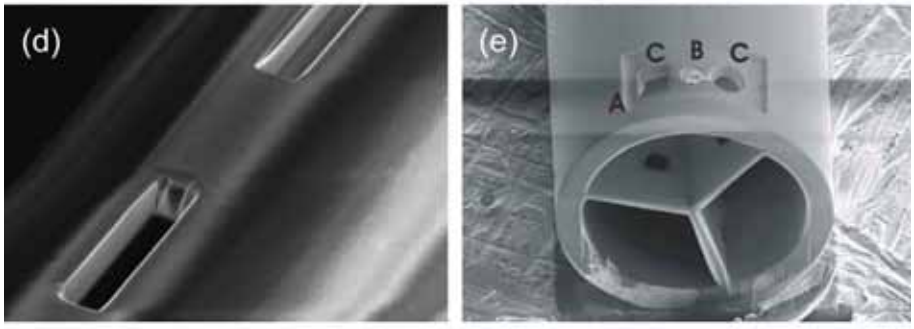

NOTE:
These figures are included on page 37 of the print copy of the thesis held in the University of Adelaide Library.

FIGURE 2.15: Side access MOFs. Images from Ref. [76] (a), Ref. [106] (b, c), Ref. [103] (d, e), and Ref. [108] (f, g).

Discussion on MOF Sensing

The various designs of microstructured optical fibres each have distinct advantages and disadvantages. Solid-core index-guiding fibres such as the suspended-core design are the simplest in terms of fabrication and filling characteristics, but generally have a smaller power fraction (of light in the holes) than liquid-core or photonic bandgap fibres. For an application such as gas absorption spectroscopy, where the analyte has essentially the same refractive index as the air holes, optimising the amount of optical power in the evanescent field is the main priority and thus photonic bandgap fibres appear to be the design of choice. However, complexities arise when sensing liquids as they have a refractive index that generally lies somewhere between air and glass, which will effect the light guidance properties of the fibre. While the liquid-core design provides a high sensitivity for liquid analyte measurements, the complicated filling requirements are a significant disadvantage. For liquid analyte sensing the solid-core fibres appear to offer the simplest and most (optically) robust solution. Solid-core fibres also give flexibility because it is possible to choose the percentage of overlap of the optical field with the analyte and can be easily modified in design to have an exposed core. For these reasons, solid-core fibres have been the focus of this project.

2.6 Coatings for Indicator Immobilisation

As has been discussed throughout this review, optical fibre sensing often makes use of indicator dyes when the intrinsic scattering, refractometric, absorptive, or fluorescence properties of the analyte are not sufficient to perform a measurement [7]. These indicators can be added to the analyte in solution. More commonly, an indicator such as an organic dye is immobilised by some means to the surface of the fibre [4, 7]. This can be achieved by physically embedding the indicator onto the surface, such as with polymer or sol-gel coatings [4, 7], by chemically attaching the indicator to the surface using silanisation [109], or use both physical and chemical interactions to immobilise the indicator using polyelectrolytes [110–112].

2.6.1 Polymer Coatings

Polymer coatings are routinely coated onto telecommunication optical fibres to protect the fibre from environmental contaminants such as moisture. In contrast, a polymer for sensing must allow at least the analyte to reach the evanescent field of the fibre, and thus efforts have been made to develop permeable polymer coatings [8].

Polymer coatings for sensing applications have used various polymer materials such as polymethyl methacrylate (PMMA), [8, 31], polyvinylalcohol (PVA) [59], and polyurethane (3-PEG/PU) [8]. Potyrailo *et al.* have investigated the use of the original (cross-linked) silicone cladding [7, 113, 114], which they argue is beneficial due to its simplicity and low degradation properties.

2.6.2 Sol-Gel Coatings

Sol-gel coatings consist of a porous glass network that can be coated onto an optical fibre surface at, or near, room temperature [115]. In principle, this produces a strong coating as the sol-gel is covalently bound directly to the glass surface [116]. Indicator molecules can be embedded into the porous glass network either in the sol-gel preparation stages or after curing. Sensing is achieved by allowing the analyte to infiltrate the porous glass network and interact with the indicator molecules, which can operate with standard processes such as absorption or fluorescence spectroscopy.

Conventional fibres with sol-gel coatings have been demonstrated for a wide variety of sensing applications including the sensing of pH [116–119], oxygen [115, 120], humidity [55], ammonia [121], quinone [116], adriamycin [28], and proteins [60]. As with polymer coatings, any chemical analyte can in principle be measured via a sol-gel coating if a suitable indicator dye can be found. An alternative concept was demonstrated by Tao *et al.* where an entire optical fibre was fabricated using sol-gel [122]. However, the high scattering losses in the fibre meant that only short pieces of fibre could be used, and 7 mm lengths were used in Ref. [122].

2.6.3 Surface Attachment - Silanisation

Polymer and sol-gel based coatings generally hold the indicator molecule to the surface via entrapment, that is, the chemical is not chemically bound to the surface. An alternative is to chemically attach the molecules to the surface via a silanisation process [109]. For example, Bhatia *et al.* demonstrated that the silanes mercaptomethyldimethylethoxysilane (MDS) and 3-Mercaptopropyltrimethoxysilane (MTS) can be used to covalently attach antibodies to the surface of optical fibres via a cross-linker (GMBS) as shown in Fig. 2.16. There have also been demonstrations of attaching silanes to the inner walls of MOFs, for the potential application of moisture protection [123]. It will also be shown in [P5] of this thesis that silanes can be used within MOFs for attaching quantum dot labelled antibodies.

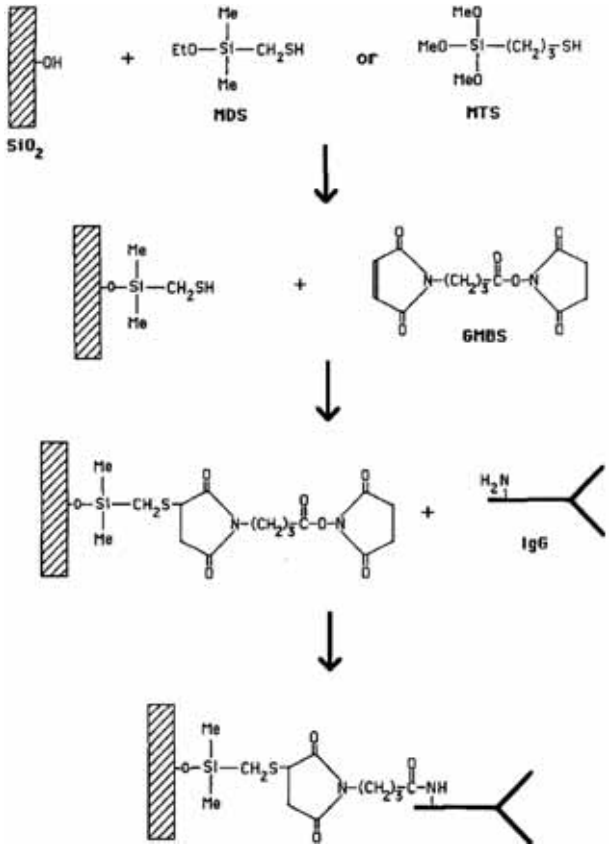

FIGURE 2.16: Chemical process used to attach proteins to an optical fibre surface using silanisation. Image from Ref. [109].

Note that an alternative to the silanisation process is to use polymer optical fibres as they are directly biocompatible, that is, compounds can be directly attached covalently to the surface [81]. This has been been demonstrated using both PMMA [81] and Topas [124] polymer microstructured optical fibres. The main disadvantage is that polymer

fibres generally exhibit higher losses over conventional silica fibres. However, note that any surface modification of a silica fibre, be it silanisation [125] or otherwise, will add to the loss of the fibre.

2.6.4 Surface Attachment - Polyelectrolytes

There has been increasing interest in using polyelectrolyte coatings for surface (including glass) functionalisation as an alternative to the silanisation method [110–112]. As will be explained in more detail in Sec. 5.5, polyelectrolytes can form a coating onto surfaces using electrostatic forces and then indicator molecules, if they have the necessary functional groups, can covalently bind to the polyelectrolyte layer.

2.6.5 Discussion

All the methods above have been used for various applications with various degrees of success. The best method of attachment depends on the application in mind. Literature trends indicate that polymer and sol-gel coatings are useful for chemical sensing, such as pH, whereas chemical attachment methods are often used for biological applications, although this is not always the case. It should be noted that the immobilisation strategy must also satisfy several other functional requirements in addition to attaching the indicator, which includes protection of the core and good optical properties. Polymer coatings and to some degree, sol-gel coatings, are more capable of providing physical protection of the core as they are a physically thicker coating and thus the functional benefits of chemical attachment methods must be strong for them to be considered.

2.7 Distributed Sensing

The ability to perform distributed sensing is one of the most commonly stated advantages of using fibre optics for chemical sensing. Indeed, successful distributed physical sensors, such as for temperature and strain, have been demonstrated that make use of either Raman or Brillouin scattering [1]. There are far fewer reports on distributed chemical sensing, particularly for continuously distributed sensing [113]. While many reported time-domain chemical sensors could in principle be used for continuously distributed

sensing [116, 126, 127], the sensor elements are generally too lossy to be used continuously along the fibre over extended lengths. This is indeed one of the greatest challenges in the development of a truly distributed chemical sensor.

2.7.1 Optical Time Domain Reflectometry

A common method for achieving distributed sensing is to use optical time domain reflectometry (OTDR) [126]. The basic principle is that as light propagates along the fibre a small fraction is reflected into the backwards direction, such as through Rayleigh, Raman, or Brillouin backscattering, and is then recorded with a photo-diode with high temporal resolution [1]. Temporal locations of reduced reflected signal correlate to locations of fibre loss and hence the key is to fabricate a sensor which causes signal loss in the presence of the analyte [126]. An example of an OTDR trace is shown in Fig. 2.17 where each drop in the reflected signal correlates to the activation of a sensor element.

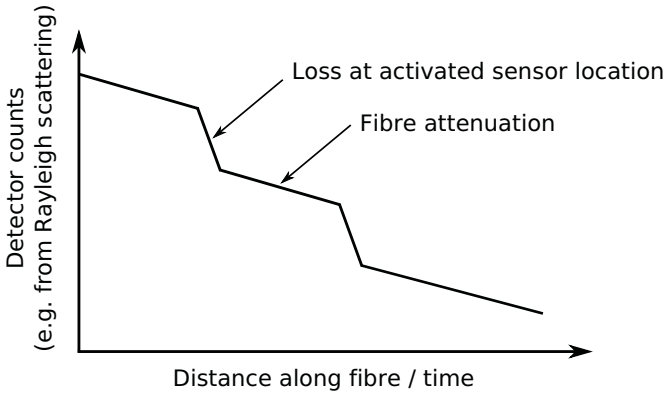

FIGURE 2.17: Example of an OTDR trace for distributed sensing.

Sumida *et al.* demonstrated a distributed hydrogen sensor where the loss mechanism was fabricated by coating the core of a fibre with platinum supported tungsten trioxide using the sol-gel method [126]. This material could react with hydrogen to form a chemical which absorbed the propagating evanescent field. Sensor element with a length of 15 cm were located at separate distances (200 m, 550 m, and 580 m) and measured using OTDR. When exposed to hydrogen the OTDR trace dropped in signal as expected. For this particular sensor the range of operation was approximately 800 m, which is dictated by fibre loss, and the resolution was in the order of a few metres.

2.7.2 Distributed Moisture Sensing

A novel approach to using OTDR for moisture sensing involves making use of the microbending properties of optical fibres in conjunction with water swelling materials [128–131]. The sensor is created by placing two fibres (one a dummy fibre) on opposite sides of a hydrogel and helically winding these together with nylon as seen in Fig. 2.18 [130]. When water is present the hydrogel expands causing strain on the optical fibre due to the nylon windings. This results in microbend losses in the fibre that can be measured using OTDR. For example, this principle was demonstrated by Michie *et al.* over a length of 30 m with a resolution of approximately one metre [130].

FIGURE 2.18: Design for a distributed moisture sensor that uses microbend losses and OTDR. Image from Ref. [130].

2.7.3 Fluorescence-Based Distributed Sensing

Distributed sensing using OTDR-type techniques is not limited to measuring loss. Wallace *et al.* demonstrated a distributed pH sensor where fluorescence was utilised using time-resolved fluorescence measurements [127]. An advantage of using fluorescence is that the signal cannot be confused with other loss mechanisms in the fibre. The sensor system was fabricated in a manner similar to other pH fluorescence sensors and strong signals were measured at locations of low pH. Similarly, Browne *et al.* demonstrated time-resolved pH and quinone sensors [116]. However, both these examples used finite sensor elements that were spliced to longer lengths of inactive fibre and thus were not continuously distributed.

2.8 Corrosion Sensing

Corrosion is a serious problem for many civil and defence structures such as bridges, buildings, and aircraft, with the cost of repair and replacement of corroded structures estimated at billions of dollars [132]. While many attempts are made to prevent and reduce the effect of corrosion, in practice it is impossible to completely avoid. For this reason it is essential that corrosion processes are monitored so that repair time and costs are minimised, and to allow for the safer use of structures such as aircraft.

There are several methods by which corrosion can currently be monitored which each have their advantages and limitations. Because corrosion is an electrochemical process methods such as potential mapping and resistivity measurements can be used [133]. Other simpler methods include visual inspection and weight monitoring [133]. A promising alternative is to use intrinsic optical fibre sensors which can potentially provide for sensitive and distributed measurements. The ability of optical fibres to withstand a large variation in operating temperature, their resistance to electromagnetic interference, and their small profile are particularly relevant when considering imbedding them into an aircraft. For example, they can be placed strategically into locations of known susceptibility to corrosion, such as lap joints, with minimal impact on the structure, and allow for monitoring of locations that would otherwise have to be physically dismantled for inspection [8].

Corrosion can be monitored indirectly by measuring environmental properties such as [8]:

1. Changes in pH
2. Oxygen level
3. Moisture content
4. Presence of salt contaminants

or directly through measurements of the metal alloy itself such as:

1. Changes in the metal alloy (Sec. 2.8.1)

2. Removal of the metal alloy (Sec. 2.8.2)

3. Corrosion products (Sec. 2.8.4 and Sec. 2.8.3)

Methods for environmental monitoring, such as pH, have been mentioned previously throughout this review. The following sections highlight some of the methods by which corrosion can be more directly measured.

2.8.1 Direct Spectroscopic Analysis

When corrosion occurs the spectroscopic properties of a metal change, an example of using optical fibres using this property was demonstrated by Fuhr *et al.* for the monitoring of steel rebar corrosion in concrete using an extrinsic optical fibre sensor [133]. A fibre was used to supply a broadband source to the steel and another fibre collected the reflected signal allowing for spectroscopic analysis of the reflected light. As expected, when the steel underwent corrosion a significant decrease in the reflected signal was observed.

2.8.2 Metal-Clad Fibres

Metal clad optical fibre sensors have been studied extensively for corrosion sensing of various metals [134–141]. To fabricate this sensor a section of unclad multimode fibre has a thin film of metal deposited onto its exposed core via vacuum deposition [138], electroless deposition [135], or thermal deposition [136]. The principle of corrosion measurement is that before corrosion the thin film does not allow total internal reflection and causes significant absorption of the higher order modes [140]. However, when corrosion occurs the thin film is removed and hence attenuation of the propagating light is reduced [140]. Thus, if corrosion of the metal film occurs this can be measured as an increase in output intensity of the fibre. By coating the sensor element with the same metal as the structure being monitored and placing it in the same location it is then assumed that if corrosion of the film is measured then corrosion of the structure has occurred [138]. One of the main benefits from using this design of sensor is that corrosion produces an increase in output intensity and hence loss mechanisms such as microbending and fibre strain will not produce false positive measurements [138]. However, Rutherford *et*

al. found that corrosion by-products can lead to signal interferences due to scattering, depending on the type of corrosion environment [134].

This design of sensor has been fabricated and tested for several different metals such as aluminium [134, 136, 138, 141], copper [135, 136], nickel [140] and steel [137, 139]. For example, Benounis *et al.* studied both aluminium and copper corrosion using a sensor fabricated via thermal deposition [136]. It was found that the sensors were able to measure the different corrosion behaviours of the two materials. This being that copper corrodes homogenously unlike aluminium which forms blisters, particularly in highly acidic conditions, due to formation of an aluminium oxide layer at the surface. This corresponded to step-like behaviour in the output intensity of the aluminium sensor.

As with other sensor configurations, spectroscopic and metal-clad corrosion sensors can be multiplexed to give quasi-distributed measurements. However, the metal-clad design cannot be used for continuous distributed measurements due to the high optical attenuation of metals.

2.8.3 Long Period Gratings

LPGs have been used for the specific application of corrosion sensing in aircraft [142–145]. This work has concentrated on the ability to measure a change in refractive index of a coating applied to the fibre [144]. By choosing different coating materials the sensor can be engineered to measure many different chemical parameters with the most useful for corrosion sensing being moisture, pH, and metal ions [145]. This technology has reached a stage of experimental implementation as described by Elster *et al.* who published plans to test flight a temperature, strain, and moisture sensor system onboard an aging aircraft [142].

As stated previously, LPG sensors can be used in a quasi-distributed arrangement. However, for a continuously distributed corrosion sensor the primary candidate is to use a fluorescence-based sensor, and has thus been chosen for study in this project (Chapter 5).

2.8.4 Fluorescence Measurements

Several examples of optical fibre aluminium corrosion sensors have been demonstrated using fluorescent indicator molecules for metal ions released during corrosion. For aluminium alloys the principle method has been to place an indicator that fluoresces in the presence of aluminium ions at the end of the fibre. McAdam *et al.* made use of 8-hydroxyquinoline (8-HQ) as an aluminium ion indicator [8]. In this study a polyurethane polymer (3-PEG/PU) was doped with 8-HQ and a bead was coated onto the end of a fibre. This point sensor produced the expected fluorescence spectrum when exposed to aluminium ions. However, while evanescent wave sensing was indicated as a primary motivator, and schematically described as shown in Fig. 2.19, experimental demonstration was not provided.

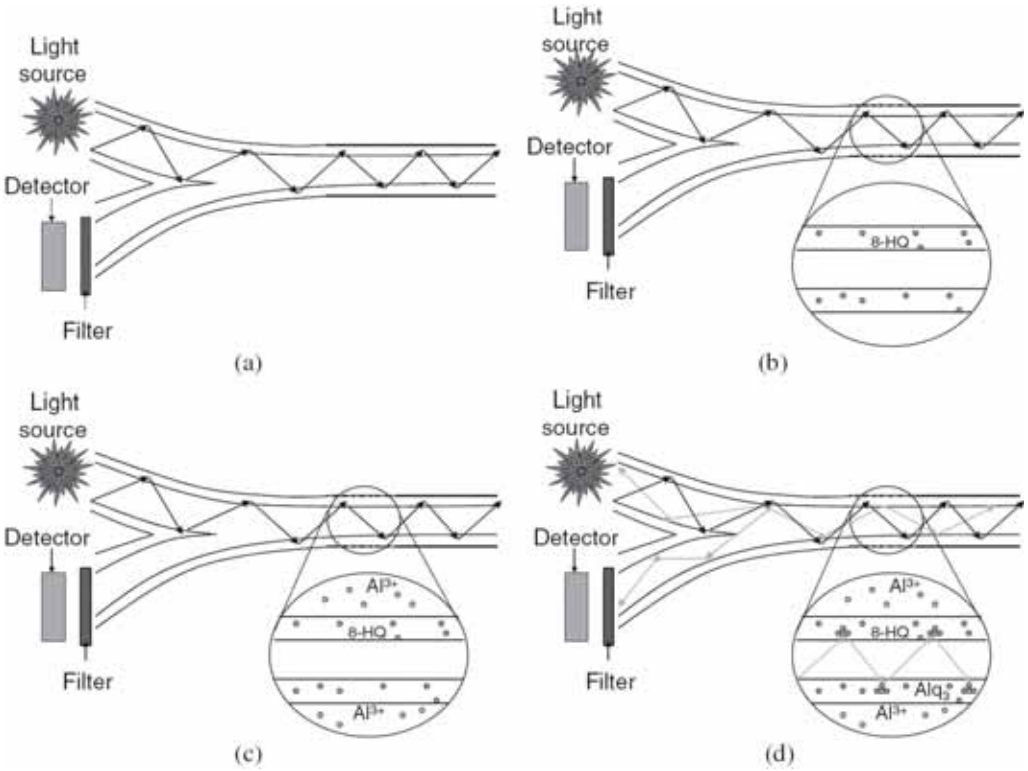

FIGURE 2.19: Evanescent field aluminium alloy corrosion sensing using the fluorescent indicator 8-HQ [8]. (a) Light is coupled into the guided modes of the fibre, which have an evanescent field that extends into the cladding. (b) A section of the cladding is sensitised using a porous polymer doped with 8-HQ. (c) The fibre is to be located such that when corrosion occurs aluminium ions are able to reach the optical fibre. (d) After sufficient time the aluminium ions penetrate into the polymer and form a fluorescent complex with 8-HQ. Image from Ref. [8].

Another commonly used indicator of aluminium is morin, as shown by Saarl *et al.* [146]. Morin was immobilised in powdered cellulose and then attached to the end of a bifurcated

optical fibre. The sensor was subsequently immersed into varying concentrations of aluminium sulphate and measurements demonstrated a fluorescence signal that was dependant upon the aluminium concentration. In a similar manner, Szunerits *et al.* made use of morin immobilised onto the end of a fibre bundle to produce an image of a corrosion site [147]. This method of obtaining an image of the corrosion site shows the possible quasi-distributed sensing possible with optical fibres, however, the sensing region in this example was limited to a diameter of approximately 350 μm. Ahmad *et al.* demonstrated the use of purpurin immobilised in a polymer attached to the end of a four-fibre bundle [148]. Satisfactory results were obtained but with multiple drawbacks. For example, the sensor had a long response time, was dependant on the pH, and had a detection limit of only 30 μM, higher than most other reported fibre sensors. It did, however, show good repeatability, reproducibility, and linearity in response to aluminium ion concentration. Many other indicator molecules have also been studied for determination of aluminium ions, such as lumogallion, but not necessary in an optical fibre configuration (Sec. 5.1.2).

2.9 Discussion and Relevance to Project

This chapter has reviewed many of the different optical fibre chemical sensing designs that exist. These designs can be grouped into extrinsic and intrinsic configurations. Extrinsic sensors can potentially be simpler in that standard optical fibre can be used without further modification, but cannot be used for distributed sensing and there is less scope for increasing the sensitivity. In contrast, intrinsic sensors use the optical fibre itself as the sensing element, where the fibre is generally modified in some way compared to a conventional fibre. For example, the cladding can be removed for evanescent field spectroscopic sensing, a grating can be written for refractive index measurements, or a metal coating can be applied for corrosion sensing or surface plasmon resonance refractive index sensing. Evanescent field sensing is the mechanism that has been chosen for study in this project due to its versatility, sensitivity, and ability to be used for distributed sensing. These properties are particularly useful for corrosion sensing, which is the application that motivated this work.

As has been seen in this review there are many options for implementing and optimising evanescent field sensing devices. When using multimode fibres the sensitivity can be

improved by increasing the launch numerical aperture or bending the fibre, which both have the effect of increasing the number of rays that propagate close to the cut-off angle and thus increasing the penetration depth of the evanescent field. Single mode fibres are generally more sensitive than multimode fibres but are physically smaller and more fragile. Due to the small dimensions required, several designs have been investigated such as tapered fibres or D-shaped fibres. The D-shape fibre allows the small core to be exposed along the fibre length but still be protected by an outer cladding. The idea of structuring the fibre can be taken a step further in the form of a microstructured optical fibre. MOFs can provide high sensitivity as the geometry and materials can be tailored to suit the application in mind, which for sensing often means increasing the percentage of the evanescent field. For this reason MOFs were studied in this project, and in Chapter 3 a new model has been derived and modelled in order to optimise the MOF design for liquid-based fluorescence sensing.

As the motivating application of this project was corrosion sensing, which generally produces aqueous by-products, solid-core index guiding fibres were chosen as they do not require any complicated filling techniques and because liquids can be measured without greatly affecting the optical performance of the sensor. Thus it is the optimisation of suspended-core fibres in particular that is studied in detail in Chapter 3. While the presence of liquids affect the modal properties of the fibre, which has been investigated in Chapter 3, detrimental propagation losses generally do not occur as would likely occur in photonic bandgap fibres.

A particular strength of the solid-core design is that it can be modified, either from the design stage or via post-processing, to have the core longitudinally exposed to the environment, thus allowing real-time and distributed sensing. The fabrication of both enclosed and exposed suspended-core fibres is demonstrated in Chapter 4, along with demonstration of real-time and distributed fluorescence sensing using exposed-core fibre.

When using evanescent field sensing an important consideration is what transduction mechanism to use, which can be based on optical phenomena such as scattering, absorption, or fluorescence. Absorption is often used for chemical gas sensing as fingerprint spectra can be used for analyte identification, whereas fluorescence is often used for biological or other chemical sensors such as for aluminium ions, which have been investigated in this project. However, it is rare that the analyte of interest will intrinsically

have suitable fluorescence properties. For biological sensing fluorescence labelling is often used, while for other chemicals such as metal ions a fluorescent indicator can be used. For example, there are several organic compounds that are known to increase in fluorescence intensity when complexed with aluminium ions, such as lumogallion. There is consequently a requirement to immobilise these indicator dyes onto the optical fibre surface and methods for this include physically imbedding into porous polymer or sol-gel coatings, or chemically attaching via silanisation or polyelectrolytes. In Chapter 5 two methods have been chosen for investigation into immobilising lumogallion onto optical fibre surfaces, which include a porous polymer coating and attachment via polyelectrolytes.

Part II

Thesis Body

Chapter 3

Fluorescence Sensing Theory

Truth in science can best be defined as the working hypothesis best suited to open the way to the next better one.

Konrad Lorenzo

In general we look for a new law by the following process. First you guess. Don't laugh, this is the most important step. Then you compute the consequences. Compare the consequences to experience. If it disagrees with experience, the guess is wrong. In that simple statement is the key to science. It doesn't matter how beautiful your guess is or how smart you are or what your name is. If it disagrees with experience, it's wrong. That's all there is to it.

Richard Feynman

3.1 Theory Overview and Motivation

The measurement of fluorescence intensity can be used for sensing, either directly from the analyte or indirectly using a fluorescent indicator. In this chapter, the theory associated with evanescent excitation and collection of fluorescence using microstructured optical fibres is studied in detail so that the sensor design can be optimised. The concept of operation is summarised in Fig. 3.1. An excitation source, whose wavelength corresponds to the absorption spectrum of the fluorophore, is coupled by some means into the optical fibre. If one or more of the fibre holes has been filled with the fluorophore then the evanescent field of the guided excitation light will overlap with the fluorophores. Consequently, fluorescence will be emitted and a portion of this fluorescence will be evanescently coupled into both the forward and backwards propagating guided modes of the fibre, with the remainder radiated away. Measurement of the fluorescence intensity, at either end of the fibre, will thus provide information on the presence and quantity of the fluorescent material. It is the aim of this chapter to determine what fibre geometry and materials optimise the percentage of fluorescence that is captured by the guided modes of the fibre.

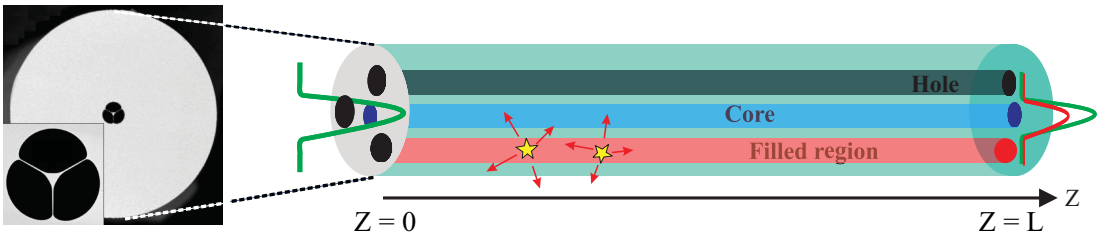

FIGURE 3.1: Schematic diagram showing evanescent field fluorescence sensing using a suspended-core microstructure optical fibre. Excitation light is coupled into the fibre at one end (green), this excites fluorophores that are filled into the fibre holes using the evanescent field. A fraction of the fluorescence (red) then couples into the guided modes of the fibre and can be measured at the output. This can be in the forwards direction (as shown) or in the backwards direction (not shown).

While evanescent field fluorescence-based sensing with optical fibres is not a particularly new concept, theoretical treatment in the literature is far from complete. This may be due to it being a conceptually simple idea within an application driven field. In any case, literature treating the theoretical components of fluorescence based optical fibre sensing are few in number (for example, Refs. [13, 14, 16–20, 149] compared to hundreds of experimental papers, such as those found within Refs. [4, 7]). As a result, most theoretical treatments that exist in the literature, while useful, are somewhat

incomplete. For example, a detailed account of how the two components of the theory, absorption and fluorescence capture, behave simultaneously along the device has not previously been described for the case where the fluorophore is evanescently excited (that is, the fibre is not side-excited as assumed in Refs. [16–20]).

Of particular relevance here is how the fluorescence capture mechanism operates in the single/ few-moded regime, a topic that has become increasingly relevant with the advent of optical nanowires and MOFs with wavelength-scaled features that cannot be modelled using ray-optics models, such as done in Refs. [13, 14]. In addition, the use of microstructured fibres, particularly those fabricated from high index materials, cannot be accurately modelled using the weak-guidance approximation, such as done in Refs. [16, 17, 149].

Understanding how optical nanowires behave as fluorescence-based sensors also brings in an array of additional questions, such as how loss affects the amount of fluorescence signal when the core diameter is reduced to extremely small values, in other words, how small is too small? It is known that reducing the core diameter to subwavelength dimensions allow the percentage of evanescent field to increase to substantial values and approaches 100 % in the limit of decreasing diameter [73]. Prior to the work within this thesis it was not known precisely how the fluorescence capture mechanism operates at these diameters or what the trade-off with loss is.

This chapter aims to answer these questions by extending on previous fluorescence-capture theory [16, 17]. Each of the five sections are based on a publication, [P1-P5], respectively. [P1] provides an outline of the theory used in this chapter, where a full derivation can be found in Appendix A. [P1] then applies the theory for the case of a suspended optical nanowire (wagon wheel) where it was found that small-core high-refractive index fibres offer the greatest fluorescence sensing characteristics. [P2] extends on this theory to compare the cases where the fluorescence signal is collected from either the input or output end of the fibre, and experimental results qualitatively confirm the predicted differences in behaviour. In [P3] the theory of [P1] is applied to the exposed-core fibre for the unique case where the exposed region is filled with a liquid, which can lead to an improved fluorescence signal due to the different refractive index profile compared with a fully-filled wagon wheel geometry. [P3] also includes a consideration of the coupling losses that are present in a partially filled fibre where the full derivation of

the coupling efficiency theory is given in Appendix B. [P4] again extends the theory of [P1] to include a host of additional components. Firstly, higher order modes are included so that the theory is applicable outside of the single mode regime, which is useful when studying optical nanowires that have core diameters close to the wavelength of the propagating light where several guided modes may exist. Additionally, experimentally measured small-core surface scattering losses are included as well as confinement loss, where a full derivation of the confinement loss theory is given in Appendix C. These additions to the theory allow two important checks to be performed. First, the theory is found to agree with an equivalent ray-optics model for a special case. Most importantly, experimental results are quantitatively compared to the theory, with good agreement. Finally, [P5] is a somewhat different application of the fluorescence capture theory where it was used to calculate surface density of surface attached fluorophores (quantum dots).

A flowchart of how the sections of this chapter relate to other sections of this thesis is shown in Fig. 3.2.

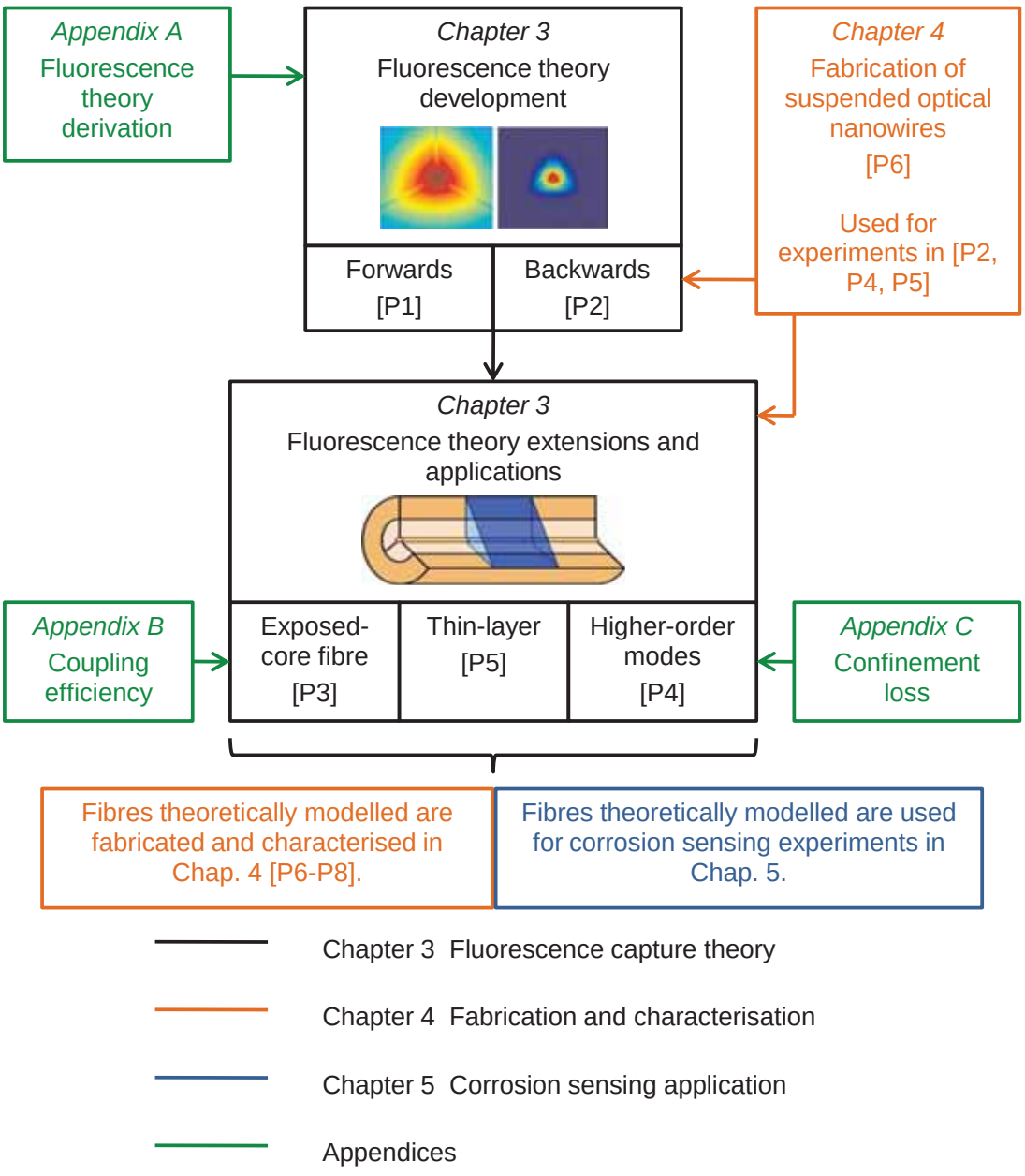

FIGURE 3.2: Flowchart showing the links between Chapter 3 and publications, appendices, and other chapters.

3.2 Fluorescence Capture Fraction: Fundamental Mode Analysis

The publication [P1] forms the basis of this section.

S. Afshar V., S. C. Warren-Smith, and T. M. Monro, "Enhancement of fluorescence-based sensing using microstructured optical fibres," *Optics Express* **15**, 17891-17901 (2007).

3.2.1 Publication Overview

Aim

The aim of this work was to develop a vectorial, modal based theory that can be used to predict the fluorescence capture efficiency of arbitrary cross-sectional structures, particularly those found within microstructured optical fibres. This theory was developed in order to improve the understanding of how this mechanism operates and what material and geometries are best suited for fluorescence-based sensing, with a particular emphasis on small-core high refractive index suspended core MOFs. A proof-of-concept experimental demonstration was also included in this work.

Field of Knowledge and Link Between Publications

The sensitivity of optical fibre sensors based on absorption and fluorescence spectroscopy is usually considered to be related solely to the power fraction of the guided mode field that is available for overlap with the material to be sensed. Such sensors are generally referred to as evanescent-field sensors, reflecting the fact that only the evanescent tail of the guided mode is available for light-matter interactions. Examples of fibre geometries used for evanescent-based sensing include; tapered fibres [149, 150], D shaped fibres [9], optical nanowires [70], solid-core MOFs [82, 151], multi-core MOFs [30, 152] and hollow-core MOFs [86].

Although different MOF-variants of fluorescence-based sensors have been reported [30, 81, 94, 152], there has been a lack of a formalism for understanding, predicting, and thus optimising the measurable fluorescence power. Models have been developed using

ray tracing methods [13, 14], however, these are unsuitable for the single/few-moded fibres considered here. A modal approach was first developed by Marcuse [16, 17] for the case of a uniform cladding excitation (for example, side excitation) and found that fluorescence capture increased with increasing V-number. This uniform excitation theory was later generalised for vectorial step-index fibre solutions and it was shown that, more specifically, capture is increased with increasing refractive index difference between the core and cladding [18–20]. However, these results did not consider the case of a core pumped fibre and did not include effects due to fibre loss or Beer's law absorption.

In this paper a general model is developed of excitation and fluorescence recapturing within an MOF based on guided mode solutions of vectorial form of Maxwell's equations and considering their losses at both emission and fluorescent frequencies. By evaluating the modal characteristics of a range of fibres at both wavelengths, ways of enhancing the sensing sensitivity by maximising the fraction of the fluorescent photons that are coupled to the guided mode(s) of the filled microstructured fibres are explored. The model was applied numerically for the commonly used suspended-core (wagon wheel) geometry [82, 88–90], however, the theory could in principle be applied to any arbitrary waveguide geometry. As will be seen, this theory is later developed and numerically modelled to include backwards directed fluorescence (Sec. 3.3, [P2]), exposed-core fibre sensing (Sec. 3.4 [P3]), to include higher order modes (Sec. 3.5, [P4]), and for thin-layer sensing (Sec. 3.6 [P5]).

Experimentally, chemical and biological sensing has been demonstrated using absorption spectroscopy in D-shaped fibres [9] and MOFs [151, 152] and fluorescence-based sensing in tapered fibres [153], liquid-filled hollow-core MOFs [94, 100], side excited MOFs [81, 94], and double-clad and multi-core (liquid filled) MOF [30]. In this paper, experimentally measured in-fibre excitation and fluorescence recapturing within a liquid-filled, solid-core, index-guiding MOF is demonstrated. However, in this paper, the experimental results are only proof-of-concept in nature for a relatively large-core fibre (1.8 μm). The fabrication of the modelled fibre geometry with small core diameters is later presented in Sec. 4.2 [P6] and the numerical predictions are quantitatively compared with experimental results in Sec. 3.5 [P4].

Discussion and Conclusions

A general model of both in-fibre excitation and fluorescence recapturing of filled solid-core MOFs by their core guided modes has been developed and numerically modelled for the fundamental mode of an important MOF geometry. The model is based on an arbitrary MOF with vectorial solutions of Maxwell's equations. It was demonstrated that the light-matter overlap alone does not determine the optimal fibre choice as is usually assumed. While low index fibres exhibit greater evanescent fields, fibre designs with sub-wavelength features and high index glass exhibit localised regions of high intensity [154, 155] that lead to enhanced fluorescence recapturing that can be exploited for sensing. One to two orders of magnitude improvement in the fluorescence capture fraction (FCF) of MOFs with high index substrate glasses and small core diameters was found in comparison with those with low index glasses. For a sensor, this means that the smallest concentration of an analyte that can be detected will thus be one to two orders of magnitude lower.

3.2.2 Statement of Contribution

Conceptualisation

The idea to develop a theory for the fluorescence-sensing properties of MOFs was first conceptualised by Tanya Monro. The method by which to achieve this was conceptualised by Stephen Warren-Smith and Shahraam Afshar V.

Realisation

The original literature review on previous theoretical models and the first construct of the theory based on previous work by Marcuse [16, 17] was done by Stephen Warren-Smith. The theory was later improved, re-formalised, and numerically modelled by Shahraam Afshar V. The theory and numerical modelling was then independently repeated and error checked by Stephen Warren-Smith.

Documentation

This paper was primarily written by Shahraam Afshar V., with editing by all other authors.

Declaration and Permission

I declare that the above statement of contribution is accurate and I give permission for this publication to be included in this thesis.

Shahraam Afshar V. Stephen C. Warren-Smith Tanya M. Monro

Enhancement of fluorescence-based sensing using microstructured optical fibres

Shahraam Afshar V., Stephen C. Warren-Smith and Tanya M. Monro

Centre of Expertise in Photonics, School of Chemistry & Physics, University of Adelaide, Adelaide, SA 5005, Australia

shahraam.afshar@adelaide.edu.au

Abstract: We develop a generic model of excitation and fluorescence recapturing within filled microstructured optical fibres (MOFs) with arbitrary structure and demonstrate that the light-matter overlap alone does not determine the optimal fibre choice. Fibre designs with sub-wavelength features and high-index glasses exhibit localised regions of high intensity, and we show that these regions can lead to approximately two orders of magnitude enhancement of fluorescence recapturing. Here we show how this regime can be exploited for sensing and demonstrate experimentally in-fibre excitation and fluorescence recapturing within a filled, solid-core MOF.

OCIS codes: (060.2370) fiber optics sensors; (060.4005) microstructured fibers; (280.1415) biological sensing and sensors

References and links

1. G. Stewart and B. Culshaw, "Optical Waveguide Modelling and Design for Evanescent Field Chemical Sensors," Opt. Quantum Electron. **26**, s249 (1994).
2. J. B. Jensen, P. E. Hoiby, G. Emiliyanov, O. Bang, L. H. Pedersen, and A. Bjarklev, "Selective Detection of Antibodies in Microstructured Polymer Optical Fibers," Opt. Express **13**, 5883–5889 (2005).
3. S. O. Konorov, A. M. Zheltikov, and M. Scalora, "Photonic-Crystal Fiber as a Multifunctional Optical Sensor and Sample Collector," Opt. Express **13**, 3454–3459 (2005).
4. L. Rindorf, P. E. Hoiby, J. B. Jensen, L. H. Pedersen, O. Bang, and O. Geschke, "Towards Biochips Using Microstructured Optical Fiber Sensors," Anal. Bioanal. Chem. **385**, 1370–1375 (2006).
5. C. M. B. Cordeiro, M. A. R. Franco, G. Chesini, E. C. S. Barretto, R. Lwin, C. H. B. Cruz, and M. C. J. Large, "Microstructured-Core Optical Fibre for Evanescent Sensing Applications," Opt. Express **14**, 13,056–13,066 (2006).
6. F. Warken, E. Vetsch, D. Meachede, M. Sokolowski, and A. Rauschenbeutel, "Ultra-Sensitive Surface Absorption Spectroscopy Using Sub-Wavelength Diameter Optical Fibers," Opt. Express **15**, 11,952–11,958 (2007).
7. S. Smolka, M. Barth, and O. Benson, "Highly Efficient Fluorescence Sensing with Hollow Core Photonic Crystal Fibers," Opt. Express **15**, 12,783 (2007).
8. W. Henry, "Evanescent Field Devices: A Comparison Between Tapered Optical Fibres and Polished or D-Fibres," Opt. Quantum Electron. **26**, s261–s272 (1994).
9. P. Lucas, M. R. Riley, C. Boussard-Pledel, and B. Bureau, "Advances in Chalcogenide Fiber Evanescent Wave Biochemical Sensing," Anal. Biochem. **351**, 1–10 (2006).
10. G. Stewart, W. Jin, and B. Culshaw, "Prospects for Fibre-Optic Evanescent-Field Gas Sensors Using Absorption in the Near-Infrared," Sens. Actuators B **38-39**, 42–47 (1997).
11. J. Lou, L. Tong, and Z. Ye, "Modeling of Silica Nanowires for Optical Sensing," Opt. Express **13**, 2135–2140 (2005).
12. Y. Zhu, H. Du, and R. Bise, "Design of Solid-Core Microstructured Optical Fiber with Steering-Wheel Air Cladding for Optimal Evanescent-Field Sensing," Opt. Express **14**, 3541–3546 (2006).

#88929 - $15.00 USD Received 23 Oct 2007; revised 12 Dec 2007; accepted 12 Dec 2007; published 14 Dec 2007

13. J. B. Jensen, L. H. Pedersen, P. E. Hoiby, L. B. Nielsen, T. P. Hansen, J. R. Folkenberg, J. Riishede, D. Noordegraaf, K. Nielsen, A. Carlsen, and A. Bjarklev, "Photonic Crystal Fiber Based Evanescent-Wave Sensor for Detection of Biomolecules in Aqueous Solutions," Opt. Lett. **29**, 1974–1976 (2004).
14. Y. K. Lize, E. Magi, V. Taeed, J. Bolger, P. Steinvurzel, and B. Eggleton, "Microstructured Optical Fiber Photonic Wires with Subwavelength Core Diameter," Opt. Express **12**, 3209–3217 (2004).
15. K. J. Rowland, S. Afshar V., and T. M. Monro, "Nonlinearity Enhancement of Filled Microstructured Fibers Operating in Nanowire Regime," in *Proceedings of OFC 2006*, p. OTuH3 (2006).
16. L. Tong, J. Lou, and E. Mazur, "Single-Mode Guiding Properties of Subwavelength-Diameter Silica and Silicon Wire Waveguides," Opt. Express **12**, 1025–1035 (2004).
17. S. Smolka, M. Barth, and O. Benson, "Selectively Coated Photonic Crystal Fiber for Highly Sensitive Fluorescence Detection," Appl. Phys. Lett. **90**, 111,101 (2007).
18. Z. Liu and J. Pawliszyn, "Capillary Isoelectric Focusing of Proteins with Liquid Core Waveguide Laser-Induced Fluorescence Whole Column Imaging Detection," Anal. Chem. **75**, 4887–4894 (2003).
19. Y. Huang, Y. Xu, and A. Yariv, "Fabrication of Functional Microstructured Optical Fibers Through a Selective-Filling Technique," Appl. Phys. Lett. **85**, 5182 (2004).
20. T. Ritari, J. Tuominen, H. Ludvigsen, J. Petersen, T. Sorensen, T. Hansen, and H. Simonsen, "Gas Sensing Using Air-Guiding Photonic Bandgap Fibers," Opt. Express **12**, 4080 (2004).
21. H. P. Kao, N. Yang, and J. S. Schoeniger, "Enhancement of Evanescent Fluorescence from Fiber-Optic Sensors by Thin-Film Sol-Gel Coating," J. Opt. Soc. Am. A **15**, 21632,170 (1998).
22. M. Nagel, A. Marchewka, and H. Kurz, "Low-Index Discontinuity Terahertz Waveguides," Opt. Express **14**, 9944 (2006).
23. G. S. Wiederhecker, C. M. B. Cordeiro, F. Couny, F. Benabid, S. A. Maier, J. C. Knight, C. H. B. Cruz, and H. L. Fragnito, "Field Enhancement Within an Optical Fibre with a Subwavelength Air Core," Nature Photonics **1**, 115 (2007).
24. N. Ganesh and B. T. Cunningham, "Photonic Crystal Enhanced Fluorescence," in *Technical Digest*, p. CThz5 (Optical Society of America, 2007).
25. V. R. Almeida, Q. Xu, C. A. Barrios, and M. Lipson, "Guiding and Confining Light in Void Nanostructure," Opt. Lett. **29**, 1209–1211 (2004).
26. R. E. Bailey, A. M. Smith, and S. Nie, "Quantum Dots in Biology and Medicine," Physica E **25**, 1–12 (2004).
27. A. W. Snyder and J. D. Love, *Optical Waveguide Theory* (Chapman and hall, 2-6 Boundary Row, London SE1 8HN, UK, 1995).
28. F. W. D. Rost, *Fluorescence Microscopy* (Cambridge University Press, Cambridge, UK, 1992).
29. D. Marcuse, "Launching Light Into Fiber Cores from Sources Located in the Cladding," J. Lightwave Technol. **6**, 1273–1279 (1988).
30. H. Ebendorff-Heidepriem, P. Petropoulos, S. Asimakis, V. Finazzi, R. C. Moore, K. Frampton, F. Koizumi, D. J. Richardson, and T. M. Monro, "Bismuth Glass Holey Fibers with High Nonlinearity," Opt. Express **12**, 5082–87 (2004).
31. C. M. B. Cordeiro, M. A. R. Franco, C. J. S. Matos, F. Sircilli, V. A. Serrao, and C. H. B. Cruz, "Single-Design-Parameter Microstructured Optical Fiber for Chromatic Dispersion Tailoring and Evanescent Field Enhancement," Opt. Lett. **32**, 3324–26 (2007).
32. A. Zheltikov, "Gaussian-Mode Analysis of Waveguide-Enhanced Kerr-Type Nonlinearity of Optical Fibers and Photonic Wires," J. Opt. Soc. Am. B **22**, 1100–1104 (2005).
33. P. Agrawal, *Nonlinear Fiber Optics*. Academic press, Burlington, (2007).
34. E. W. Washburn, "The Dynamics of Capillary Flow," Physical Review **17**, 273–283 (1921).
35. I. B. Berlman, *Handbook of fluorescence spectra of aromatic molecules* (Academic Press, New York, 1971).
36. E. Schartner, Y. Ruan, P. Hoffman, and T. M. Monro, "An Optical Fibre Protein Sensor," in *COIN-ACOFT 2007 Proceeding*, pp. WeB1–3 (Australian Optical Society, 2007).
37. Y. Ruan, W. Li, R. Jarvis, N. Madsen, A. Rode, and B. Luther-Davies, " Fabrication and Characterization of Low Loss Rib Chalcogenide Waveguide Made by Dry Etching, " Opt. Express **12**, 5140–5145(2004).
38. H. Ebendorff-Heidepriem, Y. Li, and T. M. Monro, "Reduced Loss in Extruded Microstructured Optical Fiber," Electron. Lett., **43**, 1343–1345(2007).

1. Introduction

Microstructured optical fibres (MOFs) have the potential to dramatically improve the performance of fibre optic sensors based on absorption and fluorescence spectroscopy and have recently attracted considerable interest [1, 2, 3, 4, 5, 6, 7], since a significant portion of the guided light can be located in holes within the fibre. In the literature, the sensitivity of optical fibre sensors based on absorption and fluorescence spectroscopy is usually considered to be related solely to the power fraction of the guided mode field that is available for overlap with the ma-

#88929 - $15.00 USD Received 23 Oct 2007; revised 12 Dec 2007; accepted 12 Dec 2007; published 14 Dec 2007

terial to be sensed. Such sensors are generally referred to as evanescent-field sensors, reflecting the fact that only the evanescent tail of the guided mode is available for light-matter interactions. Examples of fibre geometries used for evanescent-based sensing include; tapered fibres [8, 9], D-shaped fibres [10], optical nanowires [11], solid-core MOFs [5, 12], multi-core MOFs [3, 4] and hollow-core MOFs [13]. Most evanescent-based sensing geometries only allow a limited light-matter overlap and thus are restricted in the sensitivity that they can achieve. Some typical mode-matter overlaps that have been reported include $0.1 - 0.2\%$ for D-shaped fibres [10], 5.2% in an MOF [13], and multi-core MOFs with 6.5% [4]. Fibres with sub-wavelength cores including optical nanowires and MOFs with embedded nanowire-like cores [14, 15] allow overlaps as large as 99% as is evident from literature reports of 40% [12] and 99% [16]. These advances allow solid-core fibres to achieve light-matter overlaps as high as other field-based sensors which have access of up to 97% [17] or higher of the guided mode power such as capillary tubes [18], index-guiding filled hollow-core MOFs [19] and hollow-core photonic band gap fibres [20].

Although different MOF-variants of fluorescence-based sensors have been reported [2, 3, 4, 7, 10], the benefits that can be obtained using MOFs are far from being realised, largely due to the lack of a formalism for predicting and thus optimizing the measurable fluorescence power. Although models of the efficiency of fluorescence-based optical fibre sensors have been developed for simple structures such as tapered or D-shaped fibres, they have limited applicability because; 1) it is assumed that the modes of the fibre are the same at both the absorption and fluorescence wavelengths and 2) they are based on ray-optics [1, 21] or scalar electromagnetic fields (without including the effect of absorption loss) [8]. These models do not work well for fluorescent dyes with significant excitation-fluorescence wavelength separation (such as quantum dots), MOFs with wavelength-scale features and high contrast refractive indices, or complex sensing geometries when the hole surface of MOFs are coated (functionalized) with chemical-biological materials.

Here, we develop a general model of excitation and fluorescence recapturing within an MOF's modes based on guided mode solutions of vectorial form of Maxwell's equations and considering their losses at both emission and fluorescent frequencies. By evaluating the modal characteristics of a range of fibres at both wavelengths, we explore ways of enhancing the sensing sensitivity by maximising the fraction of the fluorescent photons that are coupled to the guided mode(s) of the filled microstructured fibres (the fluorescence capture fraction, *FCF*). We demonstrate that the light-matter overlap alone does not determine the optimal fibre choice as is usually assumed. Fibre designs with sub-wavelength features and high index glass exhibit localised regions of high intensity [22, 23], and we show that these regions lead to enhanced fluorescence recapturing and can be exploited for sensing. The significance of this parameter regime becomes clearer considering; 1) recent indication of the existence of such narrow-width high intensity regions at the interface of two different dielectrics, due to discontinuity of the electric field, in both waveguides [25] and MOFs [22, 23] and 2) sensing configurations based on surface excitation of chemical and biological layers. Recently, there have been reports on the importance of the above-mentioned parameter regime in related fields. The enhancement of fluorescent scattering of semiconductor quantum dots deposited upon photonic crystals slabs [24] and the enhancement (by few orders of magnitude) of the efficiencies of conventional surface spectroscopy by using tapered fibres [6] are two examples.

Experimentally, chemical and biological sensing have been demonstrated using absorption spectroscopy in D-shaped fibres [10] and MOFs [4, 5] and captured fluorescence-based sensing in tapered fibres [26], liquid-filled hollow-core MOFs [19, 7], side excited MOFs [2, 17], and double-clad and multi-core (liquid filled) MOF [3]. Here, we demonstrate experimentally both in-fibre excitation and fluorescence recapturing within a liquid-filled, solid-core, index-guiding

#88929 - $15.00 USD Received 23 Oct 2007; revised 12 Dec 2007; accepted 12 Dec 2007; published 14 Dec 2007

MOF [Fig. 1(b)] through its core guided modes. The experimental methods based on selective hole filling of MOFs (c.f. Ref. [19, 7] for example) or propagating modes of high index liquids (c.f. Ref. [3] for example) may be limiting in some applications. Thus, the use of high-index glass (SF57 here) solid-core MOFs allows access to high light-matter overlaps without necessitating selective hole filling while relying on solid-core modes even when the MOF holes are filled with high index liquid.

2. Theory

To develop the model, we assume that the propagating modes of an absorbing MOF are the same as nonabsorbing ones except that their powers decay with an attenuation factor of γ as they propagate. The excitation electromagnetic power in the jth mode at excitation frequency ω_E can then be expressed as: [27]

$$P_{Ej}(z) = \left|a_{Ej}\right|^2 N_{Ej} \exp(-\gamma_{Ej} z); \quad N_{Ej} = \frac{1}{2}\mathrm{Re}\left\{\int_{A_\infty} (\mathbf{e}_{Ej} \times \mathbf{h}^*_{Ej}).\hat{z} dA]\right\} \tag{1}$$

$$\gamma_{Ej} = k\left(\frac{\varepsilon_0}{\mu_0}\right)^{1/2} \frac{\int_{A_\infty} n_E n_E^i \left|\mathbf{e}_{Ej}\right|^2 dA}{N_{Ej}}, \tag{2}$$

where a_{Ej} is the expansion coefficient for mode j, $\mathbf{e}_{Ej}(x,y), \mathbf{h}_{Ej}(x,y)$, β_{Ej}, and γ_{Ej} are the j^{th} mode electric and magnetic field distributions, propagation constant and power decaying factor due to absorption, respectively. Here, we assume that γ_j represents all absorption mechanisms in the MOF, including absorption due to the Beer-Lambert law [28].

For an arbitrary filled MOF both $n_E(x,y)$ and $n_E^i(x,y)$ (real and imaginary parts of refractive indices) are functions of transverse coordinates and hence the piece-wise integral in Eq. (2) can be integrated over the glass and hole (filled) regions. Eq. (1) indicates that although the absorption of the excitation mode occurs in the filled region, through Beer-Lambert law, the peak intensity also reduces, keeping the shape of the mode and the hole power fraction constant.

Upon absorbing the excitation photons, the fluorescent species in the holes behave as sources and emit fluorescent photons in all directions. Similar to the excitation field, the emission of this new fluorescent source can in general be written [27] as the sum of forward, backward, and radiation modes of the non-absorbing MOF with the consideration of power decay due to loss at the fluorescence frequency. Based on the formalisms developed in Ref. [27, 29], we find the fluorescent power contribution to the jth forward mode of the MOF at the end of the filled region $z = L$, due to a small section $\Delta z = z_2 - z_1$ [see Fig. 1(c)], and including its loss as:

$$dP_{Fj}(z') = \frac{\pi \exp[-\gamma_{Fj}(L-z')]}{4\omega_F \mu_0 n_F^H k_F N_{Fj}} \int_H \int_{z_1}^{z_2} \left|\mathbf{e}_{Fj}\right|^2 P_D(\mathbf{r}) dz'' dA. \tag{3}$$

Here, $P_D(\mathbf{r})$ is the radiation power density of any sources within the MOF, which for the case considered here is due to the fluorescent emission of the filling material. The density of fluorescent emission at point $\mathbf{r}$ depends on the absorption of excitation field from the beginning of the filled area up to the point $\mathbf{r}$, see Fig. 1(a). Using equations (1) and (2), assuming that the fluorescent power density is proportional to the density of excitation power loss due to Beer-Lambert law in the filled region (proportionality constant ξ), and taking into account energy conservation, we have found $P_D(\mathbf{r})$ as:

$$P_D(\mathbf{r}) = \frac{1}{2}\xi \alpha_B n_E^H (\varepsilon_0/\mu_0)^{1/2} \left|a_{Ej}\right|^2 \delta_{Ej}^H \mathrm{Re}[(\mathbf{e}_{Ej} \times \mathbf{h}^*_{Ej}).\hat{z}] \exp(-\gamma_{Ej} z''), \tag{4}$$

$$\delta_{Ej}^H = \int_H \left|\mathbf{e}_{Ej}\right|^2 dA / \int_H (\mathbf{e}_{Ej} \times \mathbf{h}^*_{Ej}).\hat{z} dA. \tag{5}$$

#88929 - $15.00 USD Received 23 Oct 2007; revised 12 Dec 2007; accepted 12 Dec 2007; published 14 Dec 2007

Here, $\alpha_B = \varepsilon_\lambda C$ is the absorption coefficient due to Beer-Lambert law [28], where ε is the molar extinction coefficient of the filling material, C is the molar concentration, and superscript H refers to hole regions. Substituting Eq. (4) into Eq. (3), and taking the integral over z'' and the limit of $z_1 \to z_2$, we find

$$dP_{Fj}(z') = \frac{\pi\xi\,\alpha_B n_E^H (\varepsilon_0/\mu_0)^{1/2} \left|a_{Ej}\right|^2 \delta_{Ej}^H}{8\omega_F \mu_0 n_F^H k_F N_{Fj}} \exp[-\gamma_{Fj}(L-z')] \exp(-\gamma_{Ej} z') dz' \tag{6}$$
$$\times \int_H \left|\mathbf{e}_{Fj}\right|^2 \mathrm{Re}[(\mathbf{e}_{Ej} \times \mathbf{h}_{Ej}^*).\hat{z}] dA.$$

Integrating the fluorescent contributions of the elements from $z = 0$ to $z = L$, the fluorescence capture fraction (FCF) into the jth guided mode of the MOF can be expressed as

$$FCF = P_{Fj}(L)/P_{Ej}(0) = AB_j \frac{\exp(-\gamma_{Fj}L)}{(\gamma_{Ej} - \gamma_{Fj})}\{1 - \exp[(\gamma_{Fj} - \gamma_{Ej})L]\} \tag{7}$$

$$A = \frac{\xi\,\alpha_B \lambda^2}{8\pi (n_F^H)^2}; \quad B_j = n_F^H n_E^H \left(\frac{\varepsilon_0}{\mu_0}\right) \delta_{Ej}^H \frac{\int_H \left|\mathbf{e}_{Fj}\right|^2 \mathrm{Re}[(\mathbf{e}_{Ej} \times \mathbf{h}_{Ej}^*).\hat{z}] dA}{4 N_{Fj} N_{Ej}}. \tag{8}$$

In this equation A is a constant coefficient and $P_{Ej}(0)$ is the input excitation field power at the beginning of the filled part of the fibre, whose length is shown by L [see Fig. 1(a)]. It should be noted that throughout the text we only consider FCF into the fundamental guided mode propagating in the forward direction. To find FCF into backward propagating modes, different loss calculations should be included in the above formalism which is beyond the scope of this paper. Also, in derivation of Eq. (6) and (7), it is assumed that the whole fibre length is completely filled. For fibres that are only partially filled, the mode mismatch between the filled and unfilled sections should be considered for both excitation and fluorescence frequencies, which is beyond the scope of this paper.

3. Modelling results and discussion

The model developed in Section 2 is general and can be applied to any filled MOF with arbitrary cross section structure. Here, we consider an MOF [shown in Fig. 1(b)], which consists of a core surrounded by three large, non-circular, air holes creating a somewhat triangular core supported by three struts. This type of fibre geometry has been studied [30, 31] and is the simplest fibre geometry that can be fabricated giving rise to a well defined air-suspended core with large surrounding (fillable) air holes. To find the propagation constant and field distributions for the MOF, we solve the full vectorial form of Maxwell's equations since, for the subwavelength scales considered here, a scalar approximation gives inaccurate results [32].

We define the MOF core diameter, d, to be the diameter of a circle with area equal to that of the largest equilateral triangle that fits wholly within the substrate core region, shown as the solid circle in Fig. 1(b). For simplicity we consider an idealized MOF structure, which closely matches that of the SEM image [Fig. 1(b)]: the curvature of the core is approximated by the edges of the three dashed circles connected by the bases of three rectangles approximating the struts. To solve Maxwell's equations for this geometry we use the Finite Element Modelling (FEM) technique instantiated in the commercial FEM package COMSOL 3.2. The accuracy of the modal parameters depends heavily on the densities of the mesh in different regions, which have been set separately to achieve converged values. The parameters used for the simulations are; excitation wavelength $\lambda_E = 532$ *nm*, fluorescence wavelength $\lambda_F = 590$ *nm*, filling material: Rhodamine B dissolved in isopropanol, and five different glass materials [silica, lead silicates (LLF1, F2, and SF57), and bismuth] whose refractive indices are indicated on the figures.

#88929 - $15.00 USD Received 23 Oct 2007; revised 12 Dec 2007; accepted 12 Dec 2007; published 14 Dec 2007

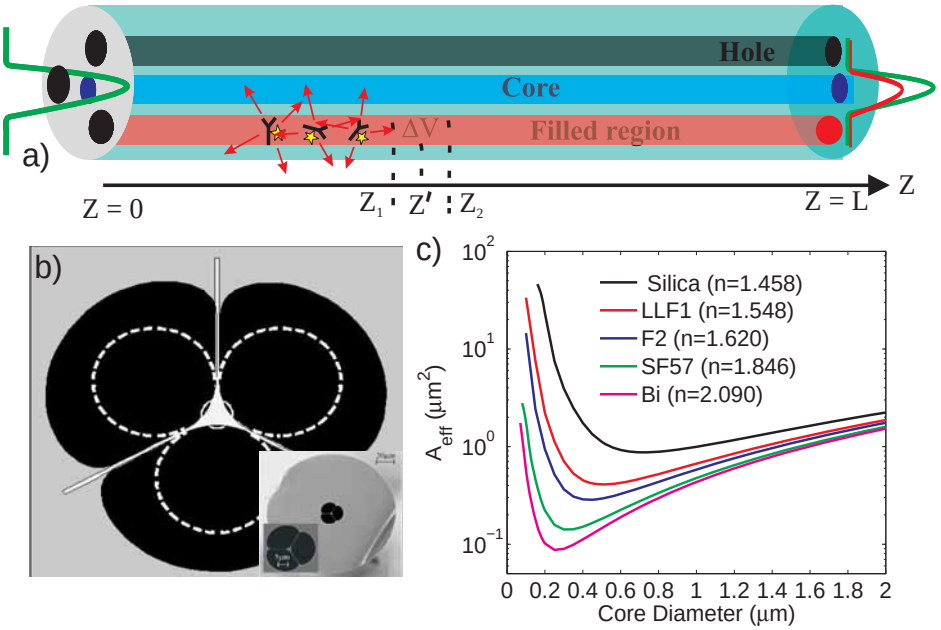

Fig. 1. Schematic of a filled MOF showing the parameters used in modelling (a) and the SEM image of the cross section of the MOF used for the modelling and experiment (b). Dashed circles in (b) show the idealized geometry used for modelling. The effective area of the fundamental mode for the geometry shown in (b) when the holes are filled with Rhodamine B in an isopropanol solution (c). The wavelength is 590 *nm*, refractive index of isopropanol is 1.3774 and different substrate glasses are marked.

Simulation results of FCF as a function of fibre length for constant core diameter and concentration, as shown in Fig. 2(a), indicate that there is an optimum fibre length $L_{opt} = \ln(\gamma_F/\gamma_E)/(\gamma_F - \gamma_E)$, which leads to maximal FCF for any fibre geometry [see Eq. (7)]. For $L < L_{opt}$ increasing the fibre length increases the absorption in the filled region via the Beer-Lambert law, and thus increases FCF. Beyond this optimum length, fibre attenuation dominates and the fluorescent power decays as $\exp(-\gamma_F L)$. Unsurprisingly, as the results in Fig. 2(a) show, the use of lower index glasses results in a higher FCF since the relatively low core-cladding index contrast leads to a higher light-matter overlap within the holes [this is also evident in the behaviour of A_{eff} in Fig. 1(c)].

Numerical simulations of the FCF also identify a less obvious and particularly interesting regime [see Fig. 2(b)]. For small core diameters ($d < 0.8\ \mu m$), the FCF can be significantly enhanced by employing high index (soft) glasses. For example, the maximum FCF (FCF at fibre length L_{opt}) for bismuth-oxide fibres at $d \approx 0.18\ \mu m$, is 2.2%, 10 times larger than the maximum FCF value for silica fibres (0.22%) at $d \approx 0.52\ \mu m$. Also, at the core size of $d \approx 0.2\ \mu m$ the maximum FCF value for bismuth fibres is 2.1%, 88 times larger than that of silica fibres (0.024%). This is contradictory to the usual assumption that sensitivity is proportional to power fraction in the holes, since high index glasses result in lower power fraction in the holes compare to that of low index glasses at small core diameter. For example, at the core diameter of $d \approx 0.2\ \mu m$ hole power fraction at excitation frequency (defined as $\eta_E^H = n_E^H (\varepsilon_0/\mu_0)^{1/2} (1/2N_{Ej}) \int_H |\mathbf{e}_{Ej}|^2 dA$) for silica and bismuth fibres are 0.97 and 0.43 re-

#88929 - $15.00 USD Received 23 Oct 2007; revised 12 Dec 2007; accepted 12 Dec 2007; published 14 Dec 2007

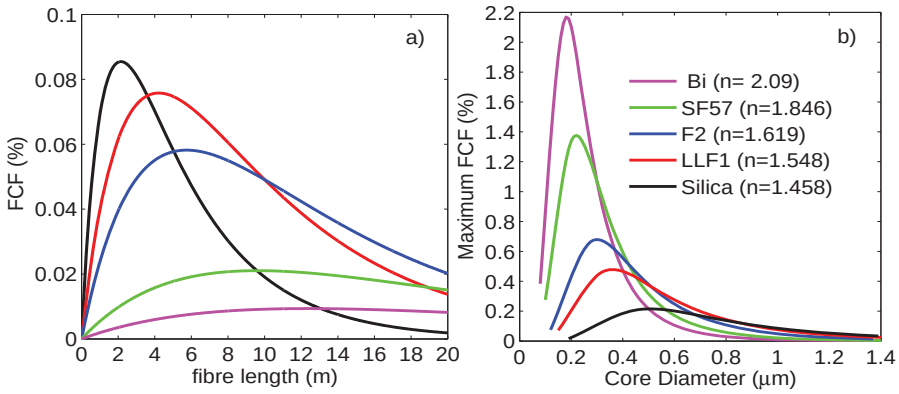

Fig. 2. Numerical results of the fluorescence capture fraction (FCF) as a function of fibre length (a) and core diameter (b) for different substrate glasses. Other parameters are; core diameter 1.0 μm, in (a) and concentration 5×10^{-5} *Mol* in (a) and (b). Maximum FCF in (b) corresponds to optimum fibre length.

spectively.

To understand this effect, we examine coefficient B_j in Eq. (8), which depends on the field distributions of the guided modes of the fibre and their overlap with the materials within the holes. We assume that the mode profiles of the excited and fluorescent fields are the same (i.e., $N_{Fj} = N_{Ej}$), which although not strictly true especially for filling materials such as quantum dots with large separation of absorbing and fluorescent wavelengths, can help provide physical insight. We rewrite coefficient B_j as $B_j = NOI_j/A_{eff}$, where;

$$NOI_j = n_E^H n_F^H \left(\frac{\varepsilon_0}{\mu_0}\right)^{1/2} \frac{\delta_{Ej}^H \int_H \left|\mathbf{e}_j\right|^2 \mathrm{Re}[(\mathbf{e}_j \times \mathbf{h}_j^*).\hat{z}]dA}{\int_{A_\infty} \left|\mathrm{Re}[(\mathbf{e}_j \times h_j^*).\hat{z}]\right|^2 dA}; \quad A_{eff} = \frac{(\int_{A_\infty} \mathrm{Re}[(\mathbf{e}_j \times h_j^*).\hat{z}dA])^2}{\int_{A_\infty} \left|\mathrm{Re}[(\mathbf{e}_j \times h_j^*).\hat{z}]\right|^2 dA}.$$

Here NOI_j is a normalized field-matter overlap integral, which approaches 1 when the core diameter becomes very small and most of the light is located outside the core [see Fig. 3(a)]. A_{eff} , defined based on z component of the Poynting vector, is a generalised form of the usual definition of A_{eff} [33].

Inspecting A_{eff} [Fig. 1(c)] and NOI [Fig. 3(a)] at a core size of $d = 0.2$ μm for both silica and bismuth, reveals that the field-matter overlap NOI for silica is 3.6 times larger than that of bismuth. However the effective area, A_{eff}, of the propagating mode for bismuth is 230 times smaller than that of silica for this core diameter, resulting in higher intensity values for bismuth and thus a larger FCF. Examining the intensity profiles of the fundamental mode for these silica and bismuth fibres [Fig. (4)], clearly shows that while the mode is well expanded into the hole region in the case of silica, it is well confined within the core for bismuth and forms a high intensity, thin layer at the core-hole interface within the filled region.

These localised high intensity regions are formed due to the discontinuity of the electric field at the interface of two dielectric media, as recently reported in slab waveguides [25] and MOFs [22, 23]. The magnitude of the discontinuity is proportional to the ratio of the dielectric

#88929 - $15.00 USD Received 23 Oct 2007; revised 12 Dec 2007; accepted 12 Dec 2007; published 14 Dec 2007

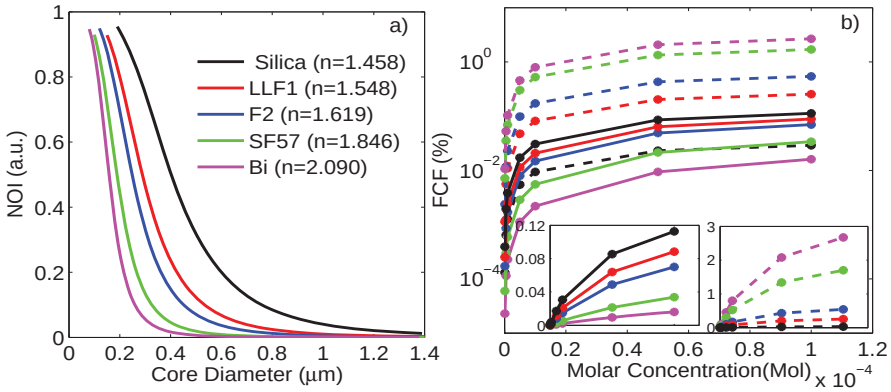

Fig. 3. Numerical results of Normalized Overlap Integral (NOI), defined in the text and calculated at the wavelength of 590 *nm* (a), and the fluorescent capture fraction (FCF) as a function concentration (b). In (b) dashed and solid lines correspond to core diameters 0.2 and 1.0 μm respectively, and the insets show the linear scale plot of the main graph over the same concentration range.

constants of the two media and hence soft glasses with higher refractive indices result in higher intensities at the glass-hole interface.

The results presented here demonstrate for the first time that overlapping localised high intensity regions in the modal field with a fluorescent material is an effective way of enhancing the performance of a sensing fibre. This enhancement is significant not only for situations where the holes are filled with liquids, but is also particularly relevant for sensing configurations where samples are coated or functionalized onto the walls of the MOF. This enhanced *FCF* regime,

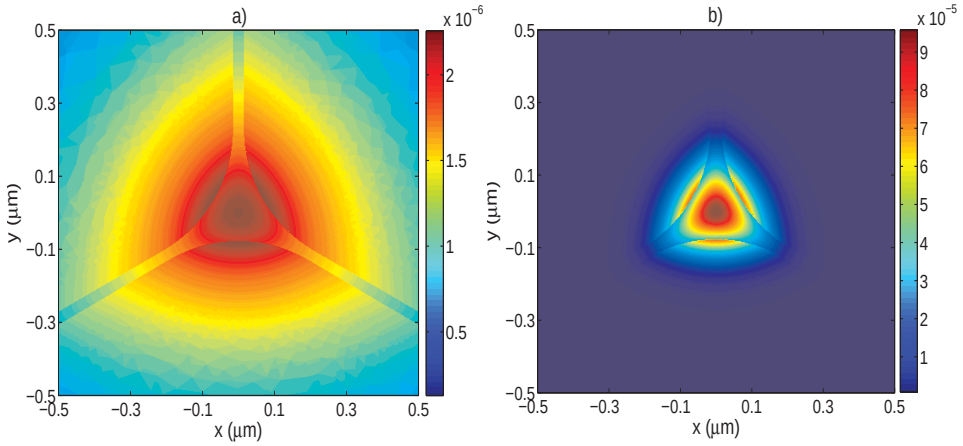

Fig. 4. Intensity distribution of the fundamental mode for Silica (a) and Bismuth (b). In both (a) and (b) core diameters are 0.2 μm and the wavelengths are 590 *nm*. The mode is more confined in (b) and a thin layer of high intensity region is formed at the glass-hole interface.

#88929 - $15.00 USD Received 23 Oct 2007; revised 12 Dec 2007; accepted 12 Dec 2007; published 14 Dec 2007

achieved by the use of small core dimensions and high index glasses, also enhances the sensitivity of FCF to concentration variations in the material to be sensed. Using Eq. (7), the FCF can be approximated as $[1-\exp(-\varepsilon_\lambda C\eta_{Ej}^H)]$ as a function of concentration C, which simplifies to $\varepsilon_\lambda C\eta_{Ej}^H$ in the limit of small concentration. This behaviour of FCF is confirmed as shown in Fig. 3(b) for two core diameters $d = 1.0$ (solid lines) and $d = 0.2\ \mu m$ (dashed lines) and different glasses. However, the behaviour of FCF as a function of concentration C is opposite for small and large core regimes. Fig. 3(b) and its insets show that for large core diameters (e.g., $d = 1.0\ \mu m$), silica has the largest asymptotic FCF value ($\sim 0.11\%$) and FCF slope ($\partial(FCF)/\partial C \sim 0.0027\%/\mu M$). Whereas, for small core diameter ($d = 0.2\ \mu m$), bismuth has the largest corresponding FCF value of (~ 2.67) and FCF slope ($\sim 0.069\%/\mu M$). As a result, both FCF and its sensitivity to small variations in concentration are enhanced in the small core, high index glass regime. This regime is expected to be of particular practical benefit in allowing observations of captured fluorescence to occur at extremely low sample concentrations, allowing for the development of sensors with competitive detection limits.

4. Experimental results

We have demonstrated experimentally in-fibre excitation and fluorescence recapturing within a filled, solid-core MOF. The holes of the MOF, shown in Fig. 1(b), were filled with Rhodamine B dissolved in isopropanol ($n = 1.3774$) using capillary action. Using the experimental setup in Fig. 5(a), Fig. 5(b) shows the experimental measurements and theoretical prediction of the filling rate. We use the filling rate equation developed in Ref. [34] for a circular capillary tube, considering the following parameters for isopropanol, its interaction with glass, and the fibre geometry; density 785 kgm^{-3}, surface tension 0.022 Nm^{-1}, viscosity $2.27\times10^{-3}\ Nsm^{-2}$, effective radius $6.11\times10^{-6}\ m$, contact angle 0°, coefficient of slip 0 m, and external pressure 0 Pa. To find the effective radius r_{eff}, we have assumed that the holes of the MOF in Fig. 1(b) are circular with the same area as that of the real fibre. This, strictly speaking, is inaccurate because capillary forces are mainly a surface effect, which depends on the radius of curvature of the different corners in the geometry, and we believe that this assumption is the main reason for the discrepancy between the theoretical and experimental results in Fig. 5(b). For these experimental measurements the position of the liquid in the holes was recorded by observing the fluorescent emission at the liquid interface in the backward direction of the laser beam in Fig. 5(a).

The setup sketched in Fig. 5(c) was used to excite the Rhodamine B molecules filled into the holes of the fibre and measure the captured fluorescence emission. The outer surface of the fibre was coated with an index matching liquid, DAG, to strip any fluorescent emission coupled to the cladding modes. This ensured that all the measured fluorescence had been captured by the relatively low-loss, core-guided modes of the fibre, as assumed by the theoretical model. The absorption and low concentration fluorescent peaks of Rhodamine B are at 540 nm [35] and 570 nm, respectively. The MOF used in the experiment has a core diameter of $d = 1.8\ \mu m$, core material of SF57 and its cross section is shown in Fig. 1(b). A CW laser at 532 nm was coupled into the MOF using an aspheric lens of $f = 2.75\ mm$ and $NA = 0.65$ and maximum coupling efficiency of around 19% was measured. The loss of the unfilled fibre at 532 nm is $5.5\pm0.5\ dB/m$, using the standard cutback method. At the output, we used a long pass filter to exclude the excitation frequency components. The fluorescence emission is then coupled into a single mode (SM) fibre, which was connected to an optical spectrum analyser for spectrum measurement.

The experimental results are presented in Fig. 5(d) clearly showing the expected fluorescence and also significant decay of the measured fluorescence over 960 seconds exposure to the excitation field. The decay in fluorescence was due to photobleaching, the photo-induced

#88929 - $15.00 USD Received 23 Oct 2007; revised 12 Dec 2007; accepted 12 Dec 2007; published 14 Dec 2007

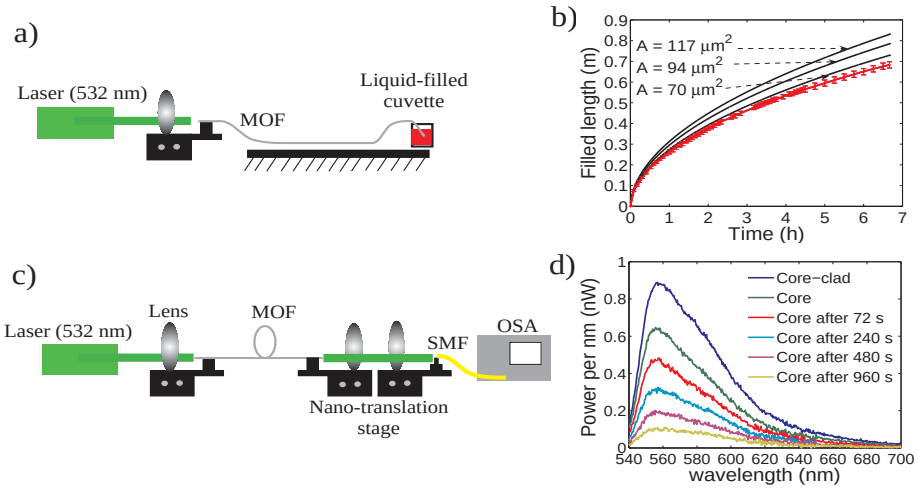

Fig. 5. Experimental setup for filling an MOF (a). The experimental and theoretical predications of filling time as a function of filled length (b). For the theoretical predictions it is assumed that the holes of the fibre are circles whose area are 1, 0.8, or 0.6 times of that of the real fibre in Fig. 1 (117, 94, and 70 μm^2 respectively). Experimental set up (c) and results (d) for capturing the fluorescent emission by the core of the MOF.

destruction of the fluorophore [28]. While partial recovery is possible, photobleaching has the potential to be problematic. For example, to measure FCF as a function of fibre length we fill a fibre and use a cut-back method to measure FCF at different lengths. However due to photobleaching effect and the time that takes to cleave, align, and couple the fluorescence beam into the OSA, it is very difficult to measure FCF as a function of length for Rhodamine B. A promising alternative is to replace organic dyes with quantum dots, which experience negligible photobleaching and have already found use in sensing such as for biological and medical applications [26, 36].

5. Discussion and conclusion

To the best of our knowledge this is the first time that a general model of both in-fibre excitation and fluorescence recapturing of filled solid-core MOFs by their core guided modes has been developed and demonstrated experimentally. An expression for the efficiency of fluorescence capture fraction has been developed for an arbitrary MOF based on vectorial solutions of Maxwell's equations and considering the modal behaviour of the MOF for distinct excitation and fluorescence frequencies. We have predicted between one to two orders of magnitude improvement in the fluorescence capture fraction (FCF) of MOFs with high index substrate glasses and small core diameters in comparison with those with low index glasses. This parameter regime results in localised, high intensity electromagnetic fields at the interface of the glass and hole regions, making it an ideal regime for thin layer sensing where chemical or biological substances are coated onto the interface.

The fluorescence capture fraction is normalised to the input power in the fibre and hence, although the small core parameter regime degrades the coupling efficiency, higher incident power (below the damage threshold of the glass) can be used to attain certain power in the fibre. Additionally, by using advanced coupling techniques such as tapers or high numerical aperture buffer fibres [37], one should be able to minimise the coupling loss into small core

#88929 - $15.00 USD Received 23 Oct 2007; revised 12 Dec 2007; accepted 12 Dec 2007; published 14 Dec 2007

fibres.

Our recent progress in fabricating soft glass MOFs with small cores, and the evidence that with careful fabrication processes fibre loss of order of $< 0.5\ dB/m$ can be achieved [38], provide an attractive new route towards the development of highly-sensitive fluorescence sensors.

Acknowledgements

We acknowledge the Defence Science and Technology Organization (DSTO), Australia, for supporting research in the Centre of Expertise in Photonics. We would also like to acknowledge the help and expertise of Dr Heike Ebendorff-Heidepriem with topics in glass chemistry and extrusion, Mr. John Debs with fibre filling experiments, and Mr. Roger Moore with fibre drawing.

#88929 - $15.00 USD Received 23 Oct 2007; revised 12 Dec 2007; accepted 12 Dec 2007; published 14 Dec 2007

3.3 Fluorescence Capture Fraction: Backwards Fluorescence Capture

The publication [P2] forms the basis of this section.

S. Afshar V., Y. Ruan, S. C. Warren-Smith, and T. M. Monro, "Enhanced fluorescence sensing using microstructured optical fibers; a comparison of forward and backward collection modes," *Optics Letters* **33**, 1473-1475 (2008).

3.3.1 Publication Overview

[P2] is a direct continuation of the work presented in Sec. 3.2 [P1]. In [P2] the fluorescence capture theory is extended in order to consider the effect of measuring fluorescence that is coupled to the backwards propagating guided modes of a waveguide, with the suspended-core (wagon wheel) geometry again used as an example.

While coupling into both forwards and backwards propagating modes is symmetric under the assumptions of uniform emission, when taking into account the fibre loss a significant difference in behaviour becomes apparent. When detecting the backwards fluorescence, the signal asymptotes to a maximum value as the fibre length increases, whereas the forwards fluorescence signal has an optimum length and decreases for long fibre lengths. In [P2] it is also noted that there are important practical aspects of using the backwards signal, such as reducing the amount of excitation light in the signal. [P2] then contains experimental results that qualitatively confirm the differences between forwards and backwards signal collection.

3.3.2 Statement of Contribution

Conceptualisation

The idea to extend the fluorescence capture theory to include the backwards propagating fluorescence was conceptualised by Shahraam Afshar.

Realisation

The derivation of the backwards fluorescence theory and numerical modelling was performed by Shahraam Afshar and error checked by Stephen Warren-Smith. The experiments were performed by Yinlan Ruan.

Documentation

This paper was primarily written by Shahraam Afshar V., with editing by all other authors.

Declaration and Permission

I declare that the above statement of contribution is accurate and I give permission for this publication to be included in this thesis.

Shahraam Afshar V. Yinlan Ruan Stephen C. Warren-Smith

Tanya M. Monro

July 1, 2008 / Vol. 33, No. 13 / OPTICS LETTERS 1473

Enhanced fluorescence sensing using microstructured optical fibers: a comparison of forward and backward collection modes

Shahraam Afshar V.,* Yinlan Ruan, Stephen C. Warren-Smith, and Tanya M. Monro

Centre of Expertise in Photonics, School of Chemistry and Physics, University of Adelaide, Adelaide, South Australia 5005, Australia

**Corresponding author: shahraam.afshar@adelaide.edu.au*

Received February 20, 2008; revised May 9, 2008; accepted May 9, 2008; posted May 21, 2008 (Doc. ID 92951); published June 24, 2008

A general model of excitation and fluorescence recapturing by the forward and backward modes of filled microstructured optical fibers (MOFs) is presented. We also present experimental results for both backward and forward fluorescence recapturing within a MOF as a function of fiber length and demonstrate a good qualitative agreement between the numerical model and experimental results. We demonstrate higher efficiency of fluorescence recapturing into backward modes in comparison with that of forward modes. © 2008 Optical Society of America

OCIS codes: 060.2370, 060.4005, 280.1415.

Microstructured optical fibers (MOFs) have recently attracted considerable interest as ideal tools for chemical or biological sensing ([1], and references therein), since a significant portion of the guided light can overlap with chemical–biological materials filled into the holes of the fibers. The sensing mechanism can be either based on absorption or fluorescence spectroscopy. Although a range of MOF variants of fluorescent-based sensors have been reported ([1], and references therein), the benefits that can be obtained using MOFs are far from being realized, largely due to the lack of a formalism for predicting and thus optimizing the measurable fluorescence power. Recently, we reported a general model for calculating the sensitivity of fluorescence-based sensing using filled MOFs [1]. The model is based on the excitation of the sensing material by the guided modes of the MOFs and the recapturing of their fluorescence emission within the forward propagating modes (the forward fluorescence capture fraction Φ_F) considering losses at both excitation and fluorescent frequencies. It demonstrates [1] that the light–matter overlap alone does not determine the optimal fiber choice as is usually assumed and that fiber designs with subwavelength features and high index glass exhibit localized regions of high intensity [2,3], which lead to enhanced fluorescence recapturing and hence higher sensing sensitivity.

In this Letter we have advanced the model presented in [1] to include the capturing of fluorescence emission into the backward propagating modes (the backward fluorescence capture fraction Φ_B). We then demonstrate that Φ_B and Φ_F show different behavior as a function of fiber length, where Φ_B can be more than 15% higher than the Φ_F, and discuss the advantages of Φ_B over those of Φ_F. Also by using an aqueous solution with quantum dots [4,5], which experience negligible photobleaching, we experimentally confirm the behavior of Φ_F and Φ_B as a function of fiber length for the first time, to the best of our knowledge. We present a monotonic behavior of ϕ_B as a function of fiber length, which demonstrates, for the first time to our knowledge, the use of microstructured fibers as a dip sensor.

We assume that the power excited in the jth mode at excitation frequency ω^E can be expressed as [6]

$$P_j^E(z) = |a_j^E|^2 N_j^E \exp(-\gamma_j^E z), \tag{1}$$

$$\gamma_j^E = k(\epsilon_0/\mu_0)^{1/2}(1/N_j^E) \times \int_\infty \mathrm{Re}(n^E)\mathrm{Im}(n^E)|\mathbf{e}_j^E|^2 \mathrm{d}A, \tag{2}$$

where $\mathbf{e}_j^E(x,y)$, $\mathbf{h}_j^E(x,y)$, and β_j^E are the jth mode electric and magnetic field distributions and propagation constant, respectively; a_j^E is the amplitude; N_j^E is the power normalization factor of mode j [6]; and $\mathrm{Re}(n^E)$ and $\mathrm{Im}(n^E)$ are real and imaginary refractive indices. Here, we assume that γ_j represents all absorption mechanisms in the MOF, including absorption due to the Beer–Lambert law. Upon absorbing the excitation photons the fluorescent species in the holes behave as sources and emit fluorescent photons in all directions. This fluorescent emission can also be written [6] as the sum of forward, backward, and radiation modes with the consideration of power decay due to loss at the fluorescence frequency. Similar to the formalisms developed in [1], we have found that the fluorescent power contribution to the ith backward mode of the MOF at $z=0$ due to a small filled section $\Delta z = z_2 - z_1$ located at z' [see Fig. 1(a)] as

$$\mathrm{d}P_{-i}^F(0,z') = \frac{\pi \exp(-\gamma_i^F z')}{4\omega_F \mu_0 n_H^F k N_i^F} \int_A \int_{z_1}^{z_2} |\mathbf{e}_{-i}^F|^2 P_D \mathrm{d}A \mathrm{d}z''. \tag{3}$$

Here, $P_D(\mathbf{r})$ is the radiation power density of the fluorescent emission of the filling material [1,7], subscript $-i$ refers to the ith backward mode, and subscript H generally refers to the filled-hole region. By using Eq. (1)—assuming that the fluorescent power density is proportional to the density of excitation

0146-9592/08/131473-3/$15.00

1474 OPTICS LETTERS / Vol. 33, No. 13 / July 1, 2008

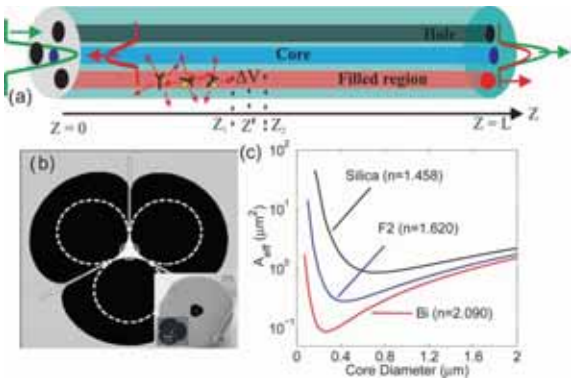

Fig. 1. (Color online) Schematic of a filled MOF showing (a) the parameters used in modeling and (b) the SEM image of the cross section of the MOF used for the modeling and experiment. (c) Effective area of the fundamental mode for the geometry shown in (b) when the holes are filled with Rhodamine B in an isopropanol solution. The wavelength is 590 nm, the refractive index of isopropanol is 1.3774, and the different substrate glasses are marked.

power loss due to the Beer–Lambert law in the filled region (proportionality constant ξ)—and evaluating the integrals in Eq. (3) with respect to z'', in the limit of $z_1 \to z_2$ and z' [see Fig. 1(a)], we find

$$\Phi_B = 2A \frac{1}{(\gamma_j^E + \gamma_i^F)} \{1 - \exp[-(\gamma_i^F + \gamma_j^E)L]\},$$

$$A = \frac{\xi \alpha_B \lambda^2 n_H^E \epsilon_0}{8\pi n_H^F \mu_0} \delta_j^E \frac{\int_H |\mathbf{e}_i^F|^2 \mathrm{Re}[(\mathbf{e}_j^E \times \mathbf{h}_j^{E*}) \cdot \hat{z}] \mathrm{d}A}{4 N_i^F N_j^E},$$

$$\Phi_F = 2A \frac{\exp(-\gamma_i^F L)}{(\gamma_j^E - \gamma_i^F)} \{1 - \exp[(\gamma_i^F - \gamma_j^E)L]\}. \quad (4)$$

Here, α_B is the Beer–Lambert absorption coefficient, $|\mathbf{e}_{-i}^F|^2 = |\mathbf{e}_i^F|$ [6]; $P_j^E(0)$ is the input excitation field power; the relation for $\Phi_F = P_i^F(L)/P_j^E(0)$ [1] is given for comparison with the $\Phi_B = P_{-i}^F(0)/P_j^E(0)$; and the factor 2 in Φ_F and Φ_B is due to the contribution from the two polarizations.

Next, we apply the developed model to an MOF, as shown in Fig. 1(b), with the following parameters: excitation wavelength $\lambda_E = 532$ nm, fluorescence wavelength $\lambda_F = 590$ nm, filling material: Rhodamine B dissolved in isopropanol, and three different glass materials [silica, lead silicate (F2), and bismuth]. We have used Rhodamine B simply to compare the results for forward and backward propagating modes. Simulation results of Φ_F and Φ_B as a function of fiber length, as shown in Fig. 2(a), indicate that while Φ_F maximizes at an optimum length, Φ_B increases rapidly for short lengths and then approaches an asymptotic value. The reason for the difference is clear: the fluorescent emission coupled to the backward mode can be detected instantaneously once the incident beam enters the filled region at $z = 0$ [(see Fig. 1(a)], while the emission coupled to the forward

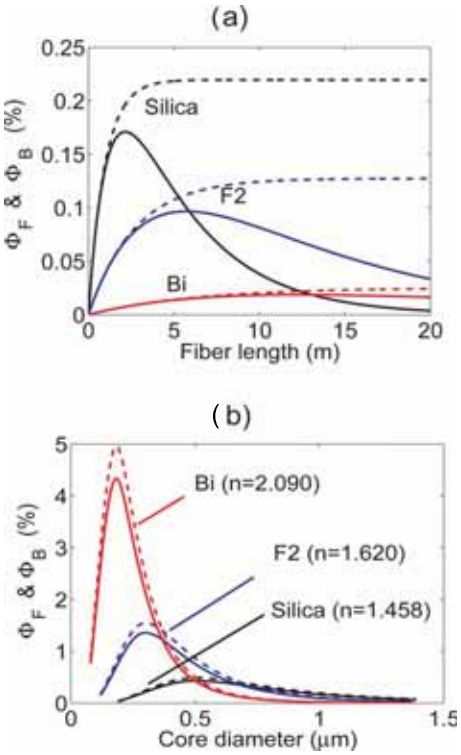

Fig. 2. (Color online) Numerical results of the fluorescence capture fraction for forward (Φ_F, solid curves) and backward (Φ_B, dashed curves) directions as a function of (a) fiber length and (b) core diameter for different substrate glasses. Other parameters are core diameter 1.0 μm in (b) and concentration 0.5 μM in (a) and (b). Φ_F and Φ_B in (b) correspond to the optimum fiber length defined at the maximum of Φ_F in (a).

mode needs to travel through the filled region, having a decay of $\exp(-\gamma^F L)$, to be detected at $z = L$. This is also evident from Eqs. (4); in the limit of $L \to \infty$ the Φ_F approaches zero but Φ_B approaches an asymptotic value. This demonstrates for the first time, to the best of our knowledge, that Φ_B can be advantageously employed for fluorescence sensing because of its higher efficiency and lower loss in comparison with Φ_F. Φ_B has other advantages over Φ_F including the possibility of using a dip-sensing configuration [see Fig. 3(a)], real time measurement, a higher signal to pump ratio, no optimal length (the longer the fiber length the higher the Φ_B), and ease of use in terms of keeping the launching end of the setup intact and using the exit end for filling.

In our previous publication we identified an interesting regime of small core diameters ($d < 0.8$ μm), for which the Φ_F can be significantly enhanced by employing high index (soft) glasses. The study of ϕ_B shows similar behavior as is evident from Fig. 2(b). For example, the maximum Φ_B for bismuth oxide fibers at $d \approx 0.18$ μm, is 4.96%, ten times larger than the maximum Φ_B value for silica fibers (0.50%) at $d \approx 0.52$ μm. Also, at the core size of $d \approx 0.2$ μm the maximum Φ_B value for bismuth fibers is 4.82%, 69

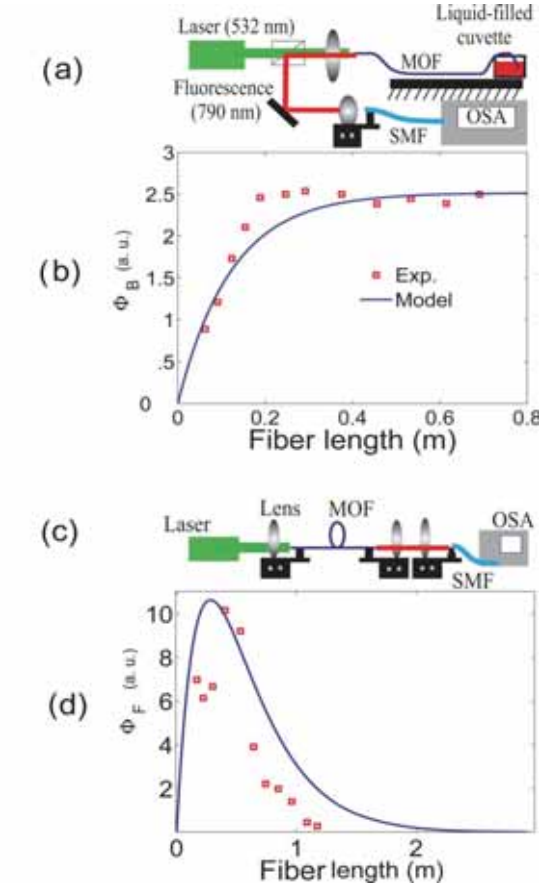

Fig. 3. (Color online) (a), (c) Experimental setups and results for measuring the fluorescence captured fraction into the (b) backward and (d) forward mode of an MOF with LLF1 substrate glass and a core diameter of 2 μm. The holes of the MOF are filled with a solution of 1 μM quantum dot. Simulation results are shown by solid curves (b) and (d).

times larger than that of silica fibers (0.07%). Similar to Φ_F [1], a thorough examination of Φ_B in Eq. (4) reveals that the sensitivity depends on both the power fraction in the holes and the intensity distribution of the modes. Therefore, fiber geometries resulting in high intensity regions may lead to high Φ_B even if they have a relatively smaller power fraction in the hole regions.

Figures 3(a)–3(d) show the experimental setup and results for measuring the fluorescence emission capturing into the backward [Figs. 3(a) and 3(b)] and forward [Figs. 3(c) and 3(d)] propagating modes as a function of fiber length. To the best of our knowledge, this is the first experimental investigation of length dependence of fluorescence capturing into the forward and backward modes of an MOF. We used MOFs similar to the one in Fig. 1(b) with substrate glasses of LLF1 ($n=1.55$) and core diameters and losses of approximately $d=2$ μm and 30 dB/m (filled fiber) at an excitation wavelength of 532 nm, respectively. The holes of the MOF were filled with an aqueous solution with 1 μM of CdTe–ZnS quantum-dot labeled goat F(ab')2 antimouse IgG conjugate from Invitrogen [8]. Experimental results qualitatively confirm the behavior of Φ_B and Φ_F as a function of length as predicted by the model. The model's results for Φ_B and Φ_F have been scaled individually to fit the experimental data. Better quantitative agreement may be achieved by having more accurate measurements of the fiber loss, quantum dot concentrations, fiber core diameter, and the loss due to mode mismatching between filled and unfilled sections of the MOF and by improving the stability and repeatability of light coupling into and out of the fiber especially for the forward approach.

A previous model of both in-fiber excitation and fluorescence recapturing of filled solid-core MOFs by their forward propagating modes [1] is generalized to include the capturing of fluorescence emission into the backward modes. Also, the capturing of fluorescence emission power into both forward and backward propagating modes of an MOF as a function of fiber length has been experimentally demonstrated and qualitatively confirmed with those of the numerical model. The numerical results presented here also demonstrate for the first time to our knowledge that the fluorescence emission coupled into the backward modes has a higher efficiency than those of the forward modes. This, however, can be confirmed experimentally by using optimized outcoupling setups or advanced coupling techniques such as tapers or high numerical aperture buffer fibers. Considering the advantages of Φ_B over Φ_F such as higher efficiency, higher signal to pump ratio, possibility of using a dip-sensing configuration [see Fig. 3(a)], ease of use in terms of experimental setup, and the previous results of our group, reporting the detection of quantum dots with a concentration as low as 1 nM using the forward approach [5], we expect to improve our detection power to picomolar concentration using our new backward approach with optimized coupling setups.

We acknowledge the Defence Science and Technology Organization (DSTO), Australia, for supporting research in the Centre of Expertise in Photonics. This research was supported under the Australian Research Council's Discovery Projects funding scheme (project DP0665486).

References

1. S. Afshar V., S. C. W. Smith, and T. M. Monro, Opt. Express **15**, 17891 (2007).
2. M. Nagel, A. Marchewka, and H. Kurz, Opt. Express **14**, 9944 (2006).
3. G. S. Wiederhecker, C. M. B. Cordeiro, F. Couny, F. Benabid, S. A. Maier, J. C. Knight, C. H. B. Cruz, and H. L. Fragnito, Nat. Photonics **1**, 115 (2007).
4. R. E. Bailey, A. M. Smith, and S. Nie, Physica E (Amsterdam) **25**, 1 (2004).
5. Y. Ruan, E. P. Schartner, H. Ebendorff-Heidepriem, P. Hoffman, and T. M. Monro, Opt. Express **15**, 17819 (2007).
6. A. W. Snyder and J. D. Love, *Optical Waveguide Theory* (Chapman and Hall, 1995).
7. D. Marcuse, J. Lightwave Technol. **6**, 1273 (1988).
8. http://probes.invitrogen.com/products/qdot/.

3.4 Fluorescence Capture Fraction: Exposed-Core Fibre

The publication [P3] forms the basis of this section.

S. C. Warren-Smith, S. Afshar V., and T.M. Monro, "Theoretical study of liquid-immersed exposed-core microstructured optical fibres for sensing," *Optics Express* **16**, 9034-9045 (2008).

3.4.1 Publication Overview

Aim

The primary aim of this publication was to use the fluorescence capture theory of [P1] to understand the fluorescence sensing properties of liquid-immersed exposed-core microstructured optical fibres and compare this to equivalent liquid-filled enclosed suspended-core (wagon wheel) fibres. The geometric difference is that the exposed-core fibre has only one hole filled and thus the sensing region is one third as large. At first sight it would appear that the exposed-core fibre would have lower efficiency due to having a smaller interaction region. However, this paper reveals that this is not necessarily the case due to how the asymmetric geometry affects the optical mode. The second half of [P3] considers the effect of liquid interface transmission losses for a multiply immersed exposed-core fibre, and how this is affected by glass refractive index choice.

Field of Knowledge and Link Between Publications

The development of the fluorescence capture theory for enclosed suspended-core (wagon wheel) fibres has been discussed in relation to [P1] (Sec. 3.2) and [P2] (Sec. 3.3). In the literature, the primary motivation for extending the optical fibre design from the enclosed suspended-core geometry to the exposed-core design stems from the low filling speed when sensing with enclosed MOFs [84]. A less stated, but also important, issue is that an enclosed MOF cannot be used for distributed sensing. As will be seen in [P7] (Sec. 4.3), the exposed-core fibre allows for real-time sensing, while it will be seen in [P8] (Sec. 4.4) that distributed sensing is possible.

The fabrication of exposed MOFs has been demonstrated by various researchers, such as the use of a fusion splicer and air pressure to blow holes within an MOF [76], use of a focused ion beam [103, 104], and femtosecond laser micromachining [105, 106]. However, these methods generally result in short exposed regions, such as the order of tens of microns. Cox *et al.* have shown that long lengths of exposed-core polymer MOF can be fabricated by creating an opening at the preform stage of the fibre fabrication, such as by drilling holes into the cladding of a polymer MOF preform [108]. Finally, fabrication of glass, in this case lead-silicate, exposed-core fibres will be demonstrated in [P7]. The advantage of the method that will be demonstrated in [P7] is that glass fibres have the potential to have lower transmission loss than polymer fibres and thus distributed sensing is possible, as will be demonstrated in [P8].

Discussion and Conclusions

In [P3] the absorption and fluorescence sensing characteristics of liquid-immersed exposed-core fibres have been modelled theoretically, and compared to an equivalent enclosed suspended-core fibre (which was first studied in [P1]). The results demonstrate that despite a smaller sensing area the asymmetric refractive index profile allows the exposed-core fibre to have competitive sensing characteristics, particularly for sufficiently small core diameters. In terms of absorption sensing, the optical field spreads in the direction of the liquid sensing region due to the smaller refractive index difference. In terms of fluorescence sensing, the relatively greater refractive index difference at the unfilled hole boundaries causes a smaller effective area, which in turn increases the fluorescence capture. The final section of [P3] then looks at predicted transmission losses that are present for a fibre that has fluid interfaces along the length, such as for a distributed-type sensor. It is shown that high refractive index materials have considerably less liquid interface losses, which is amplified if multiple interfaces are considered. This complements the general conclusions of this paper, as well as [P1, P2], which is that high refractive index fibres can exhibit greater fluorescence capture. Note that a full derivation of the coupling efficiency formulas used in this paper is provided in Appendix B.

The modelling in this paper (and in [P1, P2]) has considered the fundamental mode only. Strictly speaking, this means that the results are only applicable to the single mode regime, for which the core diameter is very small (approximately the same scale as

the wavelength or smaller). The next publication, [P4], extends the fluorescence capture theory to include higher order modes and thus make it applicable to larger range of core diameters. [P4] will show that the fluorescence capture is approximately independent of core diameter, and mostly dependant on the refractive index contrast between core and cladding, and can be understood intuitively as the fibre having a greater numerical aperture. While not explicitly stated or modelled, this implies that the greater capture predicted in [P3] for the liquid-immersed exposed-core fibre relative to the fully filled enclosed fibre should be applicable to all core diameters due to the on-average higher numerical aperture that results from the two unfilled air holes.

Finally, it should be noted that the core diameters of the fibres modelled in this paper are significantly smaller than that of reported fabricated exposed-core fibres presented in Ref. [108] and [P7]. For example, the core diameters of the fabricated fibres presented in [P7] range from 2.0 to 3.0 μm, while the core diameters considered in this paper range from 0.2 to 1.0 μm. While there currently exists a large gap between the theoretical optimum core diameter and current fabrication results, it will be shown in [P6] that enclosed suspended optical nanowires have been successfully fabricated with core diameters in this range and thus it is feasible that these dimensions will ultimately be achieved for exposed-core fibres.

3.4.2 Statement of Contribution

Conceptualisation

The idea to extend the fluorescence capture theory to the liquid-immersed exposed-core microstructured optical fibre geometry, and also to include liquid-interface transmission losses, was conceptualised by Stephen Warren-Smith.

Realisation

The development of the fluorescence capture theory was outlined previously in relation to [P1]. The numerical modelling of the fluorescence capture into the exposed-core fibre was done by Stephen Warren-Smith. Derivation of the coupling theory and subsequent numerical modelling was done by Stephen Warren-Smith.

Documentation

This paper was primarily written by Stephen Warren-Smith, with editing by all other authors.

Declaration and Permission

I declare that the above statement of contribution is accurate and I give permission for this publication to be included in this thesis.

Stephen C. Warren-Smith Shahraam Afshar V. Tanya M. Monro

Theoretical study of liquid-immersed exposed-core microstructured optical fibers for sensing

S. C. Warren-Smith*, S. Afshar V., and T. M. Monro

Centre of Expertise in Photonics, School of Chemistry & Physics, The University of Adelaide, Adelaide, SA 5005, Australia
**Corresponding author: stephen.warrensmith@adelaide.edu.au*

Abstract: The absorption and fluorescence sensing properties of liquid-immersed exposed-core microstructured optical fibers are explored for the regime where these structures act as supported nanowires with direct access to the sensing environment. For absorption-based sensing we demonstrate that the amount of power propagating in the sensing region of the exposed-core fiber can compete with that of traditional MOFs. For fluorescence-based sensing, we see that in addition to the enhanced fluorescence capture efficiency already predicted for small-core, high refractive index contrast fibers, an improvement of up to 29% can be gained by using liquid-immersed exposed-core fibers. Additionally, calculation of the losses associated with interfaces between filled and unfilled sections predict significant benefit in using high refractive index substrate glasses for liquid-immersed exposed-core fiber sensing. This work demonstrates that, for fiber dimensions of interest, the exposed-core fiber is an attractive new sensor technology.

OCIS codes: (060.2370) Fiber optics sensors; (060.4005) Microstructured fibers; (300.1030) Absorption; (300.2530) Fluorescence, laser-induced.

References and links

1. G. Stewart and B. Culshaw, "Optical waveguide modelling and design for evanescent field chemical sensors," Opt. Quantum Electron. **26**, s249-s259 (1994).
2. J. B. Jensen, P. E. Hoiby, G. Emiliyanov, O. Bang, L. H. Pedersen, and A. Bjarklev, "Selective detection of antibodies in microstructured polymer optical fibers," Opt. Express **13**, 5883-5889 (2005).
3. L. Rindorf, P. E. Hoiby, J. B. Jensen, L. H. Pedersen, O. Bang, and O. Geschke, "Towards biochips using microstructured optical fiber sensors," Anal. Bioanal. Chem. **385**, 1370-1375 (2006).
4. C. M. B. Cordeiro, M. A. R. Franco, G. Chesini, E. C. S. Barretto, R. Lwin, C. H. B. Cruz, and M. C. J. Large, "Microstructured-core optical fibre for evanescent sensing applications," Opt. Express **14**, 13056-13066 (2006).
5. Y. Zhu, H. Du, and R. Bise, "Design of solid-core microstructured optical fiber with steering-wheel air cladding for optimal evanescent-field sensing," Opt. Express **14**, 3541–3546 (2006).
6. T. Ritari, J. Tuominen, H. Ludvigsen, J. C. Petersen, T. Sorensen, T. P. Hansen, and H. R. Simonsen, "Gas sensing using air-guiding photonic bandgap fibers," Opt. Express **12**, 4080-7 (2004).
7. Y. L. Hoo, W. Jin, C. Z. Shi, H. L. Ho, D. N. Wang, and S. C. Ruan, "Design and modeling of a photonic crystal fiber gas sensor," Appl. Opt. **42**, 3509-3515 (2003).
8. C. M. B. Cordeiro, E. M. dos Santos, C. H. Brito Cruz, C. J. de Matos, and D. S. Ferreiia, "Lateral access to the holes of photonic crystal fibers – selective filling and sensing applications," Opt. Express **14**, 8403-8412 (2006).
9. C. M. B. Cordeiro, C. J. S. de Matos, E. M. dos Santos, A. Bozolan, J. S. K. Ong, T. Facincani, G. Chesini, A. R. Vaz, and C. H. Brito Cruz, "Towards practical liquid and gas sensing with photonic crystal fibres: side access to the fibre microstructure and single-mode liquid-core fibre," Meas. Sci. Technol. **18**, 3075-3081 (2007).
10. C. J. Hensley, D. H. Broaddus, C. B. Schaffer, and A. L. Gaeta, "Photonic band-gap fiber gas cell fabricated using femtosecond micromachining," Opt. Express **15**, 6690-6695 (2007).
11. A. van Brakel, C. Grivas, M. N. Petrovich, and D. J. Richardson, "Micro-channels machined in microstructured optical fibers by femtosecond laser," Opt. Express **15**, 8731-8736 (2007).
12. F. M. Cox, R. Lwin, M. C. J. Large, and C. M. B. Cordeiro, "Opening up optical fibres," Opt. Express **15**, 11843-11848 (2007).

#94852 - $15.00 USD Received 11 Apr 2008; revised 29 May 2008; accepted 29 May 2008; published 4 Jun 2008

13. T. M. Monro, H. Ebendorff-Heidepriem, Patent Application, 'Fabrication of nanowires' (PCT/AU2006/00501), October 2005.
14. H. Ebendorff-Heidepriem, P. Petropoulos, S. Asimakis, V. Finazzi, R. C. Moore, K. Frampton, F. Koizumi, D. J. Richardson, and T. M. Monro, "Bismuth glass holey fibers with high nonlinearity," Opt. Express **12**, 5082–5087 (2004).
15. M. J. Steel, T. P. White, C. M. de Sterke, R. C. McPhedran, and L. C. Botten, "Symmetry and degeneracy in microstructured optical fibers," Opt. Lett. **26**, 488-490 (2001).
16. G. S. Wiederhecker, C. M. B. Cordeiro, F. Couny, F. Benabid, S. A. Maier, J. C. Knight, C. H. B. Cruz, and H. L. Fragnito, "Field enhancement within an optical fiber with a subwavelength air core," Nat. Photonics **1**, 115-118 (2007).
17. N. Ganesh and B. T. Cunningham, "Photonic crystal enhanced fluorescence," in *Tech. Digest*, (Opt. Soc. Am., 2007) p. CThz5.
18. J. Lou, L. Tong, and Z. Ye, "Modeling of silica nanowires for optical sensing," Opt. Express **13**, 2135-2140 (2005).
19. S. Afshar V., S. C. Warren-Smith, and T. M. Monro, "Enhancement of fluorescence-based sensing using microstructured optical fibres," Opt. Express **15**, 17891-17901 (2007).
20. Y. Ruan, E. P. Schartner, H. Ebendorff-Heidepriem, P. Hoffmann, and T. M. Monro, "Detection of quantum-dot labeled proteins using soft glass microstructured optical fibers," Opt. Express **15**, 17819-17826 (2007).
21. A. W. Snyder and J. D. Love, *Optical Waveguide Theory* (Chapman and Hall, 1995).
22. Agrawal, *Nonlinear Fiber Optics* (Academic Press, 2007).
23. F. W. D. Rost, *Fluorescence Microscopy* (Cambridge University Press, 1992).
24. M. Sumetsky, Y. Dulashko, and A. Hale, "Fabrication and study of bent and coiled free silica nanowires: Self-coupling microloop optical interferometer," Opt. Express **12**, 3521-3531 (2004).
25. J. D. Love and C. Durniak, "Bend loss, tapering, and cladding-mode coupling in single-mode fibers," IEEE Photon. Technol. Lett. **19**, 1257-1259 (2007).
26. N. H. P. Kao, N. Yang, and J. S. Schoeniger, "Enhancement of evanescent fluorescence from fiber-optic sensors by thin-film sol-gel coatings," J. Opt. Soc. Am. A **15**, 2163-2171 (1998).
27. W. Henry, "Evanescent field devices: a comparison between tapered optical fibers and polished or D-fibers," Opt. Quantum Electron. **26**, s261-s272 (1994).
28. A. Cargama, "Modal analysis of coupling problems in optical fibers," IEEE Trans. Microwave Theory Tech. **MTT-23**, 162-169 (1975).
29. C. Vassallo, "On a rigorous calculation of the efficiency for coupling light power into optical waveguides," **QE-13**, 165-173 (1977).
30. M. Mostafavi, I. Itoh, and R. Mittra, "Excitation of an optical fiber by a Gaussian beam," Appl. Opt. **14**, 2190-2193 (1975).
31. J. A. Buck, *Fundamentals of Optical Fibers* (John Wiley & Sons, 2004).
32. C. Vassallo, *Optical waveguide concepts* (Elsevier 1991).
33. D. Marcuse, "Radiation losses of tapered dielectric slab waveguides," Bell Syst. Tech. J. **49**, 273-290 (1970).
34. P. A. Wallace, M. Campbell, Y. Yang, A. S. Holmes-Smith, and M. Uttamlal, "A distributed optical fibre fluorosensor for pH measurement," J. Lumin. **72-74**, 1017-1019 (1997).

1. Introduction

Microstructured optical fibers (MOFs) can be used to dramatically improve traditional absorption and fluorescence-based fiber sensors due to the ability to precisely control their optical characteristics. In particular, this control can be used to increase the amount of optical power that is available to interact with the environment that is to be sensed [1-4], and reported overlap values between the guided modes and the materials within the holes of the fiber include 6.5% for a multi-core MOF [3], 40% for a nanowire [5], and 97% or higher for an air-core photonic bandgap fiber [6]. However, these sensors require that the chemicals to be measured are located within the holes of the MOF, and generally require filling the fiber with liquids or gases. Although this approach delivers high sensitivity due to the possibility of integrating the response over the fiber length, when used in this manner, MOF-based sensors do not lend themselves to distributive sensing. In 2003 Hoo, *et al.*, proposed the introduction of periodic openings along a sensing fiber that allow access to the fiber's core [7]. Fabrication has subsequently been demonstrated by the use of a fusion splicer and air pressure to blow holes within an MOF [8], use of a focused ion beam [9], and femtosecond laser micromachining [10, 11]. Cox, *et al.*, have also demonstrated that by creating the fiber opening at the preform stage of the fiber fabrication longer lengths of exposed-core fiber can be fabricated, such as by drilling a slit into the cladding of a polymer MOF preform [12]. This exposed-core design of optical fiber sensor has advantages over other fiber based sensors such as fast-response, real-time sensing with no requirement for selective hole filling. Potential

#94852 - $15.00 USD Received 11 Apr 2008; revised 29 May 2008; accepted 29 May 2008; published 4 Jun 2008

implementations include long interaction length point sensing by use of a coiled sensing cell, multipoint sensing, and continuous distributive sensing via optical time domain reflectometry techniques.

In this paper we present the first theoretical study of the characteristics of this class of optical fiber for the case where the exposed section is immersed in a liquid for the purpose of intensity-based absorption or fluorescence sensing. The particular fiber geometry studied has a wavelength-scaled (nanowire-like) core suspended within a robust jacket that has a missing segment (or wedge); see Fig. 1(c) [13]. This geometry is as close as practically possible to the ideal case of a nanowire suspended in air (or within an environment to be sensed). From a theoretical point of view it is essentially a wagon wheel (WW) fiber (Fig. 1(a) and Fig. 1(b)) [14] (or steering wheel fiber [5]), but where one of the holes has been filled with a sensing material (the exposed section) while the others remain filled with air. If the filling material has unity refractive index (air) then the modal characteristics of the fiber are unchanged by the introduction of the wedge within the fiber jacket. When a portion of the fiber is immersed in a liquid, the mode profile spreads out into the exposed section due to the weaker confinement resulting from the raised refractive index of the liquid (for a water-based solution, n=1.33).

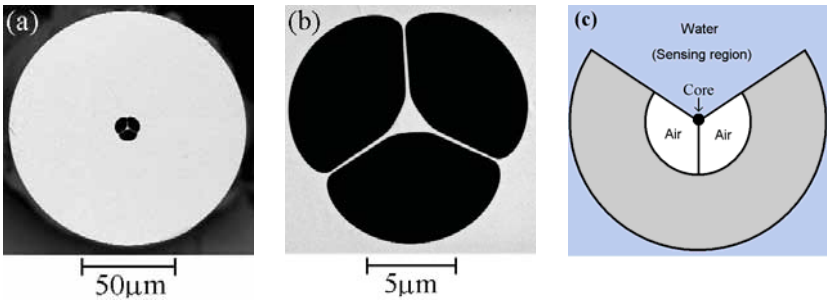

Fig. 1. Scanning electron microscope (SEM) image of an F2 (lead-silicate), wagon wheel fiber (a) and its core region (b). This fiber forms the basis of the exposed-core fiber where one of the holes is opened up to allow it to be accessible to the external environment, as shown in the schematic diagram (c).

Here we evaluate the absorption and fluorescence sensing performance for a range of fibers of this type, and compare the results to those obtained with fully filled WW fibers. The losses associated with the mode mismatch that occurs at the liquid boundaries within an exposed-core fiber are also considered. This comparison allows us to determine the feasibility of using exposed-core fibers within sensing systems, and to evaluate the impact of using an asymmetrically raised refractive index profile.

2. Numerical modeling

The field distributions corresponding to the pair of fundamental guided modes of the fiber were determined using the commercially available finite element modelling package COMSOL 3.2. For the case where all three surrounding holes are filled with water there is a three-fold rotational symmetry and hence two degenerate fundamental modes are found (to within the numerical accuracy of the model – see Sec. 3) [15]. However, when just one hole contains a liquid, as in the case of an exposed-core fiber, there is only one reflection axis of symmetry and the modes are no longer degenerate. Instead, the first two modes exhibit strong birefringence, with one mode being polarized essentially parallel to the axis of symmetry and the other orthogonal to this.

Figure 2 shows two example fundamental field distributions of a liquid-immersed exposed-core fiber for a low refractive index host material (silica, n=1.46) and a high refractive index glass host (bismuth, n=2.09). Arrows indicate the direction of the electric field and the field profile shown is the z-component of the Poynting vector. The core sizes are defined as the diameter of a circle whose area is equal to a triangle that fits wholly within the core. The core diameters were chosen so that the effective areas are located at approximately

#94852 - $15.00 USD Received 11 Apr 2008; revised 29 May 2008; accepted 29 May 2008; published 4 Jun 2008

equivalent locations on their respective effective area versus core diameter curves in order to allow comparison of their properties (see Sec. 3). The core diameters are 0.505μm for silica and 0.17μm for bismuth, resulting in effective areas of 0.76μm^2 for silica and 0.24μm^2 for bismuth at a wavelength of 590nm. In each case, the first fundamental mode is approximately linearly polarized with the direction of polarization parallel to the axis of symmetry, and exhibits a high intensity peak in the sensing region at the refractive index boundary. The higher refractive index material (bismuth in this case) exhibits greater confinement, as seen by the smaller dimensions of the bismuth fiber core, and thus has a greater high intensity peak at the boundary. This thin-layer high intensity peak has previously been investigated by other authors [16-18] and we shall see that it is beneficial for fluorescence sensing applications [19]. Note that only the mode with polarization parallel to the axis of symmetry has a high intensity peak in the sensing region for the exposed core fiber, and we will see this leads to significant differences in the relative fluorescence capture into each of the fundamental modes.

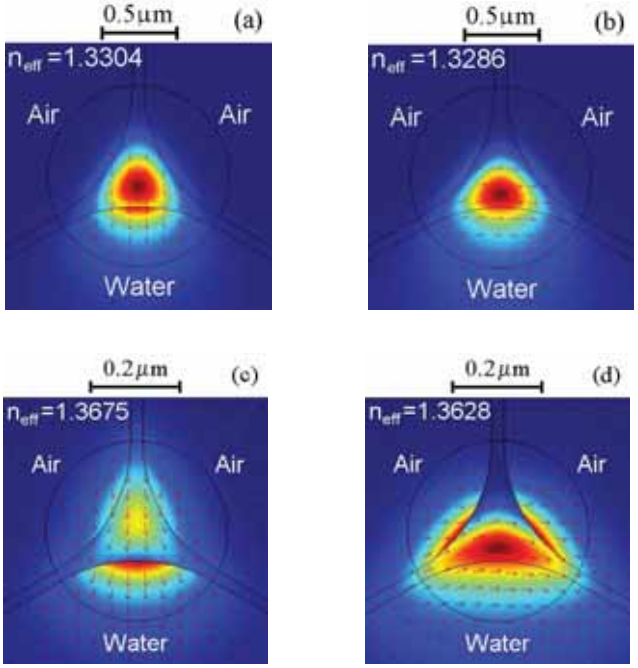

Fig. 2. Fundamental field distributions of a water-immersed exposed-core WW fiber where the substrate glass is silica with a core diameter of 0.505μm (a, b) and bismuth with a core diameter of 0.17μm (c, d). The first (a, c) and second (b, d) fundamental modes are shown for each glass type. The effective index of each mode is shown, which relates to the propagation constant (β) and the wavenumber (k) via $n_{eff}=\beta/k$.

3. Modal properties

First we consider the birefringence of the fundamental modes of the exposed-core fiber, which result from the non-degenerate solutions of this asymmetric geometry. Figure 3 shows the numerical results for the birefringence (Δn) of the exposed-core liquid-immersed fiber as compared with the case where all three holes are filled (the 3-fold symmetric case). We have chosen to consider a wavelength of 590nm as this is close to the fluorescence wavelength of many organic dyes (e.g. rhodamine B). Later, in Sec. 5, a wavelength of 532nm is used as the excitation wavelength in order to match sources used in typical experiments [20], noting that the following results are not qualitatively dependant on the exact choice of wavelength. A range of host glasses have been considered (silica = 1.46, lead silicate (F2) = 1.62, and

#94852 - $15.00 USD Received 11 Apr 2008; revised 29 May 2008; accepted 29 May 2008; published 4 Jun 2008

bismuth = 2.09) to understand the effect of varying refractive index while still considering realistic materials.

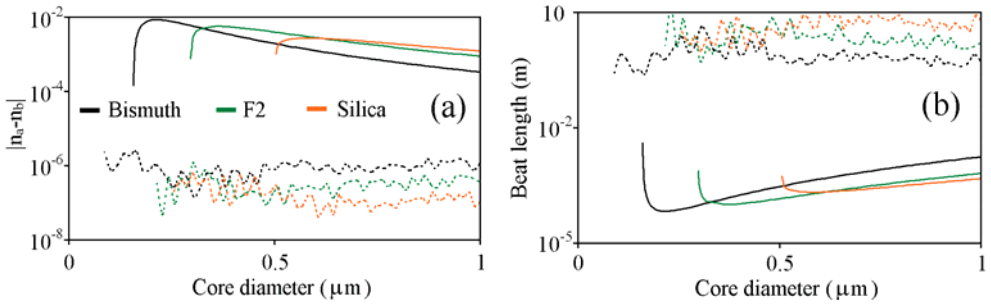

Fig. 3. (a). Difference in effective index between the two degenerate fundamental modes of a fully filled WW structured MOF (dashed lines) and the two fundamental non-degenerate modes of the exposed-core WW (solid lines) for three substrate glasses (indicated in legend). (b). The corresponding beat lengths.

Unsurprisingly, the exposed-core fiber experiences significant birefringence, and it is particularly strong in the small core regime (c.f. wavelength). For example, the predicted beat length can be as short as 68μm for a bismuth exposed-core fiber with a core diameter of 0.2μm. The low-level birefringence that is numerically calculated for the fully filled case is purely the result of numerical errors, which are introduced by the use of a mesh in the finite element modeling [15]. The birefringence measured in this case is thus a measure of the numerical accuracy for this particular geometry and mesh density (~120,000 mesh elements were used) and show that the effective index calculation is accurate to approximately six decimal places. At this point we note that while the value of the birefringence itself does not relate directly to the sensing properties of the exposed core fiber, we will now see that the non-degeneracy of the fundamental modes has consequences on the absorption and fluorescence sensing characteristics.

In order to understand the performance of sensors based on these fibers we evaluated the modal power fraction (PF) [21] within the sensing region and the effective modal area (A_{eff}), which is defined here as the vectorial equivalent to the traditional definition of A_{eff} [22]. Vectorial definitions were used because the weak guidance approximation is inappropriate for microstructured optical fibers where a large difference in refractive index exists between the core and cladding materials. The definitions are;

$$A_{eff,j} = \frac{\left| \int_{A_\infty} s_{z,j}(\vec{r}) dA \right|^2}{\int_{A_\infty} |s_{z,j}(\vec{r})|^2 \, dA}; \tag{1}$$

$$PF_j = \frac{\int_{H} s_{z,j}(\vec{r}) dA}{\int_{A_\infty} s_{z,j}(\vec{r}) dA} \tag{2}$$

where A_∞ is defined to be the infinite transverse cross section, *H* refers to integrating over the sensing region (the water containing hole(s)), *j* is the mode index, and $s_z(\mathbf{r})$ is the *z*-component of the Poynting vector. Figure 4 shows numerical results for these quantities evaluated for the parameters considered previously.

#94852 - $15.00 USD Received 11 Apr 2008; revised 29 May 2008; accepted 29 May 2008; published 4 Jun 2008

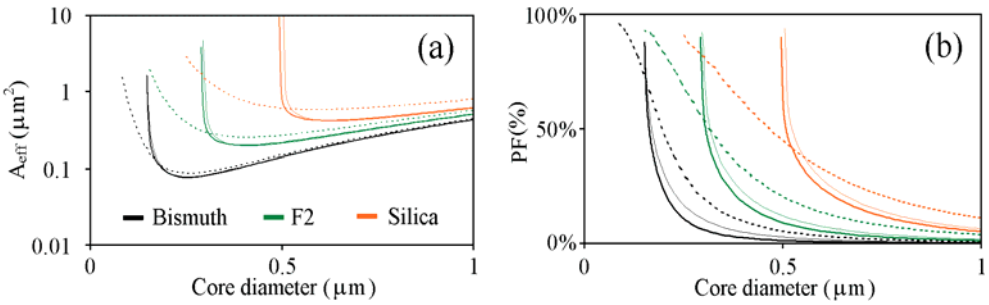

Fig. 4. Effective modal area (a) and modal power fraction (b) as a function of core diameter for three substrate glasses (indicated in legend) where the fiber is either fully filled with water (dashed) or is an exposed-core fiber with one hole containing water (solid). The thick solid lines refer to the fundamental mode of the exposed-core fiber that is polarized parallel to the axis of symmetry and the thin line is for the fundamental mode polarized in the orthogonal direction.

Figure 4(a) shows that for sufficiently large core diameters, the effective area of the exposed-core MOF is less than that for the fully filled case. This is unsurprising because air-glass boundaries provide stronger light confinement than water-glass boundaries. However, as the core size is reduced to subwavelength values, the effective mode area increases rapidly for the exposed-core fiber as the mode spreads dramatically into the water-filled hole.

In a Beer's law [23] absorption sensor the level of absorption is proportional to the available excitation power, shown in Fig. 4(b). Hence, by considering Fig. 4(b) we see that, in spite of utilizing only one out of the three cladding holes, the same absorption sensor performance can be gained for an exposed-core fiber compared to a fully filled fiber. This occurs at a core diameter of approximately 0.52μm for silica fibers (PF = 42%) and 0.15μm for bismuth fibers (PF = 70%), assuming the mode with polarization parallel to the axis of symmetry is used. It should be noted that there are limitations on how small a core size can be used such as coupling losses between filled and unfilled sections of fiber (see Sec. 5), and bend loss [24, 25].

The effects of birefringence on the sensing properties can also be seen in this data: the non-degenerate field distributions now exhibit slightly different power fractions, and hence there is a preferred direction of input coupling polarization that maximizes the power fraction. For an absorption sensor it is preferential to input couple with light polarized orthogonal to the axis of symmetry with a relative difference of 21% for silica fibers and 15% for Bismuth fibers for the core diameters considered above.

4. Fluorescence sensor performance

4.1 Theory

The model described in [19] has here been used to predict the fluorescence capturing ability of the exposed-core fiber. This approach employs the full vectorial solutions of Maxwell's equations and is therefore suitable for MOFs with wavelength-scale features and a high refractive index contrast between the core and cladding regions, unlike previous models that rely on ray-optics [26] or scalar electromagnetic fields [27]. For simplicity we now consider this model for the special case of an attenuation-free fiber of infinite length, which is filled with a solution containing a fluorescent species. In this way the theory describes the fundamental limit on the fluorescence capture possible for the sensor design, and does not depend on which end of the fiber the fluorescence is measured (forwards or backwards fluorescence propagation). Taking into account these assumptions and including the potential for fluorescence capture into multiple non-degenerate modes; the fluorescence capture fraction (FCF) from excitation mode j into modes at the fluorescence wavelength (labeled ν) is given by;

#94852 - $15.00 USD Received 11 Apr 2008; revised 29 May 2008; accepted 29 May 2008; published 4 Jun 2008

$$FCF_j = \sum_{\nu} \left[\frac{NOI_{j\nu}}{A_{eff,F_\nu}} \right] \frac{\xi {\lambda_F}^2}{16\pi (n_F^H)^2} \tag{3}$$

$$NOI_{j\nu} = n_F^H \left(\frac{\varepsilon_0}{\mu_0} \right)^{1/2} \left[\frac{\int_{A_\infty} |s_{F_\nu}(\vec{r})| \, dA}{\int_H s_{E_j}(\vec{r}) dA} \right] \left[\frac{\int_H |\vec{e}_{F\nu}|^2 s_{E_j}(\vec{r}) dA}{\int_{A_\infty} |s_{F_\nu}(\vec{r})|^2 \, dA} \right] \tag{4}$$

where n^H is the refractive index of the fluorescent region, λ_F is the fluorescence wavelength, ξ is the fluorophore efficiency, ***s(r)*** is the z-component of the Poynting vector, and *H* refers to integrating over the fluorophore-filled cross-section. *E* and *F* refer to the excitation and fluorescence wavelengths, respectively. In this loss-free case, FCF has two key terms: a normalized overlap integral (labeled NOI) and the effective area at the fluorescence wavelength, which are dependant on transverse properties of the fiber such as the geometry, refractive index profile, and fluorophore position. The optimization of NOI and A_{eff} is the key to achieving large fluorescence capture within MOF sensors. For example, the effective area can be reduced by moving to smaller core fibers with strong confinement, which we shall see is effective in increasing FCF. It is important to note that NOI in not directly proportional to the power fraction, but is a somewhat more complex expression. This highlights that power fraction alone cannot be used to optimize fluorescence-based optical fiber sensors.

4.2 Fundamental FCF numerical results

FCF was determined for the same glass materials as in Sec. 2, an excitation wavelength of 532nm, and a fluorescence wavelength of 590nm. For simplicity, the input excitation is taken to be a linearly polarized source, and we assume that this excites a single degenerate mode in the fully filled case and a mode with polarization parallel to the axis of symmetry in the exposed-core case. Fluorescence capture into both fundamental modes is then calculated, and the results are shown in Fig. 5(a).

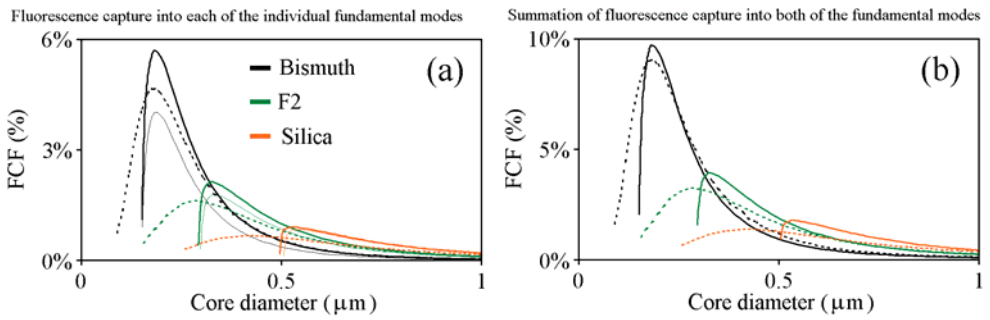

Fig. 5. FCF as a function of core diameter for three substrate glasses (indicated in legend), where the fiber is either fully filled with water (dashed) or is an exposed-core fiber with one hole containing water (solid). In (a) the thick solid lines refer to the fundamental mode of the exposed-core case that is polarized parallel to the axis of symmetry and the thin line is for the fundamental mode with orthogonal polarization. In (b) the result for each fundamental mode has been added to produce the net effect where the thick line refers to the exposed-core fiber and the dashed line is for the fully filled fiber.

The first observation is that for small core diameters, the higher refractive index fibers offer an enhanced fluorescence capture due to the formation of a thin, high-intensity layer at the core-cladding boundary that acts to confine the excited fluorescence near the core, as previously reported [19]. Equation (3) shows that the reduced effective area for high index

#94852 - $15.00 USD Received 11 Apr 2008; revised 29 May 2008; accepted 29 May 2008; published 4 Jun 2008

glasses is largely responsible for this effect and shows that high-index soft glasses such as F2 and bismuth are attractive materials for MOF sensors provided that small core dimensions are used. Figure 5(a) also shows how FCF changes for an exposed-core fiber where higher peak values can be observed for the fluorescence capture (and this achieved at slightly larger core diameters). We also see a dramatic difference in capture into each of the two non-degenerate fundamental modes, particularly for the high refractive index fibers. For example, the bismuth exposed-core fiber has a maximum fluorescence capture of 5.7% into the mode with polarization parallel to the axis of symmetry, which is greater than the fully filled case (4.7%), but only 4.0% into the orthogonal mode. This difference is due to the presence of a high intensity peak in the sensing region for the fundamental mode with polarization parallel to the axis of symmetry, which is absent for the orthogonal mode.

To directly compare the difference in fluorescence capture between the fully filled and exposed-core fibers the FCF curves for each fundamental mode are added as required by Eq. (3), with the results presented in Fig. 5(b). The results for the exposed core fiber are essentially a modification to that of the fully filled fiber where there is potential for enhancing the fluorescence capture by moving to the asymmetric geometry. Figure 5(b) shows that, for particular core diameters, FCF is greater for the exposed-core design by as much as 29% for silica fibers and 19% for F2 fibers, at their respective optimum core diameters.

To understand this effect, NOI (Eq. (4)) was evaluated and is presented in Fig. 6. We see that before the point where the modes spread out dramatically into the water filled hole there is little difference in NOI values between the two fiber designs and hence most of the behavior can be explained in terms of the effective area. The reduced effective mode area of the exposed-core fiber compared with the fully filled fiber is due to the stronger confinement at the air-glass boundaries and accounts for the observed FCF. However, there is little increase in FCF for the exposed-core Bismuth fiber because of the small relative difference between the air-glass and water-glass ratios. The refractive index of water is much closer to that of silica, and hence we see the greatest improvement in the lower refractive index glasses.

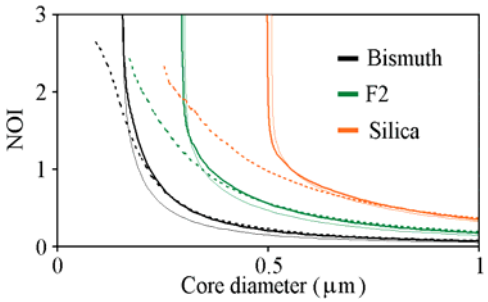

Fig. 6. Normalized overlap integral (NOI) as a function of core diameter for three substrate glasses (indicated in legend), where the fiber is either fully filled with water (dashed) or is an exposed-core fiber with one hole containing water (solid). The thick solid lines refer to the fundamental mode of the exposed-core case that is polarized parallel to the axis of symmetry and the thin line is for the fundamental mode with orthogonal polarization.

5. Coupling efficiency

There are two main coupling problems that need to be considered in the design of the class of sensor considered in this paper. The first is input coupling of an excitation source into the fiber which, although different for different fiber geometries, has largely been dealt with by other authors (for example, see [21, 28-32]). Coupling into small-core optical fibers is by no means trivial; however, the exact efficiency is largely system dependant. A more fundamental (and unavoidable) issue is the loss associated with the mode mismatch between empty regions of fiber and regions along the fiber that are locally immersed within a liquid. For systems where several locations are to be sensed, these liquid interface losses are multiplicative and thus these losses may become significant.

#94852 - $15.00 USD Received 11 Apr 2008; revised 29 May 2008; accepted 29 May 2008; published 4 Jun 2008

To evaluate the losses associated with this mode mismatch we enforce the continuity of the transverse components of electric and magnetic fundamental modes, which can be expressed as Eqs. (5) and (6),

$$\hat{\vec{E}}_{t1} + a\hat{\vec{E}}_{t1} + b\hat{\vec{E}}_{t2} = a'\hat{\vec{E}}'_{t1} + b'\hat{\vec{E}}'_{t2} + \vec{E}_{rad} \tag{5}$$

$$\hat{\vec{H}}_{t1} - a\hat{\vec{H}}_{t1} - b\hat{\vec{H}}_{t2} = a'\hat{\vec{H}}'_{t1} + b'\hat{\vec{H}}'_{t2} + \vec{H}_{rad} \tag{6}$$

where $|a|^2$, $|b|^2$ and, $|a'|^2$ and $|b'|^2$ are the reflected and transmitted coupling efficiencies into the two fundamental modes (subscripts *1* and *2* respectively), *rad* refers to the transmitted radiation field and *t* refers to the transverse components of the electric and magnetic fields. We vector multiply Eqs. (5) and (6) by the conjugated magnetic and electric fields respectively, integrate over an infinite cross section and use orthonormality of the fiber's guided and radiation modes to obtain a matrix equation for *a*, *b*, *a'* and *b'* involving cross integration terms between all four fundamental modes (two for each the filled and unfilled sections of fiber). Assumed in this approach is that the reflected light distribution at the boundary is directly proportional to the fundamental guided modes, that is, that reflection into the radiation modes is negligible [1, 33].

The liquid interface losses were determined for the case of an exposed core fiber being immersed into an aqueous solution and a corresponding WW fiber with three holes filled. These losses consist of both excitation light coupling from the unfilled region into the water containing region and then the reverse at the fluorescence wavelength (Fig. 7). Note that this analysis is appropriate for both forwards and backwards detection of fluorescence, that is, whether measuring the fluorescence from the distal end or pump end of the fiber. The results are shown in Fig. 8(a) for transmission through the boundaries of a single segment of the fiber filled with water.

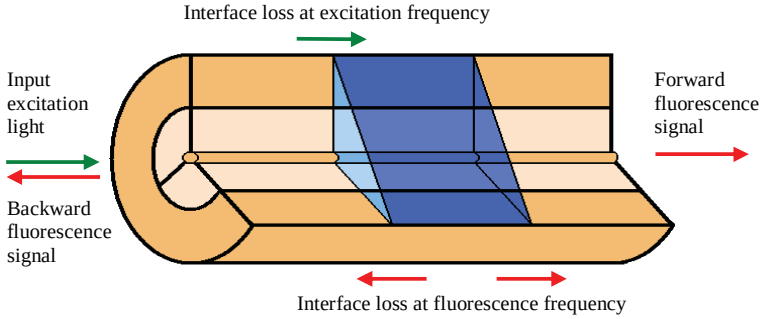

Fig. 7. Schematic of an exposed-core fiber with a section immersed in a liquid. Liquid interface losses exist for the excitation light entering the liquid filled section and for the fluorescence exiting the liquid filled section.

For both fully filled and exposed core fiber sensors, the liquid interface losses increase for small core diameters due to the increased amount of optical power in the cladding holes. Comparing the two sensing fiber designs considered here, we see that the liquid interface losses are relatively better for exposed-core fibers compared with the fully filled equivalent when large core diameters (c.f. wavelength) are used, since only one of the cladding holes is filled and therefore the geometry more closely matches the unfilled section of fiber. However, as the core diameter decreases, the exposed-core fiber experiences dramatically enhanced guidance within the single filled hole, which deforms the mode profile compared with the unfilled fiber and thus rapidly reduces transmission across the liquid interface. This, along with the above fluorescence capture results (Sec. 4), demonstrates that care must be taken in choosing a core diameter for an exposed-core fiber, as core diameters that are too small (less

#94852 - $15.00 USD Received 11 Apr 2008; revised 29 May 2008; accepted 29 May 2008; published 4 Jun 2008

than 0.16μm for bismuth and less than 0.50μm for silica) result in both significant liquid interface losses and a reduction in FCF.

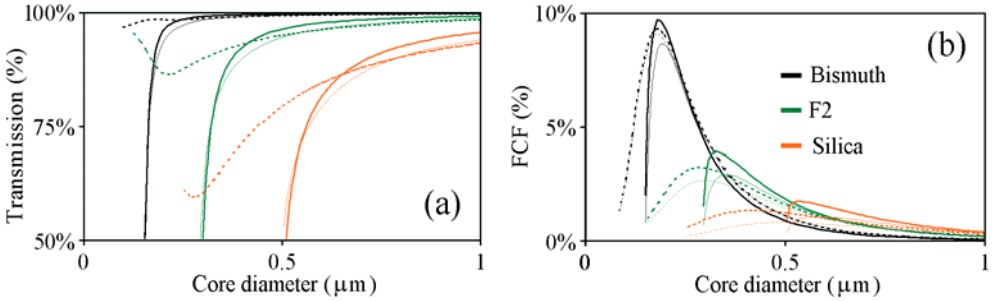

Fig. 8. Liquid interface transmission for a single coupling in and out event corresponding to one fluid-filled region (a) and FCF multiplied by this transmission (b), as a function of core diameter for three substrate glasses (indicated in legend). The fiber is either fully filled with water (dashed) or is an exposed-core fiber with one hole containing water (solid). In (a) the thick solid lines refer to the first fundamental mode of the exposed-core case and the thin line is for the second fundamental mode. In (b) the thick lines refer to FCF without considering liquid interface losses whereas the thin lines include the appropriate liquid interface losses where each non-degenerate mode of the exposed-core fiber has been considered separately.

Figure 8(b) shows the effect on the FCF results of Fig. 5(b) when liquid interface losses into and out of a single filled section of fiber are considered, as given by Eq. (7), where n (the number of boundaries the excitation light must travel through to reach the fluorescent region) and m (the number of boundaries the fluorescence must travel through to reach the output of the fiber) have been set to n=m=1. LIT refers to the liquid interface transmission, that is, the fraction of optical power that is not lost by the respective fundamental modes across the liquid interface.

$$FCF_{j,\,final} = \sum_{\nu} (LIT_{E_j})^n \times (LIT_{F_\nu})^m \times FCF_{j\nu} \tag{7}$$

We see that for bismuth fiber there is no longer an improvement in the exposed-core fiber relative to the fully filled fiber, whereas the lower index glasses are still predicted to enable a significant improvement in fluorescence capture. However, the maximum achievable fluorescence capture is still significantly greater for the high index glasses, regardless of which geometry is chosen and thus we conclude that the exposed-core fiber will still provide highly efficient fluorescence sensing in the small core, high refractive index regime.

In fact, if we consider a long distributive sensor with multiple locally-immersed sections, the advantage of using higher refractive index materials becomes evident. Consider, for example, a fluorescence-based distributive sensor where we wish to receive individual fluorescence signals from multiple sites along the length of the fiber in order to obtain spatial information using methods analogous to optical time domain reflectometry [34]. If we have, say, 5 liquid immersed sections, the excitation light must pass through nine boundaries to reach the final fluorescence region (n=9) and then the fluorescence from this section of fiber will have to propagate back through the same nine boundaries (m=9). These liquid interface losses associated with receiving fluorescence from the fifth liquid-immersed segment are shown in Fig. 9.

#94852 - $15.00 USD Received 11 Apr 2008; revised 29 May 2008; accepted 29 May 2008; published 4 Jun 2008

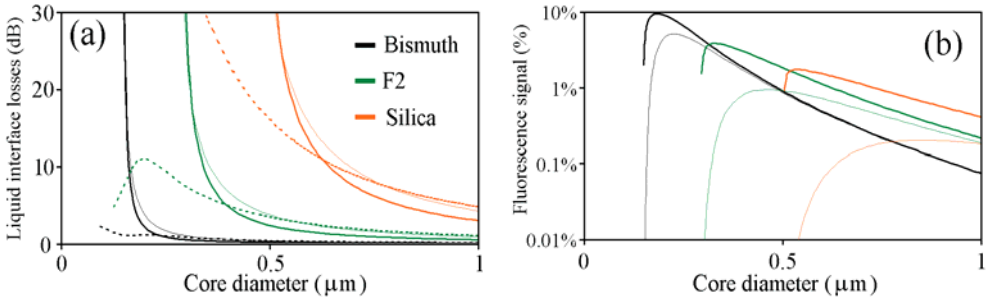

Fig. 9. Liquid interface losses for nine coupling in and out events (m=n=9) as a function of core diameter for three substrate glasses (indicated in legend) (a) and the effect on the fluorescence signal received from the far-end of the fiber (b). The liquid interface losses are associated with five fluid-filled regions, where the fiber is either fully filled with water (dashed) or is an exposed-core fiber with one hole containing water (solid). In (a) the thick solid lines refer to the first fundamental mode of the exposed-core case and the thin line is for the second fundamental mode. In (b) the thick lines refer to FCF without considering the effect of liquid interface losses whereas the thin lines do.

Here we see that the use of a small-core silica fiber introduces large losses, to the order of 10dB and greater for very small cores. In contrast, the bismuth small-core fibers experience very little liquid interface losses, such as less than 5dB for core diameters greater than 0.19μm, which is still in the regime of enhanced fluorescence capture. The effect on FCF, shown in Fig. 9(b), is again highlighted. Relatively small liquid interface losses allow the high refractive index glasses to still provide a high fluorescence signal (5% maximum for bismuth at a core size of 0.22μm) whereas the silica fiber provides a much reduced fluorescence signal (0.2% maximum at a core diameter of 0.85μm).

6. Discussion and conclusions

Exposed-core microstructured fibers have been theoretically studied to determine their potential for the use in both absorption and fluorescence based sensing and have been compared to an equivalent fully filled fiber. In particular, exposed-core liquid-based sensors are shown to enable several optical advantages due to the presence of a raised refractive index in the sensing region. These allow the exposed-core fiber to compete with a fully filled fiber as a sensor, despite utilizing only one-third of the cladding holes (in this particular implementation). Firstly, the amount of available optical power in the sensing region of an exposed-core fiber can compete with other liquid-filled MOF-based sensors due to the spreading of the mode into the sensing region. Secondly, the exposed-core fiber can provide an enhancement in fluorescence capture ability such as an increase of 19% for lead silicate fibers and 29% for silica fibers. To further consider the working characteristics of an exposed-core fiber, and any liquid filled fiber, we have also calculated the coupling losses that are introduced due to the presence of the liquid's refractive index. We have shown that while these coupling losses are present, they do not degrade the sensitivity significantly for fiber dimensions of interest, particularly where high refractive index materials are used. When considering the effects of both coupling efficiency and fluorescence capture together we have seen that small-core high refractive index glasses offer an enormous benefit in sensitivity, regardless of whether using an exposed-core or fully filled fiber.

Of course, in order to implement an exposed-core fiber in a real sensing application there are several practical issues that need to be solved. First and foremost is fiber fabrication; while several examples of exposed-core fibers have now been fabricated there is still considerable room for improvement on insertion loss (of the exposed section), fiber length, and fiber quality. Another important consideration is the coupling efficiency and stability into small-core fibers, which must be solved before sensor implementation can be made reliable and accurate. The are also application specific considerations for absorption and fluorescence

#94852 - $15.00 USD Received 11 Apr 2008; revised 29 May 2008; accepted 29 May 2008; published 4 Jun 2008

based sensors such as the choice of absorption or fluorescence material, sources, and detectors, which must all be considered in a practical system.

However, given the potential for distributive sensing, no requirement for filling, and these predicted sensing characteristics, it can be expected that exposed-core fibers will provide new opportunities for optical fiber-based sensing.

Acknowledgments

The authors acknowledge the support of the Defence Science and Technology Organisation (DSTO), Australia and in particular the DSTO Corporate Initiative on Smart Materials and Structures for sponsorship of this program of research. This research was supported under the Australian Research Council's Discovery Projects funding scheme (project number DP0665486)

#94852 - $15.00 USD Received 11 Apr 2008; revised 29 May 2008; accepted 29 May 2008; published 4 Jun 2008

3.5 Fluorescence Capture Fraction: Higher Order Modes and Experiment

The publication [P4] forms the basis of this section.

S. C. Warren-Smith, S. Afshar V., and T.M. Monro, "Fluorescence-based sensing with optical nanowires: a generalized model and experimental validation," *Optics Express* **18**, 9474-9485 (2010).

3.5.1 Publication Overview

Aim

The primary aim of this paper was to generalise the fluorescence capture theory presented in [P1], which was again used in [P2, P3], to include a number of important effects that exist in any real sensing system and compare the theoretical results with experiment. In order to achieve this aim the theory was extended to include higher order modes, and additional loss mechanisms such as confinement loss and experimentally measured small-core loss. Including these factors, and also loss due to Beer's law absorption, allowed the fluorescence capture model to be quantitatively compared to experimental results for the first time. Also, an additional check was performed to compare the modal approach (wave-optics) used in this paper with an equivalent ray-optics approach for a specific simplified example.

Field of Knowledge and Link Between Publications

As has been stated for [P1-P3], the modelling of fluorescence capture properties of optical nanowires is important due to the current interest in using these devices for sensing, which is generally attributed to the high level of evanescent field that can be used for evanescent-based sensing. While it is true that other optical waveguide designs can offer similar or better evanescent field percentages, such as band-gap fibres [95, 97] and liquid-core fibres [94, 101], it is perhaps the simple filling characteristics that make suspended optical nanowires of particular interest. This is highlighted by recent fabrication successes where optical nanowires, which are generally either free-standing

optical nanowires or suspended-core designs, have been fabricated with core diameters as small as 50 nm [73] and 400 nm [P6] respectively. Despite these encouraging results, it is important that these devices are properly understood so that they can be optimised and effectively used, and this requires that an accurate and trustworthy theoretical model is available.

Discussed in reference to [P1] in Sec. 3.2 was that fluorescence capture theory has previously been developed for ray-optics models [13–15] and also wave-optics models [16–20, 149]. For the analysis of optical nanowires a wave-optics approach must be used, and while many important characteristics of fluorescence-based optical fibre sensors were discussed in Refs. [16–20, 149], the models did not include factors such as core-pumped designs and Beer's law absorption. These factors were subsequently included for the case of a suspended-core (wagon wheel) geometry, which have similar characteristics to conventional step-index fibres [P1-P3]. However, only the fundamental mode was considered and thus it can only be considered accurate for single-mode fibres. Thus, [P4] is an extension of this theory to include higher order modes so that it is accurate outside of the single-mode regime. [P4] also provides, for the first time, experimental confirmation of the theory developed in [P1], using fibres that were fabricated in [P6].

Discussion and Conclusions

The generalisation of the fluorescence capture theory in [P1] was successfully implemented to include higher order modes. Numerical modelling of this theory for small-core fibres demonstrated that evanescently excited fluorescence is most efficiently captured into fibres made from high refractive index materials due to their relatively high numerical aperture. It was found that there is very little dependence on core diameter when considering only the fluorescence capture, which represents a significant change from the results of [P1] when only the fundamental mode was considered. However, when analyte absorption along the length of the fibre was included in the theory it was found that the high evanescent field of small core diameter fibres (for example, 500 nm compared to 2 μm) becomes advantageous when sensing low concentration samples, such as Rhodamine B with a concentration of less than 1 nM.

The next component of [P4] was to include additional loss effects that have not previously been incorporated into the theory such as confinement loss (full derivation in Appendix

C) and experimentally measured small-core loss [P6] (Sec. 4.2). These loss mechanisms have an effect on the minimum core diameter that can be usefully used, as both effects increase dramatically as the core diameter reduces below subwavelength values. For example, reducing the core diameter below 400 nm is not useful for a one meter long F2 optical nanowire.

The addition of these extra considerations allowed for the most significant conclusions in [P4], which was agreement with both a ray-optics model and experimental results. First, the modal theory (wave-optics) was compared to an equivalent ray-optics model for a simplified example of fluorescence emitted from the centre of the fibre. The models were shown to agree in the limit of increasing V-number, as expected. Secondly, suspended-core (wagon wheel) fibre was used to experimentally test the predictions of the paper. While the geometry of the suspended-core fibre is only approximated by the step-index model used for the numerical predictions, the results where in close agreement with no free parameters required.

3.5.2 Statement of Contribution

Conceptualisation

The idea to extend the fluorescence capture theory to include higher order modes was conceptualised by Stephen Warren-Smith. The concept of including confinement loss in the theory was conceptualised by Stephen Warren-Smith, while adding experimentally measured small core loss was conceptualised by Tanya Monro. The idea to use wagon wheel fibres for experimentally testing the theoretical results of the paper was conceptualised by all authors.

Realisation

The development of the fluorescence capture theory was outlined previously in relation to [P1]. The extension of the theory to include higher order modes was done by Stephen Warren-Smith. Matlab coding of the step-index model for the modelling and subsequent modelling for the fluorescence capture was done by Stephen Warren-Smith. Derivation of the W-fibre confinement loss theory, and subsequent Matlab coding and numerical

simulations was done by Stephen Warren-Smith, assisted by useful discussions with Mark Turner (The University of Adelaide). Experiments were performed by Stephen Warren-Smith.

Documentation

This paper was primarily written by Stephen Warren-Smith, with editing by all other authors.

Declaration and Permission

I declare that the above statement of contribution is accurate and I give permission for this publication to be included in this thesis.

Stephen C. Warren-Smith Shahraam Afshar V. Tanya M. Monro

Fluorescence-based sensing with optical nanowires: a generalized model and experimental validation

Stephen C. Warren-Smith*, Shahraam Afshar V., and Tanya M. Monro

Centre of Expertise in Photonics, Institute for Photonics & Advanced Sensing, School of Chemistry & Physics, University of Adelaide, Adelaide, SA 5005, Australia
**stephen.warrensmith@adelaide.edu.au*

Abstract: A model for the fluorescence sensing properties of small-core high-refractive-index fibers (optical nanowires) is developed and compared quantitatively with experiment. For the first time, higher-order modes and loss factors relevant to optical nanowires are included, which allows the model to be compared effectively with experiment via the use of fluorophore filled suspended optical nanowires. Numerical results show that high-index materials are beneficial for fluorescence-based sensing. However, both numerical and experimental results show that the fluorescence signal is relatively insensitive to core size, except for low concentration sensing where nanoscale fiber cores are advantageous due to the increased evanescent field power.

OCIS codes: (060.2370) Fiber optics sensors; (060.4005) microstructured fibers; (300.2530) fluorescence, laser-induced.

References and links

1. J. B. Jensen, P. E. Hoiby, G. Emiliyanov, O. Bang, L. H. Pedersen, and A. Bjarklev, "Selective detection of antibodies in microstructured polymer optical fibers," Opt. Express **13**(15), 5883–5889 (2005).
2. T. Ritari, J. Tuominen, H. Ludvigsen, J. C. Petersen, T. Sørensen, T. P. Hansen, and H. R. Simonsen, "Gas sensing using air-guiding photonic bandgap fibers," Opt. Express **12**(17), 4080–4087 (2004).
3. F. M. Cox, A. Argyros, and M. C. J. Large, "Liquid-filled hollow core microstructured polymer optical fiber," Opt. Express **14**(9), 4135–4140 (2006).
4. J. M. Fini, "Microstructure fibres for optical sensing in gases and liquids," Meas. Sci. Technol. **15**(6), 1120–1128 (2004).
5. S. Smolka, M. Barth, and O. Benson, "Highly efficient fluorescence sensing with hollow core photonic crystal fibers," Opt. Express **15**(20), 12783–12791 (2007).
6. Y. Ruan, T. C. Foo, S. C. Warren-Smith, P. Hoffmann, R. C. Moore, H. Ebendorff-Heidepriem, and T. M. Monro, "Antibody immobilization within glass microstructured fibers: a route to sensitive and selective biosensors," Opt. Express **16**(22), 18514–18523 (2008).
7. S. Afshar 5th, S. C. Warren-Smith, and T. M. Monro, "Enhancement of fluorescence-based sensing using microstructured optical fibres," Opt. Express **15**(26), 17891–17901 (2007).
8. S. Afshar 5th, Y. Ruan, S. C. Warren-Smith, and T. M. Monro, "Enhanced fluorescence sensing using microstructured optical fibers: a comparison of forward and backward collection modes," Opt. Lett. **33**(13), 1473–1475 (2008).
9. S. C. Warren-Smith, S. Afshar, and T. M. Monro, "Theoretical study of liquid-immersed exposed-core microstructured optical fibers for sensing," Opt. Express **16**(12), 9034–9045 (2008).
10. Y. Zhu, H. Du, and R. Bise, "Design of solid-core microstructured optical fiber with steering-wheel air cladding for optimal evanescent-field sensing," Opt. Express **14**(8), 3541–3546 (2006).
11. Y. N. Zhu, R. T. Bise, J. Kanka, P. Peterka, and H. Du, "Fabrication and characterization of solid-core photonic crystal fiber with steering-wheel air-cladding for strong evanescent field overlap," Opt. Commun. **281**(1), 55–60 (2008).
12. J. Lou, L. Tong, and Z. Ye, "Modeling of silica nanowires for optical sensing," Opt. Express **13**(6), 2135–2140 (2005).
13. Y. L. Ruan, E. P. Schartner, H. Ebendorff-Heidepriem, P. Hoffmann, and T. M. Monro, "Detection of quantum-dot labelled proteins using soft glass microstructured optical fibers," Opt. Express **15**(26), 17819–17826 (2007).
14. T. G. Euser, J. S. Y. Chen, M. Scharrer, P. St. J. Russell, N. J. Farrer, and P. J. Sadler, "Quantitative broadband chemical sensing in air-suspended solid-core fibers," J. Appl. Phys. **103**(10), 103108 (2008).
15. A. S. Webb, F. Poletti, D. J. Richardson, and J. K. Sahu, "Suspended-core holey fiber for evanescent-field sensing," Opt. Eng. **46**(1), 10501–10503 (2007).

#124483 - $15.00 USD Received 19 Feb 2010; revised 11 Apr 2010; accepted 13 Apr 2010; published 21 Apr 2010

16. L. M. Tong, R. R. Gattass, J. B. Ashcom, S. L. He, J. Y. Lou, M. Y. Shen, I. Maxwell, and E. Mazur, "Subwavelength-diameter silica wires for low-loss optical wave guiding," Nature **426**(6968), 816–819 (2003).
17. H. Ebendorff-Heidepriem, S. C. Warren-Smith, and T. M. Monro, "Suspended nanowires: fabrication, design and characterization of fibers with nanoscale cores," Opt. Express **17**(4), 2646–2657 (2009).
18. T. R. Glass, S. Lackie, and T. Hirschfeld, "Effect of numerical aperture on signal level in cylindrical wave-guide evanescent fluorosensors," Appl. Opt. **26**(11), 2181–2187 (1987).
19. H. P. Kao, N. Yang, and J. S. Schoeniger, "Enhancement of evanescent fluorescence from fiber-optic sensors by thin-film sol-gel coatings," J. Opt. Soc. Am. A **15**(8), 2163–2171 (1998).
20. D. Marcuse, "Launching light into fiber cores from sources located in the cladding," J. Lightwave Technol. **6**(8), 1273–1279 (1988).
21. D. Marcuse, "Excitation of parabolic-index fibers with incoherent sources," Bell Syst. Tech. J. **54**, 1507–1530 (1975).
22. C. O. Egalon, R. S. Rogowski, and A. C. Tai, "Excitation efficiency of an optical fiber core source," Opt. Eng. **31**(6), 1328–1331 (1992).
23. C. O. Egalon, and R. S. Rogowski, "Efficiency of core light injection from sources in the cladding - bulk distribution," Opt. Eng. **31**(4), 846–851 (1992).
24. C. O. Egalon, and R. S. Rogowski, "Theoretical-model for a thin cylindrical film optical fiber fluorosensor," Opt. Eng. **31**(2), 237–244 (1992).
25. A. W. Snyder, and J. D. Love, *Optical Waveguide Theory* (Chapman and Hall, 1983).
26. K. Okamoto, *Fundamentals of Optical Waveguides* (Academic Press, 2000).
27. P. J. Roberts, F. Couny, H. Sabert, B. J. Mangan, T. A. Birks, J. C. Knight, and P. S. Russell, "Loss in solid-core photonic crystal fibers due to interface roughness scattering," Opt. Express **13**(20), 7779–7793 (2005).
28. G. Y. Zhai, and L. M. Tong, "Roughness-induced radiation losses in optical micro or nanofibers," Opt. Express **15**(21), 13805–13816 (2007).
29. L. Tong, L. Hu, J. Zhang, J. Qiu, Q. Yang, J. Lou, Y. Shen, J. He, and Z. Ye, "Photonic nanowires directly drawn from bulk glasses," Opt. Express **14**(1), 82–87 (2006).
30. A. Bryant, S. Albin, C. O. Egalon, and R. S. Rogowski, "Changes in the amount of core light injection for fluorescent-clad optical-fiber due to variations in the fiber refractive-index and core radius - experimental results," J. Opt. Soc. Am. B **12**(5), 904–906 (1995).
31. S. Albin, A. L. Bryant, C. O. Egalon, and R. S. Rogowski, "Injection efficiency from a side-excited thin-film fluorescent cladding of a circular wave-guide," Opt. Eng. **33**(4), 1172–1175 (1994).
32. F. W. D. Rost, *Fluorescence Microscopy* (Cambridge University Press, 1992)
33. E. P. Schartner, R. T. White, S. C. Warren-Smith, and T. M. Monro, "Practical sensitive fluorescence sensing with microstructured fibres," Proc. SPIE **7503**, 75035X (2009).

1. Introduction

Fluorescence sensing is an important tool for a wide range of applications, particularly for biological sensing through the use of fluorescent labeling. It has long been realized that these fluorescence-based techniques can be incorporated into an optical fiber platform and, in particular, microstructured optical fibers (MOFs) offer advantages such as long interaction length, high sensitivity, and small volume requirements [1]. One important parameter for fiber sensing is the fraction of optical power that propagates externally to the fiber substrate and can thus be used to interact with an analyte. Several types of MOF allow for high power fractions such as band-gap fibers [2, 3], liquid-core fibers [4, 5], and small-core fibers [6–17]. In addition, small-core high-index fibers have been predicted to offer increased sensitivity due to the presence of high intensity evanescent fields adjacent to the core-cladding interface [7]. Here we concentrate on small-core fibers due to the considerable interest that has recently been shown in both fabricating and sensing with these fibers. They are generally fabricated either as free-standing optical nanowires or suspended-core designs, where core diameters have been fabricated as small as 50nm [16] and 400nm [17] respectively. Their relatively simple filling requirements, compared to selective filling designs, also make them an ideal candidate for both testing the theoretical results in this paper and for future sensing applications.

In addition to knowing the power fraction of a given fiber design, which indicates how much fluorescence can be excited, it is important to be able to predict the efficiency with which the fluorescence is captured by the guided mode(s) of the fiber. This can be calculated using ray tracing methods [18, 19], however, these are unsuitable for the single/few-moded fibers considered here. A modal approach was first developed by Marcuse [20, 21] for the case of a uniform cladding excitation (e.g. side excitation) and found that fluorescence capture increased with increasing V-number. This uniform excitation theory was later generalized for vectorial step-index fiber solutions and it was shown that, more specifically,

#124483 - $15.00 USD Received 19 Feb 2010; revised 11 Apr 2010; accepted 13 Apr 2010; published 21 Apr 2010

capture is increased with increasing refractive index difference between the core and cladding [22–24]. However, these results did not consider the case of a core pumped fiber and did not include effects due to fiber loss or Beer's law absorption. These factors have subsequently been included for the case of a suspended-core geometry (sometimes described as a wagon wheel or steering wheel), which have similar characteristics to conventional step-index fibers [7–9]. It was found that the existence of localized high-intensity electric and magnetic field layers of the fundamental mode at the boundary interface of small-core fibers leads to an increase in fluorescence capture when high index glasses are used.

In this paper the previous theoretical results [7–9] are extended to include the capture by higher order modes and to include additional loss mechanisms (confinement loss and small-core loss), which have not previously been incorporated into the theory. Combining these factors provides a rigorous model of the fluorescence sensing properties of optical nanowires, which we demonstrate is in quantitative agreement with experiment. In Sec. 2 we first describe the equations used for this numerical modeling. The fluorescence capture is then modeled, with higher order modes included, for parameters corresponding to MOFs that have recently been fabricated. To add confidence to the model numerical results are then compared with the ray optics equivalent and agreement is found in the regime of high V-number. Effects due to fluorophore absorption, confinement loss, and experimentally measured small-core loss are then included in the model. In Sec. 3 experimental results are compared with the numerical results of Sec. 2, which show quantitative agreement and also experimentally highlight which fiber parameters are best suited for low-concentration fluorescence-based sensing.

2. Numerical results

2.1 Fluorescence capture theory

The following equations (Eqs. 1(a), 1(b), and 1(c)) for the fluorescence capture are based on the derivation presented in [7]; the primary difference being that we retain the summation in Eq. 1(a) in order to include the contribution of higher order modes and thus extend our analysis to fibers that have core diameters outside of the single-mode regime. Also, additional loss mechanisms, which are implicit in the equations below, are included in Sec. 2.5.

To begin we assume that the fluorescent sources are contained within a cross sectional region *H* and that they have random phase and orientation [20]. *H* often refers to the fiber cladding (or holes), but can be any region that fluorescent sources are present, such as the centre of the core as will be considered in Sec. 2.2. Taking into account fiber loss and Beer's law absorption along the length of the fiber, the fraction of fluorescence (FCF) that is excited by excitation mode *j*, captured into all guided modes *v* of the fiber at the fluorescence wavelength, and propagates to the output end of a fiber can be expressed as [7]:

$$FCF_j = \frac{\xi\lambda^2}{16\pi n_F^{H2}} \sum_v \frac{NOI_{jv}}{A_{eff,v}} \frac{\gamma_j^H e^{-\gamma_v L}}{\gamma_v - \gamma_j} \left[e^{(\gamma_v - \gamma_j)L} - 1 \right] \tag{1a}$$

$$NOI_{jv} = n_F^H \left(\frac{\varepsilon_0}{\mu_0} \right)^{1/2} \left[\frac{\int_{A_\infty} |s_v(\vec{r})| \, dA}{\int_H s_j(\vec{r}) dA} \right] \left[\frac{\int_H |\vec{e}_v|^2 s_j(\vec{r}) dA}{\int_{A_\infty} |s_v(\vec{r})|^2 \, dA} \right] \tag{1b}$$

$$A_{eff,v} = \frac{\left| \int_{A_\infty} s_v(\vec{r}) dA \right|^2}{\int_{A_\infty} |s_v(\vec{r})|^2 \, dA} \tag{1c}$$

#124483 - $15.00 USD Received 19 Feb 2010; revised 11 Apr 2010; accepted 13 Apr 2010; published 21 Apr 2010

where A_∞ is defined to be the infinite transverse cross section, L is the fiber length, $s_j(\boldsymbol{r})$ is the z-component of the Poynting vector of the j^{th} mode, $\boldsymbol{e}_j(\boldsymbol{r})$ is the electric field of the j^{th} mode, λ is the fluorescence wavelength, ξ is the fluorophore efficiency, n_F^H is the refractive index in the region H at the fluorescence wavelength, *NOI* is a normalized overlap integral [7], A_{eff} is the modal effective area, and γ is the attenuation coefficient [25]. A similar expression can be found for fluorescence that propagates to the launch end of the fiber [8].

Equation (1) can be considered as consisting of two components, one longitudinal and the other transverse. The longitudinal component is contained within Eq. 1(a), which arises from considering the fibre attenuation at both excitation and fluorescence wavelengths, Beer's law absorption, and integration along the entire length of the fibre. The transverse component is primarily contained within Eqs. 1(b) and 1(c), where the effective area has been separated to give more physical insight into the fluorescence capture mechanism. It shows that the capture into a particular mode is proportional to how tightly that mode is confined.

2.2 Comparison between wave-optics and ray-optics approach

As the refractive index contrast is increased, the fiber becomes increasingly multi-mode and ray-tracing methods become applicable. Hence, the theory of Eq. (1) can be checked by testing convergence in the limit of increasing the number of modes. This is an important check as there are several assumptions that are associated with Eq. (1) [7] and because of the possibility of numerical errors as multiple integrations are required, particularly for highly multimode fibers. To perform the comparison we have taken the simple case of a fluorophore centered at the fiber axis (that is, in the core), and have calculated the fluorescence capture for the ideal case of a lossless step-index fiber. The step-index model with fully analytical vectorial solutions was used to determine the electric and magnetic fields [26]. The cladding refractive index was held constant at n = 1.0 and the core index varied from 1.01 to 11. For each curve the core radius was varied such that the V- number (thus number of modes) was held fixed, where $V = (2\pi a/\lambda)(n_{co}^2 - n_{cl}^2)^{1/2}$, a is the core radius, n_{co} is the core index, and n_{cl} is the cladding index [25]. Curves were then calculated with the V-number varying from 1.0 to 50. Several of these curves are displayed in Fig. 1 and are compared with the ray-tracing equivalent, which is defined as the fraction of fluorescence that is emitted within the critical angle of the fiber. This is written as *½(1-cos(θ_c))*, where θ_c is the fiber's critical angle.

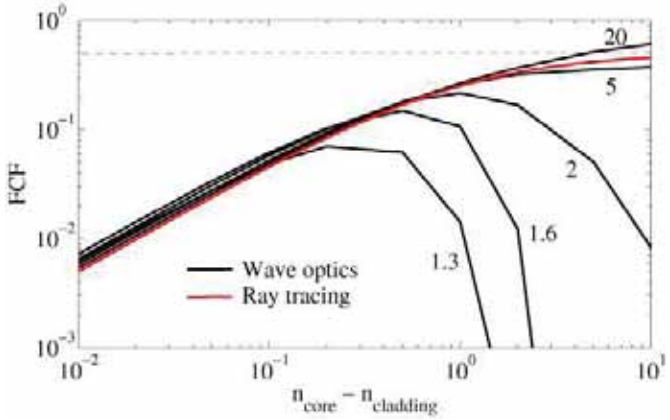

Fig. 1. Comparison of the wave-optics derived fluorescence capture fraction (FCF) for an on-axis in-core fluorophore (black) and the ray-tracing equivalent (red). The optical fiber V-number used for the wave-optics method is displayed in the figure for each corresponding curve. FCF = 0.5 (i.e. 50% capture) has been marked with a dashed line.

Figure 1 shows that the two rather different approaches agree remarkably well for sufficiently high V-number (V > 5), and also display the expected behavior. Firstly, both

#124483 - $15.00 USD Received 19 Feb 2010; revised 11 Apr 2010; accepted 13 Apr 2010; published 21 Apr 2010

demonstrate that the fluorescence capture is dependent on the numerical aperture of the fiber. Also, for very large index differences, the fluorescence capture appears to asymptote below 50%, which is required for energy conservation (with a 50% maximum possible in either forwards or backwards directions). We see that for low V-numbers, particularly where the fiber is single-moded ($V < 2.405$), the two approaches yield differing results. Hence, we see that ray-optics is not a suitable model for studying the fluorescence capture behavior of single/few-moded fibers. To demonstrate the convergence of the two models as the V-number (and hence the number of modes) is increased, the fluorescence capture has been shown for two values of Δn in Fig. 2(a) (Δn = 0.01) and Fig. 2(b) (Δn = 1.0).

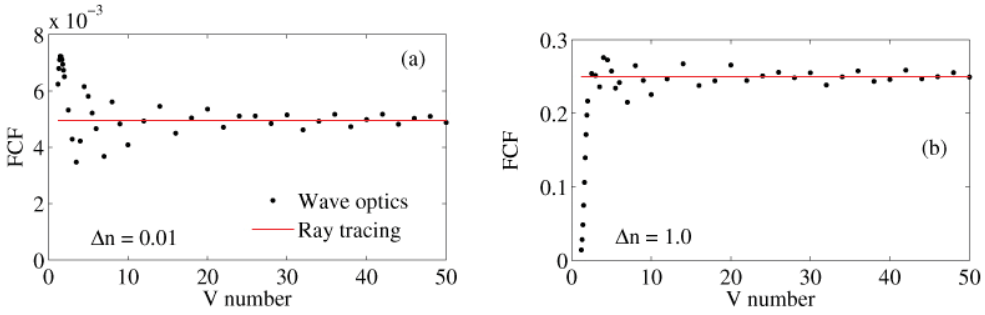

Fig. 2. Convergence of the wave-optics approach to the ray-optics approach for increasing optical fiber V-number. The difference in refractive index between the core and cladding (Δn) is 0.01 (a) and 1.0 (b).

Figure 2 shows that as the V-number is increased the two models converge to the same value. The close agreement between the two methods adds confidence to the theory of Eq. (1) and thus the following results presented in this paper.

2.3 Fluorescence capture

The fluorescence capture was then calculated for the case of a step-index fiber with a glass core and a water cladding. This is equivalent to considering an optical nanowire immersed in an aqueous analyte or approximately equivalent to a suspended-core fiber filled with an aqueous analyte. Several glass types with differing refractive index (silica ≈ 1.46, lead silicate (F2) ≈ 1.62, and bismuth ≈ 2.09) were considered for the core material, with an excitation wavelength of 532 nm and a single fluorescence wavelength of 590 nm (for example, rhodamine B dissolved in water). Unless otherwise specified, these values have been used in the remainder of this paper. To begin, the loss of the fiber was taken to be zero and the length to be infinite. In this way, the calculated FCF represents the fundamental limit on the fluorescence capture possible for the sensor design. Also, we have only used the fundamental mode to construct the excitation field, which is more or less accurate depending on the initial launch conditions. All guided modes of the fiber are excited to some degree by the fluorescence, and the results for the capture fraction summed across all of these modes are shown in Fig. 3(b).

#124483 - $15.00 USD Received 19 Feb 2010; revised 11 Apr 2010; accepted 13 Apr 2010; published 21 Apr 2010

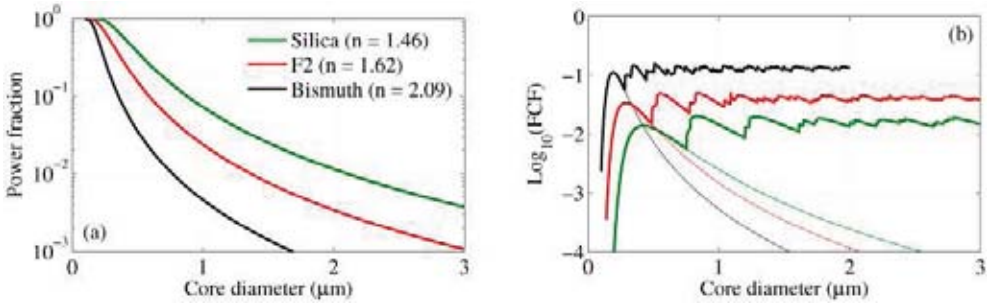

Fig. 3. (a) Fraction of fundamental mode evanescent field power located in the water for water-clad step-index fibers made from three different glass types. (b) Fluorescence capture into the fundamental mode only (thin lines) and into all guided modes (thick lines) for three different glasses where the cladding is Rhodamine B dissolved in water.

We see from Fig. 3(b) that the fluorescence capture is greatest for fibers whose core-cladding refractive index is greatest, regardless of the core diameter. That is, the result previously shown for side-excited fibers holds for core-pumped fibers [23]. This can be understood intuitively, that is, greater capture is, unsurprisingly, observed for fibers with larger numerical aperture. Additionally, we see that fluorescence capture into the fundamental mode only represents a significant portion of the overall capture for very small core diameter fibers (<< 1 micron). For core diameters larger than the single-mode regime, the fluorescence capture is achieved mostly through the higher order modes. In fact, we see that the contribution of the higher order modes is such that the fluorescence capture efficiency becomes insensitive to core diameter as the core diameter, and thus the number of modes, is increased. Note that the sharp peaks in the curves of Fig. 1(b) correspond to capture into higher order modes near cut-off. When confinement loss is considered, these peaks are smoothed, as will be discussed in Sec 2.5.

2.4 Fluorophore absorption

While the results of Fig. 3(b) show that the fluorescence capture efficiency is relatively insensitive to the core diameter, they do not consider the effect of absorption of the pump light along the length of the fiber, which depends on the fraction of power outside the core (Fig. 3(a)) as well as the chemical absorption coefficient. Assuming fundamental mode excitation, for a finite length fiber (1 m) and with varying concentrations of rhodamine B, the predicted backscattered fluorescence capture is shown in Fig. 4(a) for silica fibers and Fig. 4(b) for bismuth fibers. These calculations assume that the fiber material itself contributes no loss.

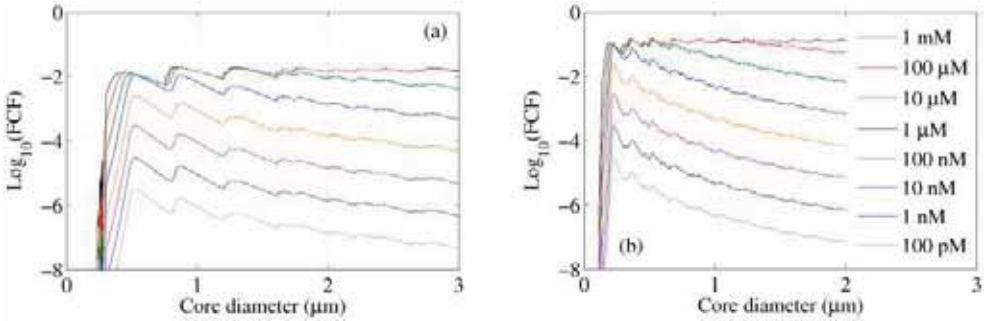

Fig. 4. Back scattered fluorescence signal for a silica fiber (a) and bismuth fiber (b) of length 1m, where the cladding contains varying concentrations of Rhodamine B.

Here we see that for high concentration solutions (e.g. > 100 μM, red and black curves), there is little core diameter dependence. This is because the excitation light is efficiently

#124483 - $15.00 USD Received 19 Feb 2010; revised 11 Apr 2010; accepted 13 Apr 2010; published 21 Apr 2010

absorbed by the fluorophore for all core diameters despite differences in the power fraction. In contrast, when lower concentrations are used the excitation light is less efficiently absorbed for larger core diameter fibers due to the lower power fraction (Fig. 3(a)), resulting in a fluorescence signal that is dependent on core diameter. In fact, the optimum core diameter (silica = 540 nm and bismuth = 240 nm), which corresponds to the peak in the fundamental mode fluorescence capture, is up to 22 times larger for silica fibers and 360 times larger for bismuth fibers compared with a 2 μm core diameter fiber (for a 1 m fiber measuring 100 pM rhodamine B). Comparing silica fibers to bismuth fibers for low concentration sensing (1 nM) we see that at the optimum core diameter bismuth fibers can provide a factor of 9 times better fluorescence capture than silica fibers. This reduces to only 44% (bismuth compared to silica) when considering a core diameter of 2 μm due to a lower power fraction. Hence, to take advantage of higher fluorescence capture using high index fibers, small core diameters need to be used.

2.5 Confinement loss and small-core loss

The results of Fig. 4 indicate that the best fluorescence signal occurs for single-mode fibers with extremely small core diameters, such as 240 nm for a bismuth fiber. In reality there are several factors that prevent this from being the optimum choice. Inherent surface roughness at the core-cladding boundary is believed to be the major contribution to loss in small-core fibers and optical nanowires [27, 28]. Experimental measurements of small-core loss have previously been compiled [17], and these results have been used here to understand the effect on optimum core diameter. In addition, suspended-core fibers have an additional loss (confinement loss) due to the presence of an outer cladding with the same refractive index as the core material. While confinement loss can be reduced by increasing the separation between the core and the fiber jacket, in practice this becomes increasingly difficult as the core size decreases relative to the wavelength of the guided light.

The confinement loss was calculated by analytically determining the dispersion equation of a jacketed air suspended rod (JASR), which is a specific example of the well known W-fiber geometry, using a method analogous to the methods used for step-index fibers [26]. First, the wave equation was solved for the core, inner cladding, and outer cladding regions of the JASR by writing the electric and magnetic fields as appropriate superpositions of Bessel functions. Continuity of the tangential components of the electric and magnetic fields at the two boundaries was then imposed to create a dispersion relation by which the complex effective index was determined using *fsolve* from Matlab's optimization toolbox. The confinement loss (in dB/m) was then determined from the imaginary component of the effective index, n_i, using $\alpha_{dB} = 20\log_{10}(e)2\pi n_i / \lambda$. Results were obtained for the same parameters used in previous sections, including both excitation and fluorescence wavelengths. The results for the fluorescence wavelength are shown in Fig. 5(a) (silica), Fig. 5(b) (F2), and Fig. 5(c) (bismuth). Here the ratio of the outer cladding radius to the core radius was set at 10, which is close to that of recently fabricated suspended optical nanowires [17].

#124483 - $15.00 USD Received 19 Feb 2010; revised 11 Apr 2010; accepted 13 Apr 2010; published 21 Apr 2010

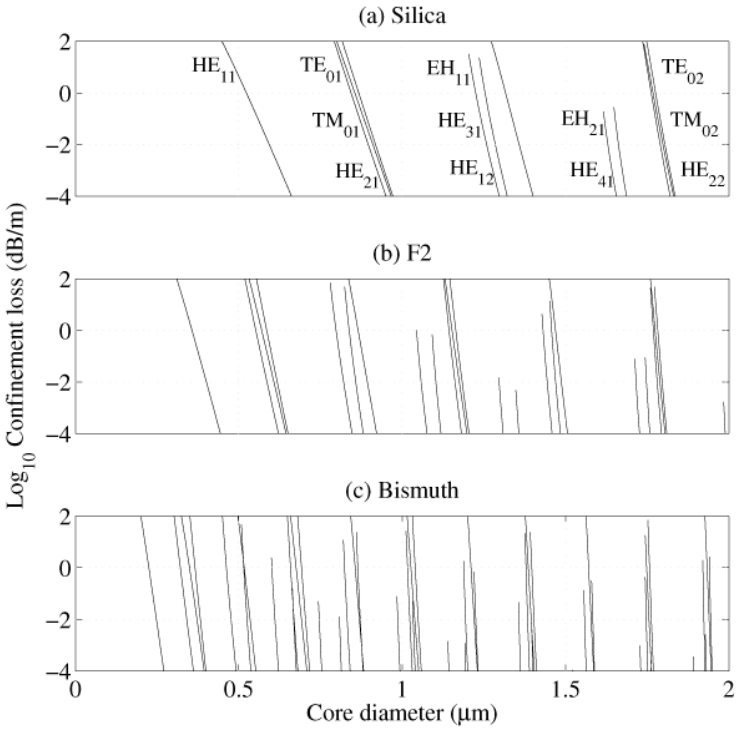

Fig. 5. Confinement loss of a W-fiber with a cladding to core ratio of 10, a wavelength of 590nm, and glass material silica (a), F2 (b), and bismuth (c). Mode labeling is shown for the silica material (a). The mode labeling is similar for F2 and bismuth but has not been displayed for clarity.

The results show a very steep increase in confinement loss as core diameter is reduced, which is steeper for higher order modes and higher index glasses. Note that they show there is only a restricted range of core diameters for which the fiber is effectively single mode. For example, if one requires a confinement loss of greater than 10 dB/m for the higher order modes in order to have effective single mode guidance, then the maximum core diameter for a single mode F2 nanowire only increases from 490 nm (for strict single mode guidance) to 540 nm (for effective single mode guidance).

To see the effect confinement loss has on the optimum core diameter for fluorescence sensing, Eq. (1) was again calculated but with the confinement loss at both excitation and fluorescence wavelengths included within the attenuation terms for a fiber of 1 m in length (Fig. 6). For clarity, the effect of fluorophore absorption was not included in these results, but will be included when comparing with experimental results in Sec. 3.

#124483 - $15.00 USD Received 19 Feb 2010; revised 11 Apr 2010; accepted 13 Apr 2010; published 21 Apr 2010

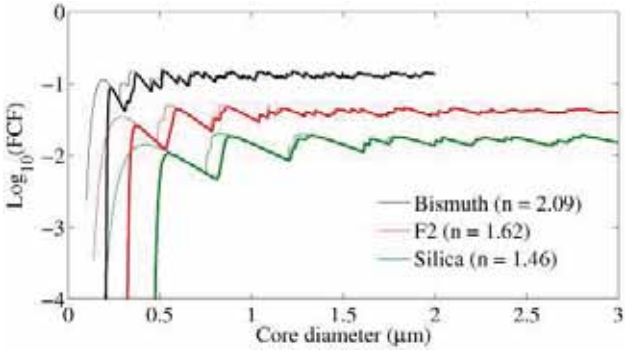

Fig. 6. Fluorescence capture into all modes of a step-index fiber with core material bismuth (black), F2 (red), and silica (green). The results of Fig. 3(b) have been shown again for the case of no confinement loss (thin lines), and then confinement loss has been included at both excitation and fluorescence wavelengths (thick lines). The fiber length has been set at 1 m, with fluorescence measured in the forward direction.

By comparing the thin lines (no confinement loss) and thick lines (confinement loss) in Fig. 6 we see that confinement loss has the effect of reducing the fluorescence capture peaks observed for the low mode number core diameters, as well as increasing the smallest core diameter fibers that can be used in practice. For example, the minimum core diameter, defined as the core diameter at which the capture is 0.1% ($\log_{10}$(FCF) = −3), increases from 90 nm to 210 nm for bismuth fibers, 150 nm to 330 nm for F2 fibers, and 230 nm to 490 nm for silica fibers. It also has the effect of smoothing the curves, as the sharp peaks observed in Fig. 3(b) were the result of capture into higher order modes near cut-off, at which point they are in reality rather lossy.

The next factor we include is experimentally measured small-core loss (Fig. 7). Experimental data for silicate fibers is shown in Fig. 7(a) [17, 29], and the line of best fit has been used to estimate the expected loss for a small-core lead-silicate (F2) fiber. Implicit is the assumption that the loss of the first silicate glass in Fig. 7(a) (Corning 0215, black data points) has similar properties to F2 glass. As with the confinement loss, the small-core loss was factored into the attenuation term of Eq. (1). The results are shown in Fig. 7(b) for an example case of a 1m long fiber with fluorescence captured in the forward direction, where confinement loss has been included for both, but fluorophore absorption effects (Fig. 4) neglected.

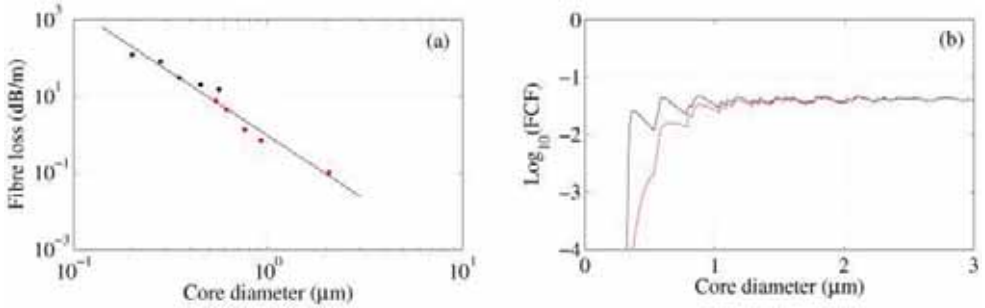

Fig. 7. (a) Measured loss at 633nm for small-core silicate tapers [29] (Corning 0215, n = 1.52, black data points) and F2 suspended-core fibers [17] (F2 Schott glass, n = 1.62, red data points). (b) Forwards fluorescence capture fraction for a 1 m F2 fiber with small-core loss considered (red) or small-core loss neglected (black). Confinement loss has also been included for both.

Figure 7(b) shows that small-core loss has a profound effect on fluorescence capture in the regime of subwavelength core diameters, dominating the impact of the confinement loss.

#124483 - $15.00 USD Received 19 Feb 2010; revised 11 Apr 2010; accepted 13 Apr 2010; published 21 Apr 2010

Indeed, fluorescence capture into the fundamental mode is almost completely lost for a fiber only one meter long, implying that single-mode, and potentially few-moded, optical nanowires are not well suited to fluorescence capture for lengths the order of one meter or more. The next step is to combine the individual effects of fluorescence capture (Fig. 3), fluorophore absorption (Fig. 4), confinement loss (Fig. 6), and small-core loss (Fig. 7). These will now be combined for a specific example and compared with experimental results.

3. Experimental results

Only a modest amount of experimental work quantifying the behavior of optical fiber fluorescence sensors has been reported in the literature. Several authors have demonstrated that the fluorescence capture is proportional to the fiber's numerical aperture [18, 30, 31]. Bryant *et al* demonstrated that the signal level obtained from thin-film side-excited fiber increases with increasing core diameter [30]. Afshar *et al* also confirmed several predictions in regards to the length dependence of an optical fiber fluorescence sensor [8], such as the presence of an optimum length when measured in the forwards direction and no optimum length for the backwards direction. For the first time, we present here experimental results that are quantitatively compared with fluorescence capture theory for small-core fibers. We compare the experimental results with predictions made in Sec. 2, in regards to the dependence of fluorescence signal on core diameter and fluorophore concentration.

To perform these experiments, a number of F2 (lead-silicate Schott glass) suspended-core fibers where fabricated with a range of core diameters (620 nm, 770 nm, 920 nm, 1290 nm, 2050 nm) [17]. These fibers were cleaved to 26 cm lengths and filled with various concentrations of Rhodamine B dissolved in water. Prior to filling, excitation light (532 nm) was launched into the fiber core and the output power was recorded to determine the coupling efficiency. After filling, the forward fluorescence signal was measured after passing through one or two 550 nm long pass filters. The measured data was corrected for the power loss due to the quantum efficiency of the Rhodamine B (70%) and the long pass filter(s) (66-89%, depending on filter used). Also, an optical spectrum analyzer (ANDO AQ6315E) was used for low concentration samples due to the need to filter out the pump light, for these the data was multiplied by 11.1 to take into account the spectral bandwidth of the fluorescence spectrum that was recorded (585 to 595 nm out of a rhodamine spectrum that ranges from approximately 520 nm to 700 nm, measured using a rhodamine B sample in a cuvette). Additionally, for the two highest concentration samples, fluorescence re-absorption was estimated using theory and was factored into the measured data (factor of up to 3.5). These experimental results are shown in Fig. 8 on the same scale as the equivalent theoretical results. The theoretical curves include all effects that were considered in Sec. 2; fluorescence capture, fluorophore absorption, confinement loss, and core-size dependent surface roughness loss. Note that no free parameters have been used.

#124483 - $15.00 USD Received 19 Feb 2010; revised 11 Apr 2010; accepted 13 Apr 2010; published 21 Apr 2010

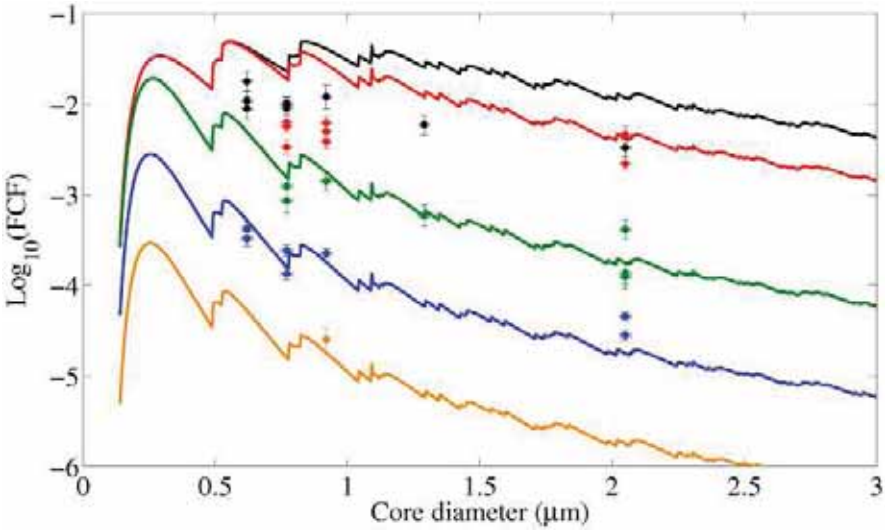

Fig. 8. Predicted forward fluorescence signal for 0.26 m long F2 step-index fibers (solid lines) and measured signal for equivalent suspended-core fibers (data points). For the predicted curves small-core loss and confinement loss has been included. The excitation wavelength was 532 nm and fluorescence wavelength for the theory was 590 nm. The rhodamine B concentrations were 50 μM (black), 25 μM (red), 1 μM (green), 100 nM (blue), and 10 nM (orange). The vertical error bars refer to signal fluctuation during measurement (≈10 s), and horizontal error bars relative to SEM resolution.

The experimental results compare well quantitatively with theory, particularly for low concentration samples. For higher concentration samples (≥ 25 μM), the measured results were found to be lower than expected, and reasons for this may include concentration quenching [32], or stronger than estimated reabsorption. Also, the lower concentration measurements (≤ 1 μM) for the 2.05 μm fiber appear to be higher than that predicted by theory. This could indicate the presence of multimode excitation light, which could be considered in future theoretical work.

The experimental results confirm several important points. Firstly, in the limit of high concentration samples the dependence on core diameter is quite small. This is due to near-complete pump absorption even at large core diameters. In contrast, stronger signals are obtained from smaller core fibers when low concentration samples are used, with up to an order of magnitude difference observed between 620 nm and 2050 nm core diameter fibers.

4. Conclusions

The fluorescence sensing properties of core-pumped high-refractive-index optical nanowires have been explored theoretically and experimentally. Evanescently excited fluorescence is most efficiently captured into fibers made from high refractive index materials due to their relatively high numerical aperture. We also predict that there is very little dependence on core diameter when considering only the fluorescence capture, due to the role of higher order modes, which have been taken into account in the model for the first time here. However, when also considering the Beer's law absorption of the excitation light the higher power fraction of small core fibers can provide a stronger fluorescence signal, particularly for low concentration sensing. We then include loss effects that are characteristic for optical nanowires, such as confinement loss and experimentally measured loss arising from surface-roughness. These effects dictate the minimum core diameter fiber that can be efficiently used for sensing. For example, a 1-meter long F2 optical nanowire would not be useful if the core diameter is less than approximately 400 nm. These results thus set a guideline for future fiber fabrication for optimal sensor design.

#124483 - $15.00 USD Received 19 Feb 2010; revised 11 Apr 2010; accepted 13 Apr 2010; published 21 Apr 2010

Of course, these results are specific to the parameters considered here and would vary for, say, different fluorophores, fluorophore concentrations, fiber lengths, and fiber substrates. For example, if only very short lengths of fiber were to be used, then the minimum useful core diameter would be reduced. Other factors, such as coupling efficiency and stability, could also be included in future analysis. In particular, coupling stability into sub-micron core optical nanowires needs careful attention before these devices are to become practical.

Our experimental results using F2 suspended-core fibers are in close agreement with the numerical results. Notably, both the theoretical and experimental results show that the advantage of using small-core fibers (e.g. 620 nm compared to 2 μm) is most significant for low concentration sensing (< 1 μM for the example in this paper); where up to an order of magnitude improvement can be obtained. The experimental results show successful fluorescence measurement for a fluorophore (rhodamine B in this case) with a concentration as low as 10 nM. While it was not the aim of this paper to present detection of extremely low concentrations, lower concentrations could be measured by using detector sources with lower noise, longer interaction lengths, and moving to higher index optical fibers. Indeed, it has been shown previously that 200 pM detection is possible using similar fibers [33].

In summary, we have presented a rigorous model for predicting the fluorescence sensing performance of optical nanowires, which is in agreement with experimental results. The model is a useful tool for the optimization of optical nanowire sensing designs and the numerical results highlight the benefits of small-core high-refractive-index optical nanowires, particularly for low concentration sensing.

Acknowledgments

We acknowledge the support of the Defence Science and Technology Organisation (DSTO), Australia, and in particular the DSTO Corporate Initiative on Smart Materials and Structures for sponsorship of this program of research. We acknowledge the Australian Research Council for funding this project (DP0880436). T. Monro acknowledges the support of an Australian Research Council Federation Fellowship. We acknowledge Heike Ebendorff-Heidepriem and Roger Moore for fiber fabrication.

#124483 - $15.00 USD Received 19 Feb 2010; revised 11 Apr 2010; accepted 13 Apr 2010; published 21 Apr 2010

3.6 Fluorescence Capture Fraction: Thin-Layer Sensing

The publication [P5] forms the basis of this section.

Y. Ruan, T. C. Foo, S. C. Warren-Smith, P. Hoffmann, R. C. Moore, H. Ebendorff-Heidepriem, and T. M. Monro, "Antibody immobilization within glass microstructured fibers: a route to sensitive and selective biosensors," *Optics Express* **16**, 18514-18523 (2008).

3.6.1 Publication Overview

Aim

The primary aim of this publication was to demonstrate that silane chemistry can be used to biologically activate the surface of glass microstructured optical fibres by attaching antibodies, thus giving the sensor specificity. However, the primary relevance to this chapter is how the fluorescence capture theory of [P1] can be applied to estimate the surface density of attachment from the corresponding measured fluorescence intensity from the output of the fibre. Therefore, only this component of the published work will be discussed here.

Field of Knowledge and Link Between Publications

The high intensity optical field that exists at the glass-air interface of MOFs, as found in [P1], shows the great potential of surface-based MOF sensing. While the diameter of the fibres used in this paper (1.3 μm) are not small enough for this effect to be particularly noticeable, the theory of [P1] can nevertheless be usefully applied, in this case to estimate the surface density of attachment of antibodies to the optical fibre surface. The estimate of the surface density of fluorophores (thus antibodies as they are labeled with fluorescent quantum dots) attached to the surface of the fibre required modification of the fluorescence capture theory presented in [P1] (Derivation in Appendix A). In [P1] it was assumed that the fluorophores are evenly distributed within the holes of the optical fibre, whereas the experiment in [P5] has the fluorophores situated on the glass-hole surface, with a uniform surface density assumed. Using a modal approach to

study surface layer fluorescence has previously been performed [17, 18, 156]. In all cases it was shown that a surface layer of fluorophores increases the fluorescence signal over an equivalent uniform cladding geometry due to the closer proximity of fluorophores to the core. However, [P5] is the first application of this theory for the purpose of characterising a surface attachment experiment.

Note that this has relevance to the corrosion sensing chapter (Chapter 5), where surface attachment of fluorophores is the primary method for sensor fabrication. While not done in Chapter 5, the methods used in [P5] could in principle be used to characterise the surface density of attachment.

Discussion and Conclusions

The fluorescence capture theory of [P1] was modified as derived in Appendix A so that it could be applied to a surface layer of fluorophores. This was then compared to an equivalent solution filled MOF with known concentration both experimentally and theoretically so that the surface density of attachment could be estimated. The results show that the predicted surface density is quite low, with a value of 1.42×10^{-18} mole/mm^2, approximately three orders of magnitude lower than found for glass slides [109] [P5].

It is important to recognise that this low value could either be due to the application of the theory, or inefficiencies in the surface coating procedure. The fluorescence capture theory makes several approximations that are potentially inaccurate. For example, the modelling in [P5] approximated the geometry as a step-index fibre, whereas the fibre geometry used in the experiment was a suspended-core (wagon wheel) fibre. This could be improved by performing finite element modelling of a realistic suspended-core geometry as was done in [P1-P3], however, the experimental results of [P4] suggest that this is a reasonable approximation. A more significant approximation was that the theory used in this paper assumed only fundamental mode coupling, which was seen to be inaccurate in [P4] for fibres with large core diameters, such as the 1.3 μm core diameter used in this experiment. In any case, on a qualitative consideration, the findings of the theoretical work both here and elsewhere [17, 18, 156] show that the fluorescence signal should be higher for a thin-layer of fluorophore over a volume distribution due to the intuitive explanation that the fluorophores are closer to the core, whereas the experimental result

showed a 10× lower signal. This suggests that despite the approximations in the theory the low fluorescence measured is primarily due to issues with coating the fluorophores, which had not been optimised. For example, the coating procedure within the confined space of the optical fibre geometry is obviously quite different to that of a glass slide and may be inherently inefficient. Note though, that this was the first experimental example of internal surfure functionalisation with fluorophores and the technique has since evolved, such as that used in Chapter 5. In any case, further characterisation of coating the insides of MOFs will need to be carried out in order to optimise and better understand the process. The technique presented in [P5] for surface density estimation is thus a useful tool for indirectly inferring the density of surface attachment and thus allowing optimisation processes to be quantified.

3.6.2 Statement of Contribution

Conceptualisation

The concept to use microstructured optical fibres for biological sensing was first conceptualised by Tanya Monro. The concept to use silane chemistry to achieve this aim was conceptualised by Yinlan Ruan. The concept to combine the fluorescence capture theory [P1] with the experimental result to estimate surface binding density was conceptualised by Tanya Monro.

Realisation

Fibre fabrication for these experiments was performed by Heike Ebendorff-Heidepriem and Roger Moore. Surface chemistry and glass slide characterisation was performed by Herbert Foo and Yinlan Ruan. Biological support for the antibody-antigen binding work was provided by Peter Hoffman. Optical fibre fluorescence measurements were performed by Yinlan Ruan. Fluorescence capture modelling was performed by Stephen Warren-Smith.

Documentation

This paper was first written by Tanya Monro for Ref. [157], then modified and extended for publication by Yinlan Ruan, with editing by all other authors.

Declaration and Permission

I declare that the above statement of contribution is accurate and I give permission for this publication to be included in this thesis.

Yinlan Ruan Tze Cheung Foo Stephen C. Warren-Smith

Peter Hoffmann Roger C. Moore Heike Ebendorff-Heidepriem

Tanya M. Monro

Antibody immobilization within glass microstructured fibers: a route to sensitive and selective biosensors

Yinlan Ruan[1], Tze Cheung Foo[1], Stephen Warren-Smith[1], Peter Hoffmann[2], Roger C. Moore[1], Heike Ebendorff-Heidepriem[1], Tanya M. Monro[1]

[1]*Centre of Expertise in Photonics, School of Chemistry & Physics*
[2]*Adelaide Proteomics Centre, School of Molecular & Biomedical Science*
University of Adelaide, Adelaide, SA 5005, Australia
[*]*Corresponding author: yinlan.ruan@adelaide.edu.au*

Abstract: Glass microstructured optical fibers have been rendered biologically active for the first time via the immobilization of antibodies within the holes in the fiber cross-section. This has been done by introducing coating layers to the internal surfaces of soft glass fibers. The detection of proteins that bind to these antibodies has been demonstrated experimentally within this system via the use of fluorescence labeling. The approach combines the sensitivity resulting from the long interaction lengths of filled fibers with the selectivity provided by the use of antibodies.

OCIS codes: (060.2370) Fiber optics sensors; (170.6280) Spectroscopy fluorescence and luminescence; (300.1030) Absorption; (300.2140) Emission.

References and links

1. J. B. Jensen, P. E. Hoiby, G. Emiliyanov, O. Bang, L. H. Pedersen, and A. Bjarklev, "Selective detection of antibodies in microstructured polymer optical fibers," Opt. Express **13**, 5883-5889 (2005), http://www.opticsinfobase.org/oe/abstract.cfm?URI=oe-13-15-5883.
2. L. Rindorf, P. E. Hoiby, J. B. Jensen, L. H. Pedersen, O. Bang, and O. Geschke, "Towards biochips using microstructured optical fiber sensors," Anal. Bioanal. Chem. **385**, 1370-5 (2006).
3. C. M. B. Cordeiro, M. A. R. Franco, G. Chesini, E. C. S. Barretto, R. Lwin, C.H.B. Cruz, and M.C.J. Large, "Microstructured-core optical fibre for evanescent sensing applications," Opt. Express **14**, 13056-13066 (2006), http://www.opticsinfobase.org/oe/abstract.cfm?URI=oe-14-26-13056.
4. Y. Zhu, H. Du, and R. Bise, "Design of solid-core microstructured optical fiber with steering-wheel air cladding for optimal evanescent-field sensing," Opt. Express **14**, 3541–3546 (2006), http://www.opticsinfobase.org/oe/abstract.cfm?URI=oe-14-8-3541.
5. T. Ritari, J. Tuominen, H. Ludvigsen, J. C. Petersen, T. Sorensen, T. P. Hansen, and H. R. Simonsen, "Gas sensing using air-guiding photonic bandgap fibers," Opt. Express **12**, 4080-4087 (2004), http://www.opticsinfobase.org/oe/abstract.cfm?URI=oe-12-17-4080.
6. Y. Ruan, E. P. Schartner, H. Ebendorff-Heidepriem, P. Hoffmann, and T. M. Monro, "Detection of quantum-dot labelled proteins using soft glass microstructured optical fibers," Opt. Express **15**, 17819-17826 (2007), http://www.opticsinfobase.org/oe/abstract.cfm?URI=oe-15-26-17819.
7. L. Rindorf, J. B. Jensen, M. Dufva, L. H. Pedersen, P. E. Høiby, and O. Bang, "Photonic crystal fiber long-period gratings for biochemical sensing," Opt. Express **14**, 8224-8231 (2006), http://www.opticsinfobase.org/oe/abstract.cfm?URI=oe-14-18-8224.
8. J. Cheng, C. Wei, K. Hsu, and T. Young, "Direct-write laser micromachining and universal surface modification of PMMA for device development," Sens. Actuators B, **99**, 186-196 (2003).
9. G. Emiliyanov, J. B. Jensen, and O. Bang, "Localized biosensing with Topas microstructured polymer optical fiber," Opt. Lett. **32**, 460-462 (2007).
10. F. M. Cox, R. Lwin, M. C. J. Large, and C. M. B. Cordeiro, "Opening up optical fibres," Opt. Express **15**, 11843-11848 (2007), http://www.opticsinfobase.org/oe/abstract.cfm?URI=oe-15-19-11843.
11. C. M. B. Cordeiro, C. J. S. de Matos, E. M. dos Santos, A. Bozolan, J. S. K. Ong, T. Facincani, G. Chesini, A. R. Vaz, and C. H. B. Cruz, "Towards practical liquid and gas sensing with photonic crystal fibers: side access to the fibre microstructured and single-mode liquid-core fibre," Meas. Sci. Technol. **18**, 3075-3081 (2007).

#101312 - $15.00 USD Received 9 Sep 2008; revised 21 Oct 2008; accepted 21 Oct 2008; published 24 Oct 2008

12. P. D. Sawant, G. S. Watson, S. Myhra, and D. V. Nicolau, "Hierarchy of DNA immobilization and hybridization on poly-L-lysine using an atomic force microscopy study," J. Nanosci. Nanotechnol. **5**, 951–957 (2005).
13. J. Debs, H. Ebendorff-Heidepriem, J. Quinton, and T. M. Monro, "A Fundamental study into the surface functionalisation of soft glass microstructured optical fibres via silane coupling agents," accepted for publication, J. Lightwave Technol. (2008).
14. S. Gosh, A. R. Bhagwat, C. K. Renshaw, S. Goh, A. L. Gaeta, and B. J. Kirby "Low-light-level optical interactions with rubidium vapor in a photonic band-gap fiber," Phys. Rev. Lett. **97**, 023603 (2006).
15. H. Ebendorff-Heidepriem and T. M. Monro, "Extrusion of complex preforms for microstructured optical fibers," Opt. Express **15**, 15086-15092 (2007), http://www.opticsinfobase.org/oe/abstract.cfm?URI=oe-15-23-15086.
16. H. Ebendorff-Heidepriem, S. C. Warren-Smith, and T. M. Monro, "Suspended nanowires: fabrication, design, and characterization of fibers with nanoscale cores," submitted to Nature Photonics.
17. S. Afshar V. S. C. Warren-Smith, and T. M. Monro, "Enhancement of fluorescence-based sensing using microstructured optical fibers," Opt. Express **15**, 17891-17901 (2007), http://www.opticsinfobase.org/oe/abstract.cfm?URI=oe-15-26-17891.
18. S. K. Bhatia, L. C. Shriver-Lake, K. J. Prior, J. H. Georger, J. M. Calvert, R. Bredehorst, and F. S. Ligler, "Use of thiol-terminal silanes and heterobifunctional crosslinkers for immobilization of antibodies on silica surfaces," Anal. BioChem, **178**, 408-413 (1989).
19. T. M. Monro, Y. Ruan, H. Ebendoff-Heideprien, H. Foo, P. Hoffmann, and R. C. Moore, "Antibody immobilization with glass microstructured fibers: a route to sensitive and selective biosensor," Proc. Internat. Soc. Opt. Engin. (SPIE) **17**, 70046Q-1-4 (2008).
20. S. C. Warren-Smith, S. Afshar, and T. M. Monro, "Highly-efficient fluorescence sensing using microstructured optical fibres; side access and thin-layer configurations," Proc. Internat. Soc. Opt. Engin. (SPIE) **17**, 70041X-1-4 (2008).
21. Http://www.invitrogen.com/site/us/en/home/brands/Product-Brand/Qdot/Technology-Overview.html.
22. Http://probes.invitrogen.com/products/qdot/.
23. J. R. Crowther, *ELISA: Theory and Practice* (Humana, 1995).
24. S. Afshar, Y. Ruan, and T. M. Monro, "Enhanced fluorescence sensing using microstructured optical fibers: a comparison of forward and backward collection modes," Opt. Lett. **33**, 1743-1745 (2008).

1. Introduction

Microstructured optical fibers (MOFs) have the potential to provide improved performance relative to more traditional spectroscopic and fluorescence-based fiber sensors [1-6]. The manipulation of the geometry of the fiber cross-section can increase the fraction of the guided light that is available to interact with the environment to be sensed. The application of MOF-based sensors for the detection of biomolecules is of particular interest, and previous work includes the detection of antibodies in solution [1], the detection of proteins in solution down to the 1 nM level [6], and the detection of the thickness of DNA layers [7]. The first two examples rely on the use of fluorescently labeled biomolecules, with the fluorescence signal being collected via excitation of the guided mode of the fiber.

The development of effective MOF-based biosensors requires: 1) a sensitive detection mechanism capable of measuring low-levels of biomolecules and 2) a means of selectively identifying specific biomolecules of interest. The first requirement can be realized by taking advantage of the long interaction lengths offered by the interaction between a guided mode in a fiber and the material of interest. It has been possible to detect proteins at the 1 nM level using soft glass MOFs [6].

The introduction of selectivity to an MOF-based sensor requires the functionalization of the otherwise inert fiber to allow its response to a biological species to be determined via optical measurements. In principle, this can either be done during the fiber fabrication process or via post-processing of the fiber.

One advantage of using polymer MOFs is that the surface can be chemically modified to allow biomolecules to be attached directly [1, 8, 9]. The low glass transition temperature (e.g. ~90 °C for PMMA) makes polymer fibers impractical for use in high temperature environments or for high power light transmission. Although glass MOFs do not allow direct functionalization, their potential benefits for biosensing are great, since they offer access to particular spectral regions such as the UV-Vis (via high purity silica glass) and the mid-IR (via soft glasses such as tellurite, fluorides, and chalcogenides). Compared to polymer MOFs,

#101312 - $15.00 USD Received 9 Sep 2008; revised 21 Oct 2008; accepted 21 Oct 2008; published 24 Oct 2008

glass MOFs have other advantages including lower loss, the potential for higher damage thresholds because of their higher glass transition temperatures, better cleaving, and easier integration with conventional fiber technologies. This motivates the investigation of approaches for functionalizing glass-air boundaries within glass MOFs.

For glass fibers, which have relatively high processing and fabrication temperatures, the most promising approach for incorporating biological functionality within the fiber is to deposit surface layers after the fiber has been drawn. This post-processing can be done from the end of the fiber or via side access holes. Side access holes can be produced by techniques such as drilling at the preform stage, or ion beam milling at the fiber stage [10,11]. While side-access is attractive for distributed detection schemes, only limited lengths have been fabricated in glass fibres [11]. For the work presented here, we choose to explore the approach of functionalizing fibers from the fiber ends, which requires the development of techniques for depositing coatings on the internal surfaces of the holes within the cross-section and along the length of the fiber.

Recently, the internal surfaces of silica MOFs have been coated with strands of DNA [7]. This approach uses poly-L-lysine to immobilize negatively charged molecules such as DNA to a solid support. Poly-L-lysine has positively charged amino-groups that can bind to the negatively charged silica surface through an ionic binding [12]. An alternate approach is based on coating the internal surfaces of soft glass MOFs with nm-scale silane layers [13]. A similar process has been used to coat the core of a photonic bandgap fiber with a silane coating [14].

Here we demonstrate that it is possible to extend this technique to allow the immobilization of antibodies inside soft glass MOFs. Soft glasses have lower glass softening points than silica, enabling preform and jacket tube fabrication via extrusion through complex stainless steel dies [15]. The extrusion technique allows a large flexibility in the preform and jacket tube geometries that can be achieved. This, in turn, has recently enabled the fabrication of fibers with nanoscale core sizes as small as 400 nm diameter (without requiring a postprocessing tapering step), which is of great advantage for sensing applications [16]. Furthermore, for nanoscale core sizes, the higher refractive indices of soft glasses compared with silica enables higher sensitivity due to enhanced fluorescence capture fraction [17].

The immobilization of antibodies inside soft glass MOFs is based on adapting the established procedure used for the immobilization of antibodies onto glass slides [18] to the internal holes within an MOF, and here we implement this procedure in non-silica glass fibers for the first time. Proof of concept of this approach was demonstrated in Ref. [19]. Here we present a detailed description of the experimental demonstration of the selective detection of immobilized proteins within a glass fiber. In Section 2, the immobilization processes and experimental results on bulk glasses are introduced. The way in which these processes can be applied to soft F2 glass MOF for biosensing is then described in Section 3.

2. Antibody immobilization on glass

To detect specific proteins, it is necessary to immobilize antibodies onto the glass surface that forms the fiber core in order to facilitate the selective binding of antigens to antibodies to occur in a region where the overlap with the guided mode of the fiber is strong. However, as mentioned above, antibodies cannot be attached directly to a glass surface. Bhatia et al. [18] immobilized antibodies onto glass slides by first introducing silane and crosslinked layers. In brief, first a silane layer is attached to the glass surface, followed by attachment of a so-called crosslinker onto the silane layer. Finally, the antibodies are attached to the crosslinker [18]. A solution containing a range of antigens that may be labeled with different dyes can then be introduced into the holes of the fiber by dipping the end of the fiber into the solution and allowing it to fill under capillary action. The antigens that correspond to the immobilized antibodies will bind to them, and any unmatched antigen can be flushed away.

Here we adapt the immobilization procedures described by Bhatia [18] for use in glass films to our fiber/glass geometry. This process begins with the cleaning of the glass surface to remove debris and to create hydroxyl groups. The next step is the silanization of the internal

#101312 - $15.00 USD Received 9 Sep 2008; revised 21 Oct 2008; accepted 21 Oct 2008; published 24 Oct 2008

surfaces (for more detail, see Ref. [13]), and then a cross-linking layer is formed to connect the silane layer to the antibody. The procedures utilize thiol-terminal silanes and heterobifunctional crosslinkers with different reactive groups on each end. One end of the crosslinker is coupled to the silane film and another end forms an amide bond with a terminal amino group on the antibody. The material we choose for silanization is 3-Mercaptopropyltrimethoxysilane [Sigma]. The organic crosslinking agent is N-γ-maleimidobutyryloxy succinimide ester (GMBS) [Merck]. Five proteins were chosen for our tests of selective detection, and they are mentioned below as required.

2.1 Demonstration of immobilization on glass plates

This immobilization process was first tested on glass plates made from 3 different glass materials: conventional glass slides, F2 and LLF1 glass plates. F2 and LLF1 glasses are commercially available Schott glasses. To obtain a hydrophilic surface for silanization, the glass plates are first cleaned with a mixture of concentrated hydrochloric acid and methanol, and then treated with concentrated sulphuric acid. After cleaning, the oxide surfaces of the glass plates exhibit a relatively low water contact angle (that is, a more hydrophilic surface). After silanization, the contact angle of water with the glass plates is 52°, in agreement with literature [18]. Similar results are obtained for the F2 and LLF1 plates. The silane and crosslinker layers were attached via immersion of the glass plates in the corresponding solutions. To reduce cost, in most of our experiments, a single drop (30 μL) of antibody/antigen solution was placed on the glass surface for incubation to achieve protein immobilization or binding.

To determine whether the antibodies were attached to the glasses, we labeled the antibodies with quantum dots, whose fluorescence was detected with a Typhoon imager. The imager is equipped with lasers at 488, 532, and 630 nm, and has filters to block the excitation light and improve the image contrast. We used two different quantum dots, which separately emit light at 800 nm (Qdot800) and at 705 nm (Qdot705).

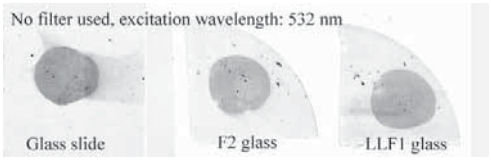

Fig. 1. Images of the glass samples with immobilized Q800-labeled antibodies.

The first antibody sample used here is Qdot800 goat F(ab')2 anti-mouse IgG conjungate. The maximum wavelength of the filters within the imager is 670 nm (30 nm bandwidth), which will block 800 nm emission from the Qdots used for antibody labeling [6]. Thus no filter was used for fluorescence measurement of the samples with Qdot800 labeled antibodies. A 532 nm laser was chosen as an excitation source. This selection was made as a result of a trade-off between the loss of the glass at the pump wavelength, the source availability, and the pump absorption. Figure 1 shows the images of the three glass plates with each treated via application of a 100 nM 30 μL antibody solution drop. The drop was firstly allowed to remain on the glass surface for one hour before the plate was rinsed using deionized water. The area the antibody drop covered appears dark in color and indicates strong fluorescence from Qdot800, demonstrating that the antibody has attached to the glass surfaces via silane and cross-linked layers. The contrast of the fluorescence signal between the droplet and the background regions is clear. The signal from the conventional slide is stronger than the other glasses, indicating higher attachment efficiency for the slides compared to the F2 and LLF1 glasses.

To further test the immobilization process, we used an antibody labeled with an alternative quantum dot (Qdot705 goat F(ab')2 anti-mouse IgG conjungate) with an emission wavelength located at 705 nm. When the image of the glass slide immobilized with this

#101312 - $15.00 USD Received 9 Sep 2008; revised 21 Oct 2008; accepted 21 Oct 2008; published 24 Oct 2008

conjungate was taken together with those of the F2 and LLF1 samples immobilized with the Qdot 800 labeled antibody (Fig. 1) using the 670 nm filter, only the glass slide presents the antibody drop image with the emissions from Qdot800 on the F2 and LLF1 glasses removed by the filter. This confirmed that all the drop images are produced by fluorescence light emitted by the Qdot-labeled antibodies.

To determine the quantity of immobilized antibody, the image of the drop with the same volume (30 μL) and concentration of the antibody on the glasses has been taken as a reference. Image analysis software (IMAGEQUANT SOLUTIONS) has been used for signal quantification. Figure 2 shows the image of the drop of 100 nM 30 μl Qdot800 goat F(ab')2 anti-mouse IgG conjungate, which remained on the glass slide when the image was taken. The object and background are defined in Fig. 2 for fluorescence analysis. The total fluorescence of the image is obtained by integrating the signal corresponding to the object and subtracting the background. Table 1 summarizes the ratios of the total fluorescence of the images shown in Fig. 1 relative to that of the standard 100 nM 30 μL antibody drop shown in Fig. 2. Based on the concentration of the drop and their image areas, the density of the immobilized antibody can be extracted. As shown in Table 1, the relative immobilization efficiency was found to be: conventional glass slide > LLF1 glass > F2 glass.

In Table 1, our results are also compared with previous results reported in Ref. [18] for glass slides and silica. Since different antibody concentrations were used, we normalized the immobilized antibody surface density, S, to the concentration of the antibody solution, C. The thus obtained parameter d = S/C represents the minimum thickness of a depletion layer at the substrate surface, i.e. it corresponds to a solution layer on the surface, which is completely depleted of antibody molecules since all the antibodies are immobilized onto the glass surface. The thus defined minimum depletion layer thickness allows comparison of immobilization results for different solution concentrations, which shows that our experiments achieve similar immobilization efficiency to that of Ref. [18]. As is shown below, this parameter also allows comparison between a larger solution volume and a solution confined in a small fiber hole.

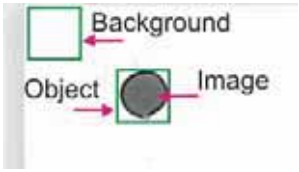

Fig. 2. Fluorescence image of the standard 30 μL100 nM antibody drop on the glass slide. The definition of the object and background for fluorescence analysis is also displayed.

Table 1. Antibody immobilization for different glasses

		antibody concentration C (nM)	fluorescence intensity relative to standard volume	immobilized surface density S (fmol/mm^2)	depletion layer thickness d = S/C (μm)
Ref. [18]	silica	312		6	19
	glass slide	312		4	13
this work	glass slide	100	0.0186	1.4	14
	LLF1 plate	100	0.0156	1.1	11
	F2 plate	100	0.0136	0.9	9
	F2 MOF	100		max. 0.2	

#101312 - $15.00 USD Received 9 Sep 2008; revised 21 Oct 2008; accepted 21 Oct 2008; published 24 Oct 2008

2.2 Quantification of the binding efficiency of the antibody to the antigen

Following the quantification of the density of the immobilized antibodies on the glass surfaces, the next step is to quantify the binding efficiency of the antibodies to the antigens. Two binding experiments were performed. For the first binding experiment, 30 μL 100 nM unlabeled antigen (purified mouse IgG) was firstly immobilized on the treated glass slide. Then one 30 μL drop of 100 nM labeled antibody (Qdot800 goat F(ab')2 anti-mouse IgG conjungate) was put on the surface of the glass slide for one hour, and then was washed away using deionized water. Usually if the antibody treated substrate is incubated in a so-called blocking agent solution, the number of the antigens attached to the crosslinker is negligible [18]. Note that for these preliminary experiments no blocking agents were used. The image of the treated glass slide is shown in Fig. 3(a). The darker area in the center corresponds to the labeled antibody drop, indicating the antibody has been attached to the substrate. The attached antibody density is 0.40 fmol/mm^2 based on its fluorescence intensity relative to the standard in Fig. 2. Since no blocker was used, this antibody density comprises antibodies immobilized to the antigens and adsorbed to the crosslinker. The total density of the antibodies coupled to the substrate relative to the density of immobilized antigens is 44%, smaller than that achieved in Ref. [18] (60%), which resulted from higher concentration (330 nM) antibody/antigen solutions for immobilization and binding. Thus the different binding efficiency is attributed to the use of F2 glass and to the use of lower concentrations (100 nM) for the antibody and antigen solutions in our experiment.

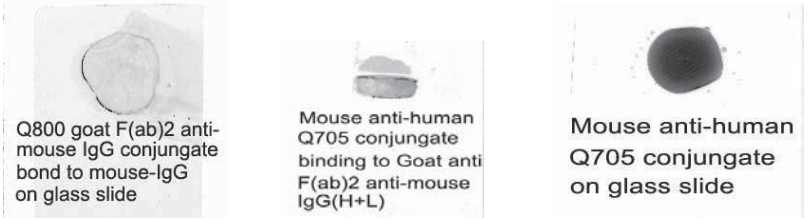

(a) (b) (c)

Fig. 3. Binding between antibody and antigen with only one of them labeled: (a) labeled antibody (Qdot800 goat F(ab')2 anti-mouse IgG conjungate) bond to unlabeled antigen (Purified mouse IgG); (b) antigen (mouse anti-human Qdot705 conjungate) bond to unlabeled antibody (Goat anti-Fab2 anti-Mouse IgG (H+L)); (c) 30 μL 100 nM antigen solution (mouse anti-human Qdot705 conjungate) as a reference.

In any practical sensor, it is necessary to use specific antibodies to detect specific antigens within the sample. Thus for the second experiment, we reversed the sequence of the antibody and antigen. The unlabeled antibody (goat anti-Fab2 anti-Mouse IgG (H+L)) was first immobilized onto the treated LLF1 glass slide. A large volume (>130 μl) was used to allow immobilization to occur across the whole surface. A high concentration (330 nM) was used to increase the density of the immobilized antibody (and of the bound antigen). Indeed, a thick antibody layer was observed after immobilization (with a 100 nM antibody solution, the layer is not evident to the eye). Following a rinse using the buffer solution, a portion of the layer washed away, indicating weak attachment between the thick antibody layer and the crosslinked film. Applying a 30 μL 100 nM antigen solution (Qdot705 mouse anti-human conjungate) on the surface of the remained thick film for one hour and then washing the antigen solution away, the image of the bound antigen is shown in Fig. 3(b). Figure 3(c) shows the image of the antigen solution drop with the same concentration/volume as that used in Fig. 3(b). Through comparing the fluorescence signals of Fig. 3(b) and 3(c), and calculated antigen number included in the antigen drop in the Fig. 3(c), the calculated density of the attached antigen in Fig. 3(b) is 2.5 fmol/mm^2. This corresponds to 68% total density of immobilized antigen relative to the density of immobilized antibody. As expected, a higher binding density results from a higher density of immobilized antibody. This value is also equivalent to that achieved on the silica substrate in Ref. [18], where no blocker was used as

#101312 - $15.00 USD Received 9 Sep 2008; revised 21 Oct 2008; accepted 21 Oct 2008; published 24 Oct 2008

well. Since no blocker was used, nonspecific binding of antigen or antibody to the crosslinker layer was not prevented. For the silica substrate, Ref. [18] demonstrated that the nonspecific binding represented 38% of the total binding to antigen and crosslinker [18]. The ratio of nonspecific binding to the specific binding is believed to be mainly dependent on respective reactivity of the antigen to the antibody and to the crosslinker. Thus we can conclude that specific antigen binding has been achieved in the LLF1 glass.

3. Application to fibers for biosensing

The F2 glass MOFs used in this work have a fiber core that is suspended in air by 3 long fine struts within a robust jacket. An SEM image of one of these fibers is shown in Fig. 4(a). These fibers have been fabricated in-house, and we have very recently achieved core diameters as small 400 nm using this design concept [16]. For the preliminary experimental work described here, MOFs with relatively large core diameter of 1.3 μm and relatively large hole radius of ~4.3 μm were chosen to enable high coupling efficiency and fast filling of the air holes. In order to adapt the immobilization processes developed for bulk glasses to the internal surfaces of optical fibers, we omitted the cleaning step for immobilization within the MOF, since the internal surfaces of the MOF are fire-polished during fabrication and are unlikely to be contaminated. After every step, in order to avoid previous chemicals left within the MOF, a specific solution (buffer or deionized water) was used to flush the MOF. A pump was used to fill and empty the fibers with the required liquids [13]. The time for filling is set to 2 hours and for emptying is 1 hour using our pumping system. Note that in a practical application this can be reduced significantly using higher pressure filling, larger holes, or both. In addition, not all of the fiber needs to be filled in order to make a measurement provided that one is not operating near the detection limit of the system. The protein used for immobilization on the internal hole surfaces of the fiber is 100 nM Qdot800 goat F(ab')2 anti-mouse IgG conjungate.

After immobilization, the loss of the F2 MOF increased to about 30 dB/m at 532 nm compared to 2 dB/m before processing. The reason for this increased fiber loss is not entirely clear and requires further investigation. Thus only a short fiber could be used for observation of fluorescence. The same setup was used for fluorescence measurement as illustrated in Ref. [6]. The measured fluorescence signals with different output power from the 19.2 cm long F2 MOF with immobilized antibodies is shown in Fig. 4(b). The background fluorescence from the MOF itself has been subtracted in Fig. 4(b). The strong fluorescence clearly indicates that antibodies have become attached to the core surface. Figure 4(c) shows the fluorescence signal of another F2 MOF with 25 cm length from the same fiber draw as that used in Fig. 4(a) but instead filled with a 100 nM antibody solution. Both fibers have the same core size, and the same experimental conditions were used. Note that the loss of the solution filled F2 MOF was only 2 dB/m. Comparing Fig. 4(b) and 4(c), it can be seen that the F2 MOF with immobilized antibody exhibits a fluorescent signal about 10% of that from the MOF filled with solution.

To predict the density of the immobilized antibody on the core surface, and also the potential of the immobilized fiber for sensing, the fluorescence capture within the immobilized MOFs is compared with solution-filled MOFs has been calculated using the models recently developed by our group [17,20]. In order to simplify these calculations, a step-index structure is used for these calculations. For the antibody solution filled fibers, the model assumes that a length of MOF is fully filled with the solution. For the immobilized fibers, a single molecular layer is assumed to be immobilized on the core surface. Thus the distance from the Qdots to the surface of the fiber core is regarded as layer thickness, and is approximately 10 nm according to the data provided by Invitrogen [21]. The extinction coefficient of the Qdots is 2×10^{8} $M^{-1}m^{-1}$ [22]. The loss of the solution-filled MOF at the excitation wavelength of 790 nm was measured as 1 dB/m using a standard cut-back measurement. The fluorescence measurements are made at the opposite end of the fiber from which the pump light is launched. The calculated ratio of the captured fluorescence in the immobilized fiber (with a loss of 30 dB/m) to that in the solution-filled MOF is shown in Fig. 5(a). This quantity is described as the ratio of the fluorescence capture fraction (FCF) in Fig.

#101312 - $15.00 USD Received 9 Sep 2008; revised 21 Oct 2008; accepted 21 Oct 2008; published 24 Oct 2008

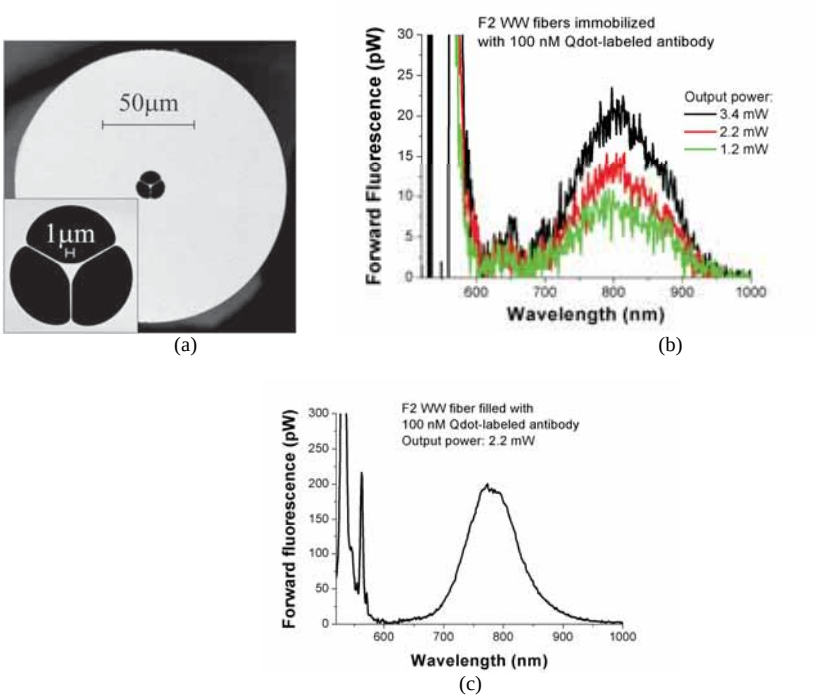

Fig. 4. Fluorescence intensity captured by the forward propagating mode of F2 MOFs using Qdot 800 labeled antibodies for the case of: (a) the SEM image of the MOF used here; (b) immobilized antibodies on the internal surfaces; (c) holes with a 100 nM solution of antibodies.

5. As a comparison, the ratio of the captured fluorescence for an immobilized fiber with a loss of 2 dB/m is also displayed in Fig. 5(b). This corresponds to assuming that no loss is introduced in the immobilization processes. It can be seen from both figures that the fluorescence signal of the immobilized F2 MOF is strongly dependent on the surface density with which the antibody attaches to the surface of the core.

Using this data, the antibody surface density corresponding to the fluorescence capture ratio of 10% (as defined above) as measured in our experiment can be estimated to be 1.42×10^{-3} fmol/mm^2 as illustrated by a grey dot in Fig. 5(a). If no additional loss is introduced to the fiber during the immobilization process, the relative fluorescence signal of fibre with immobilized antibodies could in principal be increased to 36% as shown in Fig. 5(b) (grey dot). Additionally, the lower loss of the immobilized fiber should also enable much longer fiber to be used for further fluorescence enhancement. Figure 5(c) shows length dependence of the fluorescence capture fraction of the low loss immobilized fiber. It can be seen from these results that the fluorescence signal increases with increasing fiber length, with the highest value occurring for a fiber length of approximately 2 m. For longer lengths the fluorescence decreases due to attenuation of the fluorescence signal along the fiber length. For the surface density of 1.42×10^{-3} fmol/mm^2 achieved in our experiments to date, the maximum fluorescence of the immobilized fibers can be enhanced by a factor of 4 using a 2 m length of the MOF (compared with 19.2 cm length used in these experiments).

#101312 - $15.00 USD Received 9 Sep 2008; revised 21 Oct 2008; accepted 21 Oct 2008; published 24 Oct 2008

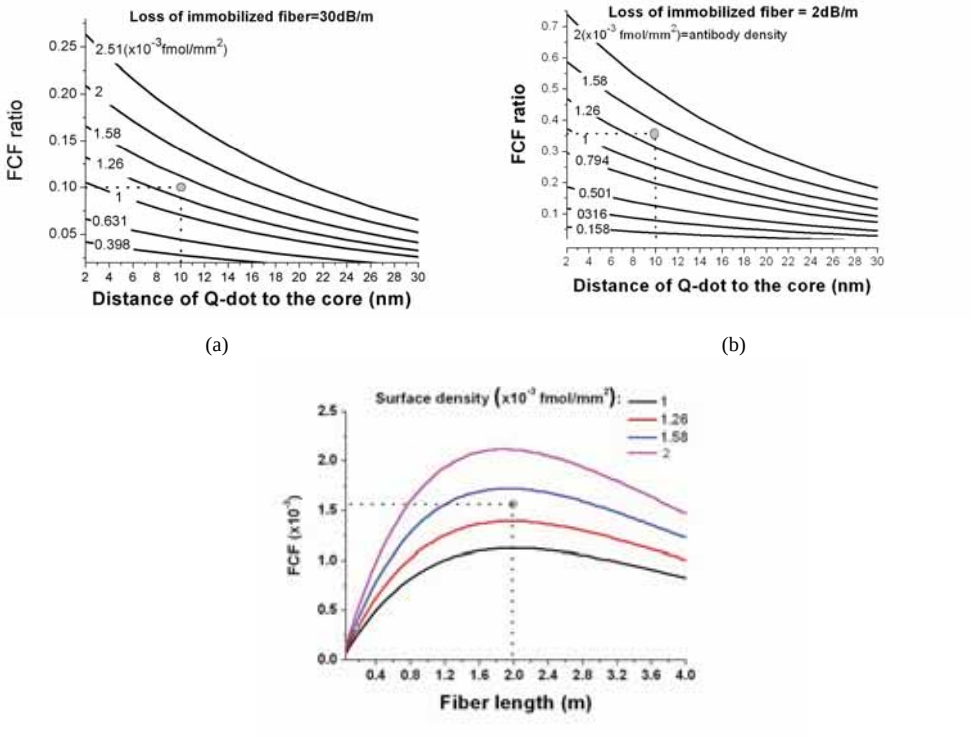

Fig. 5 Comparison of the FCF in the immobilized MOF and in the solution filled MOF. The grey dots in the figures correspond to the points with the surface density of 1.42×10^{-3} fmol/mm^2. (a) FCF ratio between two fibers with loss of immobilized fiber of 30 dB/m; (b) FCF ratio with assumed loss of the immobilized fiber as 2 dB/m; (c) length dependence of the FCF with the immobilized fiber loss of 2 dB/m.

Note that the fiber hole radius (approximately 4 μm) is smaller than the minimum depletion layer thickness of 9 μm measured for a F2 glass plate in Table 1. This suggests that it should be possible to attach all the antibodies within the solution-filled F2 MOF to the internal hole surface, which would amount to an attachment density of 0.21 fmol/mm^2 based on the size of the F2 MOF used above and the solution concentration of 100 nM. This value represents the maximum antibody density that can be immobilized for this fiber. This maximum is 150 times greater than the attached antibody density that we inferred from our experimental results (Fig. 4(a), 1.42×10^{-3} fmol/mm^2). This difference indicates that there is significant scope for substantially improving the magnitude of the fluorescence signal by optimizing the coating processes for improved antibody density.

4. Conclusion

We have successfully demonstrated the adaptation of protein immobilization and binding processes in soft F2 and LLF1 glasses, and achieved good immobilization and binding efficiency. We successfully applied these processes into microstructured fibers made of the F2 glass material. Immobilized proteins have been detected within soft glass MOFs for the first time using fluorescence labeling techniques. This paves the way to sensitive and selective biosensors through binding process. This approach lends itself to the measurement of multiple biomolecules via the immobilization of multiple antibodies. The primary task for building on this work is to optimize the coating procedures to reduce the fiber loss and increase the

#101312 - $15.00 USD Received 9 Sep 2008; revised 21 Oct 2008; accepted 21 Oct 2008; published 24 Oct 2008

density of the attached antibody after processing, which will enable high sensitivity of detection shown by our modeling.

At the same time, the fiber design can be systematically optimized for enhanced fluorescence capture by increasing the mode field fraction in the fiber holes and/or increased field intensity in the glass-air interface [17,20]. Note that when a glass-air interface within a fiber cross-section is located at a point of high intensity within a guided mode, a localized region of high intensity is created on the low-index side, and this effect is particularly striking in high index glasses. Such localized regions can be used to enhance the efficiency of excitation and capture of fluorescent photons for sensing [20]. Thus in the future, improvements in the density of antibodies immobilized on the fiber core surface combined with the deployment of new small-core high-index glass-based MOFs, promises the development of highly sensitive selective biosensors that have ability to compete with existing commercial technologies, such as ELISA [23]. While ELISA is widely used both in research and industry, it lacks the ability to perform real-time in-situ measurements. By adapting this approach to allow the detection of backscattered fluorescence from the input (launch) end of the MOFs, as demonstrated in Ref. [24] for a solution-filled biosensor, this approach promises to lead to the development of biosensors that can move beyond these limitations.

Acknowledgments

We acknowledge funding from DSTO Australia and the Australian Research Council Discovery project DP0665486 for this project, and to S. Afshar and E. Schartner for useful discussions. T. Monro acknowledges the support of an ARC Federation Fellowship.

#101312 - $15.00 USD Received 9 Sep 2008; revised 21 Oct 2008; accepted 21 Oct 2008; published 24 Oct 2008

3.7 Discussion and Conclusions

The modelling of suspended-core optical nano/micro-wires for fluorescence-based sensing has been studied in detail in [P1-P5]. In [P1] it was shown that for sufficiently small-core high-index fibres there exists a high intensity layer in the optical field that leads to a highly efficient fluorescence capture for the fundamental mode. [P2] then demonstrated the difference between forwards and backwards collection modes for fluorescence-based sensing. It was shown that the power level is predicted to be greater for the backwards collection, which complements several technical advantages such as reduced excitation signal, and optics at only one end of the fibre that allows for a dip-sensor configuration. Also, the backwards collection method does not posses an optimum length, unlike the forwards collection method, and this was confirmed experimentally. The theory was then extended to the case of a liquid-immersed exposed-core fibre in [P3] where it was shown that the asymmetric refractive index profile can be used advantageously to improve both the amount of evanescent field available and the fluorescence capture.

The main missing component to the theory considered in [P1-P3] was the evaluation of the effects of higher order modes as only the fundamental mode was considered. While accurate if the fibre is single moded, this is unlikely to be the case if the core diameter has similar or greater dimensions compared to the propagating wavelength due to the high index contrast of fibres considered here. For this reason the theory was extended to include higher order modes in [P4], as well as included other important loss effects. Significantly, the theory was found to agree quantitatively with experiments that were performed with suspended optical nanowires (wagon wheel fibre). Also important is that the theory, when higher order modes were included, was shown to be consistent with equivalent ray-optics theory.

The final paper, [P5], presented an example of how the developed theory can be used for sensor characterisation rather than performance prediction. Here the surface density of a biological sensor was estimated by equating the theory with experimental results. It is very difficult to directly measure the surface binding density of attached fluorophores within a microstructured fibre and thus this is a useful indirect characterisation technique. While many approximations and assumptions were made in doing this, the theory doubtlessly confirmed that the surface density coverage was much lower than anticipated from glass slide experiments. This result lead to the acknowledgment that the surface

attachment procedures need to be optimised, thus highlighting the usefulness of the theory for such an application.

The theory presented in this chapter is largely complete and shows good agreement with experiment. However, there are, of course, many improvements and other factors that can be modelled for the fluorescence-based optical fibre sensor. Considering the fundamental theory, it is assumed that the fluorescence sources have a uniform emission in every direction that is unaffected by the proximity to a dielectric boundary. This is not entirely accurate as it is known that fluorescence emission properties, such as emission lifetime, are affected by proximity to a dielectric boundary [158–161]. These effects can be accounted for in a pure classical theory, or a higher level of complexity would be to approach the problem from a quantum mechanical viewpoint [162–164]. Quantum mechanical effects are likely to be particularly important for thin-layer sensing where mono-layers of fluorophores are attached to the surface, even more so if a single-molecule sensor is desired.

Coupling efficiency is another problem that has not been studied completely accurately. As discussed in Appendix B, it is difficult to obtain an exact expression for coupling efficiency even for the step-index fibre and as such several approximations are generally made. As a result, the coupling efficiency can give unphysical results such as greater than 100% efficiency. Clearly there is a need to readdress this problem so that the coupling into devices such as nanowires can be modelled accurately.

Chapter 4

Optical Fibre Fabrication and Characterisation

It is a good morning exercise for a research scientist to discard a pet hypothesis every day before breakfast. It keeps him young.

Konrad Lorenz

4.1 Fabrication Overview and Motivation

The theoretical predictions of Chapter 3 demonstrated that suspended-core fibres (both enclosed and exposed core variants) have optimal fluorescence sensing performance when they have core diameters that are approximately the same dimensions of the propagating wavelength, or smaller. As will be seen in Chapter 5, fluorophores used for corrosion sensing, and indeed many other applications, operate at visible wavelengths. This implies that the optimal core diameter for a suspended-core fluorescence-based sensor is in the order of 500 nm. Thus, the primary aim of the work presented in this chapter was to fabricate suspended-core fibres (enclosed and exposed) with these core diameters. To achieve these aims the fabrication technique of extruding soft glasses was chosen due to its versatility in producing a wide variety of preforms. This is essential particularly for the exposed-core design which cannot be created using, say, capillary stacking techniques. These fibres could then be used for biological applications [P5] and corrosion sensing (Chapter 5). Of particular interest was the fabrication of exposed-core fibres which allow for real-time and distributed sensing, and experimental results demonstrating this are shown in [P7] and [P8], respectively. In addition, the fibres were used for verifying several theoretical predictions, which were presented in [P2, P4].

In this section a brief overview of optical fibre fabrication history is given, and the method of fabrication used in this project is overviewed. Then in Sec. 4.2 a description of the fabrication of enclosed suspended-core fibres is presented, which primarily includes the publication [P6]. In Sec. 4.3 the fabrication technique used in [P6] is extended for the fabrication of exposed-core fibres, and primarily includes the publication [P7]. Following [P7] is an additional section (Sec. 4.3.3) which discusses one of the primary difficulties in fabricating exposed-core fibres using the extrusion technique and methods for overcoming these difficulties. Finally, Sec. 4.4 includes the publication [P8], which presents experimental results demonstrating the ability of exposed-core fibre to be used for distributed sensing, which is a primary motivator for corrosion sensing with these fibres.

A flowchart of how the sections of this chapter relate to other sections of this thesis is shown in Fig. 4.1.

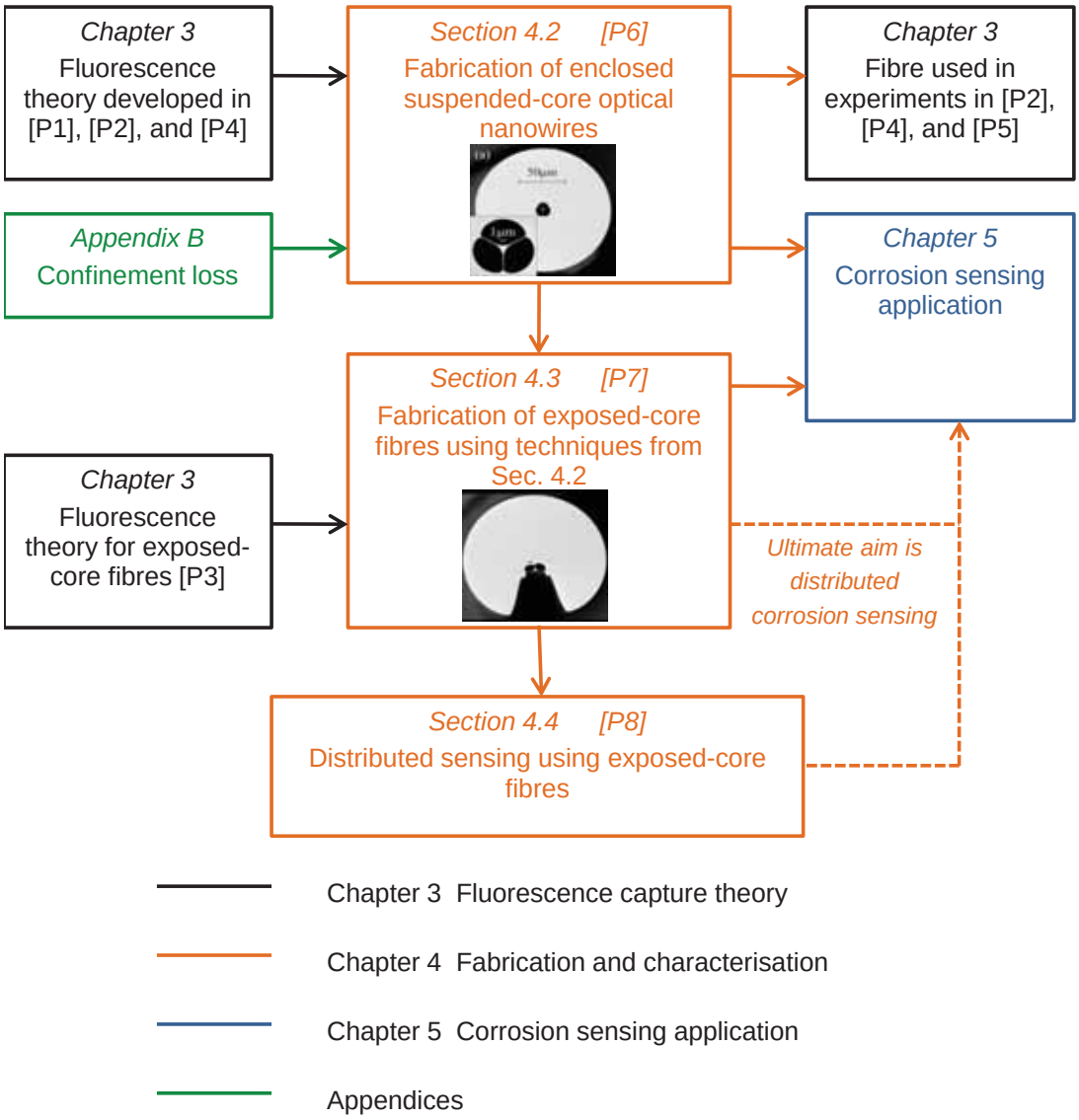

FIGURE 4.1: Flowchart showing the links between Chapter 4 and publications, appendices, and other chapters.

Optical Fibre Fabrication History

Perhaps the first demonstration of an optical waveguide was in 1854 by John Tyndall who showed that light could be guided along a water stream due to total internal reflection at the water-air interface [165]. Since this time various optical light pipes were invented, such as metal coated glass rods [165]. It was in 1954 that Abraham van Heel proposed surrounding glass rods, or fibres, with a lower index transparent cladding for the purpose of abberation free image transportation [166, 167]. It was found that the cladding protects the fibre and prevents cross talk, that is, where light rays can exit one fibre and enter an adjacent fibre [167].

However, initial optical fibres were not viewed as an alternative communications medium due to their relatively high transmission losses. Then in 1966 Charles Kao and George Hockham proposed that impurities in the glass rather than the glass itself caused the measured loss and that losses below 20 dB/km should be possible if the glass material is refined [166]. This was achieved by Corning researchers in 1970 and since this time optical fibres have revolutionised the communications industry with losses as low as 0.2 dB/km [166].

While it is straightforward to draw bare fibres from a glass rod, producing a fibre with a cladding requires more sophisticated techniques [165]. Currently, the main method for optical fibre fabrication is the process know as modified chemical vapour deposition (MCVD) [168]. MCVD was first invented by MacChesney *et al.* in 1972 at Bell Laboratories [168]. The process involves flowing chemicals such as silicon chloride and germanium chloride though a silica capillary that rotates on a lathe, and depositing these chemicals via a reaction with oxygen at high temperature using a hydrogen torch [168]. This produces a slightly higher index (compared to pure silica) germanium oxide doped layer that forms the core and provides the index contrast required for total internal reflection [165, 168].

Microstructured Optical Fibre Fabrication

Optical fibres with holes in their cross section were investigated as early as the 1970s, in an attempt to develop low-loss communications fibres [169]. However, significant interest in these fibres began in 1996, when Knight *et al.* reported the fabrication of these fibres in Ref. [75]. The intention of this design was to create a two dimensional photonic bandgap structure, where the large index difference between the silica glass and the air holes was a beneficial property for this form of light manipulation [75]. While drilling holes into glass rods is a possible MOF preform fabrication technique, the preform in Ref. [75] was fabricated by stacking capillaries and has since become the preferred and most widespread method of fabrication [10]. The main disadvantage of capillary stacking is the limitations in the possible designs, which are generally restricted to circular features. An alternative technique is to extrude glass through a die whose design is the inverse of the structure of the desired preform [74]. In principle this will allow any design to be fabricated and is the technique used in this project.

Fabrication of Fibres in this Project

The fabrication of suspended optical nanowires and exposed-core fibres is described in [P6] and [P7] respectively. In this section the fabrication process is briefly overviewed and images of the key hardware components are included.

For the fabrication of the suspended nanowires in [P6], commercial F2 lead silicate glass [170] was used. Of the commercially available soft glasses, F2 glass is attractive because it combines high transmission in the visible spectral range with a low softening temperature (592 ^{o}C) [170]. The low softening point allows use of glass extrusion through stainless steel dies for preform and jacket tube fabrication [171].

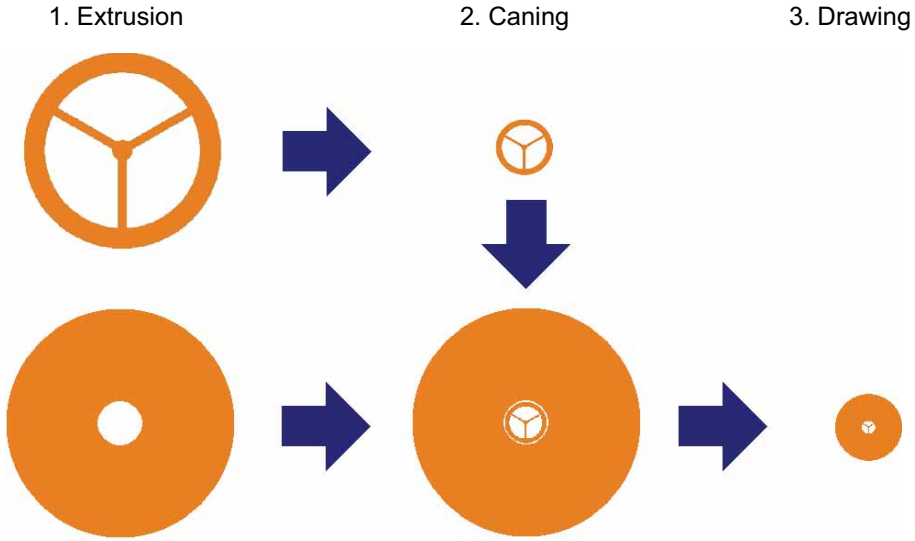

FIGURE 4.2: Schematic diagram of the fabrication process for enclosed suspended core fibres. The structured preform (top-left) and jacket tube (bottom-left) are first extruded. The structured preform is caned (top-middle) and inserted into the jacket tube (bottom-middle), which is draw into a fibre.

The fibres were made using a three step process as shown in Fig. 4.2. Firstly, the structured preform and jacket tube were manufactured from billets of glass using the extrusion technique. This was achieved by forcing the glass billet through a steel die with high temperature ($\approx 570^{o}$C) and pressure (1-10 kN across the billet cross section) using the machine shown in Fig. 4.5. The billets generally had a circular diameter of 30 mm and a height of 70 mm (Fig. 4.3), while the outer diameters of the extruded items were in the range 10-15 mm. In the second step, the preform was reduced in size to a cane of approximately 1 mm outer diameter using a fibre drawing tower (Fig. 4.6). The cane was then inserted into the jacket tube. The inner diameter of the tube is selected to provide a close fit to the cane diameter. This assembly was finally drawn down to

form the final fibre. Careful adjustment of the drawing speed allowed accurate control of the outer diameter of the fibre, which was in the range of 100-200 μm depending on drawing parameters.

FIGURE 4.3: Example of a lead-silicate glass billet used for fabricating the fibres in this project (Schott glass F2 [170]).

The method of fabrication for the exposed-core fibre expands on the method outlined above for fabricating suspended-core fibres with the main difference being that a wedged jacket is fabricated rather than a symmetric jacket tube as shown in Fig. 4.4. Note also that varients of the structured preform were fabricated in order to expose the core. As will be seen in [P7], fibres made using the structured preforms shown in Fig. 4.4 (a, b) require a post-drawing etching step in order to exposed the core, while those made from Fig. 4.4 (c) are directly drawn exposed.

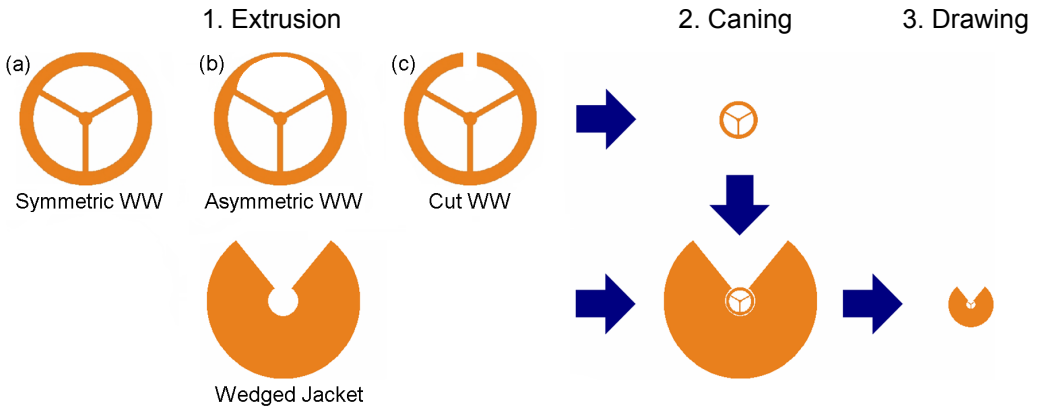

FIGURE 4.4: Schematic diagram of the fabrication process for exposed-core fibres. The structured preform (various designs, top-left) and the wedged-jacket (bottom-left) are first extruded. The structured preform is caned (top-middle) and inserted into the wedged-jacket (bottom-middle), which is draw into a fibre. Image from [P7].

The advantage of extrusion for this fibre design is significant, as it allows the fabrication of asymmetric structures such as the wedged jacket, which could not be produced by alternative methods such as capillary stacking. Though, as will be seen in Sec. 4.3.3,

this has its own intrinsic challenges. It should also be noted, that the “cut” structured preform shown in Fig. 4.4 (c) was fabricated by cutting the preform shown in Fig. 4.4 (a) using a diamond saw. Extruding this design directly may be a better alternative as it would be a cleaner process, but is a non-trivial exercise that was not successfully achieved in this project.

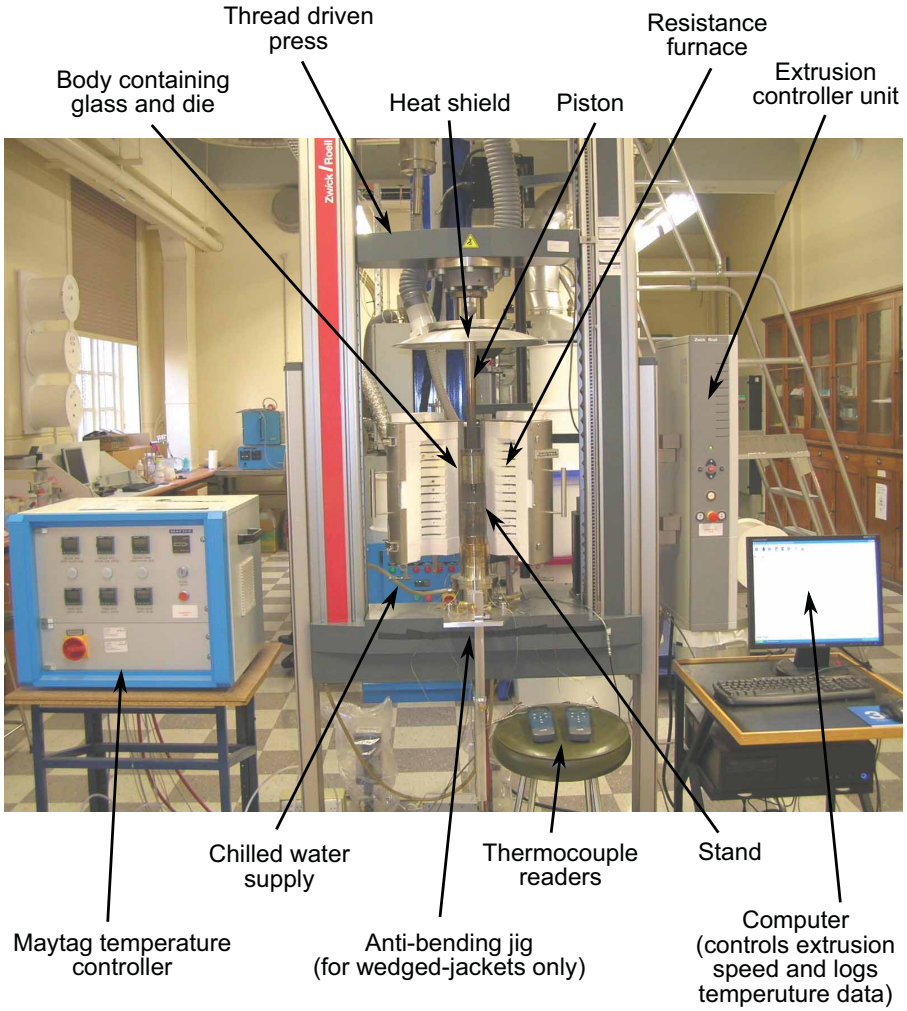

FIGURE 4.5: Extrusion machine used to fabricate soft glass preforms for suspended optical nanowires and exposed-core fibres. The soft glass billet (F2 for this project) was placed within the body, along with the steel die. The furnace is then closed and the body is heated to the required temperature (approximately 560-580^{o}C) using the temperature controller. The thread-driven press (*Zwick-Roell*) is then slowly lowered (usually 0.2 mm/min) to supply pressure to the glass via the piston and hence extrude the glass through the die. The anti-bending jig was used only for wedged jacket extrusions, which will be described in [P7] and Sec. 4.3.3.

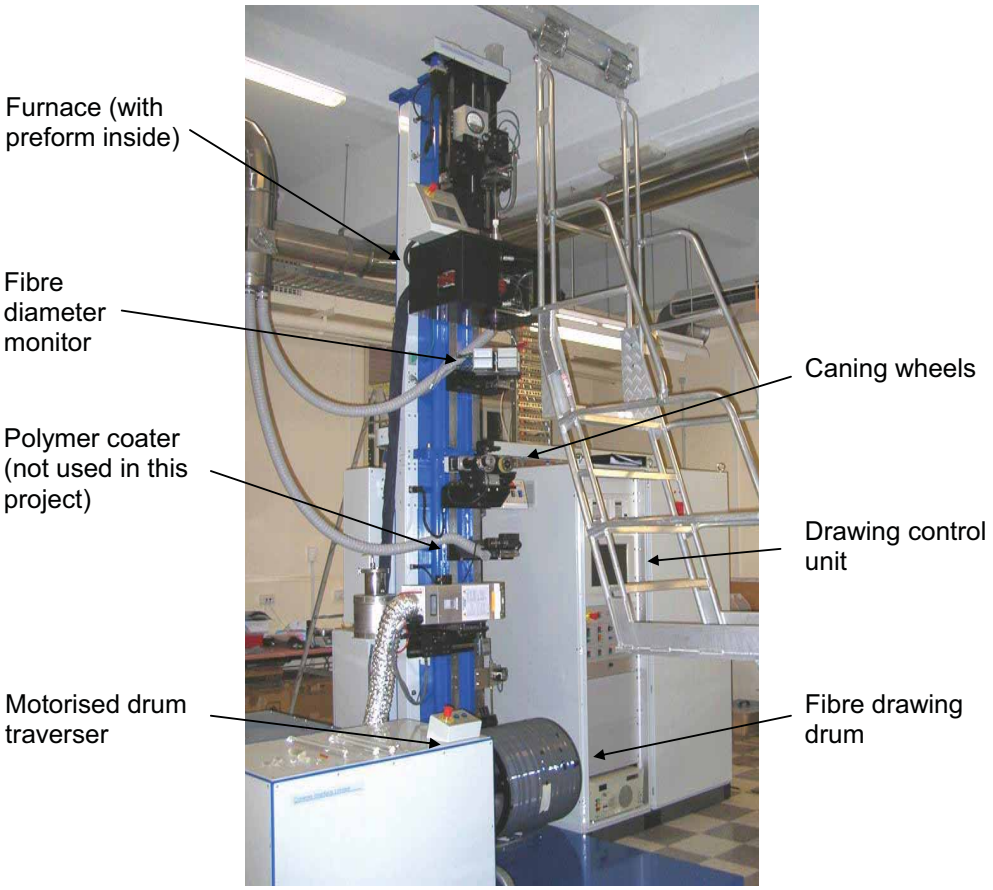

FIGURE 4.6: Soft glass fibre drawing tower used in this project to pull both enclosed and exposed suspended-core fibres. The soft glass preform is placed centered within the induction furnace. The lower end of the preform is heated to the glass melting point which tapers into a fibre. For the lead-silicate (F2) glass used in this project the susceptor temperature was approximately 860^oC. The leading end of the fibre is attached to the motorised drum which applies tension to the fibre. The preform feed speed, glass temperature, and drum speed are then adjusted to control the outer diameter of the fibre which is monitored throughout the fibre drawing. In the case of drawing a cane the specialised caning wheels are used instead of the fibre drawing drum due to the lack of flexibility of the cane.

4.2 Suspended Optical Nanowires

The publication [P6] forms the basis of this section.

H. Ebendorff-Heidepriem, S. C. Warren-Smith, and T. M. Monro, "Suspended nanowires: fabrication, design and characterization of fibers with nanoscale cores," Opt. Express 17, 2646-2657 (2009).

4.2.1 Publication Overview

Aim

The aim of this work was to demonstrate the fabrication of optical nanowires in a suspended-core microstructured optical fibre configuration. Such fibres represent the practical realisation of the fibre designs theoretically modelled in [P1, P2], and are the precursors for the exposed-core fibre design in [P7]. In addition, the optical loss characteristics of these fibres were analysed in detail, including surface scattering loss and confinement loss.

Field of Knowledge and Link Between Publications

Suspended optical nanowires (a small-core subset of wagon-wheel or steering-wheel fibres) are fibre waveguides with sub-micron core diameters [11, 70, 89, 90, 172–175] [P1-P3]. Such small core diameters offer access to fibre properties such as high nonlinearity [175], and large power fractions in the evanescent field for sensing applications [11, 70] [P1-P5].

The majority of nanowires that have been investigated prior to this work were fabricated via the tapering of fibres of standard outer diameter ($> 100\ \mu$m) to subwavelength diameters (50-900 nm) [73, 175–177], where the whole fibre cross section with nanoscale diameter acts as the fibre core. These nanowires are fragile, which makes them difficult to handle, and are fully exposed to the environment. While this is generally desired for a sensing application, without some form of protection the nanowires are susceptible to a high degree of degradation, such as an increase of 10 dB/day due to atmospheric moisture [177].

In this paper an alternative means of fabricating nanowires is demonstrated; namely the direct drawing of long length of fibres with subwavelength core sizes and practical outer diameter (> 100 μm) using the extrusion technique for preform and jacket tube fabrication. The fibre structure is based on a high air filling fraction microstructured fibre with a small core suspended via three thin struts and is essentially a suspended optical nanowire with a protective outer jacket. Previous to this paper the smallest reported suspended core diameters were approximately 800-1000 nm [89, 90, 174]. In this paper suspended core fibres with up to two times smaller core diameters (420-720 nm) have been demonstrated, which was made possible due to the use of the extrusion technique that allows nearly arbitrary design of the MOF preform.

This paper also contains results that are important to several other papers contained within this thesis. The suspended optical nanowires presented in this paper are the practical realisation of the fibres theoretically modelled in [P1, P2]. The techniques (namely extrusion of preform and outer jacket) were subsequently extended to fabricate the exposed-core fibres modelled in [P3], realised in [P7], and used for distributed sensing measurements in [P8]. In addition, the surface-induced small-core loss shown in Fig. 7 of this paper was used for the theoretical modelling in [P4], and the experimental confirmation of confinement loss (Fig. 5 of this paper) adds confidence to the confinement loss theory developed in Appendix C and used in [P4]. Similar fibres to those fabricated in this paper were also used for corrosion sensing experiments presented in Chapter 5 and the paper in Appendix D.

Discussion and Conclusions

In this paper fabrication of suspended optical nanowires with core diameters in the range of 420-720 nm was demonstrated. To the best of our knowledge this is the smallest core size reported to date for an optical fibre without a post-processing tapering step, and this approach also produces practical outer diameters of > 100 μm and long fibre lengths. This range of core diameters is sufficiently small to achieve high power fraction in the evanescent field and thus high sensitivity in a sensor device. Flexibility in the geometry of extruded preforms and jacket tubes as well as improved extrusion and fibre drawing allowed such small core sizes to be achieved. The optical loss properties were examined, and found to be consistent with previously fabricated optical nanowires. In addition, the

experimentally measured confinement loss was found to be consistent with a simplified confinement loss model.

The next challenge is to determine how far the extrusion approach can be extended towards smaller core sizes, and [P4] examined theoretically if this is indeed necessary or useful. The main difficulty is increasing the effective size of the air cladding to avoid confinement loss, which could be achieved through positive pressurisation of the holes during the fibre drawing, as has been achieved elsewhere using tellurite glass [91]. Other issues concern the fragility of such small cores and also their susceptibility to environmental degradation, particularly water [177]. For example, silane coatings [123], or other coatings may be necessary to protect these fibres from water degradation. Other issues concern the ability to couple light into these fibres and how stable this coupling is. Clearly free space optics will have issues with both reaching the dimensions required due to the diffraction limit, and also stability. Splicing conventional fibre onto suspended optical nanowires would be the preferable option, but is also a difficult task due to the fragility of the small core and struts, and the mode size mismatch.

4.2.2 Statement of Contribution

Conceptualisation

Using the extrusion technique for the fabrication of suspended optical nanowires was conceptualised by Tanya Monro and Heike Ebendorff-Heidepriem.

Realisation

Heike Ebendorff-Heidepriem designed preform die designs, assisted with other aspects of the fabrication process, and researched and collated information for Figs. 5 and 7. Stephen Warren-Smith was involved in conducting extrusion experiments, performed loss measurements, and performed numerical modelling for confinement loss (Figs. 5 and 6) and data in Fig. 4. Tanya Monro was involved in useful discussions for fibre fabrication and numerical modelling.

Documentation

This paper was primarily written by Heike Ebendorff-Heidepriem. Technical details on numerical modelling and the loss measurements were written by Stephen Warren-Smith. Editing was performed by all authors.

Declaration and Permission

I declare that the above statement of contribution is accurate and I give permission for this publication to be included in this thesis.

Heike Ebendorff-Heidepriem Stephen C. Warren-Smith

Tanya M. Monro

Suspended nanowires: Fabrication, design and characterization of fibers with nanoscale cores

Heike Ebendorff-Heidepriem, Stephen C. Warren-Smith, and Tanya M. Monro

Centre of Expertise in Photonics, School of Chemistry & Physics, University of Adelaide, SA 5005, Australia
heike.ebendorff@adelaide.edu.au

Abstract: We report a new approach for the fabrication of nanowires: the direct drawing of optical fibers with air suspended nanoscale cores. The fibers were made from lead silicate glass using the extrusion technique for preform and jacket tube fabrication. Fibers with core diameters in the range of 420-720 nm and practical outer diameters of 110-200 µm were produced, the smallest core sizes produced to date within optical fibers without tapering. We explored the impact of the core size on the effective mode area and propagation loss of these suspended nanowires relative to circular nanowires reported to date. As for circular nanowires, the propagation loss of these suspended nanowires is dominated by surface roughness induced scattering.

OCIS codes**:** (060.2270) Fiber characterization; (060.2280) Fiber design and fabrication.

References and links

1. T. M. Monro, W. Belardi, K. Furusawa, J. C. Baggett, N. G. R. Broderick, and D. J. Richardson, "Sensing with microstructured optical fibers," Meas. Sci. Technol. **12**, 854-858 (2001).
2. J. Lou, L. Tong, and Z. Ye, "Modeling of silica nanowires for optical sensing," Opt. Express **13**, 2135-2140 (2005), http://www.opticsinfobase.org/abstract.cfm?URI=oe-13-6-2135.
3. K. J. Rowland, S. Afshar V., and T. M. Monro, "Nonlinearity enhancement of filled microstructured fibers operating in the nanowire regime," in *Proc. Optical Fiber Communication Conference* (Anaheim, 2006), paper OTuH3.
4. M. A. Foster, A. C. Turner, M. Lipson, and A. L. Gaeta, "Nonlinear optics in photonic nanowires," Opt. Express **16**, 1300-1320 (2008), http://www.opticsinfobase.org/abstract.cfm?URI=oe-16-2-1300.
5. Y. Ruan, E. P. Schartner, H. Ebendorff-Heidepriem, P. Hoffmann, and T. M. Monro, "Detection of quantum-dot labeled proteins using soft glass microstructured optical fibers," Opt. Express **15**, 17819-17826 (2007), http://www.opticsinfobase.org/abstract.cfm?URI=oe-15-26-17819.
6. S. Afshar V., S. C. Warren-Smith, and T. M. Monro, "Enhancement of fluorescence-based sensing using microstructured optical fibers," Opt. Express **15**, 17891-17901 (2007), http://www.opticsinfobase.org/abstract.cfm?URI=oe-15-26-17891.
7. L. Dong, B. K. Thomas, and L. Fu, "Highly nonlinear silica suspended core fibers," Opt. Express **16**, 16423-16430 (2008), http://www.opticsinfobase.org/oe/abstract.cfm?URI=oe-16-21-16423.
8. T. G. Euser, J. S. Y. Chen, M. Scharrer, and P. St. J. Russell, "Quantitative broadband chemical sensing in air-suspended solid-core fibers," J. Appl. Phys. **103**, 103108 (2008).
9. A. S. Webb, F. Poletti, D. J. Richardson, and J. K. Sahu, "Suspended core holey fiber for evanescent-field sensing," Opt. Eng. **46**, 010503, (2007).
10. J. Y. Y. Leong, P. Petropoulos, J. H. V. Price, H. Ebendorff-Heidepriem, S. Asimakis, R. C. Moore, K. E. Frampton, V. Finazzi, X. Feng, T. M. Monro, and D. J. Richardson, "High-nonlinearity dispersion-shifted lead-silicate holey fibers for efficient 1-µm pumped supercontinuum generation," J. Lightwave Technol. **24**, 183-190 (2006).
11. D.I. Yeon, E. C. Magi, M. R. E. Lamont, M. A. F. Roelens, L. Fu, and B J. Eggleton, "Low-energy threshold supercontinuum generated in highly nonlinear As_2Se_3 chalcogenide submicron tapers," in *Proc. CLEO/QELS Conference* (San Jose, 2008), paper CMDD6.
12. E. C. Magi, L. B. Fu, H. C. Nguyen, M. R. E. Lamont, D. I. Yeom, and B. J. Eggleton, "Enhanced Kerr nonlinearity in sub-wavelength diameter As_2Se_3 chalcogenide fiber tapers," Opt. Express **15**, 10324-10329 (2007), http://www.opticsinfobase.org/abstract.cfm?URI=oe-15-16-10324.
13. V. Finazzi, *A theoretical study into the fundamental design limits of devices based on one- and two-dimensional structured fibres* (PhD thesis, University of Southampton, 2003).

#104513 - $15.00 USD Received 25 Nov 2008; revised 29 Jan 2009; accepted 1 Feb 2009; published 9 Feb 2009

14. G. Brambilla, V. Finazzi, and D. J. Richardson, "Ultra-low-loss optical fiber nanotapers," Opt. Express **12**, 2258-2263 (2004), http://www.opticsinfobase.org/abstract.cfm?URI=oe-12-10-2258.
15. G. Brambilla, F. Koizumi, X. Feng, and D. J. Richardson, "Compound-glass optical nanowires," Electron. Lett. **41**, 400-402 (2006).
16. G. Brambilla, F. Xu, and X. Feng, "Fabrication of optical fibre nanowires and their optical and mechanical characterisation," Electron. Lett. **42**, 517-519 (2006).
17. L. Tong, R. R. Gattass, J. B. Ashcom, S. He, J. Lou, M. Shen, I. Maxwell, and E. Mazur, "Subwavelength-diameter silica wires for low-loss optical wave guiding," Nature **426**, 816-819 92003).
18. L. Tong, L. Hu, J. Zhang, J. Qiu, Q. Yang, J. Lou, Y. Shen, J. He, and Z. Ye, "Photonic nanowires directly drawn from bulk glasses," Opt. Express **14**, 82-87 (2006), http://www.opticsinfobase.org/abstract.cfm?URI=oe-14-1-82.
19. L. Tong, J. Lou, R. R. Gattass, S. He, X. Chen, L. Liu, and E. Mazur, "Assembly of silica nanowires on silica aerogels for microphotonic devices," Nanoletters **2**, 259-262 (2005).
20. G. Vienne, Y. Li, and L. Tong, "Microfiber knot resonator in polymer matrix (Invited)," IEICE Trans. Electron. **E90-C**, 415-421 (2007).
21. F. Xu, P. Horak, and G. Brambilla, "Optical microfiber coil resonator refractometric sensor," Opt. Express 15, 7888-7893 (2007), http://www.opticsinfobase.org/oe/abstract.cfm?URI=oe-15-12-7888.
22. N. A. Wolchover, F. Luan, A. K. George, J. C. Knight, and F. G. Omenetto, "High nonlinearity glass photonic crystal nanowires," Opt. Express **15**, 829-833 (2007), http://www.opticsinfobase.org/abstract.cfm?URI=oe-15-3-829.
23. Y. K. Lize, E. C. Magi, V. G. Ta'eed, J. A. Bolger, P. Steinvurzel, and B. J. Eggleton, "Microstructured optical fiber photonic wires with subwavelength core diameter," Opt. Express **12**, 3209-3217 (2004), http://www.opticsinfobase.org/abstract.cfm?URI=oe-12-14-3209.
24. X. Feng, T. M. Monro, V. Finazzi, R. C. Moore, K. Frampton, P. Petropoulos, and D. J. Richardson "Extruded single-mode, high-nonlinearity tellurite glass holey fiber," Electron. Lett. **41**, 835-837 (2005).
25. H. Ebendorff-Heidepriem, P. Petropoulos, S. Asimakis, V. Finazzi, R. C. Moore, K. Frampton, D. J. Richardson, and T. M. Monro, "Bismuth glass holey fibers with high nonlinearity," Opt. Express **12**, 5082-5087 (2004), http://www.opticsinfobase.org/abstract.cfm?URI=oe-12-21-5082.
26. H. Ebendorff-Heidepriem, and T. M. Monro, "Extrusion of complex preforms for microstructured optical fibers," Opt. Express **15**, 15086-15092 (2007), http://www.opticsinfobase.org/abstract.cfm?URI=oe-15-23-15086.
27. http://www.schott.com/advanced_optics/english/our_products/materials/optical_glass.html.
28. W. Vogel, *Glass Chemistry* (Springer-Verlag Berlin Heidelberg New York, 1994), pp. 421-423.
29. K. Okamoto, *Fundamentals of Optical Waveguides* (Academic Press, San Diego, 2000).
30. H. Ebendorff-Heidepriem, Y. Li, and T. M. Monro, "Reduced loss in extruded soft glass microstructured optical fibre," Electron. Lett. **43**, 1343-1345 (2007).
31. M. Sumetsky, "How thin can a microfiber be and still guide light?," Opt. Lett. 31, 870-872 (2006), http://www.opticsinfobase.org/ol/abstract.cfm?URI=ol-31-7-870.
32. M. Sumetsky, "How thin can a microfiber be and still guide light? Errata," Opt. Lett. 31, 3577-3578 (2006), http://www.opticsinfobase.org/ol/abstract.cfm?URI=ol-31-24-3577.
33. P. J. Roberts, F. Couny, H. Sabert, B. J. Mangan, T. A. Birks, J. C. Knight, and P. St. J. Russell, "Loss in solid-core photonic crystal fibers due to interface roughness scattering," Opt. Express **13**, 7779-7793 (2005), http://www.opticsinfobase.org/abstract.cfm?URI=oe-13-20-7779.
34. G. Zhai, and L. Tong, "Roughness-induced radiation losses in optical micro or nanofibers," Opt. Express **15**, 13805-13816 (2005), http://www.opticsinfobase.org/abstract.cfm?URI=oe-15-21-13805.
35. P. J. Roberts, F. Couny, H. Sabert, B. J. Mangan, D. P. Williams, L. Farr, M. W. Mason, A. Thomlinson, T. A. Birks, J. C. Knight, and P. St. J. Russell, "Ultimate low loss of hollow-core photonic crystal fibers," Opt. Express **13**, 236-244, (2005), http://www.opticsinfobase.org/abstract.cfm?URI=oe-13-1-236.
36. P. K. Gupta, D. Inniss, C. R. Kurkjian, and Q. Zhong, "Nanoscale roughness of oxide glass surfaces," J. Non-Cryst. Solids **262**, 200-206 (2000).
37. E. Radlein, and G. H. Frischat, "Atomic force microscopy as a tool to correlate nanostructure to properties of glasses," J. Non-Cryst. Solids **222**, 69-82 (1997)
38. P. W. France, *Fluoride glass optical fibres* (CRC Press, 1990).
39. N. P. Bansal, and R. H. Doremus, J. Am. Ceram. Soc. **67**, C197-C197 (1984).

1. Introduction

Nanowires, also referred to as photonic wires, microfibers, nanofibers or nanotapers, are fiber waveguides with subwavelength core diameters (typically <1 μm). Such small core diameters offer access to extreme fiber properties such as tight mode confinement and large power

#104513 - $15.00 USD Received 25 Nov 2008; revised 29 Jan 2009; accepted 1 Feb 2009; published 9 Feb 2009

fraction in the evanescent field, which opens up new opportunities in nonlinearity and sensing applications, respectively [1-12].

Moving to smaller core sizes, towards the nanowire regime, the guided mode becomes increasingly confined, which decreases the effective mode area and thus increases the effective nonlinearity of the waveguide. For some value of the core diameter (d_{min}), minimum mode area and maximum nonlinearity is found. The value of both d_{min} and the minimum mode area decreases with increasing refractive index (n_0) of the host dielectric material and decreasing wavelength. For air-clad nanowires, d_{min} is in the range 500-1000 nm [13] for refractive indices of 1.5-2.8 at a wavelength of 1550 nm. The record fiber nonlinearity reported to date (1860 W^{-1} km^{-1} at 1550 nm) was demonstrated in a high-index lead silicate glass (Schott glass SF57, n_0=1.88) microstructured fiber with suspended core diameter of 950 nm [10]. This core size is larger than the value of d_{min} (700 nm) for this glass, however it is the closest fiber core size (relative to d_{min}) reported to date. Further nonlinearity enhancement was reported using very high index As_2Se_3 chalcogenide glass (n_0=2.8). In this work, fiber tapering was used to reduce the core diameter to 950 nm. Although this core size is significantly larger than d_{min} = 600 nm for this very high index glass, the tight mode confinement in the fiber taper combined with the high nonlinear index (n_2) of the glass still resulted in an extreme nonlinearity value of 93,000 W^{-1} km^{-1} [11]. Modeling results reported in Ref. [12] indicate that fibers or tapers with a core size of d_{min} made from this material should yield a nonlinearity of almost twice this value (~164,000 W^{-1} km^{-1}).

For core sizes that are smaller than d_{min}, the light guided by the fiber becomes increasingly located outside of the fiber core. This regime is of particular interest for sensing applications, where this light becomes accessible for light-matter interactions and thus allows the development of highly sensitive sensors [1,2,8].

The majority of glass nanowires that have been investigated to date are fabricated via the tapering of fibers of standard outer diameter (>100 μm) to subwavelength diameters (50-900 nm) [11,12,14-17]. Soft glass nanowires have also been made by direct-draw techniques [18]. For these nanowires, the whole fiber cross section with nanoscale diameter acts as the fiber core, and we refer to these structures as free-standing nanowires. Such nanowires are fragile, which makes them difficult to handle, and fully exposed to the environment, which can lead to contamination and degradation [16]. To prevent these issues, free-standing nanowires have been supported by embedding them in a porous substance such as an aerogel [19] or in a low-index polymer [20,21]. The disadvantage of this approach is that the arrangement is no longer flexible, which limits the ability to act as a sensor. Another type of nanowire can be produced by tapering a microstructured fiber [22,23]. This approach uses tapering to reduce the size of the fiber core to the subwavelength scale. This core remains supported within the air/glass structure of the cladding, and is thus protected from the environment by the solid outer cladding. Note that the length of the nanowires and microstructured fiber tapers demonstrated to date using these approaches is restricted to a few tens of centimeters due to handling and fabrication constraints, respectively.

Here we present an alternative means of fabricating nanowires; namely the direct drawing of long length of fibers with subwavelength core sizes and practical outer diameter (>100 μm). This approach avoids the need for any postprocessing tapering step, which limits the length of the nanowire. Our fiber structure is based on a high air filling fraction microstructured fiber with a small core suspended via three thin struts [3]. For nanoscale core dimensions, the core acts as a suspended nanowire. Similarly to microstructured fiber tapers, the suspended nanowire in a suspended core fiber is supported within and protected by the solid outer cladding.

To date, suspended core fibers have been made from a range of glasses, including silica [7,8,9], lead silicate [10], tellurite [24], and bismuth [25] glasses. However, the smallest suspended core diameter that has been reported in the literature to date is approximately 800 nm [8-10]. Here we demonstrate suspended core fibers with up to two times smaller core

#104513 - $15.00 USD Received 25 Nov 2008; revised 29 Jan 2009; accepted 1 Feb 2009; published 9 Feb 2009

diameters (420-720 nm), thus approaching for the first time truly nanoscale dimensions. The fibers were fabricated using the extrusion technique for preform and jacket tube fabrication. Recently, we extended the extrusion technique in terms of die design and process control [26]. This allowed us to enhance the flexibility in the selection of the preform and jacket tube geometries that can be achieved and made the fabrication of the nanoscale core fibers possible. In addition, improved drawing conditions played a role. In Section 2 of this paper, we describe the impact of the fabrication conditions on the dimensions of the transverse fiber features. In Sections 3 and 4, we compare the mode area and propagation loss of our suspended nanowires with free-standing nanowires and discuss the core size dependence.

2. Fiber fabrication and dimensions

For the fabrication of the suspended nanowires described here, we used commercial F2 lead silicate glass (Schott Glass Co). Of the commercially available soft glasses, F2 glass is attractive because it combines high transmission in the visible spectral range with a low softening temperature (592 ^{o}C) [27]. The high transmission in the visible is of particular advantage for (bio)chemical sensing applications since it allows for the efficient excitation of a range of fluorophores (for example quantum dot labeled proteins at 532 nm [5]). The low softening point allows use of glass extrusion through stainless steel dies for preform and jacket tube fabrication [26]. The refractive index of F2 glass (n_0=1.62 at 588 nm) is higher than that of silica glass (n_0=1.46 at 588 nm). Note that for nanoscale core sizes, the higher index of F2 glass relative to silica enables higher sensitivity due to enhanced fluorescence capture fraction [6], as well as offering tighter mode confinement and higher n_2 for nonlinear applications.

The fibers were made using a three step process. Firstly, the structured preform and jacket tube were manufactured from billets of glass using the extrusion technique. The outer diameter of these extruded items was in the range 10-15 mm. In the second step, the preform was reduced in size to a "cane" of ~1 mm outer diameter using a fiber drawing tower. Then the cane was then inserted into the jacket tube. The inner diameter of the tube is selected to provide a close fit to the cane diameter. This assembly was finally drawn down to form the final fiber. Careful adjustment of the drawing speed allowed accurate control of the outer diameter of the fiber (within ± 1 μm in 110 – 200 μm), and thus to a similar relative error in size of the core itself. From a single cane-in-tube assembly of the dimensions used in this work, we produced more than 100 m length of fiber, which was wound on a spool in several bands of uniform outer diameters in the range of 100-200 μm. Each band corresponds to a different choice of fiber drawing parameters.

The dimensions of the preform, cane and fiber features (outer and core diameter, strut length and thickness) were measured using cross-sectional images, which were taken using a digital camera for the preforms, an optical microscope for the canes and a scanning electron microscope (SEM) for the fibers. The results are listed in Table 1. As for previous suspended core fibers, the measured core diameter (d_m) is defined as the diameter of the largest circle that can be inscribed in the core region (Fig. 1) [8,10]. However the area of this circle is smaller than the area of the triangular core region in the fiber. Thus, to enable some comparison of suspended nanowires having triangular core region with free-standing nanowires having circular core region for a given core diameter, we also define the *effective* core diameter (d_{eff}) as the diameter of a circle whose area is equal to a triangle that fits wholly within the core (i.e. $d_{eff} = 1.286 \times d_m$), as shown in Fig. 1.

To achieve fibers with nanoscale core sizes and practical outer diameters, the jacket tube and the preform need to have large ratio of outer diameter (OD) to inner diameter (ID) and core diameter (d_m), respectively. In addition, a large ratio of strut length (s) to core diameter (d_m) in the fiber is needed to ensure that the struts have sufficient length (i.e. that the air holes are sufficiently large) to prevent leakage of the guided mode into the cladding (i.e. high confinement loss for the fundamental mode).

#104513 - $15.00 USD Received 25 Nov 2008; revised 29 Jan 2009; accepted 1 Feb 2009; published 9 Feb 2009

Table 1: Dimensions of the cross sectional features of preforms, canes and fibers made from F2 glass.

preform no.	preform strut/core	cane strut/core	tube OD ID (mm)	fiber no.	fiber strut/core	fiber core d_m d_{eff} (μm)	fiber OD (μm)
#1	1.6	1.4	10 1.2	#1	1.5	1.6 2.1	125
#2	3.1	2.1	10 1.2	#2a	2.7 2.8	1.6 2.1 1.4 1.8	150 125
		3.1	15 0.8	#2b	3.7 3.9 4.1 3.1	0.72 0.92 0.59 0.76 0.48 0.61 0.42 0.54	200 160 125 110

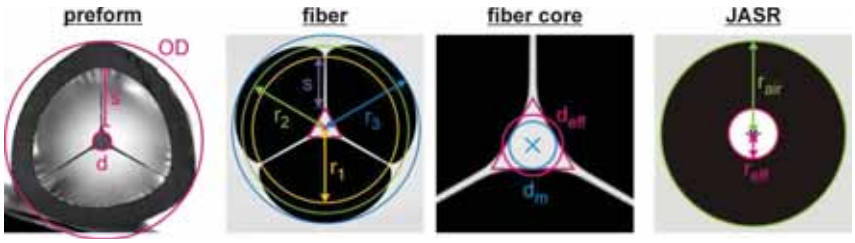

Fig. 1. Cross sectional images of preform and fiber, cross sectional structure of JASR configuration and definition of several cross sectional features.

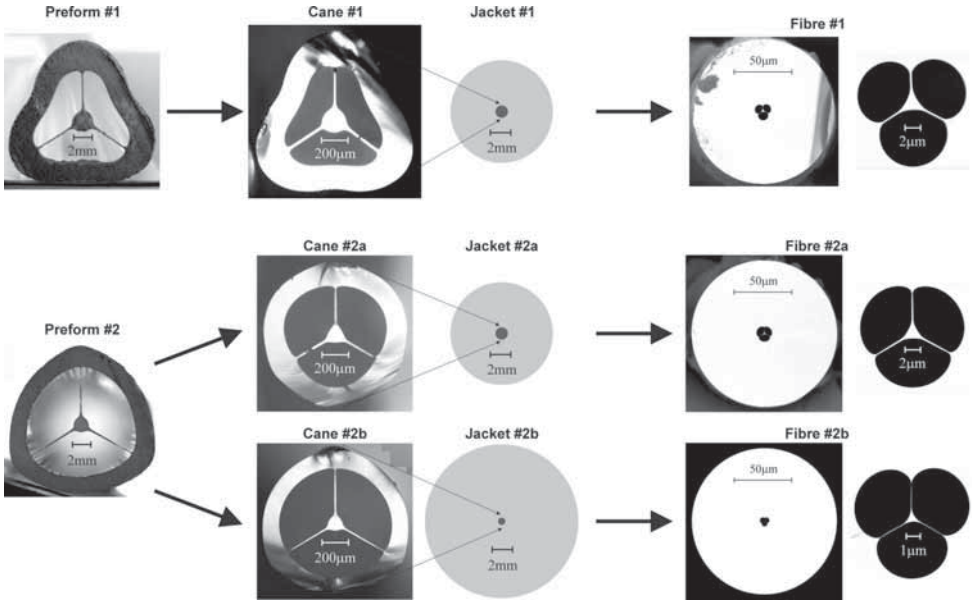

Fig. 2. Cross sectional images of preforms, canes and fibers made using F2 glass. The outer diameter of all three fibers is 125 μm. The measured core diameter for fibers #1, #2a and #2b is 1.6 μm, 1.4 μm and 0.48 μm, respectively.

#104513 - $15.00 USD Received 25 Nov 2008; revised 29 Jan 2009; accepted 1 Feb 2009; published 9 Feb 2009

For the preform extrusion, we initially used an extrusion die design that was successfully employed to fabricate suspended core fibers with core diameters of $d_m \geq 1$ μm with negligible confinement loss using high-index heavy metal oxide glasses such as bismuth and SF57 lead silicate glasses [10,25]. When using low-index F2 glass, which has a relatively small lead oxide content, the same die design resulted in a larger core size and shorter struts (i.e. smaller s/d_m ratio of 1.6) compared with a bismuth glass preform ($s/d_m = 2.1$) due to partial hole closure. This undesired structural deformation is attributed to the increase of surface tension with decreasing heavy metal content in glass [28]. For the fiber fabrication, a jacket tube OD/ID ratio of ~8 was used. The s/d_m ratio of the final fiber (#1) was 1.5 (Fig. 1, Table 1), which is too small to achieve core sizes <1 μm and low confinement loss.

To counteract this detrimental structure deformation, we modified the extrusion die design. In the new die design, the strut length was doubled while the core size and strut thickness was maintained. In a first fiber drawing trial using a piece of preform #2, we used the same cane outer diameter and tube dimensions as for the fiber #1 (Table 1). Partial hole closure occurred during the drawing step, decreasing the s/d_m ratio of the cane relative to the preform (Table 1, Fig. 1). The cane-in-jacket assembly was drawn down to a fiber (#2a) with core diameters of $d_m = 1.4$ μm and 1.6 μm and OD = 125 μm and 150 μm, respectively.

To reduce the core size in the next fiber (#2b) that was made using another piece of preform #2, we considerably increased the OD/ID ratio of the next jacket tube. Improved drawing conditions allowed the preservation of the s/d_m ratio of the preform in the cane ($s/d_m = 3.1$). Both the large OD/d_m ratio for this cane and the large OD/ID ratio of the corresponding jacket tube resulted in a fiber with core diameters as small as $d_m = 420$-720 nm, whereas the fiber ODs were in the range of 110-200 μm (Table 1, Figs. 1 and 3). This is a reduction of core size by a factor of 2 compared with the smallest previously reported suspended core fibers [8-10]. Indeed, to the best of our knowledge, these results represent the smallest core optical fibers that have ever been reported for any geometry or material. The thickness of the struts was measured to be in the range of 50-80 nm, which is close to the measurement error of ±10nm for the SEM. In order to obtain a range of core sizes, we have drawn from a single cane-in-tube assembly four fiber bands of uniform OD. Each fiber band has a length of 20-60 m. Note that it is straightforward to scale to larger fiber lengths via drawing a single fiber band from a cane-in-tube assembly and/or using longer cane and tube length.

To determine how the fiber structure and the fabrication processes contribute to the propagation loss of these suspended core fibers, we also fabricated a bare (unstructured) fiber from the same glass material using an extruded rod of 10 mm OD.

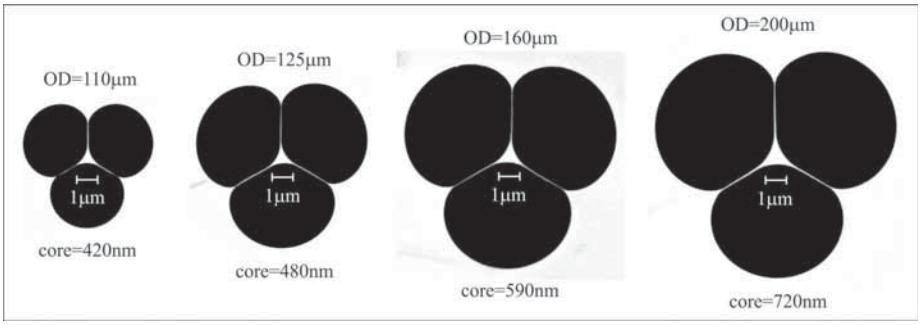

Fig. 3. Cross sectional images of the four fiber bands of fiber #2b. The values for the core size refer to the measured core diameter.

3. Core diameter and mode area

As seen in Section 2, the core shape of a suspended nanowire is triangular and thus comparison of the fiber properties with a (circular) free-standing nanowire is not immediately

#104513 - $15.00 USD Received 25 Nov 2008; revised 29 Jan 2009; accepted 1 Feb 2009; published 9 Feb 2009

straightforward. A simple method is to determine a definition of core diameter for which the effective modal area of the fundamental mode best matches between the suspended and free-standing nanowire geometries. Here we model both fiber geometries and show that the effective core diameter as defined in Section 2 for a suspended nanowire is sufficient for comparing the two geometries to first order. Note that to avoid confusion we have labeled the diameter of a (circular) free-standing nanowire as the effective core diameter.

The fundamental mode of the free standing nanowire was determined from a step index fiber solution [29]. The fundamental mode of the suspended nanowire was determined for an idealized geometry (selected to closely match the SEM images) using the commercially available finite element modeling package COMSOL 3.2 [6]. Three different wavelengths were considered (500 nm, 1000 nm, and 1500 nm) and the refractive index was found using the Sellmeier equation for F2 (n = 1.630, 1.603 and 1.596 at each wavelength respectively) [27]. The effective mode area was then calculated using the definition found in Ref. [6].

Unsurprisingly, both nanowire types show the same behavior: the mode area decreases as the core size and wavelength decreases [Fig. (4a)]. We also plotted the mode areas as a function of d_{eff}/λ [Fig. 4(b)], which shows that the minimum mode area occurs approximately at the same d_{eff}/λ ratio of ~0.6 for both nanowire types. The similarity of the core size scaling of the mode area of both nanowire types demonstrates that the effective core diameter is a suitable parameter for investigating the core size scaling of the optical properties of triangular nanowires with circular nanowires at a given core size.

The minimum mode area of the triangular-shaped suspended nanowires is ~20% higher than that of circular free-standing nanowires. For core diameters smaller than d_{min} (which is the core diameter at the minimum mode area), Figure 4 shows that the suspended nanowires exhibit smaller mode areas than the free-standing nanowires. In essence, this occurs because the struts help somewhat to confine the mode. These phenomena limit the maximum nonlinearity and the power fraction in the evanescent field that can be achieved with suspended nanowires. However, the considerably longer lengths of suspended nanowire that can be achieved relative to free-standing nanowires can readily counteract this limitation.

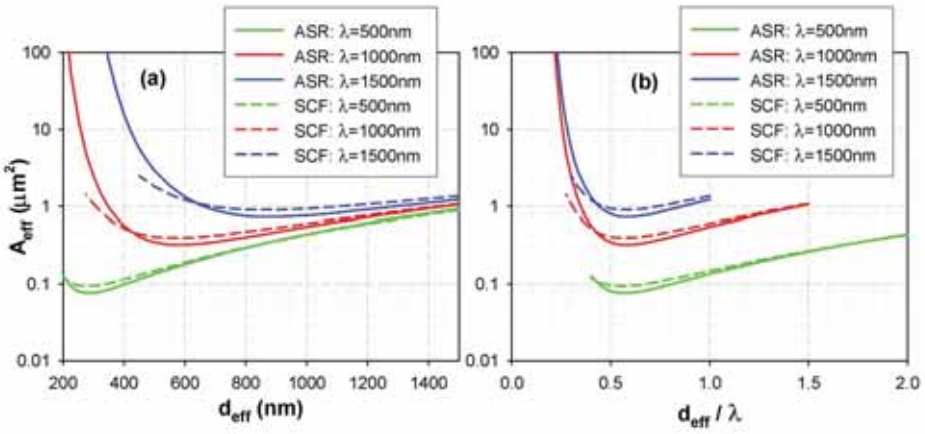

Fig. 4. Effective mode area (A_{eff}) of an air suspended rod (ASR) made of F2 glass [27] with a circular core and suspended core fiber (SCF) with a triangular core: (a) as a function of the effective core diameter, (b) as a function of the ratio of effective core diameter to wavelength.

4. Propagation loss

The propagation loss spectra of the fibers were measured using the standard cutback measurement technique. A supercontinuum white light source (KOHERAS SuperK^{TM} Compact) was collimated and then focused into the fibers using a 2.75 mm focal length lens. The output signal was launched into an optical spectrum analyzer (OSA) using free space

#104513 - $15.00 USD Received 25 Nov 2008; revised 29 Jan 2009; accepted 1 Feb 2009; published 9 Feb 2009

coupling after collimation with the use of a 40 times microscope objective. When measuring the MOF loss, the cladding (outer jacket) modes were removed with the use of Dag® graphite fluid so that only the loss of core-guided modes was measured. Both the input and output coupling was maximized at 1000 nm so that the measurements were repeatable when successive cutbacks were made. While this method of loss measurement is relatively simple, it should be noted that free space coupling into small core diameter fibers can lead to significant experimental errors due to coupling instabilities, which result from vibrations and drift of the fiber, fiber stage, optical bench, optical source, mirrors and lenses. In particular, we observed anomalous results for the fiber with core diameter d_{eff} = 610 nm due to a small spectral shift during the experiment, particularly near the optimization wavelength 1000 nm. For example, the negative loss values between 1000 nm and 1120 nm are a measurement artifact and should be discounted. This effect appeared to be minimal for fibers with core diameters of d_{eff} = 760 nm and greater.

The spectra of the bare fiber and of the suspended core fibers #2a and #2b, both made from preform #2 (Table 1) are shown in Fig. 5. The loss of the fiber #2a with 2.1 μm effective core diameter is identical to the bare fiber loss to within the measurement error. This result demonstrating negligible excess loss in the microstructured fiber is consistent with previous results for fiber #1 with similar core size and made from the same glass [30]. For fiber #2b, the loss of the fiber bands with 920 nm and 760 nm effective core diameter is only slightly larger (1.3-1.9 dB/m at 633 nm) than fiber #2a (0.7 dB/m at 633 nm). For the fiber bands with very small core sizes of 610 nm and 540 nm effective diameters, the loss in the visible spectral range is significantly higher (5-8 dB/m at 633 nm). In addition, a steep increase in loss is observed for wavelengths >900 nm for the 540 nm core and >1400 nm for the 610 nm core. Modeling, as described below, demonstrates that the steep near-infrared loss increase is due to confinement loss in the smallest core fibers.

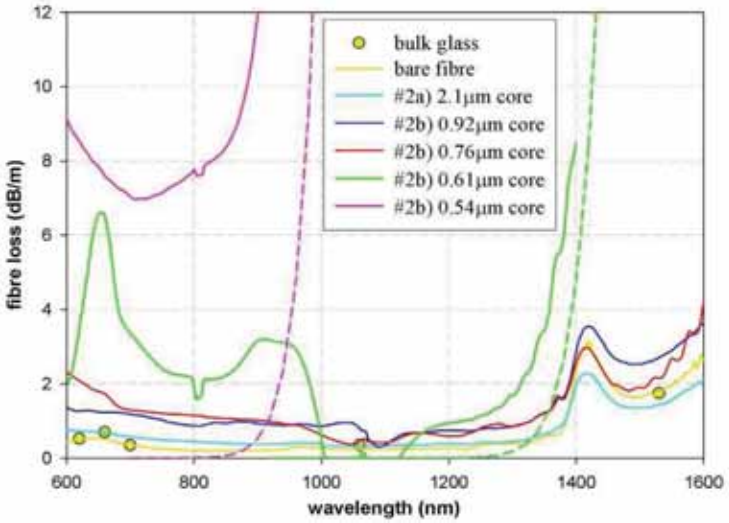

Fig. 5. Loss spectra for the bare fiber and suspended core fibers #2a and #2b made using F2 glass. The data points refer to the bulk glass loss calculated using the transmission data given in the Schott catalogue [27]. Modeled confinement loss for the two smallest core diameter fibers are shown by dashed lines.

Numerical modeling, such as finite element modelling, of the confinement loss of the suspended core fiber structure for different core sizes, strut lengths and wavelengths is computationally intensive. Thus, we considered a jacketed air suspended rod (JASR) configuration (as shown in Fig. 1) as an approximation to the true geometry. The confinement loss of the JASR was calculated by analytically determining the corresponding dispersion

#104513 - $15.00 USD Received 25 Nov 2008; revised 29 Jan 2009; accepted 1 Feb 2009; published 9 Feb 2009

equation in a method analogous to the step-index fiber [29]. First, the wave equation was solved in the core, inner cladding and outer cladding regions of the JASR by writing the electric and magnetic fields as an appropriate superposition of Bessel functions. Continuity of the tangential components of the electric and magnetic fields at the two boundaries was then imposed to create a dispersion relation by which the complex effective index was determined using *fsolve* from Matlab's optimization toolbox. The confinement loss was then determined from the imaginary component of the effective index.

As shown in Section 2, the ASR configuration provides a useful approximation to the suspended nanowire in terms of understanding the mode area characteristics. The JASR diameter corresponds approximately to the effective core diameter of a suspended core fiber. Now, to determine which definition of air hole width of the suspended nanowire best corresponds to the outer radius of the JASR (r_{air}, Fig. 1), we calculated the confinement loss for the fundamental mode of JASRs using 3 different parameters (r_1, r_2, r_3) for the air hole width (Fig. 1). The shortest width (r_1) is approximately the sum of measured core diameter and strut length. The largest air hole width is r_3 and the average of both is the medium width r_2. For the 610 nm core fiber, the best agreement between measured fiber loss and calculated JASR confinement loss is observed for the medium air hole width (r_2). For the 540 nm core fiber, the shortest air hole width (r_3) fits best the measured loss (Fig. 5). This subtle difference can be attributed to both small differences in hole shape for the two fibers (Fig. 3) and that this method is an approximation based on a circular structure without struts.

To gain more insight in the impact of strut length (i.e. air hole size) on the confinement loss, we modeled the confinement loss of the fundamental mode for a range of JASRs with different core diameters and air widths. The minimum bulk loss of the F2 glass used for the fabrication of our nanowires is 0.3 dB/m. Hence we are willing to consider values of the confinement loss in the suspended core fibers of less than 0.1 dB/m as negligible.

For different core sizes and wavelengths, we calculated the minimum ratio of the air cladding radius to effective core radius (r_{air}/r_{eff}, Fig. 1) that is required to ensure that the confinement loss is < 0.1 dB/m. The r_{air}/r_{eff} ratio increases as the core size decreases and the wavelength increases [Fig. 6(a)]. Thus, we also plotted all ratios as a function of the ratio d_{eff}/λ. Using this approach, we find that all data from Fig. 6(a) fits closely onto a single curve [Fig. 6(b)], with only slight deviations due to the difference in glass refractive index (hence modal properties) for different wavelengths. The solid red line in Fig. 6(b) shows the overlap of each of the wavelengths. This line demonstrates what minimum r_{air}/r_{eff} ratio is necessary to achieve negligible confinement loss of < 0.1 dB/m for any given d_{eff}/λ ratio. Towards small d_{eff}/λ (<0.3), the r_{air}/r_{eff} ratio needs to be enhanced drastically to ensure low confinement loss. While this general trend is unsurprising, this information is an important guide for fibre design and fabrication.

Using r_2 from Fig. 1 for the air cladding radius of fiber #2b with nanoscale core sizes, the r_{air}/r_{eff} ratio of this fiber is in the range of 9-11. This corresponds to a minimum d_{eff}/λ ratio of ~0.5 that can be achieved along with low confinement loss of <0.1dB/m [Fig. 6(b)] simply by scaling this cross-sectional structure during the fiber drawing process. Note that this lower limit of d_{eff}/λ~0.5 is somewhat smaller than the d_{eff}/λ~0.6 predicted to achieve the minimum mode area. We anticipate that it should be possible to achieve d_{eff}/λ ~ 0.4 via increasing the r_{air}/r_{eff} ratio to ~20 using further die design modification and pressurization of the preform holes during cane drawing.

At the minimum mode area, the fiber nonlinearity is highest. For core sizes smaller than that corresponding to the minimum mode area, the mode spreads out of the core. Hence with these fiber designs, maximum nonlinearity as well as high power fraction in the evanescent field can be achieved with low confinement loss. The mode confinement depends on the refractive index of the glass, which will affect the choice of the most suitable values of d_{eff}/λ (to achieve minimum mode area) and r_{air}/r_{core} (for low confinement loss). Note that when filling the fibers with materials either for (bio)chemical sensing [5,8] or nonlinearity

#104513 - $15.00 USD Received 25 Nov 2008; revised 29 Jan 2009; accepted 1 Feb 2009; published 9 Feb 2009

enhancement [3], the refractive index of the matter in the holes will have an impact on the guidance properties of the fiber, reducing the effective index contrast between core and cladding, and thus increasing the confinement loss, and necessitating the use of longer struts.

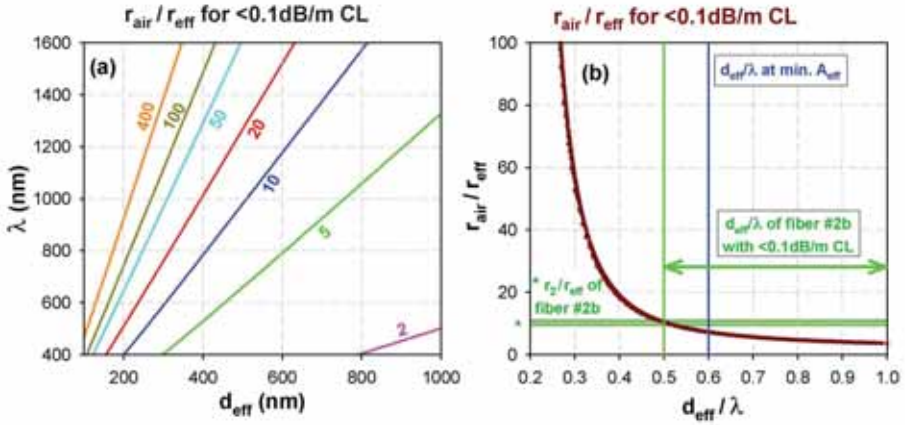

Fig. 6. (a) Contour plot of the JASR r_{air}/r_{eff} ratios for which the confinement loss is <0.1 dB/m as a function of effective core diameter and wavelength. (b) JASR r_{air}/r_{eff} ratios for which the confinement loss is <0.1 dB/m as a function of d_{eff}/λ within the wavelength range of 500-1500 nm.

In Fig. 7, the measured loss of our fibers is compared with loss results reported for free-standing nanowires at 633 nm and 1550 nm wavelength [14,16-18]. For silica glass, the bulk glass loss (<0.001 dB/m) is negligible relative to the nanowire losses (>0.1dB/m at 633 nm and 1550 nm). In contrast, for our fibers, the bulk glass loss is in the same order of magnitude compared with the fiber loss in the wavelength range of negligible confinement loss. Thus to understand the loss due to the small core size in excess over the bulk loss, we subtracted the bulk glass loss from the measured loss of our suspended core fibers. For the silicate nanowires reported by Tong et al. [18], the loss of the nanowires (≥15 dB/m at 633 nm) is considerably larger than the bulk glass loss of our silicate glass F2, which has a similar refractive index than the silicate glass used by Tong. Therefore we neglected the bulk glass loss for the silicate nanowires reported by Tong [18].

Sumetsky [31,32] predicted that propagation of light through a nanowire becomes extremely lossy if the nanowire diameter is smaller than a threshold diameter. For silica at 1550 nm wavelength and nanowire length of 10 km, the threshold diameter is «200 nm, which is below the nanowire diameter fabricated to date. The theoretical predictions of radiative losses for both long and short nanowires made in Refs [31,32] are more than an order of magnitude lower than the experimentally measured excess loss values shown in Fig. 7. This implies that the loss of these nanowires is not dominated by radiation loss, but rather by scattering of the guided modes to non-guided modes (e.g. surface modes, cladding modes) at the air/glass interface due to the inherent roughness of the glass surface [33,34]. Such roughness arises from thermally excited surface capillary waves, which become frozen-in during cooling of a glass melt (e.g. during fiber drawing or tapering) at the glass transition temperature [35]. The roughness forming process is dictated by equilibrium thermodynamics, so that it cannot be substantially reduced by technological improvements. Surface roughness measurements using atomic force microscopy demonstrated that nanowires, hollow-core fibers and fire-polished glass samples exhibit root-mean-square surface roughness amplitudes of 0.1-0.5 nm [17,35-37]. Modeling of the scattering loss due to inherent surface roughness demonstrated that it is proportional to the glass transition temperature (Tg) and the inverse of the surface tension (σ) [35]. Furthermore, the scattering loss becomes larger as the refractive index of the glass increases [34]. Accordingly, lowest scattering loss will be found for glasses

#104513 - $15.00 USD Received 25 Nov 2008; revised 29 Jan 2009; accepted 1 Feb 2009; published 9 Feb 2009

with low Tg, low n and high σ. However, these three glass properties cannot be tailored independently. For example, in heavy metal oxide glasses, Tg and σ decreases, whereas n increases with increasing heavy metal content [28]. As another example, comparing fluoride glass with silica, Tg and σ of fluoride glass is considerably lower whereas n is similar for both glass types [38,39].

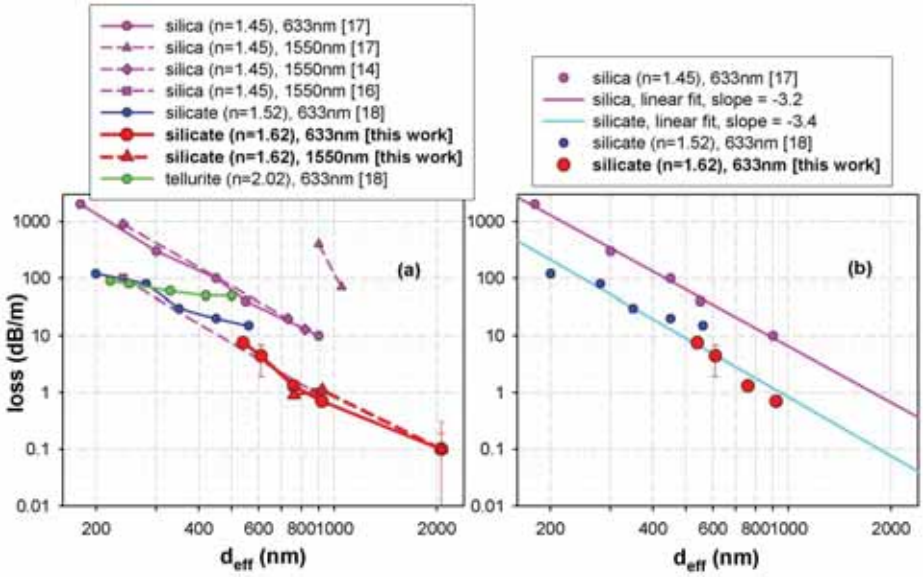

Fig. 7. (a) Loss at 633 nm and 1550 nm for a range of nanowires (free-standing and suspended) having different size and made using different glasses. (b) Selected data sets for linear regression of the logarithm of the loss as a function of the logarithm of the effective core diameter.

In addition to the inherent surface roughness, surface imperfections such as contamination and cracks also cause scattering loss. Ultrasonic cleaning of extruded performs can be used to reduce the loss of suspended core fibers with 1-2 μm effective core diameter (made from SF57 lead silicate glass) from 9 dB/m to 2 dB/m [10] due to removal of surface contamination. The loss of silica nanowires for a given core diameter reported to date in different papers varies over more than one order of magnitude [Fig. 7(a)], which demonstrates that in many cases there are other causes for loss than the inherent surface roughness. Furthermore, it was found that the nanowire loss increases with time due to formation of surface cracks as a result of exposure to moisture [16]. One attractive feature of our approach is that the nanowire-type core is enclosed within the fiber structure, providing opportunities for protecting the core surface from moisture via sealing of the fiber ends.

The loss of our suspended nanowires is very similar to the lowest loss nanowires reported to date (Fig. 7). This demonstrates the viability of our approach to fabricate nanowires with low surface roughness and contamination.

The loss of small core microstructured fibers was found to increase as the core size decreases, which has been attributed to the increased field strength at the hole interfaces leading to larger roughness scattering loss component [10,25,33]. This result is consistent with the core size scaling of free-standing nanowires [14,16-18] and our suspended nanowires (Fig. 7). To determine quantitatively the core size dependence of the scattering loss of nanowires, we used the loss data at 633 nm wavelength of the silica nanowires reported by Tong et al. [17] and of the silicate nanowires reported in this paper and by Tong et al. [18]. Note that the two silicate glasses have similar refractive indices, which implies similar glass properties and thus surface roughness. Linear regression of the logarithm of both the loss and

#104513 - $15.00 USD Received 25 Nov 2008; revised 29 Jan 2009; accepted 1 Feb 2009; published 9 Feb 2009

the core diameter yields a slope of approximately -3, i.e. that the loss is approximately inversely proportional to the cube of the core diameter [Fig. 7(b)]. The same dependence was found for the overlap of the fundamental mode with the core surface in step-index and hollow-core fibers [35].

The wavelength dependence of the surface-roughness induced scattering loss has been investigated for nanowires [34], small-core microstructured fibers [33] and hollow-core fibers [35]. In Ref [34], which considers circular nanowires, the amplitudes of the radiation modes excited by the surface roughness, and thus the loss caused by surface roughness, is modeled via the use of an induced current model. This approach predicts that the surface-roughness induced loss increases with increasing wavelength. In Ref [33], a statistical analysis of the scattering from the surface capillary waves is used to explore the surface roughness induced loss of small-core silica microstructured fibers. This analysis demonstrates a decrease in this loss with increasing wavelength, which is consistent with experimental data for these fibers. The reason for the discrepancy between these two models is not immediately apparent. For our suspended nanowires, it has not yet been possible to accurately extract the wavelength dependence of surface roughness induced loss as a result of confinement loss and measurement limitations. Further work is needed to do this.

5. Summary and conclusions

We have demonstrated that it is possible to produce suspended core fibers with nanoscale core diameters in the range 420-720 nm, 110-200 μm outer diameter and tens of meters of fiber length of uniform diameter. To the best of our knowledge this is the smallest core size reported to date for an optical fiber without post-processing tapering step, and this approach also produces practical outer diameters of >100 μm and long fiber length. These fibers present an attractive alternative approach for the fabrication of nanowires. This range of core diameters is sufficiently small to achieve maximal mode confinement (and thus to optimize the effective fiber nonlinearity) or high power fraction in the evanescent field (and thus high sensitivity in a sensor device) for fibers made from most soft glass materials. Flexibility in the geometry of extruded preforms and jacket tubes as well as improved extrusion and fiber drawing allowed us to achieve such small core sizes. The propagation of these fibers in the visible spectral range is consistent with loss values reported for free-standing nanowires. We identified an effective core diameter for our suspended nanowires with triangular shape which allows the optical properties of suspended nanowires to be compared with circular free-standing nanowires to first order. Using the effective core diameter, both the suspended and free-standing nanowires demonstrate the same scaling of the propagation loss with the core size, which is dominated by surface roughness induced scattering loss. Our approach for nanowire fabrication can be readily adapted to other glass compositions, which will have a dramatic impact on high-nonlinearity and sensing applications. Future work will determine how far this approach can be extended towards smaller core sizes. The principal challenge here will be to increase the effective size of the air cladding to avoid confinement loss issues, in order to enable such fibers to have practical applications in next generation optical fiber sensors.

Acknowledgments

We acknowledge the DSTO (Australia) for support for the Centre of Expertise in Photonics, the Australian Research Council for funding this project (DP0880436), and Roger Moore and Mark Turner at The University of Adelaide. T. Monro acknowledges the support of an Australian Research Council Federation Fellowship.

#104513 - $15.00 USD Received 25 Nov 2008; revised 29 Jan 2009; accepted 1 Feb 2009; published 9 Feb 2009

4.3 Exposed-Core Fibres

The publication [P7] forms the basis of this section.

S. C. Warren-Smith, H. Ebendorff-Heidepriem, T. C. Foo, R. Moore, C. Davis, and T. M. Monro, "Exposed-core microstructured optical fibers for real-time fluorescence sensing," Optics Express 17, 18533-18542 (2009).

4.3.1 Publication Overview

Aim

The aim of this work was to demonstrate the fabrication of exposed-core microstructured optical fibres building on the methods previously shown in [P6] for the fabrication of suspended-core optical nanowires, and is the practical realisation of the fibres theoretically modelled in [P3]. In addition, a second aim was to demonstrate experimentally that one advantage of exposing the core is the possibility of real time sensing, in addition to distributed sensing which will be demonstrated in Sec. 4.4 [P8].

Field of Knowledge and Link Between Publications

As discussed previously, MOFs have the ability to provide high sensitivity for fluorescence and absorption based sensing. While in principle long interaction lengths can be achieved using MOFs, in practice the difficulty exists that they can only be filled from one of the distal ends and filling greater than a few meters takes an impractically long time. In this configuration they cannot be used for real-time sensing, nor can they be used for distributed sensing due to a lack of access to the core along the fibre length. These issues can, in principle, be solved by exposing the core along the length of the MOF so that the entire length of fibre can be immersed instantaneously for real-time sensing, and any section of the core can be accessed independently for distributed sensing.

The exposed-core MOF was first proposed in 2003 by Hoo *et al.* [84] and fabrication has since been demonstrated by the use of a fusion splicer and air pressure to blow open holes within an MOF [76], use of a focused ion beam [103, 104], and femtosecond laser micromachining [105, 106]. However, these methods only result in short exposed regions,

of the order of tens of microns. Cox *et al.* have shown that long lengths of exposed-core polymer fibre can be fabricated by creating an opening at the preform stage of the fibre fabrication, such as by drilling holes into the cladding of a polymer MOF preform [108]. However, polymer fibres generally exhibit high optical losses and thus are unlikely to make useful distributed sensors. Hence, it was the aim of this work to develop a method for fabricating glass exposed-core fibres. These fibres have subsequently been used for various other experiments in this thesis. Firstly, distributed sensing was demonstrated using these fibres and is reported in [P8]. Also, aluminium ion sensing experiments using these fibres are presented in Chapter 5.

Discussion and Conclusions

In this paper two methods for fabricating glass exposed-core microstructured optical fibres have been demonstrated. In the first method a soft-glass extruded preform was drawn into a fibre and then chemically etched to expose the core. This method was demonstrated with two different fibre designs and it was observed that reducing the amount of glass to be etched allowed for the fabrication of consistent lengths of exposed-core fibre. In the second method the wagon wheel preform was cut prior to caning so that the drawn fibre was exposed without requiring etching. The surface roughness and resultant optical loss due to hydrofluoric acid etching meant that directly drawing exposed-core fibre was the preferred method for fibre fabrication. The exposed-core fibres were then evaluated for fluorescence-based sensing, in order to determine the measurement response time compared to equivalent enclosed MOF sensors. The signal response time was found to be significantly faster for the exposed-core fibre. For example, lengths of fibre in the order of 20 cm could be filled in one second as opposed to 30-80 minutes.

There is great scope for continuing research in the fabrication of exposed-core MOFs. As will be discussed in Sec. 4.4.3 the most significant area of improvement is to reduce the optical loss. The best loss result for the exposed-core fibre was measured to be approximately 2 dB/m at 1000 nm, which is greater than the bulk glass loss of 0.3 dB/m. This implies that a mechanism other than glass impurities is contributing to the fibre loss such as surface debris or moisture attack, and thus cleaner and drier fabrication techniques could be used to improve the loss. Another area of improvement is to increase

the structural strength of the fibres, as they are currently quite fragile. This could be achieved through improving the structural design (such as thicker struts), using silica as the substrate material, and coating the fibre with polymer, as is done for most fibres. As will be discussed in Chapter 5, a major difficulty in optical fibre sensing is to protect the fibre from unwanted environmental and mechanical degradation while still allowing it to be sensitive to the analyte of interest.

Note that several problems were encountered during the fabrication process for these fibres, most of which concern the successful extrusion of the wedged jacket, which will be discussed in more detail in Sec. 4.3.3, following [P7].

4.3.2 Statement of Contribution

Conceptualisation

Several concepts were combined in this paper in order to achieve the final result. The exposed-core fibre design was conceptualised by Tanya Monro. Using the extrusion technique for the exposed-core fibre fabrication was conceptualised by Tanya Monro and Heike Ebendorff-Heidepriem. The etching method was conceptualised by Tanya Monro while the cut preform method was conceptualised by Stephen Warren-Smith. The concept of demonstrating time-response measurements was made by Stephen Warren-Smith and Tanya Monro.

Realisation

Pivotal to this paper was previous work involving the fabrication of suspended optical nanowires, see [P6]. Many components, both successful and failed, were required in order to achieve the fabrication of the exposed-core fibres. Stephen Warren-Smith lead this research, running most extrusions, preform preparation, assisted with fibre drawing, assisted with fibre etching, assisted with preform die design, developed the straight wedged-jacket method (see Sec. 4.3.3), organised atomic force microscopy (AFM) imaging, and performed loss and real-time sensing measurements. Heike Ebendorff-Heidepriem designed preform die designs and assisted with other aspects of the fabrication process. Tze Cheung Foo was involved with chemical support for fibre etching experiments. Roger

Moore performed the fibre drawing and assisted with preform die design. Claire Davis was involved in useful discussions for fibre fabrication. Tanya Monro was involved in useful discussions for fibre fabrication and experimental design.

Documentation

This paper was primarily written by Stephen Warren-Smith, with editing by all other authors.

Declaration and Permission

I declare that the above statement of contribution is accurate and I give permission for this publication to be included in this thesis.

Stephen C. Warren-Smith Heike Ebendorff-Heidepriem Tze Cheung Foo

Roger C. Moore Claire Davis Tanya Monro

Exposed-core microstructured optical fibers for real-time fluorescence sensing

Stephen C. Warren-Smith[1,*], Heike Ebendorff-Heidepriem[1], Tze Cheung Foo[1], Roger Moore[1], Claire Davis[2], and Tanya M. Monro[1]

[1]*Centre of Expertise in Photonics, Institute for Photonics & Advanced Sensing, The University of Adelaide, Adelaide, Australia*

[2]*Defence Science and Technology Organisation, Fishermans Bend, Victoria, Australia.*

**stephen.warrensmith@adelaide.edu.au*

Abstract: New methods for fabricating glass exposed-core microstructured optical fiber are demonstrated. The fiber designs consist of an optical fiber with a suspended micron-scale core that is partially exposed to the external environment, which is particularly useful for sensing. These fibers allow for strong evanescent field interactions with the surrounding media due to the small core size, while also providing the potential for real-time and distributed measurements. The experimental performance of an exposed-core fiber is compared to an equivalent microstructured fiber with an enclosed (protected) core in terms of their performance as evanescent field sensors. We demonstrate that the exposed-core fiber can provide a significantly improved measurement response time.

OCIS codes: (060.2370) Fiber optics sensors; (060.4005) microstructured fibers; (300.2530) fluorescence, laser-induced.

References and links

1. S. V. Afshar, Y. Ruan, S. C. Warren-Smith, and T. M. Monro, "Enhanced fluorescence sensing using microstructured optical fibers: a comparison of forward and backward collection modes," Opt. Lett. **33**(13), 1473–1475 (2008).
2. S. C. Warren-Smith, S. V. Afshar, and T. M. Monro, "Theoretical study of liquid-immersed exposed-core microstructured optical fibers for sensing," Opt. Express **16**(12), 9034–9045 (2008).
3. Y. Zhu, H. Du, and R. Bise, "Design of solid-core microstructured optical fiber with steering-wheel air cladding for optimal evanescent-field sensing," Opt. Express **14**(8), 3541–3546 (2006).
4. Y. Zhu, R. T. Bise, J. Kanka, P. Peterka, and H. Du, "Fabrication and characterization of solid-core photonic crystal fiber with steering-wheel air-cladding for strong evanescent field overlap," Opt. Commun. **281**(1), 55–60 (2008).
5. H. Ebendorff-Heidepriem, S. C. Warren-Smith, and T. M. Monro, "Suspended nanowires: fabrication, design and characterization of fibers with nanoscale cores," Opt. Express **17**(4), 2646–2657 (2009).
6. Y. Ruan, T. C. Foo, S. C. Warren-Smith, P. Hoffmann, R. C. Moore, H. Ebendorff-Heidepriem, and T. M. Monro, "Antibody immobilization within glass microstructured fibers: a route to sensitive and selective biosensors," Opt. Express **16**(22), 18514–18523 (2008).
7. S. Afshar, S. C. Warren-Smith, and T. M. Monro, "Enhancement of fluorescence-based sensing using microstructured optical fibres," Opt. Express **15**(26), 17891–17901 (2007).
8. J. B. Jensen, P. E. Hoiby, G. Emiliyanov, O. Bang, L. H. Pedersen, and A. Bjarklev, "Selective detection of antibodies in microstructured polymer optical fibers," Opt. Express **13**(15), 5883–5889 (2005).
9. J. B. Jensen, L. H. Pedersen, P. E. Hoiby, L. B. Nielsen, T. P. Hansen, J. R. Folkenberg, J. Riishede, D. Noordegraaf, K. Nielsen, A. Carlsen, and A. Bjarklev, "Photonic crystal fiber based evanescent-wave sensor for detection of biomolecules in aqueous solutions," Opt. Lett. **29**(17), 1974–1976 (2004).
10. Y. L. Hoo, W. Jin, C. Shi, H. L. Ho, D. N. Wang, and S. C. Ruan, "Design and modeling of a photonic crystal fiber gas sensor," Appl. Opt. **42**(18), 3509–3515 (2003).
11. H. Lehmann, J. Kobelke, K. Schuster, A. Schwuchow, R. Willsch, and H. Bartelt, "Microstructured index-guiding fibers with large cladding holes for evanescent field chemical sensing," Proc. SPIE **7004**, 70042R (2008).
12. C. M. B. Cordeiro, E. M.D. Santos, C. H. Brito Cruz, C. J. S. de Matos, and D. S. Ferreiira, "Lateral access to the holes of photonic crystal fibers - selective filling and sensing applications," Opt. Express **14**(18), 8403–8412 (2006).
13. C. M. B. Cordeiro, C. J. S. de Matos, E. M. dos Santos, A. Bozolan, J. S. K. Ong, T. Facincani, G. Chesini, A. R. Vaz, and C. H. Brito Cruz, "Towards practical liquid and gas sensing with photonic crystal fibres: side access to the fibre microstructure and single-mode liquid-core fibre," Meas. Sci. Technol. **18**(10), 3075–3081 (2007).

#115826 - $15.00 USD Received 17 Aug 2009; revised 17 Sep 2009; accepted 24 Sep 2009; published 29 Sep 2009

14. C. Martelli, P. Olivero, J. Canning, N. Groothoff, B. Gibson, and S. Huntington, "Micromachining structured optical fibers using focused ion beam milling," Opt. Lett. **32**(11), 1575–1577 (2007).
15. A. van Brakel, C. Grivas, M. N. Petrovich, and D. J. Richardson, "Micro-channels machined in microstructured optical fibers by femtosecond laser," Opt. Express **15**(14), 8731–8736 (2007).
16. C. J. Hensley, D. H. Broaddus, C. B. Schaffer, and A. L. Gaeta, "Photonic band-gap fiber gas cell fabricated using femtosecond micromachining," Opt. Express **15**(11), 6690–6695 (2007).
17. H. C. Nguyen, B. T. Kuhlmey, E. C. Magi, M. J. Steel, P. Domachuk, C. L. Smith, and B. J. Eggleton, "Tapered photonic crystal fibres: properties, characterisation and applications," Appl. Phys. B **81**(2-3), 377–387 (2005).
18. F. M. Cox, R. Lwin, M. C. J. Large, and C. M. B. Cordeiro, "Opening up optical fibres," Opt. Express **15**(19), 11843–11848 (2007).
19. A. Karagiannis, A. N. Hrymak, and J. Vlachopoulos, "Three-dimensional non-isothermal extrusion flows," Rheol. Acta **28**(2), 121–133 (1989).
20. G. Brambilla, F. Xu, and X. Feng, "Fabrication of optical fibre nanowires and their optical and mechanical characterisation," Electron. Lett. **42**(9), 517–519 (2006).
21. Y. L. Hoo, W. Jin, H. L. Ho, D. N. Wang, and R. S. Windeler, "Evanescent-wave gas sensing using microstructure fiber," Opt. Eng. **41**(1), 8–9 (2002).
22. G. Pickrell, W. Peng, and A. Wang, "Random-hole optical fiber evanescent-wave gas sensing," Opt. Lett. **29**(13), 1476–1478 (2004).
23. T. Ritari, J. Tuominen, H. Ludvigsen, J. C. Petersen, T. Sørensen, T. P. Hansen, and H. R. Simonsen, "Gas sensing using air-guiding photonic bandgap fibers," Opt. Express **12**(17), 4080–4087 (2004).

1. Introduction

Microstructured optical fibers (MOFs) and optical nanowires have the ability to provide a large proportion of the guided optical power either to the external environment or the holes within the MOF. Of particular interest is the jacketed and suspended nano/micro-wire design [1–6] (wagon wheel fiber), as this provides a means for protecting the highly sensitive optical wire, and long lengths can be fabricated by drawing a structured preform. Currently, core diameters have been reduced to values as low as 410nm in lead silicate glass [5]. As this is smaller than the wavelength of light used in most sensing applications, a large percentage of the evanescent field can be used to interact with an analyte, allowing sensing via absorption or fluorescence processes. In addition, it has been shown theoretically that small core diameter fibers, particularly those with a high refractive index substrate material, can efficiently capture fluorescence into the guided modes of the fiber [1, 2, 7]. A broad range of sensing applications exists using this design of sensor due to the ability to functionalize the surface for biological applications [6, 8], as well as other chemical applications. While in principle long interaction lengths can be achieved using MOFs, in practice the difficulty exists that fibers of the type described above can only be filled from one of the distal ends (via capillary forces for liquids [7, 9] or diffusion for gases [10]). Typical filling times include greater than four hours to fill half a meter of fiber with isopropanol (liquid) [7] and 200 minutes to fill 1 m of fiber with acetylene (gas) [10]. While pressure can be used to improve the filling time [9], filling greater than a few meters takes an impractically long time and thus cannot lead to a real-time sensor. Likewise, there is some scope for increasing the size of the holes within the MOF so that filling times are improved [11], but again real-time sensing is not possible. Note that if the analyte changes during the measurement period, emptying and re-filling of the fiber is required. In addition, it is not possible to perform distributed sensing with traditional MOFs due to the requirement to fill from the distal ends. These issues can, in principle, be solved by exposing the core along the length of MOFs.

The exposed-core fiber was first proposed in 2003 by Hoo et al [10] and fabrication has since been demonstrated by the use of a fusion splicer and air pressure to blow holes within an MOF [12], use of a focused ion beam [13, 14], and femtosecond laser micromachining [15, 16]. Also, tapering of MOFs can allow access to the guided optical field [17]. However, these methods generally result in short exposed regions, such as the order of tens of microns. Cox *et al.* have shown that long lengths of exposed-core polymer fiber can be fabricated by creating an opening at the preform stage of the fiber fabrication, such as by drilling holes into the cladding of a polymer MOF preform [18]. In this paper we present two new methods for fabricating exposed-core fiber, and demonstrate these methods using lead-silicate glass fibers. The first method involves etching the drawn fiber to expose the core; while the second involves directly drawing the exposed-core fiber. We then demonstrate that the fabricated

#115826 - $15.00 USD Received 17 Aug 2009; revised 17 Sep 2009; accepted 24 Sep 2009; published 29 Sep 2009

fibers can successfully measure fluorescence with a response time substantially quicker than for an equivalent protected-core MOF.

2. Fabrication

Our method of fabrication expands on the method previously developed for fabricating enclosed wagon wheel (WW) fibers via preform extrusion, caning, and drawing of soft glass [5]. Here a lead-silicate glass (Schott glass F2, n ≈1.62) was used. The process is summarized in Fig. 1. First, a WW structured preform and wedged jacket were extruded from stainless steel dies at high temperature and pressure. The WW preform was caned using a fiber drawing tower and inserted into the jacket. The cane-in-jacket preform was then drawn into fiber with an outer diameter of approximately 160μm, with core diameters ranging from 2.0 to 3.0 μm. The advantage of extrusion for this fiber design is significant, as it allows the fabrication of asymmetric structures such as the wedged jacket. However, this proved to be a challenge in practice, due to the tendency of the preform to bend as a result of temperature asymmetries resulting from the use of an asymmetric wedged jacket die. This caused an asymmetry in the viscosity profile and thus bending in the preform during extrusion. In addition, the use of an asymmetric die can cause bending, even in isothermal conditions [19]. Several methods were employed to overcome preform bending. The most successful method was found to be attachment of a stainless steel pole to the wedged jacket at the start of the extrusion to mechanically force it along a straight line.

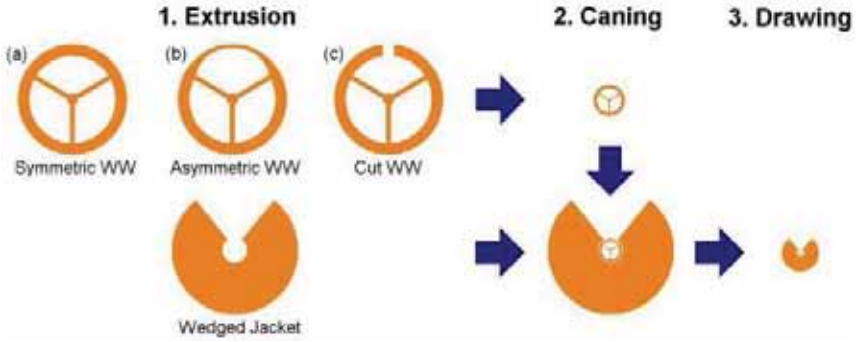

Fig. 1. Schematic diagram of the fabrication process.

As indicated in Fig. 1, several fiber designs were trialed for their suitability in fabricating this type of exposed core fiber. A summary of these trials is included here for clarity in Table 1, where a description of each of the trials follows. Loss measurements from Sec. 3 have also been briefly included.

#115826 - $15.00 USD Received 17 Aug 2009; revised 17 Sep 2009; accepted 24 Sep 2009; published 29 Sep 2009

Table 1. Summary of the exposed-core fiber fabrication trials. Loss values have been included from Sec. 3.

Trial number	WW die	Etching required	Loss before etching (dBm^{-1} at 1000nm)	Loss after etching (dBm^{-1} at 532nm)
1	Symmetric WW	Yes	2.8 ± 0.2	Fiber too damaged
2	Asymmetric WW	Yes	2.1 ± 0.2	54 ± 5
3	Cut WW (standard struts)	No	4.1 ± 0.2	N/A
4	Cut WW (thick struts)	No	2.2 ± 0.3	N/A

Using a symmetric WW preform (Fig. 1(a)), the fiber shown in Fig. 2(a) and (b) was drawn (trial #1) and by using an asymmetric WW preform (Fig. 1(b)) the fiber shown in Fig. 3(a) and (b) was drawn (trial #2). Approximately 100-150m of each fiber type was drawn, each from a single preform. Note that these fibers are not yet fully exposed at the time of drawing due to the presence of a cover layer. This cover layer was used to protect the core during the fiber drawing, and assisted in maintaining the fiber structure by allowing self-pressurization of all three fiber holes. We refer to these fibers as protected-core fibers.

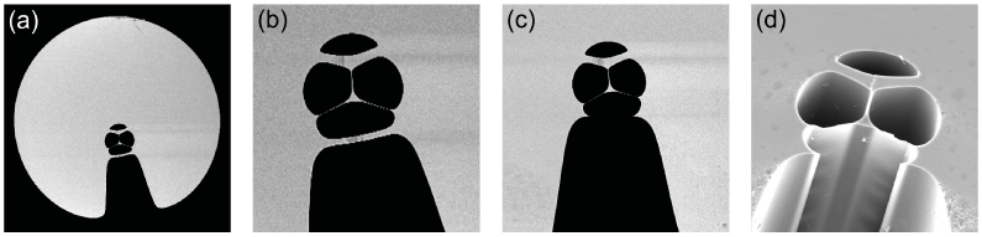

Fig. 2. Trial #1 exposed-core fibers fabricated from a symmetric WW preform, the image sizes are (a) 200μm, (b) 80μm, (c) 80μm, and (d) 40μm. Images (c) and (d) show the fiber after HF etching.

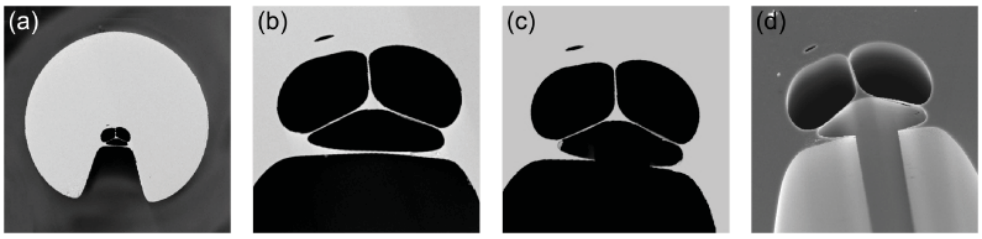

Fig. 3. Trial #2 exposed-core fibers fabricated from an asymmetric WW preform, the image sizes are (a) 200μm, (b) 35μm, (c) 35μm, and (d) 40μm. Images (c) and (d) show the fiber after HF etching.

The cover layer was removed through chemical etching with 0.056±0.001 wt. % hydrofluoric acid (HF). This was experimentally determined to have an etch rate of 30±1 nm/min at the site of the cover layer while 25 cm of a 33 cm length of fiber with both ends sealed was fully immersed in the acid, held vertically, and rotated at 78 rpm. Vertical orientation and rotation of the fiber was found to be necessary in order to produce a consistent etch rate along a reasonable length of the fiber. The required etch time was determined to be 78 mins for the trial #1 fiber (Fig. 2) and 11.3 mins for the trial #2 fiber (Fig. 3). For the fiber produced in trial #1, it was not found to be possible to completely etch through the cover layer along the entire length of fiber without etching through the struts at some point due to the cover layer being considerably larger than the struts. The fiber from trial #2 had a much

#115826 - $15.00 USD Received 17 Aug 2009; revised 17 Sep 2009; accepted 24 Sep 2009; published 29 Sep 2009

improved strut to cover layer ratio (48% compared to 12%), and was thus successfully etched without damaging the struts.

To avoid the requirement for HF etching, we trialed the direct-drawing of exposed-core fibers by cutting a thin slot into the side of a symmetric WW preform as shown in Fig. 1(c). This was then caned and drawn into the fiber shown in Fig. 4 (trial #3). The advantage of this method is that exposed-core fiber is produced straight from the fiber draw stage, which allows significantly longer lengths of exposed-core fiber to be fabricated. However, the fiber core is unprotected during the caning and drawing processes. The struts also become elongated due to surface tension effects, with a final thickness of 70±10 nm, compared with 160±10 nm for the fiber shown in Fig. 3(c). This accounts for an observed increase in fiber fragility for the directly-drawn exposed-core fiber. In particular, the core tended to break during use, even while the cladding remained intact. Also note the ribbed effect along the struts in Fig. 4(d), which indicates stress in the struts. To improve fiber strength, particularly in the region supporting the core, the strut thickness was doubled in the WW preform with the resulting fiber shown in Fig. 5 (trial #4). This fiber was significantly easier to handle, and no breakage of the core during use has yet been observed.

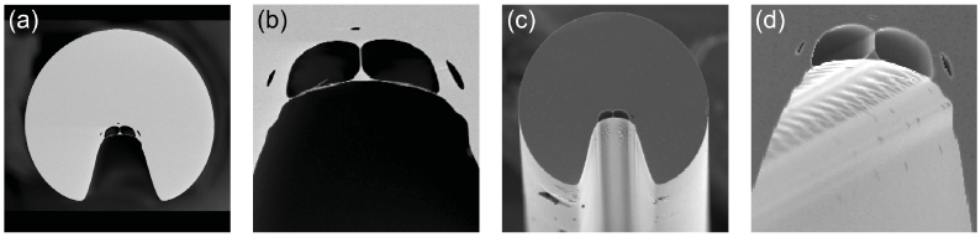

Fig. 4. Trial #3 exposed-core fibers fabricated from a symmetric WW preform with slot and standard strut thickness. The image sizes are (a) 200μm, (b) 50μm, (c) 200μm, and (d) 40μm.

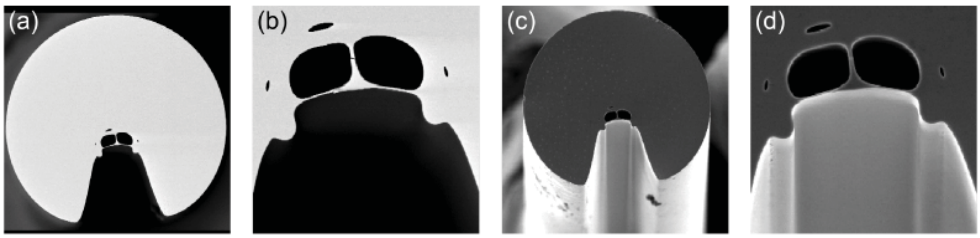

Fig. 5. Trial #4 exposed-core fibers fabricated from a symmetric WW preform with slot and increased strut thickness. The image sizes are (a) 170 μm, (b) 40 μm, (c) 200 μm, and (d) 40 μm.

To the best of our knowledge this is the first demonstration of glass exposed-core microstructured optical fiber produced directly from fiber drawing. The length of fiber produced from a single draw for both trial #3 and #4 was the order of 200 m, which is a significant improvement on previous pointwise methods where reported lengths of the exposed region include 64μm [12] and 20 μm [13].

3. Propagation loss

The propagation loss spectra of trial #1 and #2 fibers before etching, along with trial #3 and #4 fibers, were measured using the standard cutback measurement technique. A supercontinuum white light source (KOHERAS SuperK^{TM} Compact) was collimated and then focused into the fibers using a 2.75 mm focal length lens. The output signal was launched into an optical spectrum analyzer (OSA) using free space coupling after collimation with a 40X microscope objective lens. Both the input and output coupling was maximized at 1000 nm so

#115826 - $15.00 USD Received 17 Aug 2009; revised 17 Sep 2009; accepted 24 Sep 2009; published 29 Sep 2009

that the measurements were repeatable when successive cutbacks were made. The results are shown in Fig. 6.

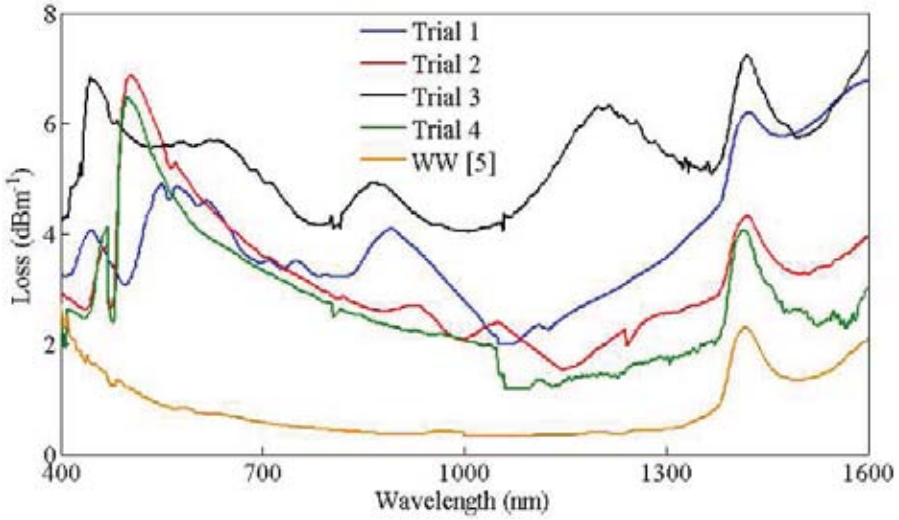

Fig. 6. Measured loss for trial #1 protected-core fiber (blue), trial #2 protected-core fiber (red), trial #3 directly-drawn exposed-core fiber (black), and trial #4 directly-drawn exposed-core fiber (green). The WW preform used to fabricate the trial #4 fiber was ultrasonically cleaned prior to fiber drawing. The loss of an enclosed wagon wheel fiber with a similar core diameter (2.1 μm, compared to 2.0-3.0 μm) has been included for comparison (orange) [5]. The WW preform used to fabricate this fiber was also ultrasonically cleaned.

The results show that the propagation loss of the first directly-drawn exposed-core fiber (trial #3) is approximately 2 dBm^{-1} higher relative to the protected-core fibers (trials #1 and #2). This is likely to be due to surface contamination post-caning and post-drawing, as no cleaning was performed beyond the preform stage. It is also possible that surface cracks may have formed in the time between drawing and measurement as a result of exposure to moisture [20], and this effect would also likely lead to increased long term loss for the fiber. For this reason the exposed-core fibers were stored in a moisture-free environment when not in use. In order to improve the directly-drawn exposed-core fiber loss, the WW preform used to fabricate the trial #4 fiber was ultrasonically cleaned prior to caning. Ultrasonic cleaning of the preform is a standard procedure for WW fiber fabrication [5], but had not been performed on previous exposed-core fiber trials due to concerns over strut fragility. The improvement can be observed by comparing the loss of trial #3 and #4 fiber in Fig. 6, where the average loss across the whole spectrum was reduced by 2.4 dBm^{-1}. However, comparing the loss between the trial #4 fiber and that of a previously reported enclosed wagon wheel fiber (Fig. 6, orange) we see that the exposed-core fiber still has significantly higher loss. The reasons for this excess loss are not yet clear, although it is anticipated that improved preform cleaning and fiber storage conditions will assist in reducing the exposed-core fiber loss.

These measurements were performed on the fiber immediately after drawing, but for trials #1 and #2 the fiber is not exposed at this point as they required chemical etching. Trial #1 fiber could not be etched consistently enough to perform a loss measurement. The loss of trial #2 fiber after HF etching was measured as 54±5 dBm^{-1} at 532 nm, compared to 6±1 dBm^{-1} for the unetched, protected-core fiber. This was measured by comparing the transmission of etched and unetched fiber of the same length (25 cm), which assumes that the coupling is the same for both cases. This high loss was caused by an increase in the surface roughness due to the HF etching, as observed with atomic force microscopy measurements performed on bare fiber (no structure) under identical etching conditions to that of the trial #2 exposed-core fiber (Fig. 7).

#115826 - $15.00 USD Received 17 Aug 2009; revised 17 Sep 2009; accepted 24 Sep 2009; published 29 Sep 2009

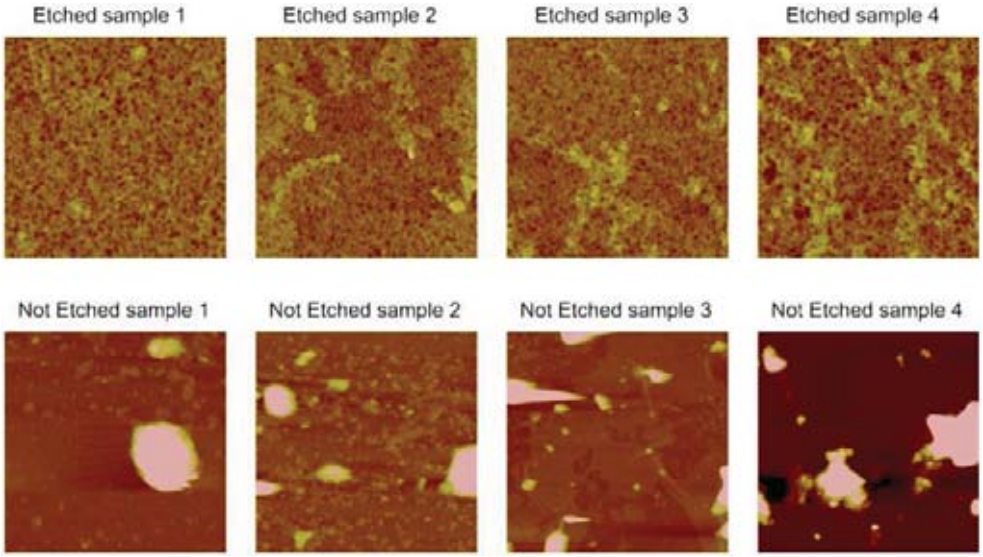

Fig. 7. Atomic force microscopy images of the surface of HF etched bare fiber (upper images) and the surface without etching (lower images). The images sizes are 5 μm x 5 μm and the image height spans 50 nm.

The images in Fig. 7 exhibit considerable differences in the surface before and after etching with HF. The etched surface appears to be considerably rougher, while the non-etched surface is relatively smooth with the exception of large pieces of debris. These large pieces are likely due to surface contamination during storage (1 month), which could not be successfully removed when cleaned with ethanol and water prior to mounting for AFM measurements. These surfaces are not likely to be representative of the fiber surface quality immediately after fabrication, particularly when considering that the exposed-core fiber is partially protected by the wedged jacket. These large pieces of debris are not visible on the etched surface, which suggests they were removed from the surface during the HF etching process. Thus, discounting the large debris pieces, the surface quality of the etched surface is visibly rougher and accounts for the high loss measured for the etched, exposed-core fiber.

Unfortunately, the high level of loss due to HF etching means this method of exposed-core fiber fabrication is not well suited to fabricating lengths of more than tens of centimeters unless the etching process can be improved. In addition, there are practical challenges in accurately etching large lengths of fiber, say, greater than one meter. However, one possibility for distributed sensing is to choose to expose only selected locations along the fiber whilst leaving the majority of the fiber inactive and thus protected. This could prove useful in applications where multi-point sensing is required in a quasi-distributed system or to improve MOF filling times.

4. Fluorescence measurements

In general, evanescent-field microstructured optical fiber sensing has either made use of absorption or fluorescence based techniques. Absorption is commonly used for gas sensing [16, 21–23] while fluorescence tends to be used for biological applications where fluorescent labels are often used [6,8]. One drawback of the MOF sensing method is that the measurement response time is related to the time required to fill the fiber. Here we demonstrate that one useful application of the exposed-core fiber is to reduce the time of filling an MOF, and thus to dramatically improve the response time of the sensor. Here we present experimental results of the response time for fluorescence sensing with exposed-core fibers, and compare these to using enclosed (protected) core fibers.

#115826 - $15.00 USD Received 17 Aug 2009; revised 17 Sep 2009; accepted 24 Sep 2009; published 29 Sep 2009

To measure the response time for the exposed-core fiber the experimental setup shown in Fig. 8(a) was used where 532 nm laser light was focused into directly-drawn exposed-core fiber (trial #4, Fig. 5), and the output was directed through a long pass filter and into a spectrometer. The fiber was placed into an empty bath which was filled with $2x10^{-6}$ M Rhodamine B in water while recording the spectral response over time.

To compare the response time an unetched, enclosed (protected) core fiber was also tested (trial #2 not-etched, Fig. 3(a, b)). For the enclosed (protected) core fiber the test fluorophore was a 91 nM solution of organic quantum dots (QDot800^{TM}, Invitrogen) dissolved in hexadecane, which was allowed to fill into the fiber via capillary forces. The experimental setup is shown in Fig. 8(b). The 532 nm excitation light was reflected from a long pass dichroic mirror (R532 T633) and focused into the fiber using a short focal length aspheric lens (f = 2.75 mm) and a nano-positioning stage. The fluorescence signal collected by the fiber was imaged using the same aspheric lens, passed through the dichroic mirror, filtered using a 550 nm long pass filter, measured using a low power photo-detector, and the data logged with a power meter.

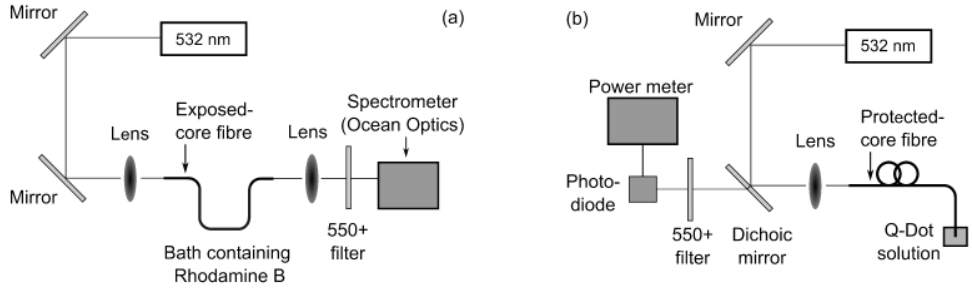

Fig. 8. Experimental setup for measuring the fluorescence sensor time response for (a) exposed-core fiber (trial #4, Fig. 5) and (b) enclosed (protected) core fiber (trial #2 not-etched, Fig. 3 (a, b)).

Note that quantum dots were used for the enclosed (protected) core fiber to avoid the effect of photobleaching, which is significant when small quantities of fluorophore are used [7]. An organic dye was used for the exposed-core fiber due to the large volume of fluorophore required to fill the bath. Also, a spectrometer was used to measure the Rhodamine B fluorescence in order to help differentiate the pump and fluorescence signals, which was not necessary for the quantum dots due to the large separation of excitation and fluorescence wavelengths. The fluorescence sensing time response measurements for the exposed-core fiber are shown in Fig. 9, and for the enclosed (protected) core fiber in Fig. 10.

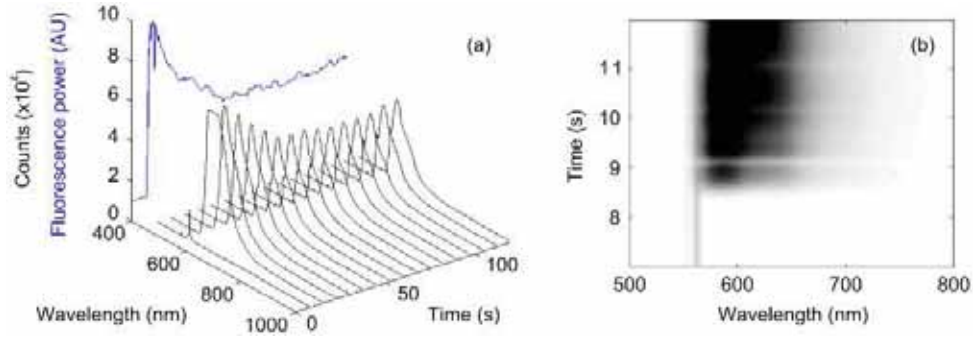

Fig. 9. (a) The spectral signal recorded over time using an exposed-core fiber (trial #4, Fig. 5) as the bath was filled with Rhodamine B. (b) Same as for (a) considering the initial few seconds only.

#115826 - $15.00 USD Received 17 Aug 2009; revised 17 Sep 2009; accepted 24 Sep 2009; published 29 Sep 2009

As expected, a strong fluorescence signal was obtained after filling the bath with Rhodamine B, which then decayed initially due to photobleaching [7], and then reached a stable level. The fluorescence power curve in Fig. 9(a), together with Fig. 9(b), shows that the time taken to reach a strong fluorescence signal is the order of one second for the exposed-core fiber. We now compare this to the results obtained using the enclosed (protected) core fiber, which are shown in Fig. 10.

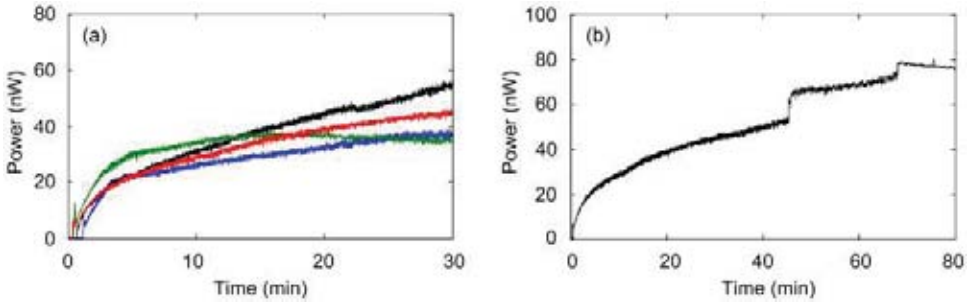

Fig. 10. Fluorescence signal measured for the enclosed (protected) core fibers (trial #2 before etching) over 30 mins (a) and 80 mins (b). Different colors refer to repeats of the same experiment.

The results in Fig. 10 for the enclosed (protected) core fiber show a more gradual increase in fluorescence, which corresponds to the capillary filling time of the fiber. The sharp steps shown in Fig. 10(b) correspond to times when the holes of the fiber became completely filled, and thus the coupling efficiency at the input end of the fiber changes (because the fluid has reached the launch end of the fibre). Comparing the two fiber designs, the exposed-core fiber reached a maximum fluorescence signal after approximately one second, while the enclosed (protected) core fiber required approximately 70 minutes to completely fill and hence reach a maximum signal.

5. Conclusions

Two methods for fabricating glass exposed-core microstructured optical fiber have been demonstrated. In the first method a soft-glass extruded preform was drawn into a fiber and then chemically etched to expose the small and thus highly-sensitive core. This method was demonstrated with two different fiber designs and it was observed that reducing the amount of glass to be etched allowed for the fabrication of consistent lengths of exposed-core fiber. In the second method the wagon wheel preform is cut prior to caning, so that the drawn fiber is exposed without requiring etching. The advantage of the etching method is that the fiber core is protected during the fabrication process, which is reflected in the reasonably low loss immediately after drawing. However, ultrasonic cleaning of the preform before caning can be used to improve the loss of directly-drawn exposed-core fiber. In addition, the surface roughness and resultant optical loss due to hydrofluoric acid etching means that directly drawing exposed-core fiber is, at present, the preferred method for fiber fabrication.

The directly-drawn exposed-core fiber was evaluated for fluorescence-based sensing, in order to determine the measurement response time and compare with enclosed MOF sensors. The exposed-core fiber was placed in a bath that was filled with a fluorophore and the measurements were made in the forwards direction. While ideal for demonstrating the capability of the exposed-core fiber, this type of experimental arrangement does not allow for small volumes of analyte to be measured. The signal response time for the exposed-core fiber was found to be significantly faster than for the enclosed (protected) core fiber. Given the ability to do almost real-time sensing and the possibility for distributed sensing it is anticipated that exposed-core fibers will in the future play an important role to the field of chemical and biological sensing.

#115826 - $15.00 USD Received 17 Aug 2009; revised 17 Sep 2009; accepted 24 Sep 2009; published 29 Sep 2009

Acknowledgments

We acknowledge the support of the Defence Science and Technology Organisation (DSTO), Australia, and in particular the DSTO Corporate Initiative on Smart Materials and Structures for sponsorship of this program of research. We acknowledge the Australian Research Council for funding this project (DP0880436). T. Monro acknowledges the support of an Australian Research Council Federation Fellowship.

#115826 - $15.00 USD Received 17 Aug 2009; revised 17 Sep 2009; accepted 24 Sep 2009; published 29 Sep 2009

4.3.3 Wedged-Jacket Extrusion

The enclosed suspended-core fibres in [P6] are symmetric structures and thus, while challenging in their own right, do not have the symmetry related problems that were present in the fabrication of the exposed-core fibres in [P7]. The majority of these problems occur at the preform stage in trying to extrude the wedged jacket, where two interrelated problems effect the quality of the preform. The most noticeable effect is that the preform bends while extruding, which has the secondary effect of distorting the cross-sectional structure.

These challenges were only briefly mentioned in [P7] and thus a more complete discussion on why these challenges arise and how they were overcome is included here.

Preform Bending

Preform bending results from using an asymmetric extrusion die, which can be due to both temperature asymmetries and intrinsic flow asymmetries [178]. For the extrusions in this project there was an inferred (though not directly measured) temperature asymmetry associated with the wedged-jacket design. Extrusion dies for this project were made of steel, which has a higher conductivity than glass. Figure 4.7 shows that heat is lost more quickly from the wedge and thus the wedge side is colder relative to the glass side. Consequently the glass on the wedged side has a higher viscosity than on the opposite side causing the preform to bend towards the colder side.

In general, it is impossible to create a perfectly symmetric temperature and flow distribution for any die design, even a circular tube, due to imperfections in the alignment and construction of the furnace and the extrusion die. However, the weight of the extruded glass is generally sufficient to force the preform to extrude straight. Initial trials, such as that shown in Fig. 4.8, demonstrated that the extrudate weight was not sufficient to force the preform straight for the case of a wedged-jacket extrusion. Observe that the right hand side, which was the first to leave the die, bent towards the wedge, which was expected given the description above.

The intuitive solution was to attach a weight to the preform at the start of the extrusion. Tests were performed by attaching a small steel tube (100 mm long $\times$ 1 mm thick $\times$ 10 mm diameter) to the glass as it begun extruding. However, this proved to have little

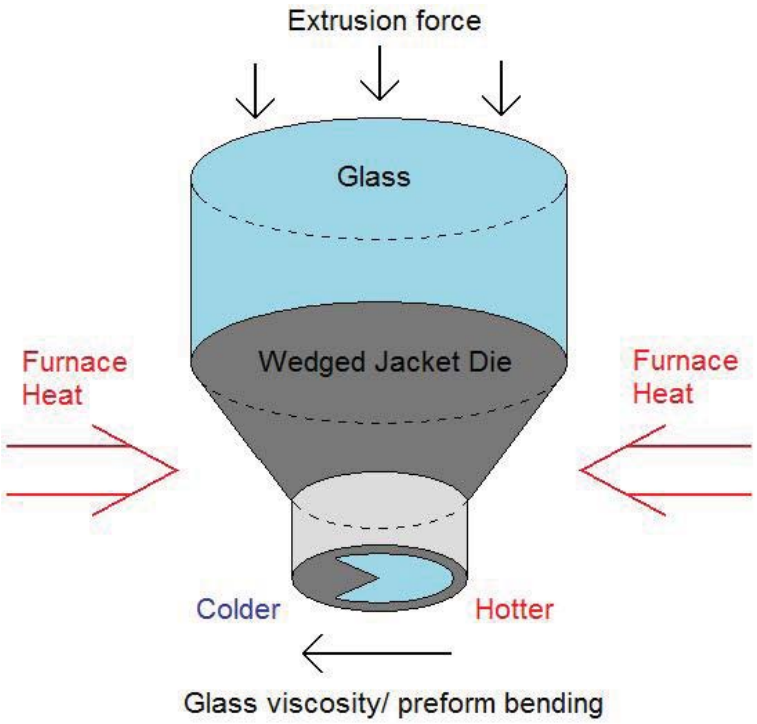

FIGURE 4.7: Schematic diagram of the extrusion process where heat is supplied externally via a furnace and glass is forced downwards through the die. The asymmetric die leads to a small temperature variation which causes preform bending.

FIGURE 4.8: Bent wedged-jacket preform with a 45^o wedge where the left hand side was the last to exit the die.

impact when tested as the jacket simply bent until it hit the extrusion machine stand (Fig. 4.5). The second approach was to attach a guiding-pole which forces the leading end of the extrudate along a straight line. The setup used to achieve this is shown in Fig 4.9 where it attaches to the extrusion machine as was shown in Fig. 4.5.

FIGURE 4.9: Guiding pole used to force the leading edge of the wedged-jacket extrusions along a straight line.

By using a combination of the guiding pole and slightly higher extrusion temperatures (565^{o}C compared to 560^{o}C previously used for symmetric tubes) the relatively straight wedged jackets shown in Fig. 4.10 were extruded. Temperature is a key parameter in the extrusion process as higher temperatures result in increased tapering, while lower temperatures result in bending that requires more force to correct.

The wedged jackets shown in Fig. 4.10 had a total bend derivation of 9 mm over the entire length of preform (3%). However, only 180 mm of the jacket was used for fibre drawing and thus the central 180 mm of the jacket had a bending deviation of only 3 mm. While deviations of less than 1 mm (for a 180 mm preform) are optimal for fibre drawing, fibres can still be successfully drawn with derivations of 3 mm.

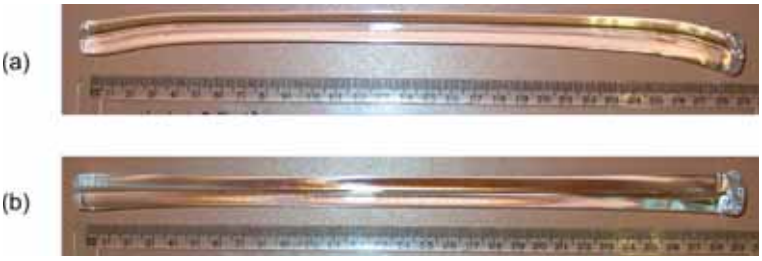

FIGURE 4.10: Examples of extruded wedged jacket preforms where the guiding pole has been used. Side view (a) and top view (b).

These results demonstrate that straight wedged jacket preforms can be successfully fabricated by forcing the preform straight during extrusion. The problem of preform bending

can be combated through the use of a guiding pole where instead of jackets with 180^o bends, the total bending deviation can be reduced to 3 mm over the entire jacket. These preforms were sufficiently straight such that the fibres in [P7] could be fabricated. Bending, however, is not the only issue to be addressed. The cross-sectional structure must also have the correct characteristics as will now be discussed.

Wedged-jacket cross-sectional structure

The goal of extrusion is to fabricate a preform that has the same cross-sectional structure as the original die design. However, several processes prevent this from occurring, particularly for asymmetric structures, such as the internal flow properties within the die and die swell. These issues were overcome in this project through a trial and error process that involved iterations to counter-act the deformations. This is a tedious process, but has nonetheless lead to successful fabrication of exposed-core fibres. An possible alternative is to model the extrusion process in order to optimise the geometry, however, this would require non-trivial three-dimensional modelling (for example, see Ref. [178]).

The key cross-sectional characteristics of the wedged-jacket that need to be present include that

1. The wedge is open in the wedged-jacket after extrusion
2. The wedge is sufficiently wide in the wedged-jacket so that it does not close during fibre drawing
3. The cane can be held within the central region of the wedged-jacket
4. Correct and fixed orientation of the cane can be achieved within the wedged-jacket

The following examples show the iterations of the wedged jacket design that were tested in this project, why certain designs were unsuccessful, and design modifications that were made in order to achieve the aforementioned aims and thus fabricate the fibres that were presented in [P7].

Example 1: Square wedged-jacket

In order to correctly orientate the struts of the structured preform within the wedged jacket several methods were tested. The first involved using a square-based structure where the central portion of the wedged jacket die has a square shape which was to have a cane inserted with a corresponding square wagon wheel design (Fig. 4.11(a)). However, extrusion of the wedged jacket led to severe deformation of the square shape due to surface tension effects rounding out the sharp features and also opening the wedge to a large angle (Fig. 4.11(b)). This led to the problem that the cane could not be held within the jacket as intended and the wagon wheel structure became distorted and incorrectly orientated.

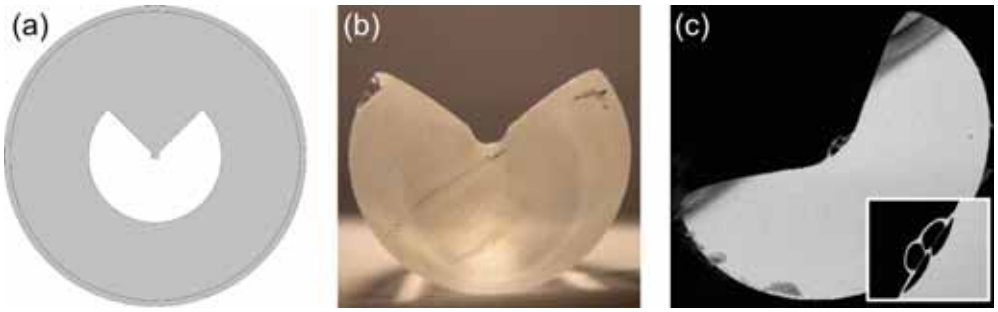

FIGURE 4.11: Square wedged-jacket die design (a), preform cross section (b), and the resulting fibre (c).

Two fibres were drawn based on the square wagon wheel approach, with neither being successful. The first design was using a 90^o wedge with the cane mechanically fixed to the jacket. A typical cross-section of this fibre is shown in Fig. 4.11(c). As the cane was not intrinsically held within the jacket it simply bonded to the outer surface of the wedged jacket. Another important point is that the wedged jacket angle increased significantly during the drawing process, this being the reason for smaller wedge angle die designs in subsequent extrusions.

Other methods for maintaining cane orientation were also trialled. For example, a lock-key method consisted of adding a notch to the wedged-jacket with the corresponding key in the wedged jacket. However, surface tension effects caused the notch and key to be smoothed out during extrusion. It was later found that a close fit between the cane and the jacket was sufficient to hold the orientation of the cane.

Example 2: 45^o wedged-jacket

A second attempt involved using a 45^o wedge. As seen from Fig. 4.12(a) this design is able to intrinsically hold the cane within the jacket. Distortions in the preform relative

to the original die design, as discussed previously, meant that the small features that were to hold the cane to the jacket were lost during extrusion and the central circular feature became elliptical. This demonstrates that there is a need to exaggerate the features of the die design in order to extrude a preform with the correct requirements.

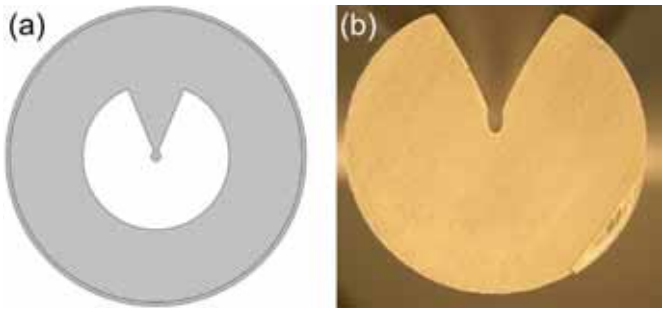

FIGURE 4.12: 45^o wedged-jacket die design (a), and preform cross section (b). Note that the fibre draw was not successful for this design due to the cane and jacket separating.

Example 3: Channeled wedged-jacket

The above design was modified to have a channeled wedge (Fig. 4.13(a)). The preform displayed reasonable retention of the cross-sectional structure, with good ability to hold the cane in place (Fig. 4.13(b)). Unwanted distortions included narrowing of the channel and the central hole becoming elliptical. The narrow channel was the eventual downfall of this design, as several drawing attempts yielded fibres that had the channel collapse as shown in Fig. 4.13(c).

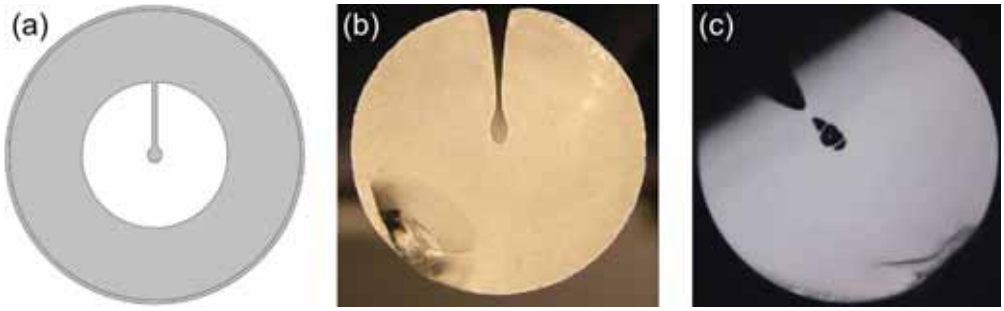

FIGURE 4.13: Channeled wedged-jacket die design (a), preform cross section (b), and the resulting fibre (c).

Example 4: D-shaped wedged-jacket

The D-shaped wedged-jacket design (Fig. 4.14(a)) was developed to counter-act the issues that were identified in the above examples. In particular, the channeled section was widened to prevent collapse during fibre drawing and the central region was manufactured to be a D-shape so that extrusion distortions caused it to become approximately

circular (Fig. 4.14(b)). As can be seen from the fibre drawn in Fig. 4.14(c), the preform was successful in being drawn into useful fibre. This design of wedged-jacket was used to fabricate the exposed-core optical fibre used in [P7] and [P8].

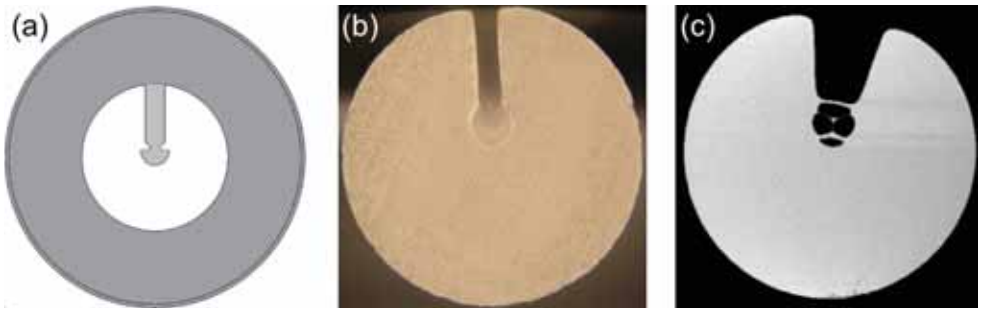

FIGURE 4.14: D-shaped wedged-jacket die design (a), preform cross section (b), and the resulting fibre (c).

4.4 Distributed Sensing using Exposed-Core Fibres

The publication [P8] forms the basis of this section.

S. C. Warren-Smith, E. Sinchenko, P. R. Stoddart, and T. M. Monro, "Distributed fluorescence sensing using exposed-core microstructured optical fiber," *Photonics Technology Letters* **22**, 1385-1387 (2010).

4.4.1 Publication Overview

Aim

The aim of this work was to demonstrate that the exposed-core fibres fabricated in [P7] can be used for fluorescence-based distributed sensing. In particular, this was the first demonstration of using microstructured optical fibres for spatially continuous fluorescence-based distributed sensing.

Field of Knowledge and Link Between Publications

Distributed sensing is a commonly stated advantage of sensing with optical fibres and many demonstrations have been reported [1]. For example, time-resolved Raman backscatter can be used for distributed temperature sensing due to the temperature dependence of the ratio of Stokes and anti-Stokes spectral bands, while frequency resolved Brillouin scattering can be used to measure parameters that affect acoustic velocity, namely temperature and strain [1]. Rayleigh backscatter can be used in optical time domain reflectometry (OTDR) to perform distributed loss measurements along a fibre [128].

However, very few examples of distributed chemical sensors exist. A notable exception is water sensing, which has been demonstrated by using OTDR to measure microbend losses due to the swelling of a polymer to which the fibre is attached [128, 130]. In particular, few reports on distributed fluorescence-based chemical sensing exist [113, 116, 127]. Fluorescence sensors are typically fabricated with a sensitised cladding surrounding the core of a multi-mode silica fibre that allows interaction between the external environment and the evanescent field [127, 128]. The limited success of distributed fluorescence

sensors to date is thought to be due to the difficulty in finding both appropriate cladding materials and fluorescent dyes, and the low percentage of evanescent field that is typically available to interact with the chemical analyte in available fibres [128]. In principle, it is this later problem that can be solved by using microstructured optical fibres. The primary challenge with distributed sensing with MOFs is that the evanescent field is generally only accessed via the distal ends of the fibre. Consequently, distributed sensing at an arbitrary position along the fibre is not possible, unless the core is exposed, such as the fibres presented in [P7].

Discussion and Conclusions

In [P8] it was demonstrated, for the first time, that fluorescence-based distributed sensing using exposed-core microstructured optical fibres can be achieved by performing time-resolved measurements when various lengths of fibre were immersed in a fluorescent material. A spatial resolution of 0.5 m was demonstrated but with a range of only 2.5 m. The primary constraint on the range being that the loss of the fibre was relatively high for this type of experiment, which was inferred to be 10.8 dB/m. Methods for improving the fibre loss, and thus the distributed sensing range, will be discussed in Sec. 4.4.3 following [P8]. It should also be noted that this was a demonstration for an ideal fluorescent liquid that has a short fluorescence lifetime (0.17 ns) and strong fluorescence, but the sensing of this liquid is not in itself of particular interest. The distributed fluorescence sensing concept is only useful if either the species of interest is fluorescent, which is uncommon, or if the cladding can be sensitised such that it produces a fluorescence response in the presence of the analyte. This will be discussed in more detail in Chapter 5 in regards to aluminium ion sensing and, consequently, corrosion sensing.

4.4.2 Statement of Contribution

Conceptualisation

Several concepts were combined in this paper in order to achieve the final result. The exposed-core fibre design was conceptualised by Tanya Monro, using these fibres in the distributed sensing at Swinburne University of Technology was first proposed by Stephen

Warren-Smith, with the experimental setup primarily designed by Paul Stoddart and Elena Sinchenko.

Realisation

Pivotal to this paper was previous work involving the fabrication of the exposed-core fibres [P7], and the design and construction of the distributed sensing experimental setup [179, 180]. The modification of the experimental setup for use with exposed-core fibres and subsequent measurements were primarily performed by Stephen Warren-Smith and Elena Sinchenko, with assistance from Daniel White.

Documentation

This paper was primarily written by Stephen Warren-Smith, with editing by all other authors.

Declaration and Permission

I declare that the above statement of contribution is accurate and I give permission for this publication to be included in this thesis.

Stephen C. Warren-Smith Elena Sinchenko Paul R. Stoddart

Tanya M. Monro

Warren-Smith, S.C., Sinchenko, E., Stoddart, P.R. and Monro, T.M. (2010)
Distributed Fluorescence Sensing Using Exposed Core Microstructured Optical Fiber
IEEE Photonics Technology Letters, v.22 (18), pp. 1385-1387, September 2010

4.4.3 Distributed Sensing: Extending the Range

In [P8] the longest piece of fibre used, 2.5 m, was found to be close to the range limit for this particular setup. This is due to the high loss (inferred to be 10.8 dB/m in [P8]) of the exposed-core fibre relative to conventional silica step-index fibre, where ranges of 10 km or more can be achieved [1]. The effect of this loss was seen by observing the peak heights in Fig. 3 [P8]. For a 0.5 m sample distance there were approximately 10^6 counts, while for a 2.5 m sample distance the counts were reduced to approximately 40 counts. In this section the data is analysed in more detail and extrapolated in order to determine what range could in principle be achieved if certain experimental and fabrication factors were improved.

To begin, note that power transmission through a fibre is written in the form [54]

$$P(z) = P_0 10^{\frac{-\alpha z}{10}}, \tag{4.1}$$

where $P(z)$ is the power transmitted after a propagation distance of z along the fibre in the axial direction, P_0 is the input power at the start of the fibre, and α is the fibre attenuation in dB/m. Assuming that both the excitation light propagation and the fluorescence propagation have the same attenuation the loss of the fibre can be determined by fitting the peak heights of Fig. 3 [P8] with the following equation,

$$log_{10}[P(L)] = -\frac{\alpha}{5}L + log_{10}(P_0), \tag{4.2}$$

where $P(L)$ is the peak height taken from the Gaussian fitting of Fig. 3 [P8], and $L = z/2$ is the length of fibre taking into account the double traverse of the excitation pulse and the fluorescence return. Note that this equation represents the line of best fit that is shown in Fig. 5 [P8]. P_0 now refers to the amount of fluorescence that would be expected from a fibre of length zero, and is related to the input excitation light by factors such as fluorophore absorption, fluorophore quantum efficiency, and fluorescence capture into the guided modes of the fibre [P1-P4]. From this, the exposed-core fibre loss was determined to be 10.8 dB/m, which is significantly higher than the value measured prior to performing the distributed sensing experiment (2.7 dB/m). However, this value includes the large peak height observed for the 0.5 m length of fibre, which may be an

anomalous result. If not included in the analysis the loss result is 5.2 dB/m, which is substantially closer to the previously measured value.

This result can be extrapolated to determine the length of fibre that could be used if parameters such as the fibre loss, coupling efficiency, or laser power are improved in the future. If P_{min} is the minimum peak height required in order to detect a signal (assumed to be 10 counts in the following calculations, which corresponds to a signal-to-noise ratio of 3) then Eq. 4.2 can be rearranged to give the expected range, L_{max}, according to

$$L_{max} = \frac{\alpha}{5} log_{10}\left(\frac{\xi P_0}{P_{min}}\right), \tag{4.3}$$

where ξ is the improvement (relative to this experiment) in factors that have the effect of linearly increasing optical power, such as coupling efficiency, laser power, and fluorescence capture fraction. P_0 is taken from the linear fit obtained using Eq. 4.2, thus allowing a direct extrapolation from the experimental results within [P8]. Equation 4.3 shows that the detection range is inversely proportional to the fibre loss, while logarithmically related to the ξ factor. As a consequence, reducing the fibre loss is the most effective way of increasing the detection range. For example, increasing the coupling efficiency from 0.1% to 10% only increases the range by a factor of 2, while reducing the loss from the current 10 dB/m to 1 dB/m gives a 10 fold increase in range. Equation 4.3 has been evaluated for a range of parameters and is presented in Fig. 4.15. Indicated on Fig. 4.15 is the current fibre loss, the material loss for F2 glass (Schott glass datasheets at 800 nm [170]), and for commercial silica fibre.

It is seen that relatively simple changes to the experiment, such as improving the fibre loss to that of the raw material (which has been achieved for enclosed suspended-core fibres of similar design [P6]) and improving the coupling efficiency from 0.1% to 10%, the range could be extended to 77 m.

It is important to note, however, that several other factors need to be considered in this analysis. In these experiments nearly the full dynamic range of the detector was used, meaning that improvements in the coupling efficiency or laser power would not necessarily provide increased range unless the dynamic range of the detector is also increased. The detection range can also be extended by increasing the laser repetition frequency and accumulation time. This serves to increase the total number of measurement cycles

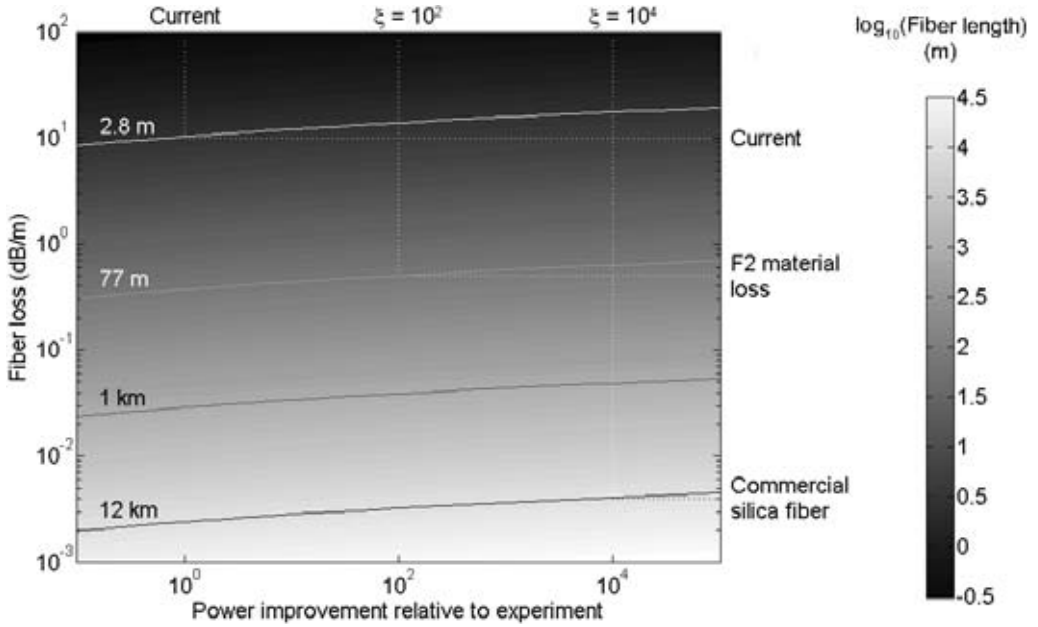

FIGURE 4.15: Analysis of parameters affecting the range of distributed sensing with the exposed-core fibre. All calculations are for a wavelength of 800nm.

N (that is, the number of laser pulses employed in the measurement), which leads to a $\sqrt{N}$ improvement in the signal-to-noise ratio. Once again, this has a relatively weak effect on the range due to the logarithmic term in Eq. 4.3. Also, the laser repetition rate is limited by the need to avoid pulse overlap within the fibre. For example, for a 100 m long fibre a repetition rate of approximately 900 kHz is theoretically acceptable, allowing a significant increase from the current experiment. However, if the fibre length is in the order of 10 km the repetition rate would have to be reduced from the current 25 kHz.

To summarise, in [P8] a detection range of 2.5 m with a spatial resolution of 0.5 m was demonstrated for this particular experimental setup. Although the range achieved in these proof-of-concept results is relatively modest, improvements in the experimental setup and fibre fabrication could lead to a significant improvement in range. A range of up to 77 m should be possible in the relatively near future.

4.5 Discussion and Conclusions

The fabrication of suspended optical nanowires [P6] and exposed-core microstructured optical fibres [P7] has been demonstrated. Both design types were fabricated using the extrusion technique to produce structured preforms which were caned and inserted into

enclosed and wedged jackets, respectively. In the case of suspended optical nanowires the extrusion technique has proven useful as it allows greater control of the cross sectional structure over capillary stacking and has thus allowed subwavelength core diameters to be produced. The usefulness of the extrusion technique is even more pronounced for the exposed-core fibre as the asymmetric wedged-jacket design would certainly not be possible with capillary stacking. While difficulties arose due to the asymmetric design such as preform bending and cross-sectional structure distortion, these were successfully overcome using simple methods.

An important issue is the loss of the fabricated fibres. The enclosed suspended-core fibres were found to have losses close to the background loss of the commercial glass billets they were fabricated from if the core diamater was sufficiently large ($\geq$ 760 μm). This loss increased as the core diameter reduced, in accordance with known theory of optical nanowire losses [177]. In contrast, the exposed-core fibre was found to have considerably higher loss than the background material regardless of the core diameter. This is likely due to environmental contamination and was found to reduce when greater care was taken of preform cleaning. In addition, when the HF etching method was used as a method to fabricate the exposed-core fibres the loss was found to dramatically increase due to an increase in the surface roughness of the core and thus an alternative method involving cutting the preform was developed. However, cutting glass preforms can damage the glass and can also leave glass particles on the surface that are difficult to clean and so future work will likely look at fabricating the open wagon wheel preform using a modified die design.

The exposed-core fibre design was used to demonstrate both real-time and distributed sensing. The real-time sensing experiments demonstrated that the open wedge of the exposed-core fibre could be filled in less than one second, as demonstrated with a fluorescence measurement. The distributed sensing experiment demonstrated that the exposed-core fibre can be used for time-domain distributed fluorescence sensing. Whilst improvements in fibre loss are required to improve the current range of 2.5 m, the results of this chapter nevertheless demonstrate the viability of using exposed-core fibres for applications where highly sensitive and distributed measurements are required, such as corrosion sensing.

Chapter 5

Corrosion Sensing Application

Four stages of acceptance

(1) This is worthless nonsense,

(2) This is an interesting, but perverse, point of view,

(3) This is true, but quite unimportant,

(4) I always said so.

J. B. S. Haldane

5.1 Chapter Overview

In order to use the optical fibres fabricated in the previous chapter as sensors there must be a transduction mechanism that turns a physical or chemical property into an optical signal. In the case of chemical sensing, this can be through intrinsic properties of the analyte itself, such as absorption or fluorescence. More commonly, an additional material provides the transduction mechanism, such as through a sensitive coating.

A flowchart of how the sections of this chapter relate to other sections of this thesis is shown in Fig. 5.1. In this chapter, a method for sensitising the optical fibre surface to be sensitive to the corrosion of aluminium alloys is studied. Firstly, a fluorescence-based indicator molecule was chosen and its properties in response to aluminium ions were characterised. The chapter is then divided into two sections. Firstly, a porous polymer was investigated for embedding the indicator molecule, where the exposed-core fibre was tested in a corrosion simulation. In the following section a surface based approach was tested using enclosed suspended-core fibres. Here only aluminium ion sensing was performed with a view that it could be expanded to corrosion sensing. The results of this later section have been compiled into a paper, which is shown in Appendix D.

5.1.1 Approach

The approach chosen for this project is to use an organic indicator molecule that fluoresces when complexed with aluminium ions, which are released in the early stages of corrosion of aluminium alloys [8]. The advantage of this method is that it can be specific and also sensitive, as very low concentrations of aluminium can be detected. For example, it has been shown that concentrations as low as 200 nM and 20 nM have been detected using the fluorescence-based organic indicator molecules morin [148] and lumogallion, respectively [148]. However, the primary motivator for using this approach is that it is amenable to spatially continuous distributed sensing by performing time domain measurements, as was demonstrated in [P8]. Methods such as metal coated fibres (Sec. 2.8.2) introduce too high a loss to the system and could thus only be used for a quasi distributed sensor.

There are a number of options for implementing a fluorescence-based indicator approach. The first consideration is the choice of the indicator molecule, which is discussed in the

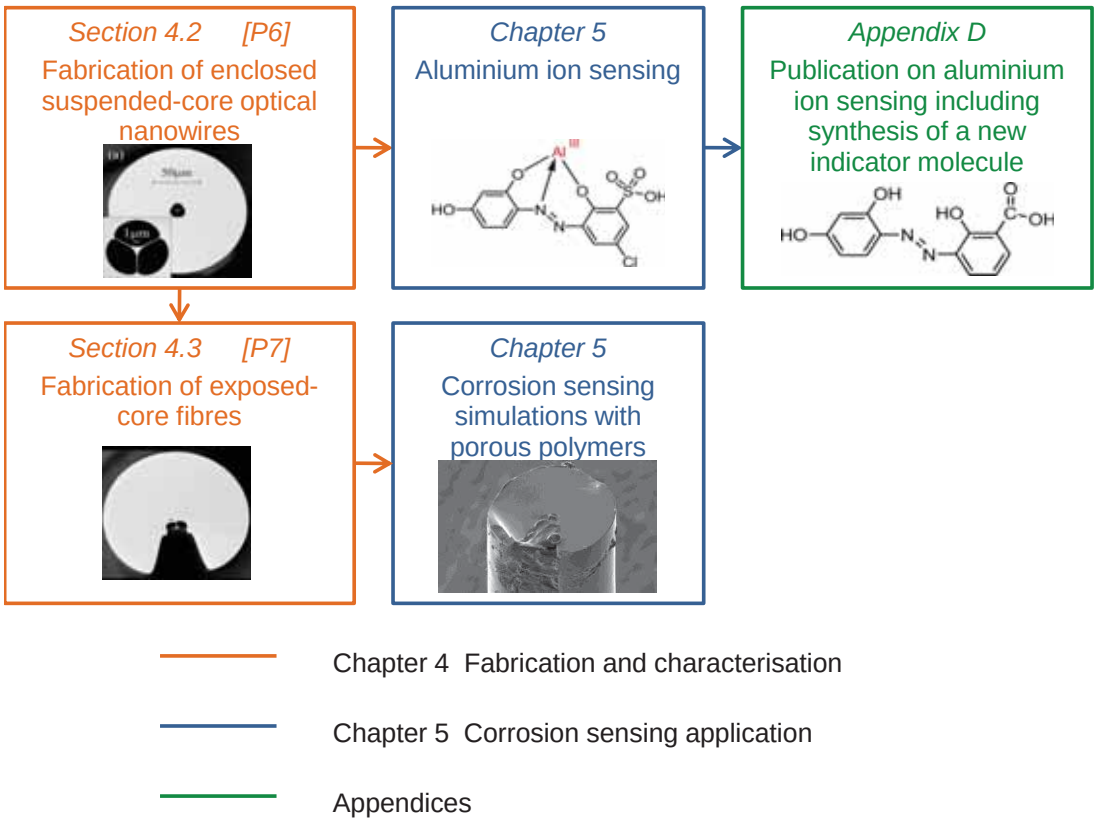

FIGURE 5.1: Flowchart showing the links between Chapter 5 and publications, appendices, and other chapters.

next section. The second consideration is selection of a method for immobilising the fluorophore to the fibre surface, which is necessary if the fibre is to be left *in-situ* and inaccessible for long periods of time as would be the case for aircraft corrosion sensing. Several methods to achieve this are available as was discussed in Sec. 2.6. In this project two methods were chosen, the first was to embed the indicator molecule into a porous polymer (Sec. 5.4) and the second was to covalently attach to a polyelectrolyte layer that is held electrostatically to the fibre surface (Sec. 5.5).

The advantage of the polymer approach is that it is able to protect the core of the fibre from unwanted environmental contaminants, but a related problem is adjusting the porosity so that the indicator molecule is trapped within the polymer, but diffusion of the analyte (aluminium ions) is possible. On the other hand, the polyelectrolyte method, as will be seen, produces a very thin layer. This means that the aluminium ions can easily reach the indicator molecule but the fibre core is not well protected. Other important considerations include the longevity of the coating, where the polymer will likely be superior, and how well the indicator is immobilised. A porous polymer only

holds the indicator by physical entrapment while the polyelectrolytes attach the indicator to the surface via electrostatic and covalent bonding. However, it is unclear which is superior as it would depend on many factors such as polymer porosity, environmental conditions, and the chemistry of either the porous polymer or the polyelectrolytes.

5.1.2 Choice of Organic Fluorophore

The ideal characteristics of a fluorescent indicator for aluminium include the following.

1. Fluorescence increase when complexed to aluminium. In contrast, quenching based systems can suffer from erroneous results due to variations in system power, such as from fibre degradation, reduced coupling efficiency, or photobleaching.

2. Stability and operation in a suitable pH range. Most corrosion occurs in either strongly acidic or strongly basic conditions [8]. It is unlikely that a single type of molecule would be able to operate (that is, fluoresce in response to aluminium ions) in both strongly acidic and basic conditions and thus the work in this chapter will concentrate on acidic conditions.

3. The excitation and fluorescence wavelengths of the molecule should be in the high transmission window of the optical fibre. As was seen in [P6] and [P7], this occurs between approximately 500 nm to 1500 nm for the lead-silicate (F2) glass used in this project.

4. High chemical and photo stability. These are often not quoted in literature but are essential for a sensor that is intended to be operational for long periods of time. This is particularly important for this project given that the sensor will need to survive for a long period of time after it is embedded into a structure.

5. Selective to aluminium. This is not a significant issue for this particular application as the detection of any metal ions in solution would also likely correspond to corrosion, but could be important for other aluminium-ion sensing applications such as water quality testing.

A list of potential candidates that satisfy some of the above conditions are shown in Table 5.1. The molecule chosen for this project is lumogallion due to its visible light operation,

suitable pH range, and commercial availability. The principle of operation is shown in Fig. 5.2. When not complexed to aluminium ions, lumogallion is weakly fluorescent. When complexed to aluminium ions, the molecule becomes strongly fluorescent due to an increase in rigidity that reduces non-radiative losses [181].

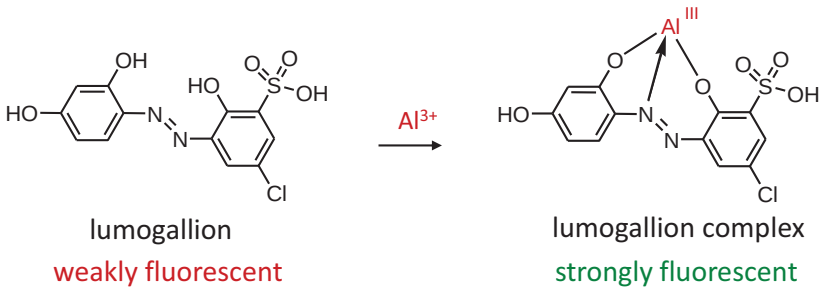

FIGURE 5.2: Chemical structure for lumogallion and how it can form a fluorescent complex with aluminium (III) ions [182, 183].

Table 5.1: List of fluorescence-based indicator molecules for detecting aluminium ions

Common name or abbreviation	Chemical name	Excitation wavelength[1] (nm)	Fluorescence wavelength[2] (nm)	pH range[3]	References
Purpurin	1,2,4-trihydroxyanthaquinone	540	600	5 to 7	[148]
DHAB	2,2'-dihydroxyazobenzene	505	600	6 to 8	[184–189]
Lumogallion	4-chloro-3-(2,4-dihydroxyphenylazo)-2-hydroxybenzene-1-sulphonic acid	502	588	2 to 5.7	[182, 183, 190–193]
Morin	2',3,4',5,7-Pentahydroxyflavone	430	500	7	[147, 182, 190]
8-HQ	8-hydroxyquinoline	360 to 390	520	acidic	[8, 194]
PAN	1-(2-pyridylazo)-2-naphthol	535	560	3 to 6	[195]
Alizaren Red PS	1,2,4-trihyroxy 9,10-anthraquinone-3-sulfonic acid	480	564	3 to 4	[196]
SAPH	Salicylaldehyde picolinoylhydrazone	384	468	5.4	[197]
DBIH	Dihyroxybenzaldehyde-Isonicotinylhydrazone	394	484	3.5 to 5.5	[198]

1. Most commonly used wavelength, usually close to absorption peak. Note however that the absorption spectrum is usually quite broad ($\geq$ 40 nm).
2. Center of the fluorescence emission when excited at the specified excitation wavelength. Note however that the fluorescence spectrum is usually quite broad ($\geq$ 40 nm).
3. Based on pH ranges used in experiments in literature. Generally not conclusive as this is often not thoroughly studied, to be taken as a guide only.

5.2 Characterisation of Lumogallion

The first experiments performed were cuvette spectroscopic and fluorometric measurements in order to confirm the expected behaviour of lumogallion.

5.2.1 Sample Preparation

All lumogallion used in this project (unless modified, as in Sec. 5.5) was purchased from TCI-America (98% purity). Unless otherwise stated, the lumogallion was dissolved into an acetic acid buffer solution. Acetic acid and sodium acetate were purchased from Sigma-Aldrich. Aluminium ions were in the form of hydrated aluminium (III) potassium sulphate, also purchased from Sigma-Aldrich. Throughout this chapter the presence of hydrated aluminium (III) potassium sulphate will simply be referred to as *aluminium ions*. Unless otherwise stated, all cuvette samples were prepared without any further purification or modification at room temperature using distilled water as the solvent. Disposable plastic 1 cm $\times$ 1 cm $\times$ 4.5 cm cuvettes were used for all cuvette measurements.

5.2.2 Absorption Measurements

Absorption measurements were performed using an incandescent lamp, a fibre coupled cuvette holder (Ocean Optics, CUV-ALL-UV), and a CCD-array spectrometer (iHR 320 spectrometer with Synapse CCD detector). The concentration of lumogallion was 50 μM and the concentration of aluminium ions was chosen to be 0 μM and 100 μM. This meant that the spectrum was measured for uncomplexed lumogallion (0 μM Al^{3+}) and fully complexed lumogallion (100 μM Al^{3+}). That is, for the 100 μM Al^{3+} sample the number of aluminium ions outnumbers the number of lumogallion molecules and thus it is assumed that the majority of lumogallion molecules in the sample have formed a complex. The pH was set to pH = 5 for this experiment, which corresponds to potentially corrosive conditions, which is close to the optimum value of pH = 5.2 [182, 190, 191], where the fluorescence emission is greatest.

The results of Fig. 5.3 show that lumogallion has strong visible light absorption, as expected. In its uncomplexed form lumogallion has an absorption peak at approximately

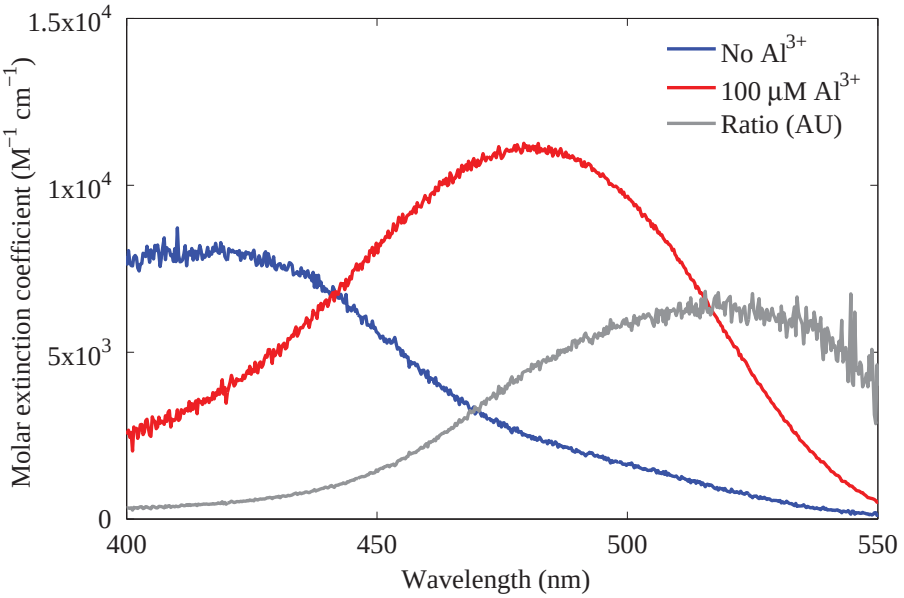

FIGURE 5.3: Cuvette measurements for the spectral absorption of lumogallion at pH = 5 where two different concentrations of aluminium (III) ions are present. The concentration of lumogallion was 50 μM. The ratio indicates the relative absorption for the 100 μM aluminium ion sample compared to the 0 μM aluminium ion sample.

425 nm, whereas the complexed form has a shifted absorption peak centred at approximately 480 nm, noting that both peaks are relatively broad (> 50 nm). The strongest fluorescence can thus be obtained by exciting close to 480 nm, such as 488 nm from an argon-ion laser. Also shown in Fig. 5.3 is the ratio of the complexed absorption spectrum to the uncomplexed absorption spectrum (grey curve). This is important because, as will be seen shortly, it is the background fluorescence of the uncomplexed lumogallion that determines the lowest concentration of aluminium ions that can be detected. Figure 5.3 shows that the peak in this ratio occurs at longer wavelengths, such as 532 nm from a doubled Nd:YAG laser (which has thus been used in the following measurements), where the excitation of uncomplexed lumogallion is low. This is particularly important for a distributed sensor where the light source will need to propagate with low loss over long distances without significant absorption from the indicator molecule when uncomplexed.

5.2.3 Fluorescence Measurements

In this section the fluorescence response of lumogallion to various concentrations of aluminium ions was tested in order to to determine the linearity of the response, which is

important if a quantitative sensor is to be made, and to determine the lowest concentration that can be measured. These are both effected by the noise characteristics of the source and detector, the source power, as well as the behaviour of the chemical.

The cuvette fluorescence measurements were performed using a similar experimental setup to that used for the absorption measurement. A 532 nm laser (JDSU, Solid-State, Compact) was directed via a multimode fibre (MMF) into the cuvette which was held within a fibre coupled cuvette holder (Ocean Optics, CUV-ALL-UV). Fluorescence was captured perpendicular to the excitation pump into a multi-mode fibre (MMF) and directed into a CCD-array spectrometer (iHR 320 spectrometer with Synapse CCD detector). The experimental setup is shown in Fig. 5.4.

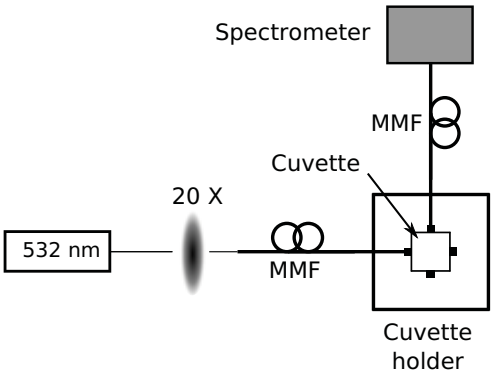

FIGURE 5.4: Experimental setup for fluorescence measurements using cuvettes.

The raw spectra are shown in Fig. 5.5 where it is seen that the fluorescence intensity increases approximately linearly with increase in aluminium ion concentration over the range of 0.2 μM to 50 μM. The spectra were then integrated from 540 nm to 800 nm and divided by the 0 μM sample (Fig. 5.6) so that the curve demonstrates the relative level of fluorescence measured compared to the uncomplexed sample. Note that the lower integration limit of 540 nm was chosen to avoid excitation light, and the upper limit of 800 nm was chosen because the fluorescence spectrum was over an order of magnitude lower than the peak value at wavelengths beyond this.

Figure 5.6 confirms that the response is close to linear from 0.2 μM to 50 μM, with a linear fit R^2 value of 0.98 in this range (with a base 10 logarithm taken of the data). The minimum concentration detected was approximately 0.2 μM, where below this the fluorescence from the small proportion of complexed lumogallion could not be distinguished from that of the uncomplexed lumogallion for this particular experimental configuration. Figure 5.5 shows that it is the background fluorescence of the uncomplexed lumogallion

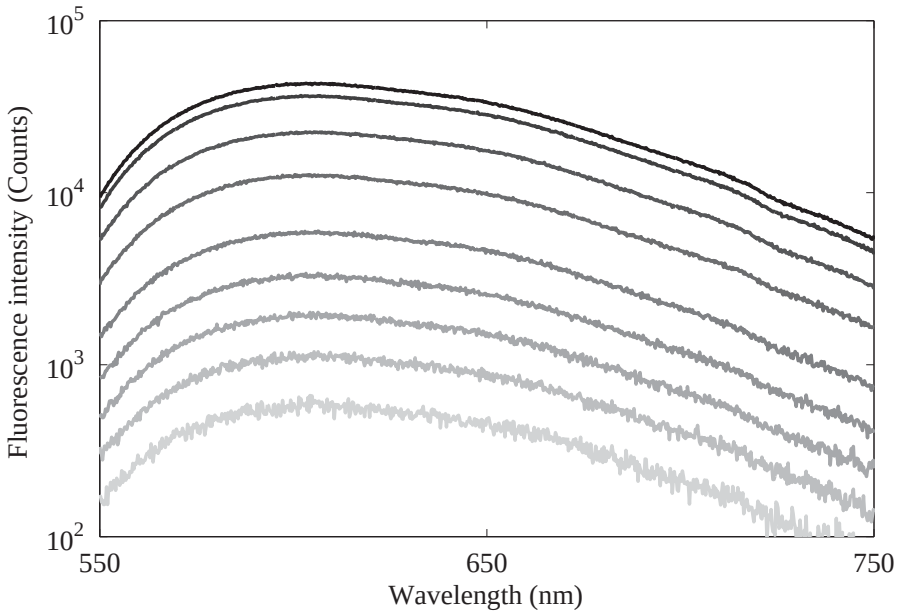

FIGURE 5.5: Cuvette measurements for the fluorescence of 50 μM lumogallion at pH = 5 for various concentrations of aluminium (III) ions present, excited at 532 nm. The aluminium ion concentration increases with increasing line darkness, 0 μM (lightest grey), to 0.2 μM, 0.5 μM, 1 μM, 2 μM, 5 μM, 10 μM, 20 μM, 50 μM (black).

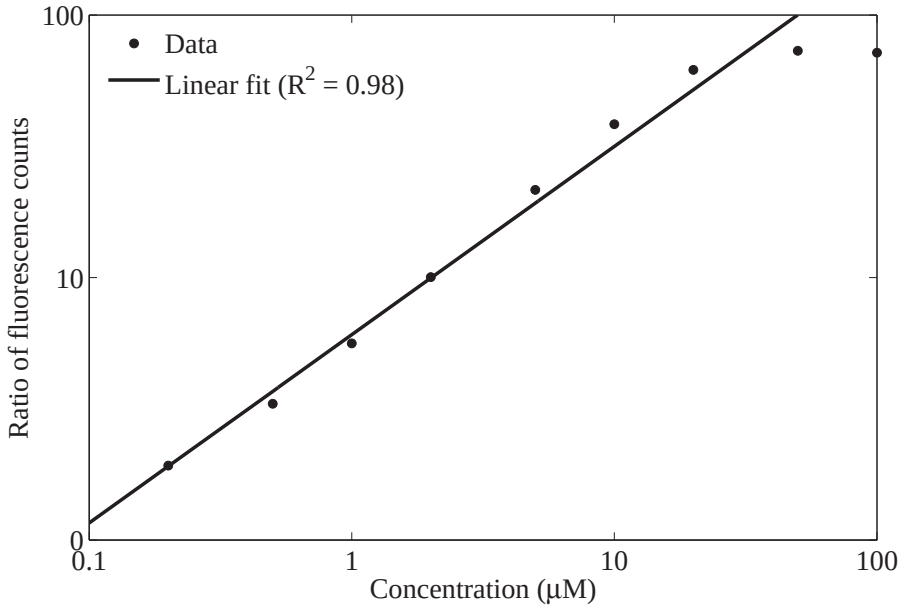

FIGURE 5.6: Cuvette measurements for the fluorescence of 50 μM lumogallion at pH = 5 for various concentrations of aluminium (III) ions present, excited at 532 nm. The spectra from Fig. 5.5 have been integrated and divided by the 0 μM aluminium ion sample. The linear fit is for the data between 0.2 μM and 50 μM.

that sets the minimum concentration that could be detected, rather than limits in the measurement system noise. This could either be due to impurities in the purchased lumogallion or from intrinsic fluorescence of the molecule. In principle, this could be reduced by lowering the lumogallion concentration, which would also reduce the maximum concentration that can be detected. Thus, a more useful figure of merit is that approximately two orders of magnitude of aluminium ion concentration can be linearly measured, provided that noise does not prevent the lower concentrations from being measured.

5.3 Exposed-Core Fibre Solution Measurements

The ultimate aim is to immobilise lumogallion molecules onto an MOF surface by some means. However, a first step is to test the ability to use an MOF for measuring lumogallion fluorescence when in solution form. This was achieved by immersing short lengths of exposed-core fibre into lumogallion-aluminium solutions and then measuring the fluorescence coupled into the core of the fibre. Note that similar experiments could be done using enclosed suspended-core fibre and should, in principle, yield similar results.

The exposed-core fibres used in this experiment were described in detail in [P6]. They were from trial #4, with a core diameter of 3.2 μm, a loss of 2-6 dB/m at the wavelengths used here (500 to 800 nm), and were made from lead-silicate (F2) glass.

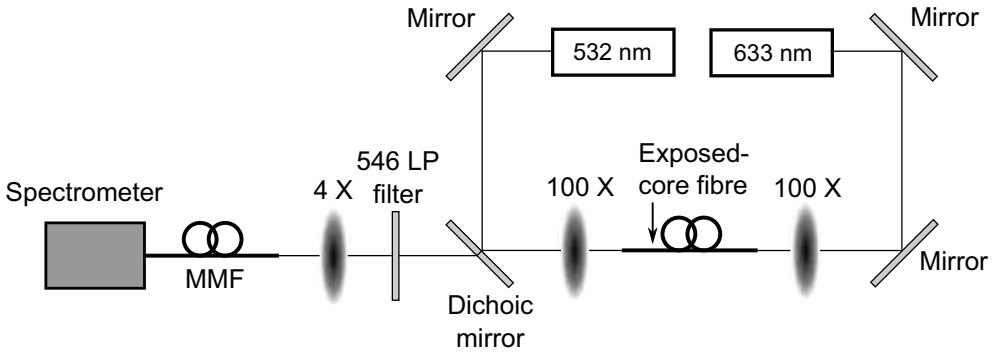

FIGURE 5.7: Experimental setup used to measure the fluorescence captured by an exposed-core fibre when immersed into a lumogallion solution containing varied concentrations of aluminium ions. Note that the details of the immersion setup are not shown here. The 633 nm HeNe laser was only used for alignment of the multi-mode fibre (MMF) prior to immersion. After alignment it was then turned off and the right-hand end of the fibre was immersed into the lumogallion solution.

As shown in Fig. 5.7, 532 nm laser light (JDSU, Solid-State, Compact) was coupled into the exposed-core fibre using a 100× microscope objective. Prior to measurement the coupling into the core of the fibre was measured using a power meter and this value was later used for normalising the results to the coupling efficiency. This was necessary due to the variability that can result from coupling into small-core fibres using free space optics, as was done here. Note that the output power was assumed to be proportional to the coupling efficiency due to the fibre length being short compared to the expected loss (12 cm compared to 2-6 dB/m in [P7]), and the length being consistent between samples. The 633 nm HeNe was then coupled into the opposite end of the fibre so that alignment into the multi-mode fibre (MMF) and thus the spectrometer (iHR 320 spectrometer with Synapse CCD detector) could be optimised. It was subsequently turned off. The right hand side of the exposed-core fibre was then flame-sealed so that the resulting measurements would be from the exposed region of the fibre, rather than from the internal holes. That is, the end of the fibre was placed briefly (approximately one second) into a naked flame so that the end of the fibre melted and the holes closed. The sealed end of the fibre was then immersed into the lumogallion solution, where 2 cm out of a total length of 12 cm was immersed. Note that longer lengths could have been used but this was not found to be necessary in order to achieve a strong signal in this experiment. After 10 seconds of immersion a spectral scan was recorded. The spectra were integrated and then normalised to both the initial coupled power (which varied between 8 μW and 12 μW and was measured previously with a power meter) and the spectrometer integration time (0.1 to 1.0 seconds). The integrated results were then then divided by the 0 μM Al^{3+} sample. The results are shown in Fig. 5.8 and are the exposed-core fibre equivalent of the cuvette measurements in Fig. 5.6.

The results of Fig. 5.8 show a near linear response to aluminium ion concentration, thus demonstrating that exposed-core fibres can be used for sensing of aqueous chemicals. However, these results show a greater variability compared to the previous cuvette measurements, where the R^2 value for a linear fit between 0.5 μM to 50 μM was 0.90, compared to 0.98 for the cuvette measurements (where the 0.2 μM sample was also included). This is likely attributed to variations in coupling efficiency, which would be far greater for the exposed-core fibre setup compared to the cuvette setup. This could potentially be solved in future by splicing the exposed-core fibre to another fibre that has better coupling stability. Note that an advantage of using an exposed-core fibre in a

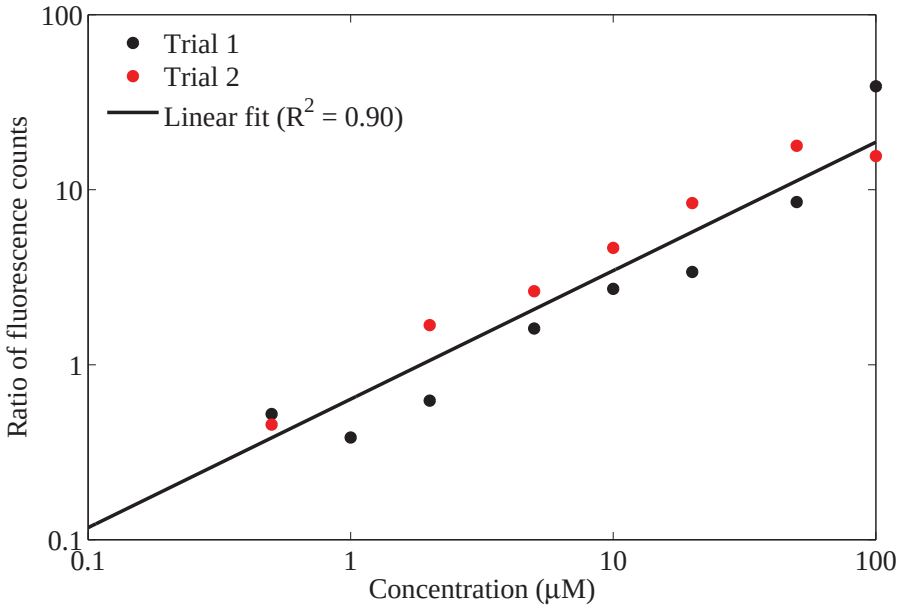

FIGURE 5.8: Integrated fluorescence response of 50 μM lumogallion at pH = 5 for various concentrations of aluminium (III) ions present. The spectra obtained were integrated and divided by the 0 μM aluminium ion sample. The linear fit is for the data between 0.5 μM and 50 μM.

spliced configuration is that there would be no issues with gas pressure build-up within the holes of the fibre when filling with liquids as would be the case with an enclosed MOF.

The minimum concentration of aluminium that could be detected, that is, where the data was reliably greater than unity in Fig. 5.8, was 5 μM. Unfortunately, this is higher than the 0.2 μM that was measured using the cuvette samples despite using the same spectrometer and laser for both experiments. This is due to low coupling efficiency into the exposed-core fibre (approximately 10-20%), transmission loss of the fibre, and increased background signal from the glass background fluorescence [4, 199, 200]. The glass background fluorescence arises from impurities within the glass and adds a baseline signal to the results that interferes with the intended fluorescence measurement.

The interaction length and power fraction are also important factors. They can be used to define an effective interaction length, often called sensitivity [9], as power fraction (PF) $\times$ immersed fibre length (L). This effective interaction length is proportional to the fluorescent signal in the absence of fibre loss and when the pump is not absorbed significantly by the fluorophore. By extrapolating from the numerical results of [P3], the fundamental mode power fraction of the exposed-core fibre used in these experiments

(core diameter of 3.2 μm) is predicted to be approximately 0.1%. Thus, the effective interaction length is approximately PF $\times$ L = 0.1% $\times$ 2 cm = 20 μm, which is 500$\times$ smaller than the 1 cm interaction length of the cuvette, and also approximately 6000$\times$ smaller than the interaction length of the background glass fluorescence (12 cm).

By reducing the optical loss and background fluorescence via the use of higher purity glass, reducing the core diameter (for increased power fraction [P3]), and optimising the coupling efficiency it should be possible to reduce the minimum concentration that can be detected to the same levels as measured for the cuvette samples where it was the intrinsic background fluorescence of the lumogallion that prevented lower levels from being measured.

5.4 Porous Polymer Coating

5.4.1 Overview

In this experiment the porous polymer originally developed in Ref. [8] was used to immobilise lumogallion onto the surface of several types of optical fibres, and then the fluorescence response to aluminium ions was measured. Two types of experiments were performed. For the first experiment the optical fibres were dip coated with the polymer, the polymer was embedded with lumogallion, and then the fluorescence response was measured when dipped into an aqueous aluminium ion solution. In the second experiment the fibres were placed into model aluminium lap joints and held into a small groove with the porous polymer, which was then embedded with lumogallion. The lap joints were placed into a salt spray chamber which accelerated the corrosion of the aluminium plates and the fluorescence response was measured to determine if corrosion could be detected.

All porous polymer experiments (Sec. 5.4) were performed at the Defence Science and Technology Organisation (DSTO) in collaboration with Silvia Tejedor, Claire Davis, and Grant McAdam. The F2 exposed-core fibres and F2 bare fibres used in these experiments were prepared at The University of Adelaide as part of this project and taken to DSTO. The fibre coatings, salt spray chamber experiments, and optical measurements were all performed as a collaborative experiment at DSTO run primarily by

Stephen Warren-Smith and Silvia Tejedor. Data analysis and scanning electron microscope (SEM) imaging was performed at The University of Adelaide.

5.4.2 Material Preparation

The porous polymer is based on previous work performed by DSTO [8], which was subsequently refined and presented in Ref. [201]. The polymer preparation is designed to provide a highly porous membrane that, in principle, will embed the lumogallion but allow diffusion of the aluminium ions.

The porous polymer was prepared by combining 2 ml Poly(oxyethylene-co-oxypropylene)-triol (3-PEG) with 500 mg Tolonate HDT-LV2 (crosslinker) and 40 mg CAT TD33 amine catalyst. The coatings were applied within a short period of time of the polymer preparation ($<$ 20 mins) so that it did not start curing before it was coated. The polymer was then allowed to cure fully overnight.

In these experiments, the lumogallion was not embeded into the porous polymer until after the polymer had cured. Note that it may be possible in future to incorporate the lumogallion into the polymer preparation stage, but it is not yet known if this would interfere with the polymerisation reaction. Thus, embedding the lumogallion involved immersing the polymer samples into lumogallion solutions. For this purpose a 0.1 w/w% lumogallion solution was prepared by dissolving 0.1 g in 100 ml distilled water, which was further diluted to 0.001 w/w% by adding 1 ml to 100 ml distilled water.

For the dip-coated fibres, the final stage of the experiments was to immerse the fibres into an aluminium ion solution. For this a high concentration sample (compared to the cuvette experiments) was prepared in order to optimise the probability of a positive result given that the diffusion rate of aluminium through the polymer is unknown and could be quite low. That is, a 1 w/w% aluminium sulphate solution was prepared by dissolving 1 g in 100 ml distilled water.

5.4.3 Dip Coated Fibre Experiments

Eighteen optical fibres were dip-coated with the polymer. Six were F2 exposed-core fibres, six were F2 bare fibres (BF), that is, with no structure and thus an air cladding,

and six were silica bare fibres. The silica fibres were originally polymer-clad but this was stripped so that the porous polymer could be coated onto them. The outer diameters of these fibres were 160 μm, 160 μm, and 600 μm, respectively. The fibres were held vertically and manually dipped into the polymer solution for a length of approximately 2-3 cm. After curing overnight, lumogallion was embedded into the polymer by immersing the polymer coated section of the fibres into the 0.001 w/w% lumogallion solution for 16 hrs. Images of the F2 and silica bare fibres are shown in Fig. 5.9, noting that the exposed-core fibres appeared very similar to the F2 bare fibres due to their similar outer diameter.

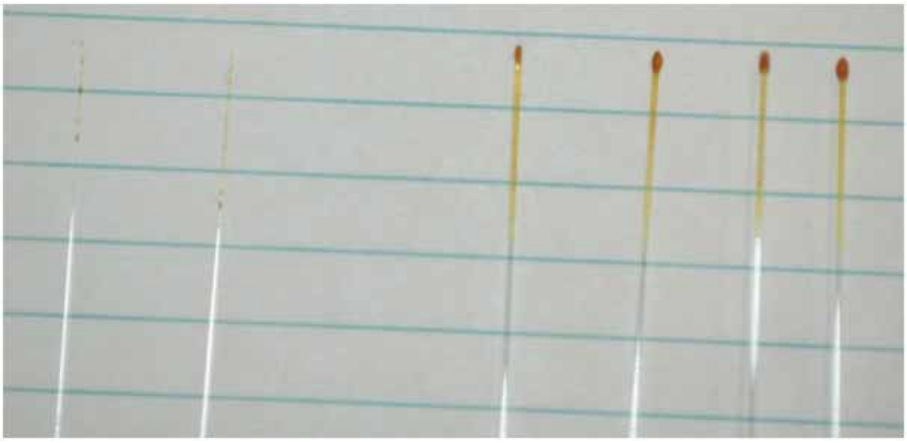

FIGURE 5.9: Images of two F2 fibres (left) and four silica fibres (right) after dip-coating with the porous polymer and then immersing into the 0.001% lumogallion solution overnight. The near-horizontal lines are 8 mm apart (as an indication of the scale of this image).

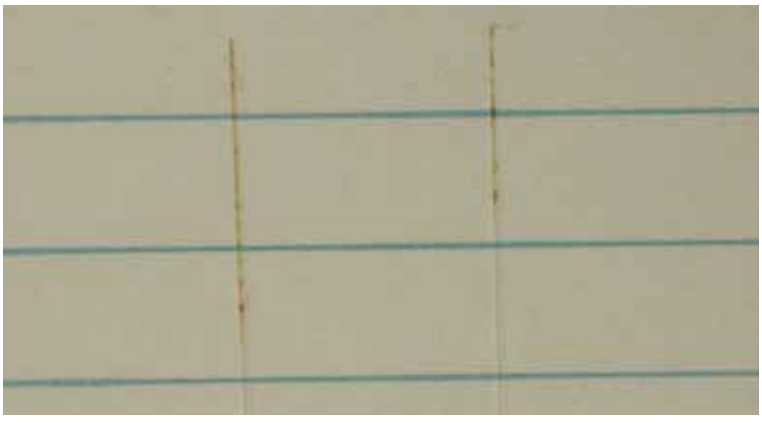

FIGURE 5.10: Images of two F2 bare fibres showing the inconsistent polymer coating. The near-horizontal lines are 8 mm apart.

The orange colouration of the polymer coating in Fig. 5.9 suggests that lumogallion was successfully embedded into the polymer. The colouration could also indicate simple surface adsorption but this is unlikely the case as the colour did not fade after rinsing.

The polymer coating appears to have better consistency for the larger silica fibre. The F2 bare and exposed-core fibres tended to have large conglomerations of polymer along the length as shown in Fig. 5.10.

To test how well the polymer infiltrated the wedged region of the exposed-core fibre several scanning electron microscope (SEM) images were taken of the fibre after cleaving at a coated region of the fibre. Samples of these images are shown in Fig. 5.11.

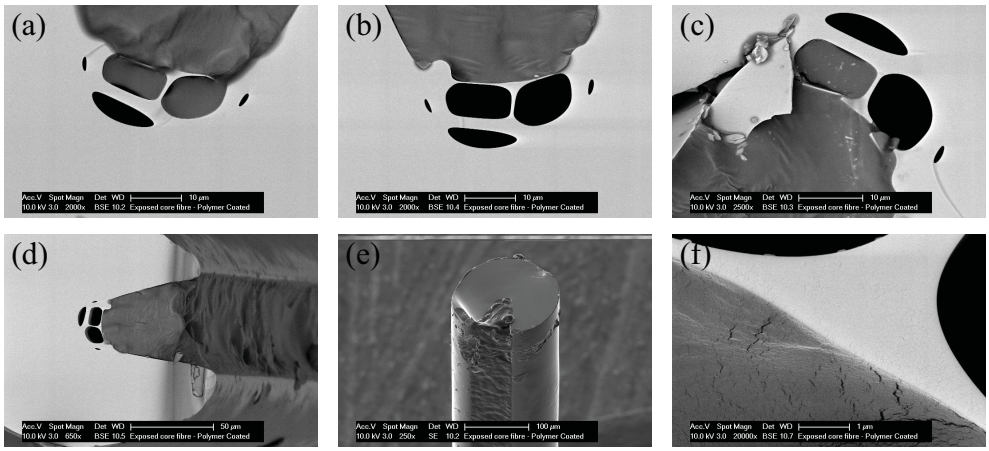

FIGURE 5.11: Scanning electron microscope (SEM) images of F2 exposed-core fibre after dip-coating with the porous polymer. (a) Core region where both holes were infiltrated, (b) no holes infiltrated, and (c) one hole infiltrated with the polymer. (d, e) Shows how the polymer fills the wedged region of the fibre. (f) Cracks observed in the polymer near the core of the exposed-core fibre.

The SEM images show that the polymer successfully infiltrated the wedged region and makes close contact to the core of the fibre. Unfortunately, the polymer sometimes infiltrates the holes of the fibre due to the struts breaking. Also, small cracks were observed in the polymer near the core of the fibre, which could partially explain the high losses in the polymer coated exposed-core fibres in the results that follow.

To measure the fluorescence response of the dip-coated fibres the setup shown in Fig. 5.7 was used except that the spectrometer was a USB2000 Ocean Optics spectrometer. Also, the 100× microscope objectives were replaced with 4× microscope objectives for the F2 and silica bare fibres and a 1.8 optical-density neutral density filter was used in front of the 532 nm laser to reduce the effects of photobleaching.

A background signal was recorded prior to immersing the ends of the fibres into the aluminium solution. This background signal is a result of glass fluorescence [199] and uncomplexed lumogallion fluorescence, and was found to be proportional to input excitation power. The coated end of the fibres were then immersed into the 1 w/w%

aluminium solution and the fluorescence spectra recorded over time. The spectra were then integrated and normalised to the background fluorescence signal prior to immersion. For controls, some of the fibres were immersed into distilled water only. The results are shown in Fig. 5.12. Note that some of the samples are not present, such as a water immersion measurement for the exposed-core fibre, which was due to fibre breakage during handling.

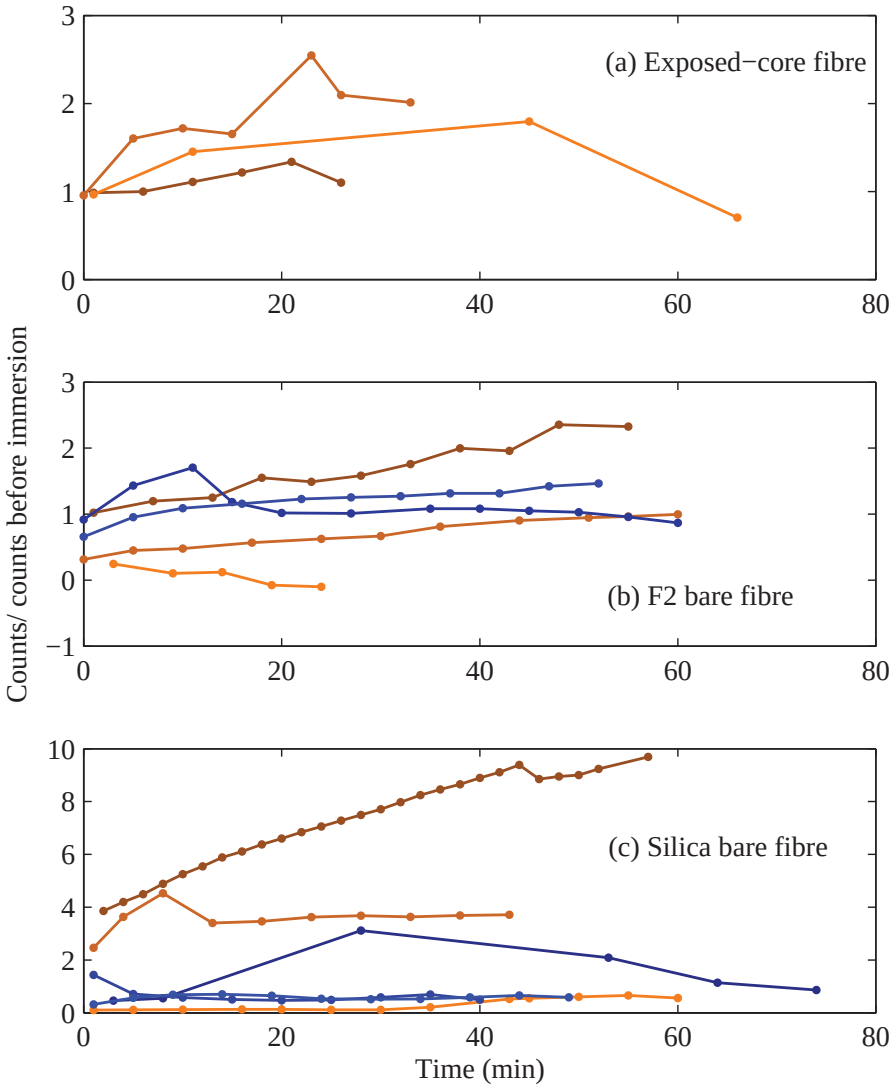

FIGURE 5.12: The fluorescence response for the dip coated fibres as a function of time. The orange curves (three shades, repeated experiment) correspond to when the fibres were immersed into the aluminium solution while the blue curves (three shades, repeated experiment) correspond to being immersed into distilled water only.

Unfortunately, the results of Fig. 5.12 do not show a strong correlation with time immersed into the aluminium ion solution. There are several possible reasons for this. First, the penetration depth of lumogallion or aluminium ions into the polymer is not

known and thus it is possible that the lumogallion or aluminium ions have not reached the evanescent field of the fibre. Alternatively, the evanescent field interaction of the bare fibres may not have been sufficient to provide a measurable signal, while the coupling efficiency and loss of the exposed-core fibre prevented the fluorescence being measured. For example, the output power of the third exposed-core fibre in Fig. 5.12 prior to immersion was only 8.3 μW out of a laser power of 24 mW when no neutral density filter was used. Assuming even a very poor coupling efficiency of 1% this still implies a fibre loss of approximately 1 dB/cm for the 15 cm long fibre. This was found to be similar, or worse, for the other exposed-core fibres after being coated with the polymer. Indeed, the increased loss of the exposed-core fibres after being coated with the polymer is a significant problem. It likely arises from a combination of scattering loss from the porous nature of the polymer and also the high intrinsic optical absorption of the polymer, given it had an opaque white appearance prior to lumogallion immersion. Improving the coated fibre optical loss could be achieved through both the fibre fabrication and polymer preparation. Of course, decreasing the background loss of the exposed-core fibre would assist towards reducing the overall loss after coating with a polymer. Also, improving the structural strength, such as with increased strut thickness, could prevent damage to the fibre as the polymer cures. Likewise, improving the optical transparency and consistency of the polymer is desirable, and it may be that a compromise between porosity and transparency is required.

In summary, a variety of optical fibres have been coated with a porous polymer coating that has been embedded with lumogallion. While the experimental results did not conclusively demonstrate a sensitivity to aluminium ions, the results show that a porous polymer can be successfully coated onto an exposed-core fibre, as well as bare F2 and silica fibres.

5.4.4 Lap Joint Experiments

Three lap joints were prepared for corrosion simulations, one with dimensions of approximately 10 $\times$ 10 cm^2 (short lap joint) and two with dimensions 10 $\times$ 20 cm^2 (long lap joint). The lap joints consisted of a perspex sheet with three 1 mm grooves, which was then bolted to an aluminium sheet. Each perspex sheet had an F2 exposed-core fibre, an F2 bare fibre, and a silica bare fibre placed individually into the grooves. The groove

was then filled with the polymer solution and was allowed to cure overnight. The lap joints, without the aluminium sheet, were then immersed into the 0.001 w/w% lumogallion solution for 16 hrs. An image of the lap joint after the lumogallion immersion but without the aluminium sheet attached is shown in Fig. 5.13

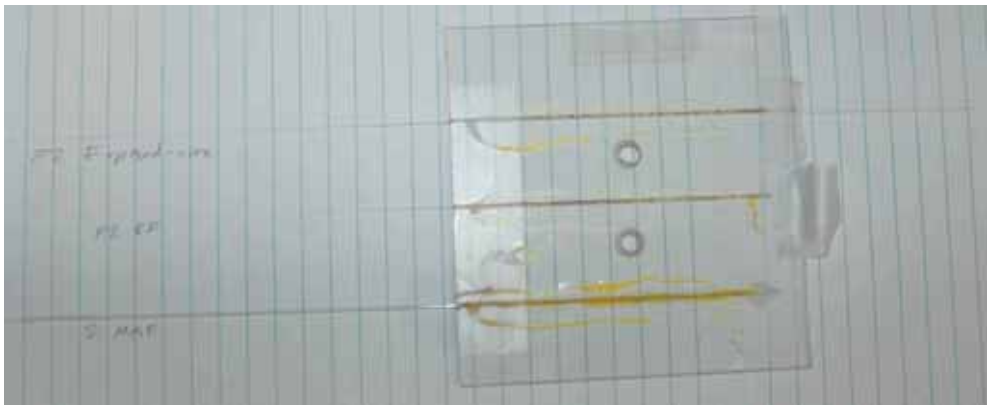

FIGURE 5.13: Image of the short lap joint image after the fibres have been embedded using the polymer and then immersed into lumogallion. Note that only the perspex side of the lap joint is shown, an aluminium plate was subsequently attached for the corrosion experiments.

The aluminium sheets were then attached to the lap joints and placed into a salt spray chamber (Ascott) that was located at DSTO, which is shown in Fig. 5.14. The purpose of the salt spray chamber is to rapidly accelerate the rate of corrosion for these types of experiments. An image of the lap joints with the aluminium sheets attached and after 16 hrs of being in the salt spray chamber is shown in Fig. 5.15.

The fluorescence of the fibres embedded in the lap joints was measured after each processing step using the same optics setup as used for the dip-coated fibres. The fluorescence was then measured after 16 hrs, 39 hrs, and 60 hrs in the salt spray chamber. The fluorescence spectra were then integrated with the results shown in Fig. 5.16. Only the F2 and silica bare fibres have been shown as the exposed-core fibres did not survive beyond the polymer coating step, that is, no measurable amount of optical power could be coupled into and out of the core of the fibre. This agrees with the findings for dip-coated fibres (Sec. 5.4.3) where very little power could transmit through the fibre, noting that the coating length for the dip-coated fibres was only 2 cm compared to 10 cm and 20 cm for the lap joints.

Unlike the dip-coated fibre results, the results for the lap-joint fibres in Fig. 5.16 show an increase in the fluorescence signal for increased exposure to a corrosive environment.

FIGURE 5.14: Salt spray chamber used to accelerate the rate of corrosion of the aluminium lap joints.

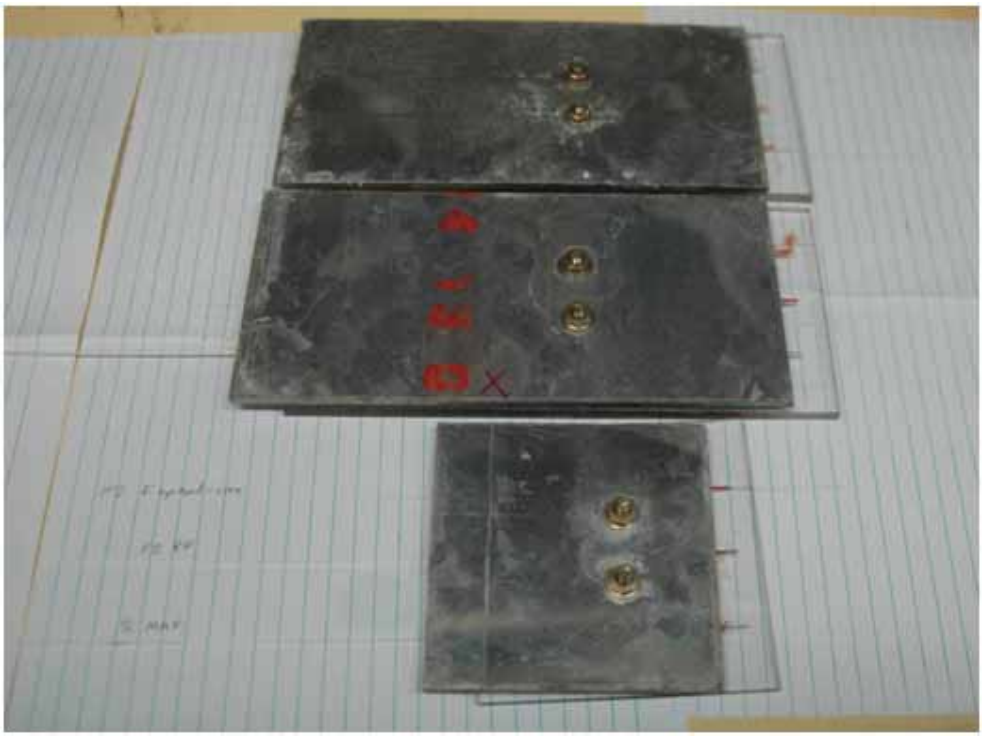

FIGURE 5.15: Images of all the lap joints with the aluminium plates attached. Image taken after 16 hrs in the salt spray chamber, where salt deposits and early corrosion can be seen on the aluminium plates.

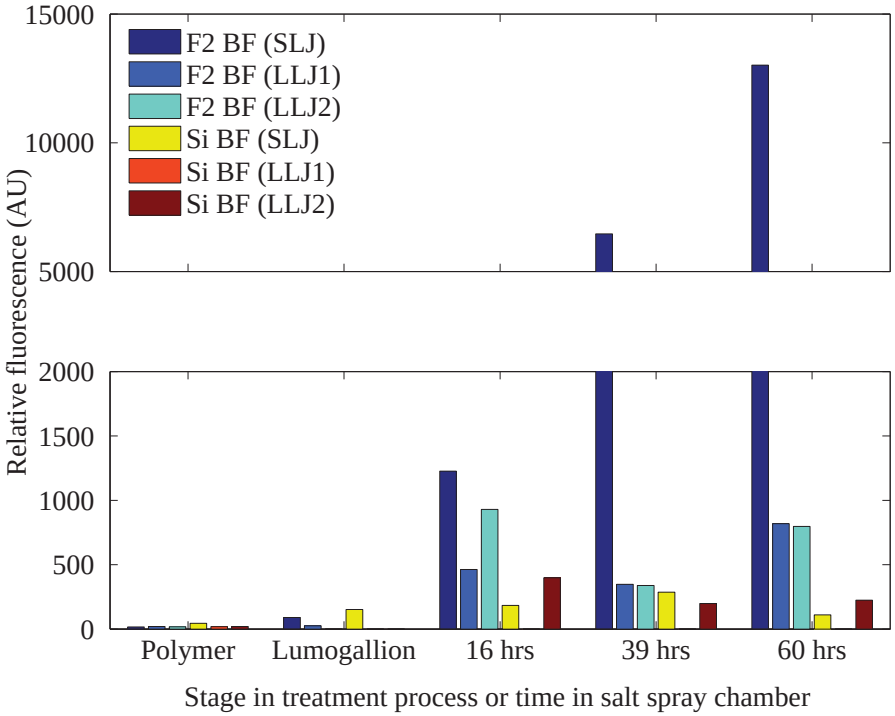

FIGURE 5.16: Fluorescence measured for the fibres embedded into the lap joints after polymer coating, lumogallion immersion, and three different lengths of time in the salt spray chamber. SLJ refers to the short lap joint and LLJ refers to the long lap joint.

This increase in fluorescence is strongest for the F2 bare fibre, which agrees with evanescent field theory that smaller core fibres should have higher sensitivity, and that the higher refractive index material should have a greater fluorescence capture [P4]. However, the results suffer from large inconsistencies, particularly seen by the anomalously high result for the F2 bare fibre in the short lap joint. It is unclear what has caused these inconsistencies. It is unlikely that a lack of repeatability in coupling into the fibres or the spectrometer is the cause as coupling into large core diameter fibres is generally repeatable to within approximately 10%. Explanations could include that the coating was not consistently applied to the fibre surface or perhaps free lumogallion was still present in the short lap joint for the F2 bare fibre. Alternatively, the corrosion itself may have not been consistent for the different lap joints, particularly given that aluminium alloys generally exhibits blisters and pitting rather than uniform corrosion [136, 202].

5.4.5 Discussion and Conclusions

Three different optical fibres were successfully coated with a porous polymer. The coating adhered well to the surface and did not appear to remove after immersion into

the lumogallion or when either placed into an aluminium ion solution or the salt-spray chamber. Lumogallion was also seen to incorporate into the polymer coating, seen by the colouration of the polymer after being immersed into the lumogallion solution. However, the dip coated fibres suffered from poor coating consistency. The coating appears more uniform for the larger silica bare fibre compared to the F2 bare fibres and exposed-core fibres. Meanwhile, the lap joint polymer coating appeared to form bubbles along the length of the channel. The solution to this problem will likely be optimising the coating procedure, as manual dip coating is unlikely to yield uniform coatings. Alternatives could include robotically controlled dip coating or coating that is performed as part of the fibre drawing process. In addition, modification of the chemistry so that the curing time is reduced will also be beneficial, otherwise the polymer will simply deform once coated onto the fibre.

Fluorescence measurements were performed with both dip-coated and lap-joint embedded fibres. The dip coated fibre measurements did not show a consistent increase in signal when immersed into an aluminium ion solution. In contrast, the lap-joint fibre results demonstrated a correlation, albeit somewhat inconsistent, between measured fluorescence and time spent in a corrosive environment, particularly for the F2 bare fibres.

As has been stated, there are several (addressable) reasons for the results having some inconsistencies. While the optical setup is a contributing factor, it is unlikely to be the primary reason, particularly for the large diameter bare fibres. This implies the chemistry of either the polymer, the lumogallion, the aluminium ions, or a combination of all three must be hampering the results. For example, the diffusion rates of the lumogallion and the aluminium ions through the polymer is an unknown that needs to be investigated more thoroughly. The porosity of the polymer should also be characterised in order to understand the diffusion behaviour.

In regards to applying this method to microstructured optical fibre sensing, these experiments demonstrate that a porous polymer can be coated onto an exposed-core fibre and fully infiltrate the wedged region of the fibre. However, it was found that the exposed-core fibre suffered from an increase in optical loss after being coated with the polymer. In this case, the high sensitivity of the MOF can cause it to also become highly sensitive to the coating consistency and absorption properties. This is an issue that will need to be solved if distributed sensing is desired.

5.5 Polyelectrolyte Attachment

5.5.1 Concepts

In this section the second method of attaching lumogallion to the surface of optical fibres is studied. Here a polyelectrolyte coating was first electrostatically coated onto the glass surface and then a derivative of the lumogallion molecule was covalently attached to this layer.

Polyelectrolytes provide a method for giving functionality to the surface of otherwise inactive surfaces such as glass [112]. In these experiments a polyelectrolyte with an amine functional group (PAH, poly(allylamine hydrochloride)) was used so that compounds with carboxylic functional groups can be attached using a standard carboxyl-amine coupling reaction. The polyelectrolyte attaches to the glass surface using electrostatic forces. PAH is a strongly electropositive polymer that can bind to the weakly electronegative glass surface as shown in the bottom half of Fig. 5.17. The advantage of this method is that it can be used for many different surfaces, including different glass surfaces [110], but suffers from the fact that the interaction with glass is relatively weak compared to, say, a covalent bond.

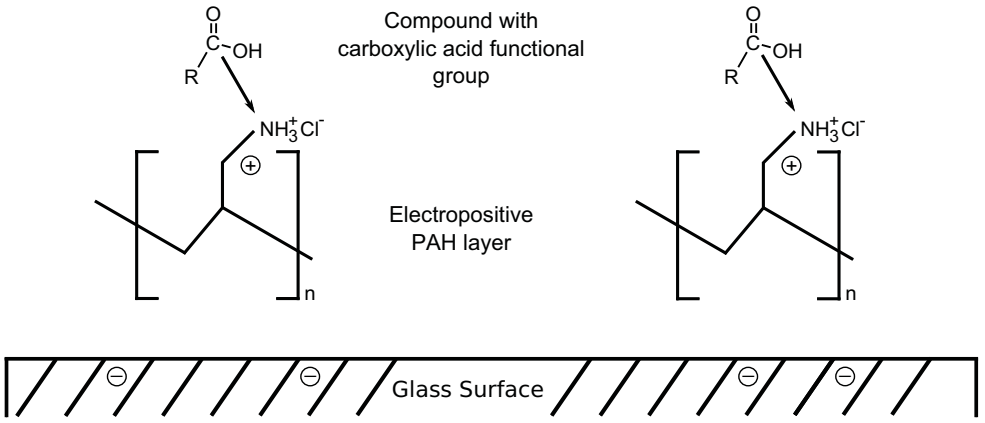

FIGURE 5.17: The polyelectrolyte, PAH in this case, forms an electrostatic interaction with the glass surface. The amine functional groups can then be used to attach other compounds with suitable functional groups for binding, such as a carboxylic acid functional group.

However, observe in Fig. 5.18 that the original lumogallion compound does not have a suitable functional group to couple to a PAH layer. Therefore a derivative of lumogallion was synthesised (by Sabrina Heng, The University of Adelaide, as a collaboration created to support the chemical aspects of this corrosion sensing project) so that it would have

similar aluminium ion complexing abilities to lumogallion but has a carboxylic acid functional group (Fig. 5.18) that can, in the presence of suitable coupling reagents, couple to PAH as shown in Fig. 5.17. Observe that the lumogallion derivative still has the components required for it to be able to form a fluorescent complex with aluminium.

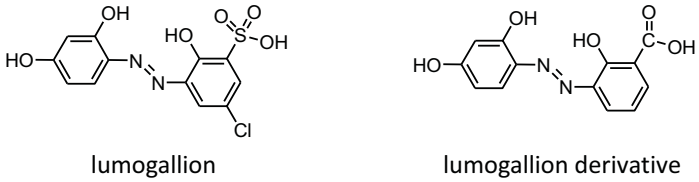

FIGURE 5.18: Chemical structure for lumogallion and the derivative used for polyelectrolyte-based attachment.

The work in this section, including the synthesis of the lumogallion derivative, has been prepared for publication. As it was prepared after this chapter was drafted it is included in Appendix D. A statement of contribution is also included at the start of Appendix D.

5.5.2 Compound Characterisation

Before testing the attachment of the lumogallion derivative (L2) to glass surfaces, its absorption and fluorescence properties were tested in comparison to the original lumogallion compound (L1). Cuvette samples were prepared and measurements were performed as described in Sec. 5.2. The absorption measurements are shown in Fig. 5.19 and the fluorescence measurements are shown in Fig. 5.20. The results of the original lumogallion compound (L1) have been shown again for comparision.

Figures 5.19 and 5.20 show that both the absorption and fluorescence of the lumogallion derivative (L2) is similar to that of the original lumogallion compound (L1). The fluorescence results of Fig. 5.20 show that the fluorescence intensity of the lumogallion derivative is lower compared to the original lumogallion compound. However, this occurs for both complexed and uncomplexed forms of the compound and thus is not necessarily disadvantageous when competition with the uncomplexed lumogallion background is the limiting factor in the measurement. For this reason, the data in Fig. 5.21 shows the fluorescence results when the spectra have been integrated, the dark noise subtracted, and divided by the associated 0 μM Al^{3+} measurement, as was done for Figs. 5.6 and 5.8. Figure 5.21 shows there is very little difference in aluminium ion

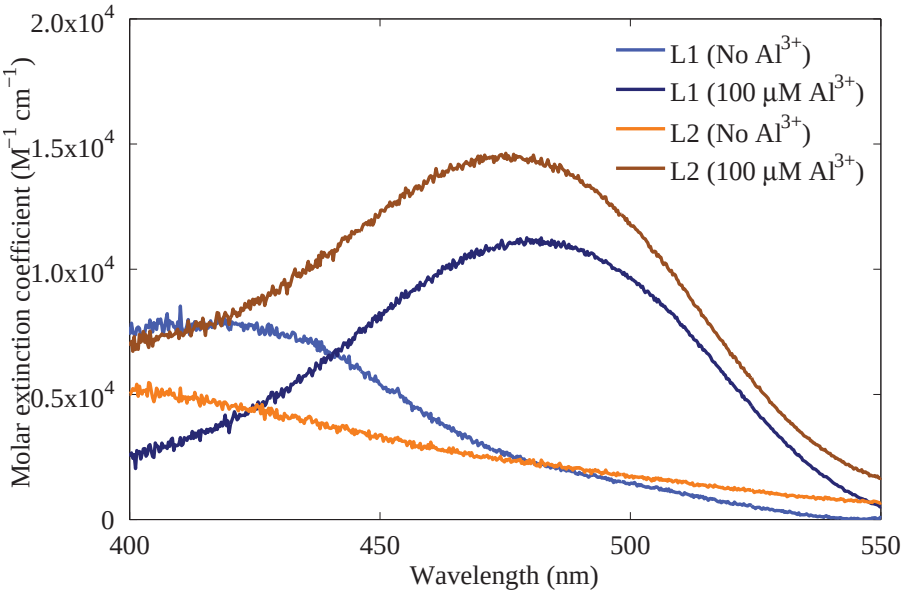

FIGURE 5.19: Cuvette measurements for the spectral absorption of commercial lumogallion (L1, blue curves) and the in-house synthesised lumogallion derivative (L2, orange curves) at pH = 5 for various concentrations of aluminium (III) ions present (shown in legend). The concentration of both the original lumogallion (L1) and the lumogallion derivative (L2) was 50 μM.

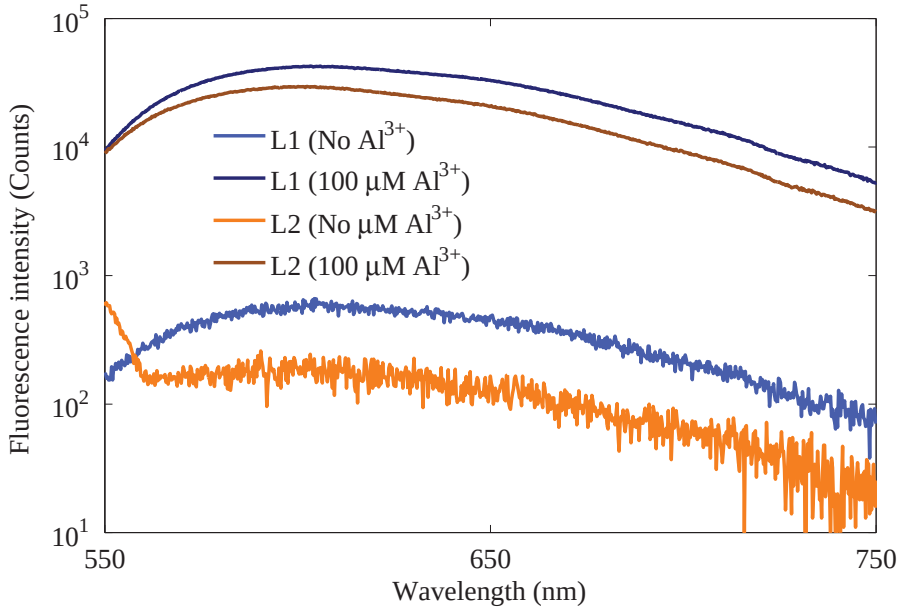

FIGURE 5.20: Cuvette measurements for the fluorescence of 50 μM original lumogallion (L1, blue curves) and 50 μM lumogallion derivative (L2, orange curves) at pH = 5 for various concentrations of aluminium (III) ions present (shown in legend), excited at 532 nm.

sensing performance between the two compounds. Most importantly, Fig. 5.21 shows that the lumogallion derivative emits fluorescence that increases linearly with increasing aluminium concentration, making it suitable for a sensing application.

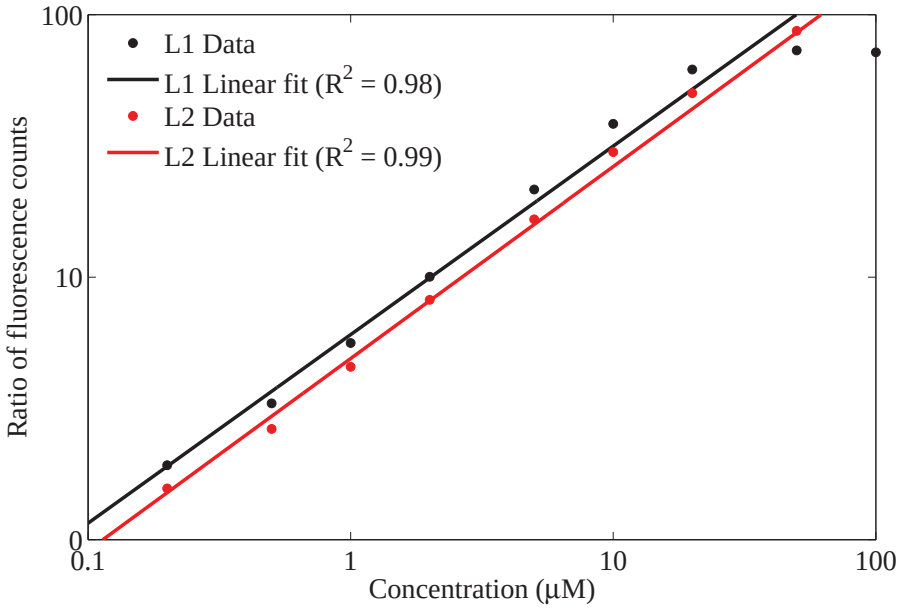

FIGURE 5.21: Integration of the results in Fig. 5.20, where the dark noise has been removed and each data point has been divided by the associated 0 μM Al^{3+} measurement.

5.5.3 Glass Slide Experiments

Glass slides were used to test and optimise the ability to attach the lumogallion derivative to a glass surface. While the glass and coating procedures necessarily vary from that used for optical fibre experiments, this allowed the concept to be demonstrated for a simpler physical arrangement. The primary differences between the glass slide experiments and the MOF experiments were differences in glass chemistry and the coating procedure. The MOFs were fabricated from lead-silicate (F2) glass, compared to the primarily silica microscope slides. Also, the glass slides were coated by immersing them into the required solution whereas coating the MOFs, as will be seen in Sec. 5.5.4, required forcing the liquids through the small MOF holes.

In the following experiments two coating layers were applied to the glass slides, a single polyelectrolyte layer and a lumogallion layer.

For each experiment eight glass slides were prepared by cutting standard microscope slides into dimensions of 1×2.5 cm^2. The slides were then rinsed thoroughly with distilled water and methanol, and then dried with nitrogen gas. The slides were placed vertically onto a teflon rack (length 10 cm), which fit into the 30 ml teflon bath shown in Fig. 5.22.

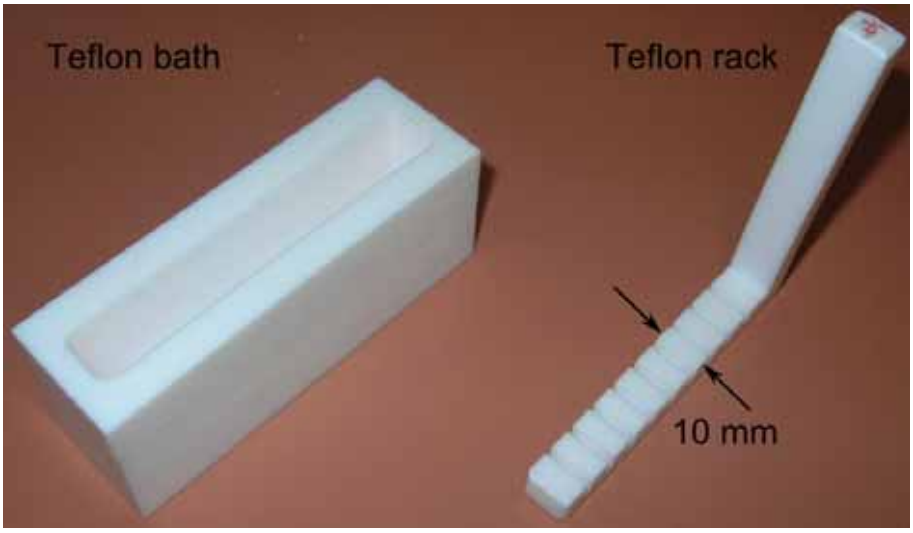

FIGURE 5.22: Teflon bath and rack used for coating glass slides

The polyelectrolyte layer consisted of PAH (poly(allylamine hydrochloride)), prepared with a concentration of 2 mg/ml in 1 M NaCl. The PAH solution was then placed into the teflon bath and allowed to sit for one hour. The slides were then rinsed with distilled

water only, as organic solvents can remove the PAH coating. The lumogallion solution was prepared with a concentration of 100 μM in distilled water, with 200 μl of EDC (1-Ethyl-3-(3-dimethylaminopropyl)carbodiimide) and NHS (N-hydroxysuccinimide) solution (Biacore coupling solutions) added to 60 ml of the lumogallion solution, of which approximately 30 ml was used for each experiment. The teflon bath, containing the glass slides and teflon rack, was then filled with the lumogallion solution for approximately three hours. The slides were then rinsed thoroughly with distilled water and dried with nitrogen gas.

Controls for the experiment were prepared with either only the PAH layer or only the lumogallion layer, the order of these controls are shown in Fig. 5.23(a) with respect the the results that follow.

To measure the fluorescence response of the coated slides to aluminium ions a fluorescence imager was used (Typhoon Variable Mode Imager). The glass slides were placed onto the surface and drops of aluminium ion solution (approximately 25 μl each) were placed onto the slides with the arrangement shown in Fig. 5.23(a). That is, two drops were placed onto each slide with various concentrations. The slides were then scanned with an excitation wavelength of 532 nm, a 560 nm long pass filter, normal sensitivity, a resolution of 200 μm, and a photomultiplier tube (PMT) voltage of either 600 or 650 V (see Fig. 5.23 caption).

For the first experiment the aluminium ion solutions were buffered at pH = 5 using the same acetic acid buffer used previously. The fluorescence imaging results are shown in Fig. 5.23(b).

It is seen in Fig. 5.23(b) that there is an increase in fluorescence intensity that correlates with aluminium ion concentration, particularly for the two higher concentrations (100 μM and 1 mM). However, there is also a considerable increase in fluorescence for the negative controls relative to outside the aluminium drop. Another important consideration is how well the coating survives the acidic buffer solution, given that polyelectrolytes are generally used for biological applications in near neutral conditions. To test this later point the experiment was repeated but where two of the slides were rinsed with the buffer solution prior to fluorescence imaging (last two right hand side slides in image). The results are shown in Fig. 5.23(c).

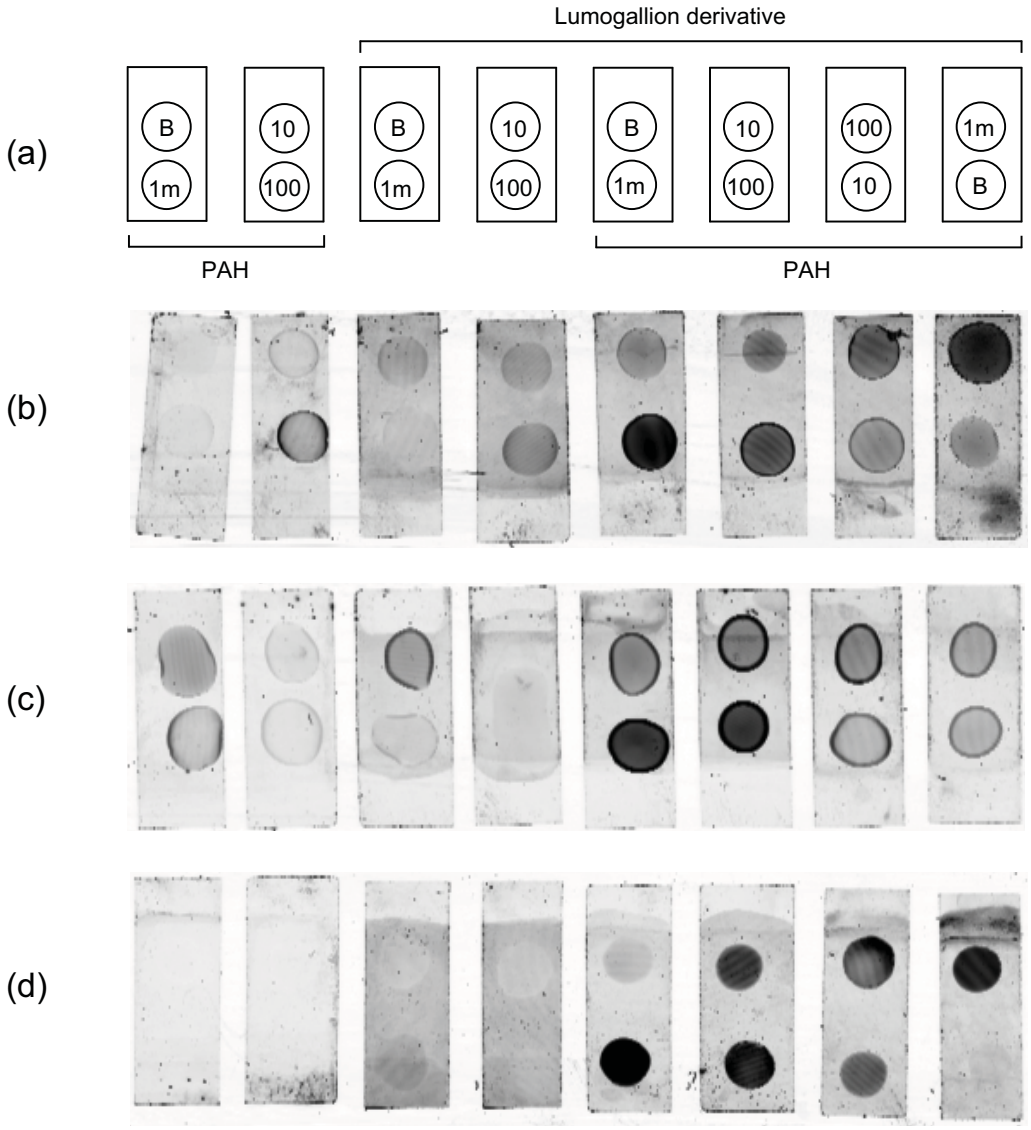

FIGURE 5.23: (a) Order of coating and aluminium solution drops for glass slide experiments. B refers to a drop of the buffer (or water), 10 = 10 μM Al^{3+}, 100 = 100 μM Al^{3+}, and 1m = 1 mM Al^{3+}. The first four slides are negative controls. (b-d) Fluorescence image results for glass slides (1 × 2.5 cm^2) coated with a single PAH layer and then a lumogallion derivative layer where darker indicates greater fluorescence. The aluminium ion solutions were buffered at pH = 5 in (b, c) and were in distilled water in (d). The PMT voltage was 650 V in (b) and 600 V in (c, d). In (c) the last two slides were rinsed with the pH = 5 acetic acid buffer solution prior to fluorescence imaging. The images were recorded 22, 30, and 45 minutes after placing the aluminium ion drops in (b, c, d), respectively. Note that only approximately the upper 80% of the slides were coated in (b, c) and the lower 80% in (d).

The results of Fig. 5.23(c) show that after rinsing with the buffer there is no longer a correlation between fluorescence intensity and the aluminium ion concentration, indicating that the coating was removed. A possible explanation is that the acetic acid forms a salt with the polyelectrolyte, allowing it to be rinsed off. To circumvent this problem the glass slides were then tested in distilled water (near neutral pH, slightly acidic due to carboxylic acid). While the fluorescence response is expected to be greatest in acidic conditions, cuvette measurements (not shown here) still showed a sufficient response in a distilled water solution. Thus, the previous experiment was repeated but with a water-only aluminium ion solution. The coating times were also extended to counter the expected lower fluorescence signal, the PAH coating step was four hours and the lumogallion step for 18 hours. In principle, the extended coating time should allow for a greater surface density of PAH and lumogallion. The results are shown in Fig. 5.23(d).

Figure 5.23(d) shows a strong correlation between aluminium ion concentration and fluorescence intensity. Interestingly, the control slides show a reduced background signal compared to when the acetic acid buffer was used, indicating that the acidic buffer had a background signal that was previously interfering with the results.

The results in this section demonstrate that the lumogallion derivative can be attached to a glass surface using the polyelectrolyte method and aluminium ions can subsequently be detected using fluorescence measurements. Unfortunately, but as expected, the polyelectrolyte method appears to be unstable in acidic conditions. This is unsurprising given that polyelectrolytes are generally used for near-neutral biological applications. Thus, improving the coating stability will be an important avenue of research if this method is to used for corrosion sensing. Possible improvements could be to increase the number of polyelectrolyte layers or to instead use an approach where a covalent bond is used rather than electrostatic forces, such as through the use of silanes [109] [P5], which should provide a more robust coating.

5.5.4 Microstructured Optical Fibre Experiments

The process used in Sec. 5.5.3 was then applied for a microstructured optical fibre, in this case an enclosed suspended-core fibre (wagon wheel fibre) with an effective core diameter (see [P6] for definition) of approximately 1.7 μm and a hole diameter of 12 μm (Fig. 5.24). Note that this fibre was fabricated in a different project. It was fabricated

using the techniques presented in [P6] but using active pressurisation of the fibre holes in order to increase the hole diameter, and thus improve liquid filling speeds and reduce hole blockages.

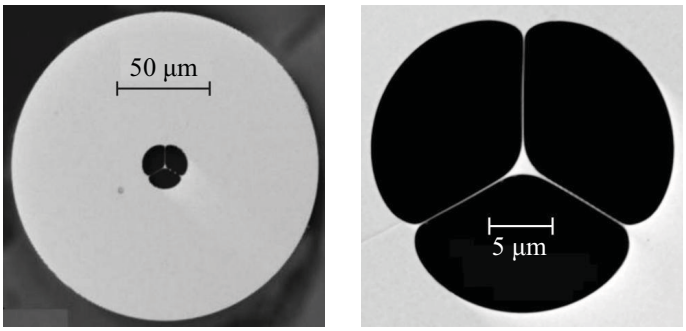

FIGURE 5.24: Scanning electron microscope image (SEM) of the inflated suspended-core fibre (WW) fibre used in this experiment.

The coating procedure is significantly different for the suspended-core fibre compared to the glass slide experiment. The primary difference is that rather than being immersed into the coating solutions, the coating solutions are forced through the fibre's internal holes using positive pressure. To apply the pressure the fibres were sealed into a metal chamber using a rubber seal and regulated nitrogen gas was fed into the chamber using a pressurised nitrogen gas bottle. The pressure filling setup is shown in Fig. 5.25.

FIGURE 5.25: Pressure filling setup used to coat the internal surfaces of MOFs. The fibre is inserted into the rubber seal using a syringe. A sample vial is then positioned into the chamber, which is closed before applying pressure via the nitrogen gas bottle and regulator.

The coating procedure went as follows. The PAH solution was flushed through 2 × 60 cm lengths of suspended-core fibre with 20 psi pressure for three hours. The fibres were then flushed with water for 30 mins at 40 psi and then nitrogen gas for 30 mins at 40 psi. The lumogallion solution was prepared with a concentration of 50 μM in distilled

water, with 200 μl of EDC and NHS solution added to 10 ml of the lumogallion solution, of which approximately 2 ml was used for the experiment. The fibres were then flushed with the lumogallion solution for three hours at 20 psi, then rinsed with distilled water and nitrogen as done after the PAH coating. Note that the fibres were cleaved at both ends after each step to prevent residue blocking the holes. Also, the whole length of the fibre was checked under an optical microscope after each nitrogen flushing step to ensure that all liquid was removed from the fibre.

The fibres were cleaved into 60 mm pieces and placed into the setup shown in Fig. 5.7. The fibres were filled with various concentrations of aluminium ion solutions for 10 minutes using capillary forces only. Spectra were recorded before and 10 minutes after filling with the alumimium ion solution. No change in the background fluorescence was observed with filling with the aluminium ion solution for concentrations equal to or below 3 mM, but the results for concentrations of 10 mM and 30 mM are shown in Fig. 5.26.

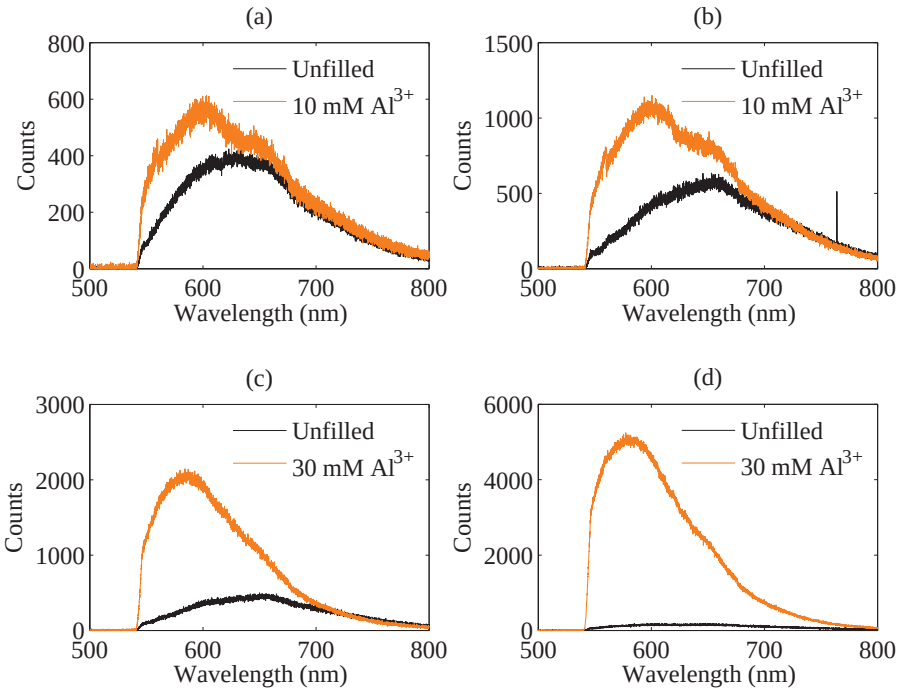

FIGURE 5.26: Spectra recorded after filling a PAH and lumogallion coated suspended-core fibre with aluminium ion solutions. The left and right spectra are repeats of the same measurement using a different piece of the coated fibre.

For the 10 mM samples there is a small increase in the fluorescence signal after filling with the aluminium ion solution, and a large increase for the 30 mM sample. This

demonstrates that the suspended-core fibre can be used for aluminium ion sensing using the PAH-lumogallion coating method. However, the concentrations that could be detected are two order of magnitude higher than that measured using the glass slide arrangement. This is due to the large amount of background fluorescence from the uncomplexed lumogallion that is present. This background fluorescence (black curves in Fig. 5.26) was only present after the coating procedure, that is, it is not the glass background fluorescence. This implies that the surface density of attached lumogallion is actually too high to measure lower concentrations of aluminium. Further experiments could thus be performed to understand how the coating procedure can be altered to produce a surface density that allows lower concentrations to be measured. For example, the lumogallion solution concentration or the flushing time through the fibre could be reduced. Note that a method for estimating the surface density of an attached fluorophore was developed in [P5] and could be used here in order to assist the optimisation process.

As a final comment, the polyelectrolyte coating method was tested with the exposed-core fibre several times (not shown here). Unfortunately, no increase in the fluorescence signal was observed after immersing the exposed-core fibres into various aluminium ion solutions. It is unclear why this was the case, but a possible explanation is that the difference in the coating procedure prevented a successful coating of lumogallion from being applied to the fibre core. That is, instead of flowing the coating solution through the fibre holes as was the case for the enclosed MOF, the exposed-core fibres were immersed into a measuring cylinder containing the coating solution. This is a considerably more static condition compared to the enclosed MOF. Also, access to the core of the exposed-core fibre is considerably more restricted compared to the glass slides, which were coated statically. Thus, these factors may have prevented sufficient amounts of the coating materials from reaching the fibre core.

5.6 Discussion and Conclusions

In this chapter a method for sensitising microstructured optical fibres for corrosion sensing of aluminium alloys was identified and tested. The method uses a fluorescence-based organic indicator molecule (lumogallion) that fluoresces when complexed with aluminium

ions. The benefits of using this method include high sensitivity and specificity, but challenges include implementing a method for immobilising the compound reliably onto the fibre surface and potentially low chemical and photo stability, as is generally the case when using organic dyes.

Initial characterisation of the lumogallion compound showed favourable results with a strong and linear response to aluminium ions over a broad range of concentrations. A potential disadvantage was found to be the absorption characteristics in the uncomplexed form, which would limit the length of distributed sensing that could be achieved. However, this can be minimised by sacrificing some absorption by choosing a longer wavelength for excitation, such as 532 nm, as the complexed form absorbs relatively higher at longer wavelengths. A closely related problem is that the compound appears to have background fluorescence in the uncomplexed form, which sets a limit on the minimum concentration of aluminium ions that can be detected. However, the minimum concentration detected was found to be quite low at 0.2 μM using cuvettes and 5 μM using exposed-core fibres, and either should be sufficient for measuring corrosion where high concentrations of aluminium ions are generally present.

After choosing the type of indicator molecule the second aspect of this chapter was to determine and test methods for immobilising this molecule onto the optical fibre surface. Two methods were identified and tested; the first was to embed lumogallion into a porous polymer and the second was to attach lumogallion to the glass surface via polyelectrolytes.

The potential advantages of the porous polymer method is that it intrinsically provides protection for the optical fibre and can easily be used for mass production. Three types of optical fibre were successfully coated with the porous polymer, F2 exposed-core fibre, F2 bare fibre, and silica bare fibre. The fibres were then immersed into a lumogallion solution, which appeared to embed successfully into the polymer. This approach showed encouraging results for bare F2 and silica fibres when used in a corrosion simulation. In contrast, the loss of the exposed-core fibre increased dramatically when coated with the polymer. In addition to increased fibre loss, this method suffered from poor coating uniformity and high opacity. Improvements in the polymer chemistry, particularly to reduce the resultant optical loss, will need to be carried out before this method is to be used successfully in a distributed setup.

The polyelectrolyte method allows the lumogallion compound to be bound to the surface via a covalent bond to the polyelectrolyte and then an electrostatic interaction to the glass. An advantage of this method over the porous polymer method is that aluminium diffusion to the lumogallion molecule is guaranteed, although this is a trade-off with protection of the core from unwanted environmental contaminants (as opposed to aluminium ions which are a desired environmental contaminant). In this chapter a derivative of lumogallion that has a carboxylic acid functional group was synthesised (see Appendix D) that can couple to the electropositive polyelectrolyte PAH. This derivative was then coated onto glass slides and onto the internal surface of an MOF. Positive results were found for both these configurations when using water solutions. This, to the best of my knowledge, is the first demonstration of a surface funtionalised chemical ion sensor using microstructured optical fibres. It is also significant progress towards the eventual aim of corrosion sensing, where the next step would be to improve this technique so that the coating can be used in corrosive environments.

Chapter 6

Conclusions and Future Work

This is not the end.
It is not even the beginning of the end.
But it is, perhaps, the end of the beginning.

Winston Churchill

Years from now you will be more disappointed by the things you didn't do than the ones you did do. So throw off the bow lines, sail away from safe harbour. Catch the trade winds in your sails. Explore. Dream. Discover.

Mark Twain

If you're not hurting you're not riding hard enough.
If you're not hungry you've eaten too much.
If you're not cold you're carrying too many clothes.
If you know you will succeed it's too easy.

Alastair Humphreys

This thesis shows that fluorescence based sensing using suspended core optical micro/nanowires, including those with the core partially exposed along their length, are an attractive platform for chemical sensing. Theoretical modelling shows that these fibres can exhibit high fluorescence capture fractions compared to conventional fibres, particularly when high refractive index materials are used. Fabrication of these fibres has been demonstrated using the technique of extrusion of soft glasses. Extrusion allows for great flexibility in the cross sectional geometry of a fibre, which is highly relevant for the fibres created in this project that have small features and, for the exposed-core fibre, asymmetry. Corrosion sensing motivated this work, and thus motivated the choice of using fluorescence as the transduction mechanism, as well as the design and development of exposed-core fibres. This is because exposed-core fibres can provide the high sensitivity of a traditional MOF, but also allow for real-time and distributed sensing, both of which were demonstrated experimentally. Methods for sensitising these fibres for aluminium ion, and thus aluminium alloy corrosion, sensing were demonstrated. While work needs to be carried before such devices are to be installed in a real structure such as an aircraft, the results contained within this thesis demonstrate the feasibility of distributed corrosion sensing using exposed-core microstructured optical fibres.

In Chapter 3 a new model for evaluating the performance of optical fibre fluorescence sensors with arbitrary geometries was developed. Unlike previous models, this model combined vectorial solutions to Maxwell's equations, fibre attenuation factors, and in-fibre excitation into a single framework. The model was applied for the fundamental mode of a suspended optical nanowire where it was found that small-core high-refractive index fibres offer the greatest fluorescence sensing characteristics. The theory was then applied to the exposed-core fibre for the unique case where the exposed region is filled with a liquid, which is particularly relevant to corrosion sensing as corrosion by-products are generally aqueous. It was found that the liquid immersion can lead to an improved fluorescence signal due to the different refractive index profile compared to an enclosed geometry. Higher order modes were then included in the theory so that the theory is applicable outside of the single mode regime, which is useful when studying suspended-core fibres that have core diameters close to the wavelength of the propagating light where several guided modes may exist. This is generally the case for exposed-core fibres where a compromise between sensitivity, and fibre strength and coupling efficiency must be considered. Additionally, experimentally measured small-core surface scattering

loss and confinement loss were included into the model, which allowed the model to be compared successfully with experimental results and also indicated that there is a fundamental limit on how usefully small a suspended-core fibre can be made. The final section of Chapter 3 was a somewhat different application of the fluorescence capture theory where it was used to calculate surface density of a surface attached fluorophore (quantum dot). This is relevant from the point of view that one of the methods for sensitising the exposed-core fibre to corrosion is to form a thin-layer onto the surface using polyelectrolytes. As the layer is very thin it is necessary to have a method by which the attachment density can be estimated and thus optimised.

In Chapter 4 the fabrication of both enclosed and exposed suspended-core fibres was demonstrated using the technique of extrusion of soft glasses. In the case of enclosed suspended optical nanowires the extrusion technique was shown to be useful because it allows greater control of the cross sectional structure compared to, say, capillary stacking, and has thus allowed subwavelength core diameters to be produced. The versatility of the extrusion technique is even more pronounced for the exposed-core fibre where the fabrication of an asymmetric wedged-jacket was required. The second component of Chapter 4 was the demonstration that real-time and distributed fluorescence sensing can be achieved using exposed-core fibres. These are both made possible due to the core being exposed along the entire length of the fibre. For real-time sensing the entire fibre can be immersed into a liquid and the liquid then infiltrates to the core nearly instantaneously. This was experimentally measured using a fluorescent liquid and was shown to occur within one second. For distributed sensing, time resolved measurements were recorded when different lengths of fibre where immersed into a fluorescent liquid, which corresponded with the spatial location of the liquid. This, to the best of my knowledge, is the first demonstration of distributed fluorescence sensing using microstructured optical fibres.

In Chapter 5 the sensing of aluminium ions, and thus corrosion sensing of aluminium alloys was investigated. The chosen transduction method was the use of an indicator molecule, lumogallion, which increases its fluorescence emission when complexed with aluminium ions. Initial experiments showed that the exposed-core fibre was able to successfully measure aluminium ion concentration when immersed into a lumogallion solution. Two methods were then tested for immobilising lumogallion onto the surface

of glass, and thus optical fibres. In the first method a porous polymer was successfully coated onto F2 exposed-core fibres, F2 bare fibres, and silica bare fibres. This approach showed positive results for bare F2 and silica fibres when used in a corrosion simulation, but not for the dip-coated fibres. Unfortunately, the loss of the exposed-core fibre increased dramatically when coated with the polymer and prevented results from being measured, showing that there is a compromise between sensitivity and loss. For the second method, polyelectrolytes were used to electrostatically attach a derivative of lumogallion to the glass surface. Positive results were found for both glass slides and enclosed suspended-core microstructured optical fibres. This, to the best of my knowledge, is the first demonstration of a surface funtionalised chemical ion sensor using microstructured optical fibres.

As stated previously, the results of this thesis demonstrate the feasibility of distributed corrosion sensing using exposed-core microstructured optical fibres. In order to reach a stage where the technology is mature enough to be used in a real device there are several optimisations that would need to be achieved. These can be broadly classified as improvements in the optical fibre, and improvements in the chemical transduction method.

The exposed-core fibres fabricated in this thesis have been demonstrated as being a useful sensing platform for real-time and distributed sensing. However, the distributed sensing results highlighted the limitations that resulted from the fibre's loss, and the polymer coating experiments revealed the fragility of the current exposed-core fibres. In future, the fibre loss could be reduced by using cleaner fabrication techniques, such as the use of a clean room. Also, higher purity starting materials would contribute to reducing the loss. The exposed-core fibre fragility results from the thin struts that suspend the core. In future the fragility could be improved by finding, theoretically and then experimentally, the best compromise between strut thickness and confinement loss. Adding a protective coating will also likely assist with improving the fibre durability but, as seen with the porous polymer coating, this itself may induce damage to the fibre and thus the polymer, and the method by which it is applied, must be selected carefully.

The other factor for improvement is the chemical transduction method. The concept of using an organic fluorescence-based indicator appears to be sound, as cuvette and

exposed-core fibre solution measurements show high linearity with aluminium ion concentration and a low detection limit. However, the method for immobilising lumogallion to the glass surface has not yet been developed to a stage where a reliable and durable sensor can be fabricated. The porous polymer method suffers from high optical loss and low repeatability in the resultant measurements. Future investigations into the polymer chemistry, and the resultant loss and porosity need to be carried out. In contrast, the polyelectrolyte method shows a high repeatability and produces a low enough loss such that it can be used within microstructured optical fibres. However, the polyelectrolyte coating method suffers from low adhesion to the glass surface and degradation in acidic buffers, making it currently of little use for corrosion sensing. This can likely be improved by either increasing the number of polyelectrolyte layers or using a covalent binding method such as silanisation for the chemical attachment.

Appendix A

Fluorescence Capture Fraction Derivation

This is the full derivation of the fluorescence capture theory that is developed and used in various parts of [P1-P5]. It was developed in order to be able to predict the fluorescence sensing efficiency of fibres that were fabricated in [P6, P7]. The theory builds on previous formalisms by Marcuse [16, 17], and Snyder and Love [54]. Where equations are the same, or equivalent, to equations presented or used in [P1-P5] a specific reference has been made.

A.1 Power Propagation in the Fibre

To begin, the excitation power of the j^{th} mode along the z axis of the fibre is represented as [54]

$$P_j(z) = P_j(0)e^{-\gamma_j z} = |a_j|^2 N_j e^{-\gamma_j z}, \tag{A.1}$$

where a_j is the modal amplitude, γ_j is defined below, and N_j is the mode normalisation which is defined as

$$N_j = \frac{1}{2}\left[\int_{A_\infty} (\mathbf{e}_j \times \mathbf{h}_j^* \cdot \hat{\mathbf{z}}) dA\right], \tag{A.2}$$

where $\mathbf{e}_j$ and $\mathbf{h}_j$ are the j^{th} electric and magnetic bound modes for the waveguide, respectively. The integration is over an infinite cross-section, A_∞, and implicit throughout this derivation is an (x, y) (transverse) dependance. That is, the longitudinal component has been separated due to cylindrical symmetry. Substituting Eq. A.2 into Eq. A.1 thus gives the following expression for power propagation along the fibre

$$P_j(z) = \frac{1}{2}|a_j|^2 \left[\int_{A_\infty} (\mathbf{e}_j \times \mathbf{h}_j^* \cdot \hat{\mathbf{z}}) dA\right] e^{-\gamma_j z}. \tag{A.3}$$

In the above equations γ_j is the attenuation coefficient which contains attenuation due to fibre loss and Beer's law absorption. This is defined as [54]

$$\gamma_j = k \left(\frac{\varepsilon_0}{\mu_0}\right)^{\frac{1}{2}} \int_{A_\infty} \frac{n(x,y) n_i(x,y) |\mathbf{e}_j|^2}{N_j} dA. \tag{A.4}$$

The integral in Eq. A.4 can be split into fluorophore containing hole (MOF air-hole) regions (F), non-fluorophore containing hole regions (H), and glass regions (G), as shown in Eq. A.5. From now the superscript refers to the region in which the parameter is for, that is, fluorophore, hole, or glass region. Also, in this derivation the real part of the refractive index is shown as n, while the imaginary part is shown as n_i. Note that Eqs. A.1 to A.4 are equivalent to Eqs. 1 and 2 in [P1].

$$\gamma_j = \frac{k}{N_j} \left(\frac{\varepsilon_0}{\mu_0}\right)^{\frac{1}{2}} \left(n^G n_i^G \int_G |\mathbf{e}_j|^2 dA + n^H n_i^H \int_H |\mathbf{e}_j|^2 dA + n^F n_i^F \int_F |\mathbf{e}_j|^2 dA\right) \tag{A.5}$$

By making the following definition

$$\eta_j^R = n^R \left(\frac{\varepsilon_0}{\mu_0}\right)^{\frac{1}{2}} \left(\frac{1}{2N_j}\right) \left(\int_R |\mathbf{e}_j|^2 dA\right), \tag{A.6}$$

for any regions R = (G, H, F) and noting that the imaginary part of the refractive index is replaced with the exponential definition of loss via

$$\alpha = 2kn_i, \tag{A.7}$$

then Eq. A.5 becomes

$$\gamma_j = \alpha_j^G \eta_j^G + \alpha_j^H \eta_j^H + \alpha_j^F \eta_j^F + \alpha_B \eta_j^F, \tag{A.8}$$

where α_B is the absorption due to the Beer-Lambert law at the excitation wavelength and has been separated from the absorption due to fibre loss at locations of the fluorophore, α^F. α^G and α^H refer to fibre loss at regions of the fibre containing glass and air holes, respectively.

In summary, the above equations give an expression for the power propagation of the excitation light that travels along the fibre and decays due to fibre losses and fluorophore absorption.

A.2 An Expression for the Captured Fluorescence

The next step is to calculate the efficiency of coupling emitted fluorescence into the electric and magnetic fields of the fibre. To begin, the total fluorescence electric field, E, is written as a linear combination of the allowed modes of the fibre (Eq. A.9). A different mode index, ν, is used in order to avoid confusion with the excitation mode indices, which may be different. For example, a single mode could be excited at the excitation wavelength but, after absorption, is coupled into all the modes of the the fibre at the fluorescence wavelength. Throughout this derivation the convention has been used that expressions subscripted by j refer to the excitation wavelength and any fields subscripted by ν refer to the fluorescence wavelength. This method of wavelength distinction has also been used for terms that are not modal dependant, such as refractive index, n, and wavelength, λ.

$$\mathbf{E}(\mathbf{r}) = \sum_{\nu} a_\nu \mathbf{e}_\nu e^{i\beta_\nu z} + \sum_{\nu} a_\nu \mathbf{e}_{-j} e^{-i\beta_\nu z} + \mathbf{E}_{rad}(\mathbf{r}). \tag{A.9}$$

Note that the summation of modes here must take into account any degenerate modes that are present (that is, for a structure that has greater than 2-fold rotational symmetry [203]). Note that it is assumed that the fibre and the fluorescent material is weakly

absorbing and so β is assumed to be real in Eq. A.9 and power propagation along the fibre is thus approximately considered by using Eq. A.3.

To determine the modal amplitudes in Eq. A.9 it is assumed that the fluorescent sources can be described as current sources of distribution $J(\mathbf{r})$ within a volume V and hence, from Eq. 31-35 in Ref. [54]

$$a_\nu = -\frac{1}{4N_\nu}\int_V \mathbf{e}_\nu^* \cdot \mathbf{J}(\mathbf{r}) e^{-i\beta_\nu z} dV. \tag{A.10}$$

To determine the power emitted into fibre modes the square of Eq. A.10 is taken to give [16, 17]

$$\left\langle |a_\nu|^2 \right\rangle = \frac{1}{16N_\nu^2}\int_{V'}\int_V S(\mathbf{r})\delta^3(\mathbf{r}-\mathbf{r'})|\mathbf{e}_\nu|^2 dV dV', \tag{A.11}$$

where $S(\mathbf{r})$ is a source strength term. Implicit in this step is that the fluorescence is emitted with random direction and polarisation. The value of $S(\mathbf{r})$ is then determined by inputting a plane wave solution into Eq. A.11 which has a known solution [16, 17]. This gives

$$\left\langle |a_\nu|^2 \right\rangle = \frac{\lambda_\nu^2}{4\pi n_\nu^F}\left(\frac{\varepsilon_0}{\mu_0}\right)^{\frac{1}{2}}\frac{1}{4N_\nu^2}\int_V P_D(\mathbf{r})|\mathbf{e}_\nu|^2 dV, \tag{A.12}$$

where $P(\mathbf{r})$ is the fluorescent power per unit volume emitted from the source located at the position $\mathbf{r}$. In order to calculate how the power is transferred from the excitation wavelength modes into the fluorescence wavelength modes along the length of the fibre, the fibre is split up into infinitesimal segments which will later be integrated. The amount of fluorescence power emitted from a thin volume disc from $z = (z', z' + dz')$, coupled into the ν^{th} forward propagating guided modes, and propagates to the end of a fibre of length L is given by

$$dP_\nu(z') = \left[\ \left\langle |a_\nu|^2 \right\rangle\ \right]_{z'}^{z'+dz'} N_\nu e^{-\gamma_\nu(L-z')}. \tag{A.13}$$

The total amount of guided fluorescence power that reaches the end of the fibre is given by the summation of all the guided modes at the fluorescence wavelength

$$dP(z') = \sum_{\nu} \Big[\left\langle |a_\nu|^2 \right\rangle \Big]_{z'}^{z'+dz'} N_\nu e^{-\gamma_\nu (L-z')}. \tag{A.14}$$

That is, dP represents the total amount of fluorescence power that is emitted from the region $z = (z', z' + dz')$ and propagates to the end of the fibre. Substituting Eq. A.12 into Eq. A.14 gives

$$dP(z') = \sum_{\nu} \lim_{z' \to 0} \frac{\lambda_F^2}{4\pi n_\nu^F} \left(\frac{\varepsilon_0}{\mu_0} \right)^{\frac{1}{2}} \frac{e^{-\gamma_j (L-z')}.}{4N_\nu} \int_{A_\infty} \int_{z'}^{z'+dz'} P_D(\mathbf{r}) |\mathbf{e}_\nu|^2 dz'' dA. \tag{A.15}$$

This expression is the multimode equivalent of Eq. 3 in [P1], due to the summation over all fluorescence wavelength modes.

A.3 Calculating the Power Density Function

The next step is to calculate the fluorescence power density function, $P_D(\mathbf{r})$, which is the density of the fluorescence emission at the source location. There are several assumptions which are made so that $P_D(\mathbf{r})$ can be determined from the excitation field profile and absorption characteristics of the fibre, these are:

1. The fluorescence power density function is directly proportional to the power of the excitation mode, at locations where fluorophores are present.
2. The power per unit length of the fluorescence power is equal to the power per unit length of the excitation light lost due to the Beer-Lambert law multiplied by the fluorescent dye's efficiency. Implied here is that the source emission is not affected by proximity to a dielectric boundary.
3. There is a single excitation bound mode, with mode label j. This simplification has been used in all calculations in [P1-P5].
4.

To implement step (1) the argument is made that the amount of fluorescence that is emitted per unit volume is proportional to the Poynting vector of the excitation

fields. The approximation is made that only the z component of the Poynting vector is considered, which is approximately true for guided modes. This is represented by

$$P_D(\mathbf{r}) = \Gamma\xi(x,y)\left(\mathbf{e}_j \times \mathbf{h}_j^* \cdot \hat{\mathbf{z}}\right) e^{-\gamma_j z}, \tag{A.16}$$

where Γ is the constant of proportionality which will be determined shorty and $\xi(x,y)$ describes the fluorophore efficiency across the cross-section of the fibre, it has the property that

$$\xi(x,y) = \begin{cases} \xi & \text{in regions containing fluorescent sources (F),} \\ 0 & \text{elsewhere.} \end{cases}$$

The next step is to relate Eq. A.16 with the amount of excitation power lost per unit length due to Beer-Lambert law absorption at $z = z'$. First note that the total amount of excitation power lost per unit length is given by differentiating Eq. A.1 with respect to z

$$\frac{d}{dz}(P_j(z)) = \frac{d}{dz}\left(P_j(0)e^{(-\gamma_j z)}\right) = -\gamma_j P_j(z). \tag{A.17}$$

From Eq. A.8 note that the attenuation term is comprised of several components. For the purposes of satisfying step (2) only the amount of power lost due to the Beer-Lambert law is of interest and so this is given by

$$\left[\frac{d}{dz}(P_B(z))\right]_{Beer-Lambert} = -\alpha_B \eta_j^F P_j(z). \tag{A.18}$$

Step (2) is now solved by using Eq. A.16 and Eq. A.18 in

$$\int_{A_\infty} P_D(\mathbf{r}) dA = \xi\left[\frac{d}{dz}(P_B(z))\right]_{Beer-Lambert}, \tag{A.19}$$

$$\int_{A_\infty} \left(\Gamma\xi(x,y)(\mathbf{e}_j \times \mathbf{h}_j^* \cdot \hat{\mathbf{z}})e^{-\gamma_j z}\right) dA = -\xi\alpha_B \eta_j^F P_j(z). \tag{A.20}$$

Substituting Eq. A.3 into Eq. A.20 gives

$$\Gamma \int_{A_\infty} \xi(x,y)(\mathbf{e}_j \times \mathbf{h}_j^*) \cdot \hat{\mathbf{z}} dA e^{-\gamma_j z} = -\xi \frac{1}{2} |a_j|^2 \alpha_B \eta_j^F \int_{A_\infty} (\mathbf{e}_j \times \mathbf{h}_j) \cdot \hat{\mathbf{z}} dA e^{-\gamma_j z}. \quad \text{(A.21)}$$

Rearranging and making use of the properties of $\xi(x,y)$ gives

$$\Gamma \int_F (\mathbf{e}_j \times \mathbf{h}_j^*) \cdot \hat{\mathbf{z}} dA = -\frac{1}{2} |a_j|^2 \alpha_B \eta_j^F \int_{A_\infty} (\mathbf{e}_j \times \mathbf{h}_j^*) \cdot \hat{\mathbf{z}} dA, \quad \text{(A.22)}$$

which gives the following expression for the constant of proportionality Γ

$$\Gamma = -\frac{1}{2} |a_j|^2 \alpha_B \eta_j^F \frac{\int_{A_\infty} (\mathbf{e}_j \times \mathbf{h}_j^*) \cdot \hat{\mathbf{z}} dA}{\int_F (\mathbf{e}_j \times \mathbf{h}_j^*) \cdot \hat{\mathbf{z}} dA}. \quad \text{(A.23)}$$

Substituting this expression for Γ into Eq. A.16 gives us the full expression for $P_D(\mathbf{r})$

$$P_D(\mathbf{r}) = -\frac{1}{2} \xi(x,y) \alpha_B \eta_j^F |a_j|^2 \frac{\int_{A_\infty} (\mathbf{e}_j \times \mathbf{h}_j^*) \cdot \hat{\mathbf{z}} dA}{\int_F (\mathbf{e}_j \times \mathbf{h}_j^*) \cdot \hat{\mathbf{z}} dA} \left(\mathbf{e}_j \times \mathbf{h}_j^* \cdot \hat{\mathbf{z}} \right) e^{-\gamma_j z}. \quad \text{(A.24)}$$

Substituting η_j^F from Eq. A.6 into Eq. A.24 gives

$$P_D(\mathbf{r}) = -\frac{1}{2} \xi(x,y) \alpha_B n_j^F \left(\frac{\varepsilon_0}{\mu_0} \right)^{\frac{1}{2}} |a_j|^2 \frac{\int_F |\mathbf{e}_j|^2 dA}{\int_F (\mathbf{e}_j \times \mathbf{h}_j^*) \cdot \hat{\mathbf{z}} dA} \left(\mathbf{e}_j \times \mathbf{h}_j^* \cdot \hat{\mathbf{z}} \right) e^{-\gamma_j z}, \quad \text{(A.25)}$$

which is equivalent to Eq. 4 in [P1].

A.4 Calculating the Fluorescence Capture Fraction

By substituting Eq. A.25 into Eq. A.15 an expression for the amount of fluorescence that is emitted from the segment $z = (z', z' + dz')$ and propagates to the output end of the fibre is obtained

$$dP_j^F(z') = \sum_\nu \lim_{dz'\to 0} P_j(0)\frac{\xi\alpha_B\lambda_\nu^2}{8\pi}\frac{n_j^F}{n_\nu^F}\left(\frac{\varepsilon_0}{\mu_0}\right)\frac{\int_F |\mathbf{e}_j|^2 dA}{\int_F(\mathbf{e}_j\times\mathbf{h}_j^*)\cdot\hat{\mathbf{z}}dA} \times \frac{\int_F(\mathbf{e}_j\times\mathbf{h}_j^*)\cdot\hat{\mathbf{z}}|\mathbf{e}_j|^2 dA}{4N_\nu N_j} e^{-\gamma_\nu(L-z')}\int_{z'}^{z'+dz'} e^{-\gamma_j z''}dz''. \tag{A.26}$$

Integrating over the entire length of the fibre from $z = (0, L)$ gives the total fluorescence capture fraction, Φ, to be

$$\Phi_j = \frac{1}{P_j(0)}\int_0^L dP_j^F(z), \tag{A.27}$$

$$\Phi_j = \sum_\nu \frac{\xi\alpha_B\lambda_\nu^2}{8\pi}\frac{n_j^F}{n_\nu^F}\left(\frac{\varepsilon_0}{\mu_0}\right)\frac{\int_F |\mathbf{e}_j|^2 dA}{\int_F(\mathbf{e}_j\times\mathbf{h}_j^*\cdot\hat{\mathbf{z}})dA} \times \frac{\int_F(\mathbf{e}_j\times\mathbf{h}_j^*\cdot\hat{\mathbf{z}})|\mathbf{e}_j|^2 dA}{4N_\nu N_j}\frac{e^{-\gamma_\nu L}}{\gamma_\nu-\gamma_j}\left(e^{(\gamma_\nu-\gamma_j)L}-1\right). \tag{A.28}$$

This can be rearranged into a form that contains the modal effective area, A_{eff}, and a normalised overlap integral, NOI, as defined below

$$\Phi_j = \sum_\nu \frac{\xi\lambda_\nu^2}{16\pi n_\nu^{F2}}\frac{NOI_{j\nu}}{A_{eff,\nu}}\frac{\gamma_j^F e^{-\gamma_\nu L}}{\gamma_\nu-\gamma_j}\left(e^{(\gamma_\nu-\gamma_j)L}-1\right), \tag{A.29}$$

$$NOI_{j\nu} = n_\nu^F\left(\frac{\varepsilon_0}{\mu_0}\right)^{\frac{1}{2}}\frac{\int_{A_\infty} s_\nu dA}{\int_F s_j dA}\frac{\int_F s_j|\mathbf{e}_\nu|^2 dA}{\int_{A_\infty} s_\nu^2 dA}, \tag{A.30}$$

$$A_{eff,\nu} = \frac{|\int_{A_\infty} s_\nu dA|^2}{\int_{A_\infty}|s_\nu|^2 dA}. \tag{A.31}$$

This expression for the fluorescence capture fraction is equivalent to Eq. 7 in [P1].

A.5 Variations of the Fluorescence Capture Fraction Equations

The above equations refer to the case where excitation light of a single mode is coupled into one end of the fibre that excites fluorescence which is outputted at the opposite end of the fibre. In this case one or more of the holes are uniformly filled with a fluorophore and all loss characteristics of the fibre are included. Several variations of this theory have been used in [P2-P5] and these are now discussed.

1. Backwards fluorescence capture fraction

The above theory assumes that the fluorescence is emitted uniformly in all directions. This implies that the backwards propagating modes of the fibre should be equally excited. This means that the fluorescence signal can be detected at the same end of the fibre as the light source, and this is indeed a more practical approach in many circumstances. The primary difference in the derivation is that Eq. A.14 becomes

$$dP_\nu(z') = \left[\left\langle |a_\nu|^2 \right\rangle \right]_{z'}^{z'+dz'} N_\nu e^{-\gamma_j z'}. \tag{A.32}$$

This slightly modifies the integration in Eq. A.27 such that Eq. A.29 is now

$$\Phi_j = \sum_\nu \frac{\xi \lambda_\nu^2}{16\pi n_\nu^{F2}} \frac{NOI_{j\nu}}{A_{eff,\nu}} \frac{\gamma_j^F}{\gamma_\nu + \gamma_j} \left(e^{-(\gamma_\nu+\gamma_j)L} - 1 \right). \tag{A.33}$$

Equations A.29 and A.33 are equivalent to Eq. 4 in [P2].

2. Thin-layer sensing

The above equations have all considered the case of one or more holes in the fibre being filled uniformly with a fluorophore. In many applications the fluorophore will be coated onto the walls of the fibre holes and thus the fluorescence emmission will come from a thin-layer near the surface of the core. In the case of a finite sized layer all that is required is that the region F in Eq. A.29 refers to the thin layer. However, when considering an infinitely small layer, such as in [P5], some of the integrals in Eq. A.29 can be simplified to line integrals along the region of the fluorophore. In [P5] the simplification was made that the fluorophore was a constant distance, $r = r_f > r_{core}$, from the axis of a circularly

symmetric step-index fibre. In this case the expression for the fluorescence capture is modified by using

$$\frac{NOI_{j\nu}}{A_{eff,\nu}} = \left(\frac{n_\nu^F}{N_\nu}\right)\left(\frac{\varepsilon_0}{\mu_0}\right)^{\frac{1}{2}} \frac{\int_0^{2\pi} s_j(r_f,\theta)|\mathbf{e}_\nu(r_f,\theta)|^2 d\theta}{\int_0^{2\pi} s_j(r_f,\theta) d\theta} \tag{A.34}$$

in Eq. A.29, instead of Eqs. A.30 and A.31.

The γ terms (Eq. A.8), are also modified such that

$$\alpha_B \eta_j^F = \left(\frac{n_\nu^F \epsilon \sigma r_f}{2N_j}\right)\left(\frac{\varepsilon_0}{\mu_0}\right)^{\frac{1}{2}} \int_0^{2\pi} \mathbf{e}_j(r_f,\theta) d\theta, \tag{A.35}$$

where σ is the surface density of the fluorophore.

3. The no loss case

An important simplification is to consider the special case of an attenuation-free fibre of infinite length. In this way the theory describes the fundamental limit on the fluorescence capture possible for the sensor design, and does not depend on which end of the fibre the fluorescence is measured (forwards or backwards fluorescence propagation). It can be regarded as the fundamental fluorescence capture efficiency of the fibre and has the form

$$\Phi_j = \sum_\nu \frac{\xi \lambda_\nu^2}{16\pi n_\nu^{F2}} \frac{NOI_{j\nu}}{A_{eff,\nu}}. \tag{A.36}$$

This is equivalent to Eq. 3 in [P3] and Eq. 1 in [P4].

Equation A.36 shows that the fluorescence capture efficiency (independent of absorption) is directly proportional to the normalised overlap integral (NOI), which depends on the power fraction, and inversely proportional to the effective area.

4. Comparison with ray-optics model

In Sec. 2.2 of [P4] the modal theory for fluorescence capture developed in this appendix is simplified in order to compare with a ray-optics equivalent. It is assumed that the fluorophore is centered at the fibre axis and there is no fibre loss. In this case Eq. A.36 reduces to the following equation

$$\Phi_j = \sum_{\nu} \frac{\xi \lambda_\nu^2}{16\pi n_\nu^F N_\nu} \left(\frac{\varepsilon_0}{\mu_0}\right)^{\frac{1}{2}} |\mathbf{e}_\nu(0,0)|^2. \tag{A.37}$$

As was seen in [P4], this expression becomes equivalent to the solid-angle of fluorescence emitted within the critical angle of the fibre when a fibre of sufficiently high V-number, and thus number of modes, is considered.

Appendix B

Coupling Efficiency Derivation

The optical fibres considered in this thesis are suspended-core MOFs with very small cores, generally 2.0 μm or smaller. Consequently, coupling into these fibres becomes a critical issue, particularly as the core size is close to the diffraction limit of commonly used optics. For example, only 19% efficiency was achieved for coupling into a suspended-core fibre in the experiment in [P1], which was measured via a cut-back loss measurement using a 532 nm CW laser with $M^2 < 1.3$ (JDSU, Solid-State, Compact), and an aspheric lens with a focal length of 2.75 mm and a numerical aperture of 0.65. This coupling efficiency value is typical for coupling into this class of fibre. Also, commonly used equations for coupling efficiency are not accurate when considering small-featured fibres with large refractive index differences as they are based on the weak guidance approximation. Indeed, while much work has been done on the coupling efficiency of waveguides (for example, see Refs. [54, 204–216]), an exact solution for an arbitrary geometry with vectorial solutions has not been found.

In this section is a derivation of coupling efficiency for these types of fibres and a discussion on why finding an exact solution is more complex than perhaps first thought. Specifically, derivations for two important and related problems for optical fibre sensing (and optical fibre use more generally) are shown, these are:

1. Free space coupling from an external light source into an optical fibre.
2. Coupling between two sections of an optical fibre. This could be where two fibres with different geometries and/or refractive indices are spliced. Alternatively, this

is where an MOF has been filled with a liquid and the light is transferring from the unfilled to filled regions or vice versa as was discussed in [P3].

B.1 Free Space Coupling

The task at hand is to determine the efficiency of coupling an external light source into the guided mode(s) of an optical fibre. This will be achieved by matching the transverse electric and magnetic fields of the input light and the modes of the fibre at the boundary as shown in Fig. B.1.

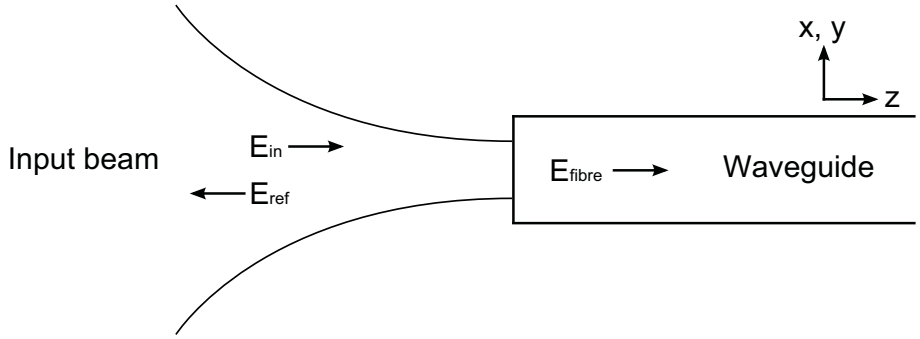

FIGURE B.1: Schematic diagram of the free space coupling problem. An input field $\mathbf{E}_{in}$ is coupled into a waveguide (fibre in this case) with transmission $\mathbf{E}_{fibre}$ and reflection $\mathbf{E}_{ref}$. Note that the arrows indicate wave propagation, not polarisation.

The transverse components of the input electric and magnetic fields of the light source at the boundary are designated as $\mathbf{E}^t_{in}(x,y)$ and $\mathbf{H}^t_{in}(x,y)$, respectively, which could have a Gaussian distribution (for example, a single transverse mode laser) as shown in Eqs. B.1 and B.2, or can be any arbitrary distribution.

$$\mathbf{E}^t_{in}(x,y) = \hat{\mathbf{x}} E_0 e^{-\left(\frac{r}{r_0}\right)^2} \tag{B.1}$$

$$\mathbf{H}^t_{in}(x,y) = \hat{\mathbf{y}} H_0 e^{-\left(\frac{r}{r_0}\right)^2}, \tag{B.2}$$

where E_0 and H_0 are constants that relate to the input field power, $r = \sqrt{x^2+y^2}$ is the radial variable, and r_0 is the Gaussian beam radius. On the waveguide side of Fig. B.1 the transverse electric and magnetic fields ($\mathbf{E}_{fibre}$ and $\mathbf{H}_{fibre}$) are written as a superposition of all the forward propagating guided and radiation modes of the fibre [54]

$$\mathbf{E}^t_{fibre}(x,y) = \sum_j a_j \mathbf{e}_{tj}(x,y) + \mathbf{E}^t_{rad}(x,y) \tag{B.3}$$

$$\mathbf{H}^t_{fibre}(x,y) = \sum_j a_j \mathbf{h}_{tj}(x,y) + \mathbf{H}^t_{rad}(x,y), \tag{B.4}$$

where $\mathbf{e}_{tj}$ and $\mathbf{h}_{tj}$ are the transverse components of the bound electric and magnetic fields of the fibre and a_j is the j^{th} field coefficient. $\mathbf{E}^t_{rad}$ and $\mathbf{H}^t_{rad}$ are the transverse components of the electric and magnetic radiation fields of the fibre at the boundary. Note that the backwards propagating modes are not included as there cannot be a leftwards travelling wave inside the optical fibre as it is assumed to extend to infinity. That is, there are no reflections from, nor coupling into, the right hand side of the fibre.

The task is to now use continuity of the above equations to find an expression for a_j, which will allow the amount of coupled power into the guided modes of the fibre to be determined through [54]

$$P_{guided} = \sum_j |a_j|^2 N_j, \tag{B.5}$$

where N_j is a normalisation term with the form

$$N_j = \frac{1}{2}\int_{A_\infty} (\mathbf{e}_j \times \mathbf{h}^*_j \cdot \hat{\mathbf{z}}) dA. \tag{B.6}$$

Therefore the coupling efficiency (CE) is given by

$$CE = \frac{\sum_j |a_j|^2 N_j}{\frac{1}{2}\int_{A_\infty} (\mathbf{E}_{in} \times \mathbf{H}^*_{in} \cdot \hat{\mathbf{z}}) dA}. \tag{B.7}$$

Alternatively, by using normalised fields then

$$\begin{aligned} \hat{\mathbf{e}}_j &= \frac{\mathbf{e}_j}{\sqrt{N_j}} \\ \hat{\mathbf{h}}_j &= \frac{\mathbf{h}_j}{\sqrt{N_j}} \\ CE &= |a_j|^2. \end{aligned} \tag{B.8}$$

From this point onwards in the derivation normalised fields will be used so that Eq. B.8 is valid.

To determine a_j the transverse components of the electric and magnetic fields are matched at the boundary

$$\hat{\mathbf{E}}_{in}^{t} + \mathbf{E}_{ref}^{t} = \sum_{j} a_j \hat{\mathbf{e}}_{tj} + \mathbf{E}_{rad}^{t} \tag{B.9}$$

$$\hat{\mathbf{H}}_{in}^{t} + \mathbf{H}_{ref}^{t} = \sum_{j} a_j \hat{\mathbf{h}}_{tj} + \mathbf{H}_{rad}^{t}, \tag{B.10}$$

where $\mathbf{E}_{ref}$ and $\mathbf{H}_{ref}$ are yet to be specified reflected fields of the light source off the optical fibre boundary.

The next step is to use orthonormality of the guided and radiation modes. Taking the right cross product of Eq. B.9 with the complex conjugate of the j^{th} magnetic guided field, using orthnormality of the guided and radiation modes, and integrating across the boundary yields Eq. B.11. Taking the left cross product of Eq. B.10 with the complex conjugate of the j^{th} electric guided field, using orthnormality of the guided and radiation modes, and integrating across the boundary yields Eq. B.12.

$$a_j = \frac{1}{2}\int_{A_\infty} \hat{\mathbf{E}}_{in} \times \hat{\mathbf{h}}_j^{*} \cdot \hat{\mathbf{z}} dA + \frac{1}{2}\int_{A_\infty} \mathbf{E}_{ref} \times \hat{\mathbf{h}}_j^{*} \cdot \hat{\mathbf{z}} dA \tag{B.11}$$

$$a_j = \frac{1}{2}\int_{A_\infty} \hat{\mathbf{e}}_j^{*} \times \hat{\mathbf{H}}_{in} \cdot \hat{\mathbf{z}} dA - \frac{1}{2}\int_{A_\infty} \hat{\mathbf{e}}_j^{*} \times \mathbf{H}_{ref} \cdot \hat{\mathbf{z}} dA. \tag{B.12}$$

Note that the subscript t has been dropped as the cross-sectional integral implicitly involves the transverse components only.

Up to this point the derivation has been exact. However, the difficulty in solving these equations lies in the fact that the unknown reflection terms are present, and these are extremely complicated to calculate exactly [54]. Hence, several approximations have been suggested as will now be discussed.

1. Ignore reflections

The simplest approximation is to ignore the reflection terms altogether in Eqs. B.11 and B.12, this is known as the Born approximation [207]. This results in the following two equations that should, in principle, be equivalent

$$a_j = \frac{1}{2}\int_{A_\infty} \hat{\mathbf{E}}_{in} \times \hat{\mathbf{h}}_j^* \cdot \hat{\mathbf{z}} dA \tag{B.13}$$

$$a_j = \frac{1}{2}\int_{A_\infty} \hat{\mathbf{e}}_j^* \times \hat{\mathbf{H}}_{in} \cdot \hat{\mathbf{z}} dA. \tag{B.14}$$

However, it was found by Marcuse [217] that these equations lead to different values and thus he took the geometric mean

$$a_j = \frac{1}{2}\sqrt{\int_{A_\infty} \hat{\mathbf{E}}_{in} \times \hat{\mathbf{h}}_j^* \cdot \hat{\mathbf{z}} dA \int_{A_\infty} \hat{\mathbf{e}}_j^* \times \hat{\mathbf{H}}_{in} \cdot \hat{\mathbf{z}} dA}. \tag{B.15}$$

While Eq. B.15 provided reasonable and generally intuitive results, there were cases where the coupling efficiency exceeded unity, which violates energy conservation [217].

2. Reflection proportional to input beam

The next level of complexity is to assume that the reflected fields have the same spatial distribution, but different power, to the input fields. This is an exact solution if the *waveguide* is a uniform dielectric and the input beam is at normal incidence to the boundary, and the problem becomes a derivation of normal-incidence Fresnel equations. However, when the waveguide is not a uniform dielectric, such as an optical fibre, the reflected fields have a more complicated structure [54]. This then becomes an approximation, which assumedly becomes less accurate the less the optical fibre resembles a uniform dielectric. For example, application of this theory to a small-core air-clad high-refractive-index fibre is expected to be poor.

By making this approximation Eqs. B.9 and B.10 become,

$$\hat{\mathbf{E}}_{in}^t + b\hat{\mathbf{E}}_{in}^t = \sum_j a_j \hat{\mathbf{e}}_{tj} + \mathbf{E}_{rad}^t \tag{B.16}$$

$$\hat{\mathbf{H}}_{in}^{t} - b\hat{\mathbf{H}}_{in}^{t} = \sum_{j} a_j \hat{\mathbf{h}}_{tj} + \mathbf{H}_{rad}^{t}. \tag{B.17}$$

where b is the reflection coupling coefficient that plays a similar role to a_j but for the reflected energy. Note that a π phase change has been written for the reflected magnetic field, which is necessary for the leftwards travelling wave. That is, a relative π phase difference between the electric and magnetic fields indicates travelling in the opposite direction.

Solving the above equations in the same manner used to find Eq. B.11 and B.12 gives

$$a_j = \frac{\left(\int_{A_\infty} \hat{\mathbf{E}}_{in} \times \hat{\mathbf{h}}_j^{*} \cdot \hat{\mathbf{z}} dA\right)\left(\int_{A_\infty} \hat{\mathbf{e}}_j^{*} \times \hat{\mathbf{H}}_{in} \cdot \hat{\mathbf{z}} dA\right)}{\int_{A_\infty} \hat{\mathbf{E}}_{in} \times \hat{\mathbf{h}}_j^{*} \cdot \hat{\mathbf{z}} dA + \int_{A_\infty} \hat{\mathbf{e}}_j^{*} \times \hat{\mathbf{H}}_{in} \cdot \hat{\mathbf{z}} dA} \tag{B.18}$$

$$b = \frac{\int_{A_\infty} \hat{\mathbf{e}}_j^{*} \times \hat{\mathbf{H}}_{in} \cdot \hat{\mathbf{z}} dA - \int_{A_\infty} \hat{\mathbf{E}}_{in} \times \hat{\mathbf{h}}_j^{*} \cdot \hat{\mathbf{z}} dA}{\int_{A_\infty} \hat{\mathbf{E}}_{in} \times \hat{\mathbf{h}}_j^{*} \cdot \hat{\mathbf{z}} dA + \int_{A_\infty} \hat{\mathbf{e}}_j^{*} \times \hat{\mathbf{H}}_{in} \cdot \hat{\mathbf{z}} dA}. \tag{B.19}$$

If the weak guidance approximation is used then the modes are purely transverse and the above equations can be reduced to a more commonly seen expression. The electric and magnetic fields are related by

$$\mathbf{H}_j(\mathbf{r}) = n\left(\frac{\varepsilon_0}{\mu_0}\right)^{\frac{1}{2}} \hat{\mathbf{z}} \times \mathbf{E}_j(\mathbf{r}), \tag{B.20}$$

and by using the following vector identity

$$\mathbf{A} \times (\mathbf{B} \times \mathbf{C}) = (\mathbf{A} \cdot \mathbf{C})\mathbf{B} - (\mathbf{A} \cdot \mathbf{B})\mathbf{C}, \tag{B.21}$$

the normalisation term becomes

$$N_j = \frac{1}{2} n \left(\frac{\varepsilon_0}{\mu_0}\right)^{\frac{1}{2}} \left[\int_{A_\infty} |\mathbf{E}_j|^2 dA\right], \tag{B.22}$$

where n is the refractive index. By using Eqs. B.20, B.21, and B.22, then Eq. B.18 becomes

$$a_j = \sqrt{\left(\frac{4n_1}{(n_1+1)^2}\right)} \int_{A_\infty} \hat{\mathbf{E}}_{in} \cdot \hat{\mathbf{e}}_j^* dA, \tag{B.23}$$

where n_1 is the refractive index of the fibre and the refractive index external to the fibre is unity (for example, air). Thus, it is seen that the standard Fresnel transmission formula comes out of the derivation as expected. Often the term is neglected as it contributes only approximately 4% for the case of a silica-air boundary, that is

$$a_j = \int_{A_\infty} \hat{\mathbf{E}}_{in} \cdot \hat{\mathbf{e}}_j^* dA. \tag{B.24}$$

It has also been shown for TE modes that the coupling efficiency can approximately be given by [212]

$$a_j = \sqrt{\left(\frac{4n_{eff}}{(n_{eff}+1)^2}\right)} \int_{A_\infty} \hat{\mathbf{E}}_{in} \cdot \hat{\mathbf{e}}_j^* dA, \tag{B.25}$$

where n_{neff} is the effective index of the mode of interest.

3. Write the reflection term as a superposition of Laguerre-Gaussian modes

If the input beam is normal to the boundary and circularly symmetric then the reflection term can be written as a superposition of Laguerre-Gaussian modes as was suggested in Ref. [216]. That is, the electric and magnetic reflection fields are written as

$$\mathbf{E}_{ref}(r) = \sum_l b_l LG_l^0(r, r_0)\hat{\mathbf{x}} = \sum_l b_l exp\left(-\frac{r^2}{r_0^2}\right) L_l^0\left(-\frac{2r^2}{r_0^2}\right)\hat{\mathbf{x}} \tag{B.26}$$

$$\mathbf{H}_{ref}(r) = n\left(\frac{\varepsilon_0}{\mu_0}\right)^{\frac{1}{2}} \sum_l b_l LG_l^0(r, r_0)\hat{\mathbf{y}} = n\left(\frac{\varepsilon_0}{\mu_0}\right)^{\frac{1}{2}} \sum_l b_l exp\left(-\frac{r^2}{r_0^2}\right) L_l^0\left(-\frac{2r^2}{r_0^2}\right)\hat{\mathbf{y}}, \tag{B.27}$$

which satisfies the following orthogonality condition

$$\int_{r=0}^{\infty} r LG_m^0(r, r_0) LG_n^0(r, r_0) dr = \frac{r_0^2}{4}\delta_{mn}. \tag{B.28}$$

The problem exists that there are $l + j$ unknowns, but $2j$ equations, that is, from matching the fields at the boundary. However, the orthogonality condition in Eq. B.28 can be used by taking the cross product of the Laguerre-Gaussian modes with Eqs. B.9 and B.10. This gives $2(l + j)$ equations with $l + j$ unknowns. The complication is that this involves integration over the optical fibre radiation fields, which are complicated even for a step-index fibre [54].

B.2 Numerical Modelling of Free Space Coupling into Optical Nanowires

To better understand how the above definitions for coupling efficiency behave a step-index fibre example was modelled. Here a linearly-polarised Gaussian beam was assumed for the input fields while the fibre was set to be an air-clad step-index fibre. The core material was set to be the lead-silicate glass SF57, which has a refractive index of approximately 1.8, so that the refractive index contrast is large and thus the weak guidance approximation is not valid. The step-index fibre guided modes were solved analytically using equations found in Ref. [218]. The coupling efficiency integrals from Eqs. B.15, B.18, B.23, B.24, and B.25 were calculated using Matlab [219] for a variety of core diameters. For each core diameter the input Gaussian beam size was varied until the maximum coupling efficiency was determined, with the results shown in Fig. B.2.

In Fig. B.2 it is seen that each definition has a different result for the coupling efficiency, indicating the approximations made are not particularly accurate. Note that Eq. B.18, which arguably has the least approximations, exceeds unity for a small range of core diameters, which is unphysical. Despite these peculiarities, there are several features displayed in Fig. B.2 that are consistent with expectation:

1. For large core diameters the curves tend to the same values depending on whether reflections were included or ignored. The difference between these is equal to that expected by Fresnel reflection (approximately 9% for the case here where n $\approx$ 1.8).

2. All curves (except Eq. B.23) approach the same value for very small core diameters. This is because the mode for these core diameters lies mostly outside of the glass core and in the air cladding and thus there is no reflection. Only Eq. B.23 does

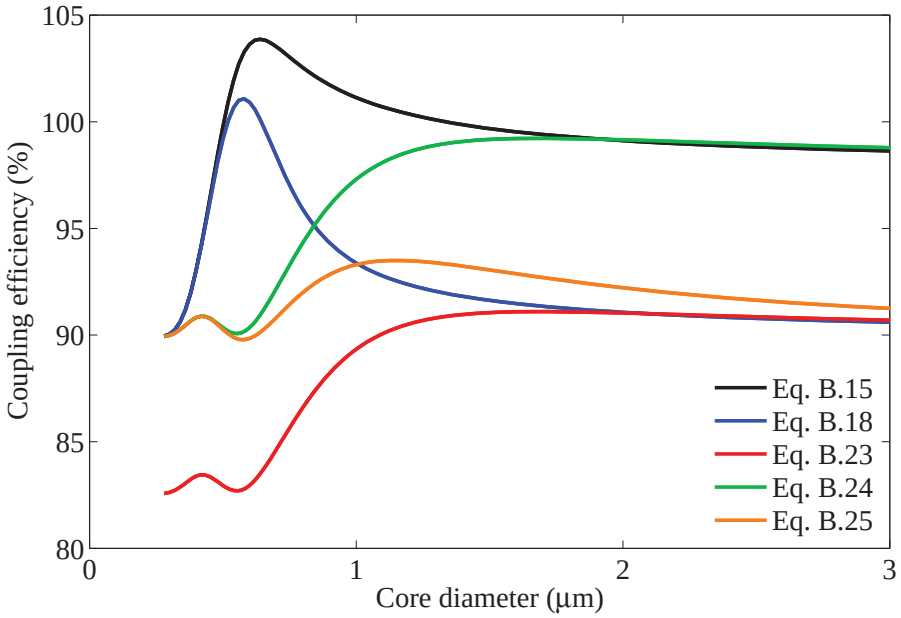

FIGURE B.2: Numeric results showing how the various coupling efficiency definitions differ for a specific example. The input field had a Gaussian distribution with optimised radius. The optical fibre was set to be an air-clad SF57 step-index fibre with variable core diameter.

not approach this value as the reflection term is set to the glass Fresnel reflection value.

Figure B.2 shows that none of the simple coupling efficiency definitions derived in this appendix are likely to give a completely accurate value of the coupling efficiency. However, due to their relative ease of use they can be useful for giving an approximate range of possible coupling efficiencies. For example, Fig. B.2 shows that the maximum coupling efficiency into an optical nanowire using a Gaussian beam is at least 80 %, which is much larger than that commonly found experimentally (for example, 19 % in [P1]).

In order to improve the coupling efficiency equations, such as to prevent unphysical results such as greater than 100% coupling, the derivations above suggest that a full treatment of the optical fibre radiation modes as well as reflections off the fibre end-face is required. As mentioned previously, neither of these factors are simple to calculate analytically. Alternatively, methods such as finite difference time domain (FDTD) techniques could be used, at the expense of numerical complexity.

B.3 Coupling Between Two Waveguides

The second coupling efficiency problem considered in this appendix concerns the coupling from one waveguide into another adjacent waveguide. This can be useful for a variety of applications, such as splicing or butt-coupling of two optical fibres. Of particular interest here is where a single MOF is either filled with a liquid (enclosed suspended-core fibre) or immersed into a liquid (exposed-core fibre, Fig. 7 in [P3]). Consequently, the propagating mode(s) must travel between liquid and non-liquid regions, and there are associated mode mismatch losses when this occurs. To determine the efficiency with which a particular mode can travel across these boundaries the coupling efficiency can be calculated by using a method analogous to that used for the free-space coupling. The primary difference being that instead of a Gaussian input beam with an unknown reflection, the input is some distribution of the guided modes of the fibre and the reflection is a superposition of all the guided and radiation modes of the fibre. That is, Eq. B.9 becomes

$$\sum_j a_j \hat{\mathbf{e}}_{tj} + \sum_j b_j \hat{\mathbf{e}}_{t,-j} + \mathbf{E}_{rad}^{(1)} = \sum_\nu c_\nu \hat{\mathbf{e}}_{t\nu} + \mathbf{E}_{rad}^{(2)}, \tag{B.29}$$

which can be simplified to [54]

$$\sum_j a_j \hat{\mathbf{e}}_{tj} + \sum_j b_j \hat{\mathbf{e}}_{tj} + \mathbf{E}_{rad}^{(1)} = \sum_\nu c_\nu \hat{\mathbf{e}}_{t\nu} + \mathbf{E}_{rad}^{(2)}, \tag{B.30}$$

where a_j are the modal coefficients for the forward propagating electric field modes, $\mathbf{e}_j$, of the first fibre, while b_j are the modal coefficients for the reflected electric field modes, $\mathbf{e}_- j$, of the first fibre. c_ν are the modal coefficients for the electric field modes, $\mathbf{e}_\nu$, of the second fibre. $\mathbf{E}_{rad}^{(1)}$ is the reflected radiation field of the first fibre and $\mathbf{E}_{rad}^{(2)}$ is the radiation field of the second fibre. Note that only the transverse components of the electric fields are included as only these components have continuity across the boundary.

Similarly for the magnetic field

$$\sum_j a_j \hat{\mathbf{h}}_{tj} - \sum_j b_j \hat{\mathbf{h}}_{tj} + \mathbf{H}_{rad}^{(1)} = \sum_\nu c_\nu \hat{\mathbf{h}}_{t\nu} + \mathbf{H}_{rad}^{(2)}. \tag{B.31}$$

For this problem the coefficients a_j are known as they are set by the initial launch conditions of the first fibre. This could be approximated as the fundamental mode only, as was done in [P3], or could be a more complicated superposition of all modes in the fibre. For now all modes will be retained but it is to be understood that all a_j terms are already known by some means.

The aim now is to determine the unknown coefficients, which are the reflection b_j and transmission a_ν coefficients. These are determined using orthonormality of the modes as was done previously for the free space coupling problem. Taking the right cross product of Eq. B.30 with the complex conjugate of the ν^{th} magnetic guided field, using orthnormality of the guided and radiation modes, and integrating across the boundary yields Eq. B.32.

$$\begin{aligned} c_\nu = \frac{1}{2}\Bigg(&\sum_j a_j \int_{A_\infty} \hat{\mathbf{e}}_j \times \hat{\mathbf{h}}_\nu^* \cdot \hat{\mathbf{z}} dA + \sum_j b_j \int_{A_\infty} \hat{\mathbf{e}}_j \times \hat{\mathbf{h}}_\nu^* \cdot \hat{\mathbf{z}} dA \\ &+ \int_{A_\infty} \mathbf{E}_{rad}^{(1)} \times \hat{\mathbf{h}}_\nu^* \cdot \hat{\mathbf{z}} dA \Bigg). \end{aligned} \tag{B.32}$$

Similarly, taking the left cross product of Eq. B.31 with the complex conjugate of the j^{th} electric guided field, using orthnormality of the guided and radiation modes, and integrating across the boundary yields Eq. B.33.

$$\begin{aligned} c_\nu = \frac{1}{2}\Bigg(&\sum_j a_j \int_{A_\infty} \hat{\mathbf{e}}_\nu^* \times \hat{\mathbf{h}}_j \cdot \hat{\mathbf{z}} dA - \sum_j b_j \int_{A_\infty} \hat{\mathbf{e}}_\nu^* \times \hat{\mathbf{h}}_j \cdot \hat{\mathbf{z}} dA \\ &+ \int_{A_\infty} \hat{\mathbf{e}}_\nu^* \times \mathbf{H}_{rad} \cdot \hat{\mathbf{z}} dA \Bigg). \end{aligned} \tag{B.33}$$

Similarly, orthonormality of the modes in the first fibre can be used to obtain another set of equations. However, note at this point that Eqs. B.32 and B.33 contain integrals over the radiation modes of the first fibre. As stated previously, these are complicated to

calculate and thus the approximation is made that coupling into the reflected radiation modes is zero. After this approximation Eqs. B.32 and B.33 become

$$c_\nu = \frac{1}{2}\left(\sum_j a_j \int_{A_\infty} \hat{\mathbf{e}}_j \times \hat{\mathbf{h}}_\nu^* \cdot \hat{\mathbf{z}} dA + \sum_j b_j \int_{A_\infty} \hat{\mathbf{e}}_j \times \hat{\mathbf{h}}_\nu^* \cdot \hat{\mathbf{z}} dA\right) \tag{B.34}$$

$$c_\nu = \frac{1}{2}\left(\sum_j a_j \int_{A_\infty} \hat{\mathbf{e}}_\nu^* \times \hat{\mathbf{h}}_j \cdot \hat{\mathbf{z}} dA - \sum_j b_j \int_{A_\infty} \hat{\mathbf{e}}_\nu^* \times \hat{\mathbf{h}}_j \cdot \hat{\mathbf{z}} dA\right). \tag{B.35}$$

Eqs. B.34 and B.35 are most easily solved by putting them into matrix form. To do this the following vectors are defined

$$\begin{aligned} \mathbf{a} &= [a_1, a_2, \ \ldots a_j \ \ldots] \\ \mathbf{b} &= [a_1, a_2, \ \ldots b_j \ \ldots] \\ \mathbf{c} &= [b_1, b_2, \ \ldots c_\nu \ \ldots], \end{aligned} \tag{B.36}$$

and the following matrices are defined

$$\begin{aligned} M_{j\nu} &= \tfrac{1}{2}\textstyle\int_{A_\infty} \hat{\mathbf{e}}_\nu^* \times \hat{\mathbf{h}}_j \cdot \hat{\mathbf{z}} dA \\ N_{j\nu} &= \tfrac{1}{2}\textstyle\int_{A_\infty} \hat{\mathbf{e}}_j \times \hat{\mathbf{h}}_\nu^* \cdot \hat{\mathbf{z}} dA. \end{aligned} \tag{B.37}$$

Using these definitions Eqs. B.34 and B.35 become

$$\begin{aligned} \mathbf{c} &= \mathbf{a}N + \mathbf{b}N \\ \mathbf{c} &= \mathbf{a}M - \mathbf{b}M. \end{aligned} \tag{B.38}$$

Solving Eq. B.38 gives the coupling coefficients as

$$\mathbf{c} = 2\mathbf{a}(N^{-1} + M^{-1})^{-1} \tag{B.39}$$

B.4 Coupling Equations used in [P3]

In [P3] the coupling efficiency across a liquid boundary in both a fluid filled wagon wheel fibre and a liquid immersed exposed-core fibre was calculated. As was done to obtain Eq.

B.39, the reflected radiation fields were neglected. In addition, only the fundamental modes were used in Eq. B.39. That is, for the symmetric wagon wheel fibre the two degenerate fundamental modes were used, while for the exposed-core fibre the two non-degenerate fundamental modes were used. Additionally, it was assumed that the input fields comprised of only one of the fundamental modes and its corresponding coefficient was set to unity so that $|c_j|^2$ directly gives the coupling efficiency into the j^{th} mode. As shown in [P3], this simplifies Eqs. B.30 and B.31 to

$$\hat{\mathbf{e}}_{t1} + b_1\hat{\mathbf{e}}_{t1} + b_2\hat{\mathbf{e}}_{t2} = c_1\hat{\mathbf{e}}'_{t1} + c_2\hat{\mathbf{e}}'_{t2} + \mathbf{E}^{(2)}_{rad} \tag{B.40}$$

$$\hat{\mathbf{h}}_{t1} - b_1\hat{\mathbf{h}}_{t1} - b_2\hat{\mathbf{h}}_{t2} = c_1\hat{\mathbf{h}}'_{t1} + c_2\hat{\mathbf{h}}'_{t2} + \mathbf{H}^{(2)}_{rad}, \tag{B.41}$$

where $\hat{\mathbf{e}}_t$ and $\hat{\mathbf{h}}_t$ are the transverse components of the electric and magnetic fields of the first fibre, and $\hat{\mathbf{e}}'_t$ and $\hat{\mathbf{h}}'_t$ are the transverse components of the electric and magnetic fields of the second fibre. The subscripts 1 and 2 refer to the two fundamental modes.

Equations B.40 and B.41 correspond to Eq. B.39 but where

$$\begin{aligned} j &= 1, 2 \\ \nu &= 1, 2 \\ \mathbf{a} &= [1, 0] \textit{ or } [0, 1]. \end{aligned} \tag{B.42}$$

Appendix C

W-fibre Confinement Loss

The propagating modes of a suspended-core fibre, or any single material MOF, are not true guided modes due to the presence of the outer cladding which has the same refractive index as the core. Instead, these fibres propagate leaky modes, which can behave similar to guided modes except that the propagation constant is complex, leading to an intrinsic decay term (confinement loss). This can be determined numerically, such as by using finite element modelling as was done to determine the modes of suspended-core fibres in [P1-P3]. This involves optimising perfectly matched layers (PMLs) at the solution boundary [220]. A computationally faster and more precise (but less accurate) alternative is to approximate the suspended-core fibre as a jacketed air-suspended rod, or W-fibre (Fig. C.1), which can be solved for exactly.

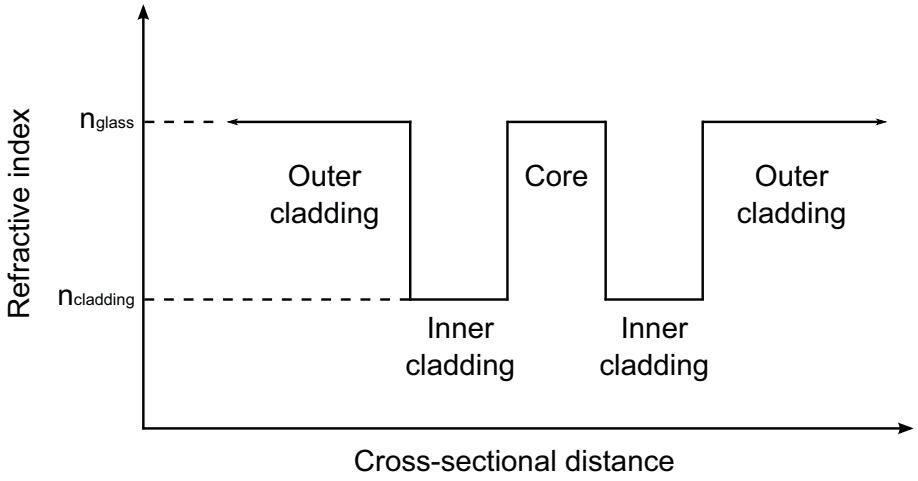

FIGURE C.1: Refractive index profile for a W-fibre for the special case where the core and outer cladding refractive indices are equal, which approximates a suspended-core fibre. Throughout this derivation the refractive indices will be defined as n_1 for the core index, n_2 for the inner cladding index, and n_3 for the outer cladding index.

In this appendix is a derivation of the W-fibre confinement loss equations, which were used to calculate the confinement loss of the fundamental mode in [P6] and for all modes in [P4]. In both [P4] and [P6] it was assumed that the core and outer cladding indices were equal, as is the case for a suspended-core fibre, and thus all propagating modes found will be leaky modes. The theory outlined in this appendix does not necessarily make this assumption, and as such the refractive indices will be defined as n_1 for the core index, n_2 for the inner cladding index, and n_3 for the outer cladding index. Note that if $n_1 > n_2 > n_3$ the propagating modes will not have any confinement loss and if $n_1 > n_3 > n_2$ there may exist both leaky modes (with confinement loss) and guided modes (with no confinement loss).

Calculation of confinement loss for W-fibres has previously been derived for weakly guiding fibres [221–223], and this has been applied to microstructured optical fibres [224]. However, here the derivation is shown for vectorial solutions to the wave equation and thus is applicable to both weakly and strongly guiding fibres.

To start, cylindrical coordinates (r, θ, z) are chosen where z is along the fibre axis, r is in the radial direction with origin at the fibre centre, and θ is the azimuthal variable. It can then be shown from Maxwell's equations that the two sets of wave equations for optical fibres are [218]

$$\frac{\partial^2 E_z}{\partial r^2} + \frac{1}{r}\frac{\partial E_z}{\partial r} + \frac{1}{r^2}\frac{\partial^2 E_z}{\partial \theta^2} + [k^2 n(r,\theta)^2 - \beta^2]E_z = 0 \tag{C.1}$$

$$\frac{\partial^2 H_z}{\partial r^2} + \frac{1}{r}\frac{\partial H_z}{\partial r} + \frac{1}{r^2}\frac{\partial^2 H_z}{\partial \theta^2} + [k^2 n(r,\theta)^2 - \beta^2]H_z = 0, \tag{C.2}$$

where E_z and H_z are the z-component of the electric and magnetic fields, respectively, and $n(r, \theta)$ is the refractive index profile. β is the propagation constant, which is related to the effective (phase) index n_{eff}, where $n_{eff} = \beta/k$, $k = 2\pi/\lambda$ is the wavenumber, and λ is the free-space wavelength.

As the W-fibre is axially symmetric the refractive index profile is independent of θ and can be expressed as $n(r)$. The transverse electric and magnetic fields can then be written as [218]

$$E_\theta = -\frac{j}{[k^2 n(r)^2 - \beta^2]} \left(\frac{\beta}{r} \frac{\partial E_z}{\partial \theta} - \omega \mu_0 \frac{\partial H_z}{\partial r} \right) \tag{C.3}$$

$$E_r = -\frac{j}{[k^2 n(r)^2 - \beta^2]} \left(\beta \frac{\partial E_z}{\partial r} + \frac{\omega \mu_0}{r} \frac{\partial H_z}{\partial \theta} \right) \tag{C.4}$$

$$H_\theta = -\frac{j}{[k^2 n(r)^2 - \beta^2]} \left(\frac{\beta}{r} \frac{\partial H_z}{\partial \theta} + \omega \epsilon_0 n(r)^2 \frac{\partial E_z}{\partial r} \right) \tag{C.5}$$

$$H_r = -\frac{j}{[k^2 n(r)^2 - \beta^2]} \left(\beta \frac{\partial H_z}{\partial r} - \frac{\omega \epsilon_0 n(r)^2}{r} \frac{\partial E_z}{\partial \theta} \right), \tag{C.6}$$

where E_r and H_r are the radial components of the electric and magnetic fields, respectively, and E_θ and H_θ are the azimuthal components of the electric and magnetic fields, respectively. μ_0 is the free-space magnetic permeability and ω is the angular frequency, which is related to the wavenumber by $\omega = kc$, where c is the speed of light in a vacuum.

The next step is to solve the wave equation and apply boundary conditions to the tangential components of the electric and magnetic fields. This will provide a dispersion relation for which the propagation constant, β, can be determined. How this is determined depends upon whether the modes are transverse-electric (TE), transverse magnetic (TM), or hybrid (HE).

C.1 TE Modes

By definition, TE modes have $E_z = 0$, which is a solution to Eq. C.1. By noting that the azimuthal dependency of the electric and magnetic fields in axially symmetric fibres is expressed by $cos(n\theta + \psi)$ or $sin(n\theta + \psi)$ (ψ is a phase constant and n is an integer), the wave equation in Eq. C.2 becomes [218]

$$\frac{\partial^2 H_z}{\partial r^2} + \frac{1}{r} \frac{\partial H_z}{\partial r} + \left[k^2 n(r)^2 - \beta^2 - \frac{n^2}{r^2} \right] H_z = 0. \tag{C.7}$$

The radial and azimuthal electric and magnetic field components from Eqs. C.3 to C.6 become

$$E_\theta = \frac{j\omega\mu_0}{[k^2 n(r)^2 - \beta^2]} \frac{\partial H_z}{\partial r} \tag{C.8}$$

$$E_r = -\frac{j\omega\mu_0}{[k^2 n(r)^2 - \beta^2]} \frac{1}{r} \frac{\partial H_z}{\partial \theta} \tag{C.9}$$

$$H_\theta = -\frac{j\beta}{[k^2 n(r)^2 - \beta^2]} \frac{1}{r} \frac{\partial H_z}{\partial \theta} \tag{C.10}$$

$$H_r = -\frac{j\beta}{[k^2 n(r)^2 - \beta^2]} \frac{\partial H_z}{\partial \theta}. \tag{C.11}$$

The magnetic field in the core and cladding regions is written as [218]

$$H_z = \begin{cases} f(r)cos(n\theta + \psi) & (0 \leq r \leq a) \\ g(r)cos(n\theta + \psi) & (a \leq r \leq b) \\ h(r)cos(n\theta + \psi) & (r \geq b), \end{cases} \tag{C.12}$$

where $f(r)$, $g(r)$, and $h(r)$ are arbitrary functions and ψ is an arbitrary phase constant.

In the next step, the tangential field components, H_z and H_θ, are matched at the $r = a$ boundary so that a simplification can be obtained. Matching these fields at $r = a$ gives

$$f(a) = g(a) \tag{C.13}$$

$$\frac{j\beta}{[k^2 n_1^2 - \beta^2]} \frac{n}{a} g(a) sin(n\theta + \psi) = \frac{j\beta}{[k^2 n_2^2 - \beta^2]} \frac{n}{a} h(a) sin(n\theta + \psi). \tag{C.14}$$

The only possible solution for these equations is $n = 0$, and as a result there is no azimuthal dependency for TE modes. Applying this to Eqs. C.7 to C.11 gives the following expressions for the electric and magnetic fields

$$\frac{d^2 H_z}{dr^2} + \frac{1}{r} \frac{dH_z}{dr} + [k^2 n(r)^2 - \beta^2] H_z = 0 \tag{C.15}$$

$$E_\theta = \frac{j\omega\mu_0}{[k^2 n(r)^2 - \beta^2]} \frac{dH_z}{dr} \tag{C.16}$$

$$H_r = \frac{-j\beta}{[k^2 n(r)^2 - \beta^2]} \frac{dH_z}{dr} \tag{C.17}$$

$$E_r = H_\theta = 0. \tag{C.18}$$

For simplification, the following definitions are made

$$\begin{aligned} u_1 &= \sqrt{k^2 n_1^2 - \beta^2} \\ u_2 &= \sqrt{\beta^2 - k^2 n_2^2} \\ u_3 &= \sqrt{k^2 n_3^2 - \beta^2}. \end{aligned} \tag{C.19}$$

Implicit in this step is that $n_2 k < \beta < n_1 k$ and $\beta < n_3 k$, as is the case if $n_1 = n_3$. This will be assumed to be the case for the remainder of this derivation. However, if the refractive index profile is such that this is not the case then the derivation follows closely but with a more appropriate definition for u_1, u_2, and/or u_3. Also, the wave equations and resulting dispersion equation may become slightly altered depending on the refractive index profile.

Using these definitions the wave equation in each region of the fibre is

$$\frac{d^2 H_z}{dr^2} + \frac{1}{r}\frac{dH_z}{dr} + u_1^2 H_z = 0 \qquad (0 \le r \le a) \tag{C.20}$$

$$\frac{d^2 H_z}{dr^2} + \frac{1}{r}\frac{dH_z}{dr} - u_2^2 H_z = 0 \qquad (a \le r \le b) \tag{C.21}$$

$$\frac{d^2 H_z}{dr^2} + \frac{1}{r}\frac{dH_z}{dr} + u_3^2 H_z = 0 \qquad (r \ge b). \tag{C.22}$$

Eqs. C.20 to C.22 are Bessel equations, with Bessel function solutions [225]. The solution to Eq. C.20 is a linear combination of $J_0(u_1 r)$ and $Y_0(u_1 r)$ Bessel functions. However,

$Y_0(u_1 r)$ diverges at $r = 0$ and thus the associated coefficient is set to zero so that a physical solution is found. The solution to Eq. C.21 is a linear combination of $K_0(u_2 r)$ and $I_0(u_2 r)$ modified Bessel functions. Both of these solutions are kept as neither diverges in the region $a \leq r \leq b$. The solution to Eq. C.22 is a linear combination of $H_0^{(1)}(u_3 r)$ and $H_0^{(2)}(u_3 r)$ Bessel functions (Hankel functions). Physically, $H_0^{(1)}(u_3 r)$ refers to an outward propagating wave while $H_0^{(2)}(u_3 r)$ refers to an inwards propagating wave. As physically there cannot be an inward propagating wave the coefficient associated with $H_0^{(2)}(u_3 r)$ is set to zero.

Using the above arguments

$$H_z = \begin{cases} AJ_0(u_1 r) & (0 \leq r \leq a) \\ BK_0(u_2 r) + CI_0(u_2 r) & (a \leq r \leq b) \\ DH_0^{(1)}(u_3 r) & (r \geq b) \end{cases}, \tag{C.23}$$

where A, B, C, and D are constants.

Continuity of the above equations at $r = a$ and $r = b$ gives

$$AJ_0(u_1 a) = BK_0(u_2 a) + CI_0(u_2 a) \tag{C.24}$$

$$BK_0(u_2 b) + CI_0(u_2 b) = DH_0^{(1)}(u_3 b). \tag{C.25}$$

Continuity of E_θ (found by substitution of Eq. C.23 into Eq. C.16) at $r = a$ and $r = b$ gives

$$A\frac{J_0'(u_1 a)}{u_1} = -B\frac{K_0'(u_2 a)}{u_2} - C\frac{I_0'(u_2 a)}{u_2} \tag{C.26}$$

$$-B\frac{K_0'(u_2 b)}{u_2} - C\frac{I_0'(u_2 b)}{u_2}A = D\frac{H_0^{(1)\prime}(u_3 b)}{u_3}. \tag{C.27}$$

The Bessel function derivatives in Eqs. C.26 and C.27 can be simplified by using the following identities

$$\begin{aligned} J_0'(z) &= -J_1(z) \\ K_0'(z) &= -K_1(z) \\ I_0'(z) &= I_1(z) \\ H_0^{(1)\,\prime}(z) &= -H_1^{(1)}(z). \end{aligned} \tag{C.28}$$

Eqs. C.24 to C.27 can then be put into the following homogeneous matrix equation

$$\mathbf{Mx} = \mathbf{0}, \tag{C.29}$$

where $\mathbf{x} = (A, B, C, D)$ and

$$\mathbf{M} = \begin{pmatrix} -J_0(u_1a) & K_0(u_2a) & I_0(u_2a) & 0 \\ 0 & K_0(u_2b) & I_0(u_2b) & -H_0^{(1)}(u_3b) \\ \frac{J_1(u_1a)}{u_1} & \frac{K_1(u_2a)}{u_2} & -\frac{I_1(u_2a)}{u_2} & 0 \\ 0 & \frac{K_1(u_2b)}{u_2} & -\frac{I_1(u_2b)}{u_2} & \frac{H_1^{(1)}(u_3b)}{u_3} \end{pmatrix}. \tag{C.30}$$

Equation C.29 is a homogeneous matrix equation and as such can only have a nontrivial solution if and only if the determinant of $\mathbf{M}$ is zero (Cramer's Rule [225]). Thus, the following equation can be used to determine the complex propagation constant β

$$det(\mathbf{M}) = 0, \tag{C.31}$$

and from this the loss, α_{dB} (in dB/m), can be determined using

$$\alpha_{dB} = Im(\beta)20log_{10}(e). \tag{C.32}$$

C.2 TM Modes

The propagation constant, and hence confinement loss, for the TM modes is determined in an analogous method to the TE modes except that $H_z = 0$ instead of $E_z = 0$. Consequently, the wave equation for E_z and the electric and magnetic fields are expressed as

$$\frac{d^2E_z}{dr^2} + \frac{1}{r}\frac{dE_z}{dr} + [k^2n(r)^2 - \beta^2]E_z = 0 \tag{C.33}$$

$$E_r = -\frac{j\beta}{[k^2n(r)^2 - \beta^2]}\frac{dE_z}{dr} \tag{C.34}$$

$$H_\theta = \frac{-j\omega\epsilon_0 n(r)^2}{[k^2n(r)^2 - \beta^2]}\frac{dE_z}{dr} \tag{C.35}$$

$$E_\theta = H_r = 0. \tag{C.36}$$

As discussed in regards to the TE modes, the solution to Eq. C.33 is a physically-appropriate superposition of Bessel functions. By applying continuity of the tangential components of the electric and magnetic fields (E_z and H_θ) at the two boundaries ($r = a$ and $r = b$) a matrix equation similar to Eq. C.29 is found, but where

$$\mathbf{M} = \begin{pmatrix} -J_0(u_1a) & K_0(u_2a) & I_0(u_2a) & 0 \\ 0 & K_0(u_2b) & I_0(u_2b) & -H_0^{(1)}(u_3b) \\ \frac{n_1^2}{u_1}J_1(u_1a) & \frac{n_2^2}{u_2}K_1(u_2a) & -\frac{n_2^2}{u_2}I_1(u_2a) & 0 \\ 0 & \frac{n_2^2}{u_2}K_1(u_2b) & -\frac{n_2^2}{u_2}I_1(u_2b) & \frac{n_3^2}{u_3}H_1^{(1)}(u_3b) \end{pmatrix}. \tag{C.37}$$

Again, the confinement loss is determined by solving Eqs. C.31 and C.32.

C.3 Hybrid (HE) Modes

The third, more general, solution to the wave equations in Eqs. C.1 and C.2 is that neither E_z or H_z are zero. The solutions are then a product of n^{th} order Bessel functions and either $cos(n\theta + \psi)$ or $sin(n\theta + \psi)$ [218]. The propagation constant(s) are found in a manner analogous to the TE and TM modes, but where eight coefficients are present (instead of four) due to construction of both the E_z or H_z fields. That is, the fields are expressed as

$$E_z = \begin{cases} AJ_n(u_1 r)cos(n\theta + \psi) & (0 \leq r \leq a) \\ [BK_n(u_2 r) + CI_n(u_2 r)]\, cos(n\theta + \psi) & (a \leq r \leq b) \\ DH_n^{(1)}(u_3 r)cos(n\theta + \psi) & (r \geq b) \end{cases} \tag{C.38}$$

$$H_z = \begin{cases} FJ_n(u_1 r)sin(n\theta + \psi) & (0 \leq r \leq a) \\ [GK_n(u_2 r) + LI_n(u_2 r)]\, sin(n\theta + \psi) & (a \leq r \leq b) \\ MH_n^{(1)}(u_3 r)sin(n\theta + \psi) & (r \geq b) \end{cases}, \tag{C.39}$$

where A, B, C, D, F, G, L, and M are constants.

Continuity of E_z and H_z from the Eqs. C.38 and C.39 at the boundaries $r = a$ and $r = b$ yields four out of the eight required simultaneous equations. Continuity of E_θ and H_θ at the boundaries $r = a$ and $r = b$ yield the other four simultaneous equations. These fields are determined by substituting Eqs. C.38 and C.39 into Eqs. C.3 and C.5, respectively.

By using the following Bessel function derivative identities

$$\begin{aligned} J_n'(z) &= \tfrac{1}{2}[J_{n-1}(z) - J_{n+1}(z)] \\ I_n'(z) &= \tfrac{1}{2}[I_{n-1}(z) + I_{n+1}(z)] \\ K_n'(z) &= -\tfrac{1}{2}[K_{n-1}(z) + K_{n+1}(z)] \\ H_n^{(1)\,\prime}(z) &= \tfrac{1}{2}[H_{n-1}^{(1)}(z) - H_{n+1}^{(1)}(z)], \end{aligned} \tag{C.40}$$

the eight continuity equations can be placed into a matrix equation (C.29) where **M** is given by

$$
\mathbf{M} = \begin{pmatrix}
-J_n(u_1a) & K_n(u_2a) & I_n(u_2a) & 0 \\
0 & K_n(u_2b) & I_n(u_2b) & -H_n^{(1)}(u_3b) \\
\frac{\omega\epsilon_0 n_1^2}{2u_1}[J_{n-1}(u_1a) - J_{n+1}(u_1a)] & -\frac{\omega\epsilon_0 n_2^2}{2u_2}[K_{n-1}(u_2a) + K_{n+1}(u_2a)] & \frac{\omega\epsilon_0 n_2^2}{2u_2}[I_{n-1}(u_2a) + I_{n+1}(u_2a)] & 0 \\
0 & -\frac{\omega\epsilon_0 n_2^2}{2u_2}[K_{n-1}(u_2b) + K_{n+1}(u_2b)] & \frac{\omega\epsilon_0 n_2^2}{2u_2}[I_{n-1}(u_2b) + I_{n+1}(u_2b)] & \frac{\omega\epsilon_0 n_3^2}{2u_3}[H_{n-1}^{(1)}(u_3b) - H_{n+1}^{(1)}(u_3b)] \\
0 & 0 & 0 & 0 \\
0 & 0 & 0 & 0 \\
\frac{n\beta}{u_1^2a}J_n(u_1a) & \frac{n\beta}{u_2^2a}K_n(u_2a) & \frac{n\beta}{u_2^2a}I_n(u_2a) & 0 \\
0 & \frac{n\beta}{u_2^2b}K_n(u_2b) & \frac{n\beta}{u_2^2b}I_n(u_2b) & \frac{n\beta}{u_3^2b}H_n^{(1)}(u_3b)
\end{pmatrix}
$$

$$
\begin{pmatrix}
0 & 0 & 0 & 0 \\
0 & 0 & 0 & 0 \\
\frac{n\beta}{u_1^2a}J_n(u_1a) & \frac{n\beta}{u_2^2a}K_n(u_2a) & \frac{n\beta}{u_2^2a}I_n(u_2a) & 0 \\
0 & \frac{n\beta}{u_2^2b}K_n(u_2b) & \frac{n\beta}{u_2^2b}I_n(u_2b) & \frac{n\beta}{u_3^2b}H_n^{(1)}(u_3b) \\
-J_n(u_1a) & K_n(u_2a) & I_n(u_2a) & 0 \\
0 & K_n(u_2b) & I_n(u_2b) & -H_n^{(1)}(u_3b) \\
\frac{\omega\mu_0}{2u_1}[J_{n-1}(u_1a) - J_{n+1}(u_1a)] & -\frac{\omega\mu_0}{2u_2}[K_{n-1}(u_2a) + K_{n+1}(u_2a)] & \frac{\omega\mu_0}{2u_2}[I_{n-1}(u_2a) + I_{n+1}(u_2a)] & 0 \\
0 & -\frac{\omega\mu_0}{2u_2}[K_{n-1}(u_2b) + K_{n+1}(u_2b)] & \frac{\omega\mu_0}{2u_2}[I_{n-1}(u_2b) + I_{n+1}(u_2b)] & \frac{\omega\mu_0}{2u_3}[H_{n-1}^{(1)}(u_3b) - H_{n+1}^{(1)}(u_3b)]
\end{pmatrix}. \qquad \text{(C.41)}
$$

Again, the propagation constant β, and thus the confinement loss, is determined by solving Eqs. C.31 and then C.32.

Note that the upper-left 4×4 elements in Eq. C.41 correspond to the TM mode matrix in Eq. C.37 when $n = 0$, while the lower-right 4×4 elements correspond to the TE mode matrix in Eq. C.30 when $n = 0$. In fact, the matrix in Eq. C.41 can be used to solve all modes of the W-fibre by appropriately setting the value of n. That is, TE modes ($n = 0$), TM modes ($n = 0$), and HE modes ($n \geq 1$).

Note also that the matrix in Eq. C.41 can be reduced to a smaller 4×4 matrix, or even a single equation. However, the 8×8 format is useful for error checking as each row corresponds to a continuity equation and no algebraic manipulation is required.

C.4 Implementation of Confinement Loss Theory

The confinement loss theory detailed in this appendix was used to calculate the confinement loss of water-clad optical nanowires in [P4] in order to determine how this influences the fluorescence-sensing efficiency for such devices. In [P4] the confinement loss was determined for all modes of the fibre to complement the fluorescence capture fraction, which was also calculated for all modes. Below is an outline of the practical implementation of this confinement loss theory, which was calculated in Matlab [219]. Also, in [P6], the confinement loss of the fundamental mode was calculated using a method similar to that outlined below.

1. The propagation constant of the fibre was first determined for the simpler case where the outer cladding was ignored, that is, a step-index fibre. This was found using the dispersion equation in Ref. [218] and a modified bisection method for root finding (rather than bisection multiple points were used to take into account multiple roots).

2. Mode labelling was applied to each solution using the convention specified in Ref. [54].

3. Each solution found for the step-index dispersion equation was used as a start value for finding the zeros of the determinant of the matrix in Eq. C.41. Roots were found using *fsolve* from Matlab's optimisation toolbox.

This method works well because the outer cladding can generally be considered as a small perturbation to the equivalent step-index solution. This breaks down when the imaginary part of the propagation constant for the W-fibre becomes large (if say, $a \approx b$ and/or $a \ll \lambda$), in which case the confinement loss is extremely large and generally not of interest.

Appendix D

Aluminium Ion Sensing Publication

This appendix contains a paper that has been compiled from the surface functionalisation work that was presented in Chapter 5. It will be submitted to the *Journal of the American Chemical Society* shortly after submission of this thesis. It shows how an aluminium ion dip sensor can be created by surface functionalising a microstructured optical fibre using a derivative of lumogallion and a polyelectrolyte base layer.

S. C. Warren-Smith, S. Heng, H. Ebendorff-Heidepriem, A. D. Abell, T. M. Monro, "Fluorescence-based aluminum ion sensing using a surface functionalized microstructured optical fiber," to be submitted to *Journal of the American Chemical Society*.

D.1 Statement of Contribution

Conceptualisation

The concept of attaching a derivative of lumogallion to glass surfaces was originally conceptualised by Markus Pietsch and Heike Ebendorff-Heidepriem. A potential chemical synthesis that would allow for this was proposed by Markus Pietsch and Andrew Abell, which was later simplified, improved, and realised by Sabrina Heng. Alexandre Francois suggested using polyelectrolytes as the base layer upon which to attach the lumogallion derivative.

Realisation

Chemical synthesis of the lumogallion derivative in this paper was done by Sabrina Heng. Cuvette measurements, glass slide experiments, and microstructured optical fibre experiments were done by Stephen Warren-Smith. The inflated wagon wheel fibres were fabricated by Heike Ebendorff-Heidepriem and Roger Moore.

Documentation

This paper was primarily written by Stephen Warren-Smith and Sabrina Heng, with editing by all authors.

Declaration and Permission

I declare that the above statement of contribution is accurate and I give permission for this publication to be included in this thesis.

Stephen C. Warren-Smith Sabrina Heng Heike Ebendorff-Heidepriem

Andrew D. Abell Tanya M. Monro

Warren-Smith, S.C., Heng, S., Ebendorff-Heidepriem, H., Abell, A.D. and Monro, T.M. (2011) Fluorescence-Based Aluminum Ion Sensing using a Surface Functionalized Microstructured Optical Fiber
Langmuir, v.27 (9), pp. 5680-5685, April 2011

Bibliography

[1] B. Culshaw. Optical fiber sensor technologies: opportunities and-perhaps-pitfalls. *J. Lightwave Technol.*, 22:39–50, 2004.

[2] B. Lee. Review of the present status of optical fiber sensors. *Optic. Fiber Technol.*, 9:57–79, 2003.

[3] D. A. Krohn. *Fiber optic sensors*. Instrument Society of America, 2000.

[4] O. S. Wolfbeis. Fiber-optic chemical sensors and biosensors. *Anal. Chem.*, 78: 3859–3874, 2006.

[5] B. D. Gupta and R. K. Verma. Surface plasmon resonance-based fiber optic sensors: principle, probe designs, and some applications. *J. Sensors*, Article ID: 979761, 2009.

[6] P. R. Stoddart and D. J. White. Optical fibre SERS sensors. *Anal. Bioanal. Chem.*, 394:1761–1774, 2009.

[7] R. A. Potyrailo, S. E. Hobbs, and G. M. Hieftje. Optical waveguide sensors in analytical chemistry: today's instrumentation, applications and trends for future development. *Fresen. J. Anal. Chem.*, 362:349–373, 1998.

[8] G. McAdam, P. J. Newman, I. McKenzie, C. Davis, and B. R. W. Hinton. Fiber optic sensors for detection of corrosion within aircraft. *Struct. Health Monit.*, 4: 47–56, 2005.

[9] G. Stewart, W. Jin, and B. Culshaw. Prospects for fibre-optic evanescent-field gas sensors using absorption in the near-infrared. *Sens. Act. B - Chem.*, 38:42–47, 1997.

[10] J. Laegsgaard and A. Bjarklev. Microstructured optical fibers-fundamentals and applications. *J. Am. Ceram. Soc.*, 89:2–12, 2006.

[11] T. M. Monro, W. Belardi, K. Furusawa, J. C. Baggett, N. G. R. Broderick, and D. J. Richardson. Sensing with microstructured optical fibres. *Meas. Sci. Technol.*, 12:854–858, 2001.

[12] O. Frazao, J. L. Santos, F. M. Araujo, and L. A. Ferreira. Optical sensing with photonic crystal fibers. *Laser and Photonic Reviews*, 2:449–459, 2008.

[13] T. R. Glass, S. Lackie, and T. Hirschfeld. Effect of numerical aperture on signal level in cylindrical wave-guide evanescent fluorosensors. *Appl. Optics*, 26:2181–2187, 1987.

[14] H. P. Kao, N. Yang, and J. S. Schoeniger. Enhancement of evanescent fluorescence from fiber-optic sensors by thin-film sol-gel coatings. *J. Opt. Soc. Am. A*, 15:2163–2171, 1998.

[15] G. Stewart and B Culshaw. Optical waveguide modeling and design for evanescent field chemical sensors. *Opt. Quant. Electron.*, 26:S249–S259, 1994.

[16] D. Marcuse. Excitation of parabolic-index fibers with incoherent sources. *Bell Syst. Tech. J.*, 54:1507–1530, 1975.

[17] D. Marcuse. Launching light into fiber cores from sources located in the cladding. *J. Lightwave Technol.*, 6:1273–1279, 1988.

[18] C. O. Egalon and R. S. Rogowski. Theoretical-model for a thin cylindrical film optical fiber fluorosensor. *Opt. Eng.*, 31:237–244, 1992.

[19] C. O. Egalon and R. S. Rogowski. Efficiency of core light injection from sources in the cladding - bulk distribution. *Opt. Eng.*, 31:846–851, 1992.

[20] C. O. Egalon, R. S. Rogowski, and A. C. Tai. Excitation efficiency of an optical fiber core source. *Opt. Eng.*, 31:1328–1331, 1992.

[21] S. J. Spammer, P. L. Fuhr, M. Nelson, and D. Huston. Rebar-epoxied optical fiber Bragg gratings for civil structures. *Microw. Opt. Techn. Let.*, 18:214–219, 1998.

[22] M. Zavrsnik and G. Stewart. Analysis of quasi-distributed optical sensors combining rf modulation with the FMCW method. *Opt. Eng.*, 39:3053–3059, 2000.

[23] B. Culshaw, G. Stewart, F. Dong, C. Tandy, and D. Moodie. Fibre optic techniques for remote spectroscopic methane detection-from concept to system realisation. *Sens. Act. B - Chem.*, 51:25–37, 1998.

[24] G. Stewart, C. Tandy, D. Moodie, M. A. Morante, and F. Dong. Design of a fibre optic multi-point sensor for gas detection. *Sens. Act. B - Chem.*, 51:227–232, 1998.

[25] J. I. Peterson, S. R. Goldstein, R. V. Fitzgerald, and D. K. Buckhold. Fiber optic pH probe for physiological use. *Anal. Chem.*, 52:864–869, 1980.

[26] O. S. Wolfbeis, L. J. Weis, M. J. P. Leiner, and W. E. Ziegler. Fiber-optic fluorosensor for oxygen and carbon dioxide. *Anal. Chem.*, 60:2028–2030, 1988.

[27] X-B. Zhang, C.-C. Guo, Z.-Z. Li, G.-L. Shen, and R.-Q. Yu. An optical fiber chemical sensor for mercury ions based on a porphyrin dimer. *Anal. Chem.*, 74: 821–825, 2002.

[28] L. Wen-xu and C. Jian. Continuous monitoring of adriamycin in vivo using fiber optic-based fluorescence chemical sensor. *Anal. Chem.*, 75:1458–1462, 2003.

[29] M. T. Myaing, J. Y. Ye, T. B. Norris, T. Thomas, J. R. Baker Jr., W. J. Wadsworth, G. Bouwmans, J. C. Knight, and P. St J. Russell. Enhanced two-photon biosensing with double-clad photonic crystal fibers. *Opt. Lett.*, 28:1224–1226, 2003.

[30] S. O. Konorov, A. M. Zheltikov, and M. Scalora. Photonic-crystal fiber as a multifunctional optical sensor and sample collector. *Opt. Express*, 13:3454–3459, 2005.

[31] M. Ghandehari and C. S. Vimer. In situ monitoring of pH level with fiber optic evanescent field spectroscopy. *NDT and E International*, 37:611–616, 2004.

[32] Y.-L. Lo and F.-Y. Xiao. Measurement of corrosion and temperature using a single-pitch Bragg grating fiber sensor. *J. Intel. Mat. Syst. Str.*, 9:800–807, 1998.

[33] Y.-L. Lo and F.-Y. Shaw. Development of corrosion sensors using a single-pitch Bragg grating fiber with temperature compensations. *Proc. SPIE*, 3325:64–72, 1998.

[34] A. Trego, E. O. Haugse, and E. Udd. Material removal rate fiber optic corrosion sensor. *Proc. SPIE*, 3489:105–109, 1998.

[35] J. A. Greene, M. E. Jones, P. G. Duncan, C. L. Kozikowski, T. A. Bailey, R. G. May, K. A. Murphy, and R. O. Claus. Grating-based optical fiber corrosion sensors. *Proc. SPIE*, 3042:260–266, 1997.

[36] M. E. Jones, J. A. Greene, V. Bhatia, T. D'Alberto, G. A. Ten Eyck, P. M. Schindler, K. A. Murphy, and R. O. Claus. Optical fiber grating-based strain and corrosion sensors. *Proc. SPIE*, 2948:94–100, 1996.

[37] M. P. DeLisa, Z. Zhang, M. Shiloach, S. Pilevar, C. C. Davis, J. S. Sirkis, and W. E. Bentley. Evanescent wave long-period fiber Bragg grating as an immobilized antibody biosensor. *Anal. Chem.*, 72:2895–2900, 2000.

[38] T. Allsop, L. Zhang, and I. Bennion. Detection of organic aromatic compounds in paraffin by a long-period fiber grating optical sensor with optimized sensitivity. *Opt. Commun.*, 191:181–190, 2001.

[39] A. D. Kersey, M. A. Davis, H. J Patrick, M. LeBlanc, K. P. Koo, C. G. Askins, M. A. Putnam, and E. J. Friebele. Fiber grating sensors. *J. Lightwave Technol.*, 15:1442–1463, 1997.

[40] F. Abdelmalek. Study of the optical properties of corroded gold-aluminum films using surface plasmon resonances. *Thin Solid Films*, 389:296–300, 2001.

[41] R. C. Jorgenson and S. S. Yee. A fiber-optic chemical sensor based on surface plasmon resonance. *Sens. Act. B - Chem.*, 12:213–220, 1993.

[42] K. Kim, S. J. Yoon, and D. Kim. Nanowire-based enhancement of localized surface plasmon resonance for highly sensitive detection: a theoretical study. *Opt. Express*, 14:12419–12431, 2006.

[43] B. Gauvreau, A. Hassani, M. F. Fehri, A. Kabashin, and M. A. Skorobogatiy. Photonic bandgap fiber-based surface plasmon resonance sensors. *Opt. Express*, 15:11413–11426, 2007.

[44] A. Hassani and M. Skorobogatiy. Design of the microstructured optical fiber-based surface plasmon resonance sensors with enhanced microfluidics. *Opt. Express*, 14: 11616–11621, 2006.

[45] M. Hautakorpi, M. Mattinen, and H. Ludvigsen. Surface-plasmon-resonance sensor based on three-hole microstructured optical fiber. *Opt. Express*, 16:8427–8432, 2008.

[46] B. Lee, S. Roh, and J. Park. Current status of micro- and nano-structured optical fiber sensors. *Optic. Fiber Technol.*, 15:209–221, 2009.

[47] A. Wang, A. Docherty, B. T. Kuhlmey, F. M. Cox, and M. C. J. Large. Side-hole fiber sensor based on surface plasmon resonance. *Opt. Lett.*, 34:3890–3892, 2009.

[48] M. K. K. Oo, Y. Han, J. Kanka, S. Sukhishvili, and H. Du. Structure fits the purpose: photonic crystal fibers for evanescent-field surface-enhanced Raman spectroscopy. *Opt. Lett.*, 35:466–468, 2010.

[49] D. Pristinski and H. Du. Solid-core photonic crystal fiber as a Raman spectroscopy platform with a silica core as an internal reference. *Opt. Lett.*, 31:3246–3248, 2006.

[50] R. Wang, J. Wang, F. Hao, M. Zhang, and Q. Tian. Tip-enhanced Raman spectroscopy with silver-coated optical fiber probe in reflection mode for investigating multiwall carbon nanotubes. *Appl. Optics*, 49:1845–1848, 2010.

[51] D. J. White and P. R. Stoddart. Nanostructured optical fiber with surface-enhanced Raman scattering functionality. *Opt. Lett.*, 30:598–600, 2005.

[52] D. J. White, A. P. Mazzolini, and P. R. Stoddart. Fabrication of a range of SERS substrates on nanostructured multicore optical fibres. *J. Raman Spectrosc.*, 38: 377–382, 2007.

[53] J. Baldwin, N. Schuhler, I. S. Butler, and M. P. Andrews. Integrated optics evanescent wave surface enhanced Raman scattering (IO-EWSERS) of mercaptopyridines on a planar optical chemical bench: binding of hydrogen and copper ion. *Langmuir*, 12:6389–6398, 1996.

[54] A. W. Snyder and J. D. Love. *Optical Waveguide Theory.* Chapman and Hall, 1983.

[55] L. Xu, J. C. Fanguy, K. Soni, and S. Tao. Optical fiber humidity sensor based on evanescent-wave scattering. *Opt. Lett.*, 29:1191–1193, 2004.

[56] C. O. Egalon, E. A. Mendoza, A. N. Khalil, and R. A. Lieberman. Modeling an evanescent field absorption optical fiber sensor. *Opt. Eng.*, 34:3583–3586, 1995.

[57] D. Bunimovich, E. Belotserkovsky, and A. Katzir. Fiberoptic evanescent wave infrared spectroscopy of gases in liquids. *Rev. Sci. Instrum.*, 66:2818–2820, 1995.

[58] R. A. Potyrailo, S. E. Hobbs, and G. M. Hieftje. Near-ultraviolet evanescent-wave absorption sensor based on a multimode optical fiber. *Anal. Chem.*, 70:1639–1645, 1998.

[59] W. Grahn, P. Makedonski, J. Wichern, W. Kowalsky, and S. Wiese. Fiber optic sensors for an in-situ monitoring of moisture and pH-value in reinforced concrete. *Proc. SPIE*, 4480:395–404, 2002.

[60] P. V. Preejith, C. S. Lim, A. Kishen, M. S. John, and A. Asundi. Total protein measurement using a fiber-optic evanescent wave-based biosensor. *Biotechnol. Lett.*, 25:105–110, 2003.

[61] R. A. Lieberman, L. L. Blyler, and L. G. Cohen. A distributed fiber optic sensor based on cladding fluorescence. *J. Lightwave Technol.*, 8:212–220, 1990.

[62] S. K. Khijwania and B. D. Gupta. Fiber optic evanescent field absorption sensor: effect of fiber parameters and geometry of the probe. *Opt. Quant. Electron.*, 31: 625–636, 1999.

[63] V. Ruddy, B. D. MacCraith, and J. A. Murphy. Evanescent wave absorption spectroscopy using multimode fibers. *J. Appl. Phys.*, 67:6070–6074, 1990.

[64] B. D. Gupta and Ratnanjali. A novel probe for a fiber optic humidity sensor. *Sens. Act. B - Chem.*, 80:132–135, 2001.

[65] S. Pilevar, C. C. Davis, and F. Portugal. Tapered optical fiber sensor using near-infrared fluorophores to assay hybridization. *Anal. Chem.*, 70:2031–2037, 1998.

[66] D. Maraldo, P. M. Shankar, and R. Mutharasan. Measuring bacterial growth by tapered fiber and changes in evanescent field. *Biosens. Bioelectron.*, 21:1339–1344, 2006.

[67] X.-J. Huang and Y.-K. Choi. Chemical sensors based on nanostructured materials. *Sens. Act. B - Chem.*, 122:659–671, 2007.

[68] O. H. Elibol, D. Morisette, D. Akin, J. P. Denton, and R. Bashir. Integrated nanoscale silicon sensors using top-down fabrication. *Appl. Phys. Lett.*, 83:4613–4615, 2003.

[69] Y. Im, C. Lee, R. P. Vasquez, M. A. Bangar, N. V. Myung, E. J. Menke, R. M. Penner, and M. Yun. Investigation of a single Pd nanowire for use as a hydrogen sensor. *Small*, 2:356–358, 2006.

[70] J. Lou, L. Tong, and Z. Ye. Modeling of silica nanowires for optical sensing. *Opt. Express*, 13:2135–2140, 2005.

[71] X. T. Zhou, J. Q. Hu, C. P. Li, D. D. D. Ma, C. S. Lee, and S. T. Lee. Silicon nanowires as chemical sensors. *Chem. Phys. Lett.*, 369:220–224, 2003.

[72] Y. Zhang, K. Yu, D. Jiang, Z. Zhu, H. Geng, and L. Luo. Zinc oxide nanorod and nanowire for humidity sensor. *Appl. Surf. Sci.*, 242:212–217, 2005.

[73] L. M. Tong, R. R. Gattass, J. B. Ashcom, S. L. He, J. Y. Lou, M. Y. Shen, I. Maxwell, and E. Mazur. Subwavelength-diameter silica wires for low-loss optical wave guiding. *Nature*, 426:816–819, 2003.

[74] H. Ebendorff-Heidepriem, K. Furusawa, D. R. Richardson, and T. M. Monro. Fundamentals and applications of silica and non-silica holey fibers. *Proc. SPIE*, 5350:35–49, 2004.

[75] J. C. Knight, T. A. Birks, P. St. J. Russell, and D. M. Atkin. All-silica single-mode optical fiber with photonic crystal cladding. *Opt. Lett.*, 21:1547–1549, 1996.

[76] C. M. B. Cordeiro, E. M. dos Santos, C. H. Brito Cruz, C. J. S. de Matos, and D. S. Ferreira. Lateral access to the holes of photonic crystal fibers - selective filling and sensing applications. *Opt. Express*, 14:8403–8412, 2006.

[77] T. A. Birks, J. C. Knight, and P. St. J. Russell. Endlessly single-mode photonic crystal fiber. *Opt. Lett.*, 22:961–963, 1997.

[78] J. Broeng, S. E. Barkou, A. Bjarkiev, T. Sondergaard, and E. Knudsen. Review paper: crystal fibre technology. *DOPS-NYT*, 15:22–28, 2000.

[79] T. M. Monro, D. J. Richardson, and P. J. Bennett. Developing holey fibres for evanescent field devices. *Electron. Lett.*, 35:1188–1189, 1999.

[80] Y. L. Hoo, W. Jin, H. L. Ho, D. N. Wang, and R. S. Windeler. Evanescent-wave gas sensing using microstructure fiber. *Opt. Eng.*, 41:8–9, 2002.

[81] J. B. Jensen, P. E. Hoiby, G. Emiliyanov, O. Bang, L. H. Pedersen, and A. Bjarklev. Selective detection of antibodies in microstructured polymer optical fibers. *Opt. Express*, 13:5883–5889, 2005.

[82] Y. Zhu, H. Du, and R. Bise. Design of solid-core microstructured optical fiber with steering-wheel air cladding for optimal evanescent-field sensing. *Opt. Express*, 14: 3541–3546, 2006.

[83] J. Laegsgaard, N. A. Mortensen, J. Riishede, and A. Bjarklev. Material effects in air-guiding photonic bandgap fibers. *J. Opt. Soc. Am. B*, 20:2046–2051, 2003.

[84] Y. L. Hoo, J. Wei, C. Shi, H. L. Ho, D. N. Wang, and S. C. Ruan. Design and modeling of a photonic crystal fiber gas sensor. *Appl. Optics*, 42:3509–3515, 2003.

[85] G. Pickrell, W. Peng, and A. Wang. Random-hole optical fiber evanescent-wave gas sensing. *Opt. Lett.*, 29:1476–1478, 2004.

[86] J. B. Jensen, L. H. Pedersen, P. E. Hoiby, L. B. Nielsen, T. P. Hansen, J. R. Folkenberg, J. Riishede, D. Noordegraaf, K. Nielsen, A. Carlsen, and A. Bjarklev. Photonic crystal fiber based evanescent-wave sensor for detection of biomolecules in aqueous solutions. *Opt. Lett.*, 29:1974–1976, 2004.

[87] L. Rindorf, J. B. Jensen, M. Dufva, L. H. Pedersen, P. E. Hoiby, and O. Bang. Photonic crystal fiber long-period gratings for biochemical sensing. *Opt. Express*, 14:8224–8231, 2006.

[88] Y. Zhu, R. T. Bise, J. Kanka, P. Peterka, and H. Du. Fabrication and characterization of solid-core photonic crystal fiber with steering-wheel air-cladding for strong evanescent field overlap. *Opt. Commun.*, 281:55–60, 2008.

[89] T. G. Euser, J. S. Y. Chen, M. Scharrer, P. St. J. Russell, N. J. Farrer, and P. J. Sadler. Quantitative broadband chemical sensing in air-suspended solid-core fibers. *J. Appl. Phys.*, 103:103108–1–7, 2008.

[90] A. S. Webb, F. Poletti, D. J. Richardson, and J. K. Sahu. Suspended-core holey fiber for evanescent-field sensing. *Opt. Eng.*, 46:10503–1–3, 2007.

[91] M. Liao, C. Chaudhari, X. Yan, G. Qin, C. Kito, T. Suzuki, and Y. Ohishi. A suspended core nanofiber with unprecedented large diameter ratio of holey region to core. *Opt. Express*, 18:9088–9097, 2010.

[92] H. Lehmann, J. Kobelke, K. Schuster, A. Schwuchow, R. Wilsch, and H. Bartelt. Microstructured index-guiding fibers with large cladding holes for evanescent field chemical sensing. *Proc. SPIE*, 7004:70042R, 2008.

[93] S. Afshar V., W. Q. Zhang, H. Ebendorff-Heidepriem, and T. M. Monro. Small core optical waveguides are more nonlinear than expected: experimental confirmation. *Opt. Lett.*, 34:3577–3579, 2009.

[94] S. Smolka, M. Barth, and O. Benson. Selectively coated photonic crystal fiber for highly sensitive fluorescence detection. *Appl. Phys. Lett.*, 90:111101, 2007.

[95] T. Ritari, J. Tuominen, H. Ludvigsen, J. C. Petersen, T. Sorensen, T. P. Hansen, and H. R. Simonsen. Gas sensing using air-guiding photonic bandgap fibers. *Opt. Express*, 12:4080–4087, 2004.

[96] K. J. Rowland, S. Afshar V., and T. M. Monro. Spectral properties of liquid-core Bragg fibers. *Conference on Lasers and Electro-Optics*, 2009.

[97] F. M. Cox, A. Argyros, and M. C. J. Large. Liquid-filled hollow core microstructured polymer optical fiber. *Opt. Express*, 14:4135–4140, 2006.

[98] B. Zou, Y.-G. Liu, J.-B. Du, Z. Wang, T.-T. Han, J.-B. Xu, Y. Li, and B. Liu. Transmission bandwidth tunability of a liquid-filled photonic bandgap fiber. *Chin. Phys. Lett.*, 26:044210–1–3, 2009.

[99] W. Yuan, L. Wei, T. T. Alkeskjold, A. Bjarklev, and O. Bang. Thermal tunability of photonic bandgaps in liquid crystal infiltrated microstructured polymer optical fibers. *Opt. Express*, 17:19356–19354, 2009.

[100] Y. Huang, Y. Xu, and A. Yariv. Fabrication of functional microstructured optical fibers through a selective-filling technique. *Appl. Phys. Lett.*, 85:5182–5184, 2004.

[101] J. M. Fini. Microstructure fibres for optical sensing in gases and liquids. *Meas. Sci. Technol.*, 15:1120–1128, 2004.

[102] E. W. Washburn. The dynamics of capillary flow. *Phys. Rev.*, 17:273–283, 1921.

[103] C. M. B. Cordeiro, C. J. S. de Matos, E. M. dos Santos, A. Bozolan, J. S. K. Ong, T. Facincani, G. Chesini, A. R. Vaz, and C. H. Brito Cruz. Towards practical liquid and gas sensing with photonic crystal fibres: side access to the fibre microstructure and single-mode liquid-core fibre. *Meas. Sci. Technol.*, 18:3075–3081, 2007.

[104] C. Martelli, P. Olivero, J. Canning, N. Groothoff, B. Gibson, and S. Huntington. Micromachining structured optical fibers using focused ion beam milling. *Opt. Lett.*, 32:1575–1577, 2007.

[105] A. van Brakel, C. Grivas, M. N. Petrovich, and D. J. Richardson. Micro-channels machined in microstructured optical fibers by femtosecond laser. *Opt. Express*, 15: 8731–8736, 2007.

[106] C. J. Hensley, D. H. Broaddus, C. B. Schaffer, and A. L. Gaeta. Photonic band-gap fiber gas cell fabricated using femtosecond micromachining. *Opt. Express*, 15: 6690–6695, 2007.

[107] Y. L. Hoo, S. Liu, H. L. Ho, and W. Jin. Fast response microstructured optical fiber methane sensor with multiple side-openings. *IEEE Photonic. Tech. L.*, 22: 296–298, 2010.

[108] F. M. Cox, R. Lwin, M. C. J. Large, and C. M. B. Cordeiro. Opening up optical fibres. *Opt. Express*, 15:11843–11848, 2007.

[109] S. K. Bhatia, L. C. Shriver-Lake, K. J. Prior, J. H. Georger, J. M. Calvert, R. Bredehorst, and F. S. Ligler. Use of thiol-terminal silanes and heterobifunctional crosslinkers for immobilization of antibodies on silica surfaces. *Anal. Biochem.*, 178:408–413, 1989.

[110] T. C. Foo, A. Francois, H. Ebendorff-Heidepriem, C. Sumby, and T. M. Monro. Comparison of surface functionalisation on silica and soft glasses for optical fibre sensing applications. *Australian Conference on Optical Fibre Technology*, 2009.

[111] M. Losche, J. Schmitt, G. Decher, W. G. Bouwman, and K. Kjaer. Detailed structure of molecularly thin polyelectrolyte multilayer films on solid substrates as revealed by neutron reflectometry. *Macromolecules*, 31:8893–8906, 1998.

[112] G. Decher. *Comprehensive Supramolecular Chemistry (vol. 9)*. Pergamon Press, 1996.

[113] R. A. Potyrailo and G. M. Hieftje. Spatially resolved analyte mapping with time-of-flight optical sensors. *Trends Anal. Chem.*, 17:593–604, 1998.

[114] R. A. Potyrailo and G. M. Heiftje. Use of the original silicon cladding of an optical fiber as a reagent-immobilization medium for intrinsic chemical sensors. *Fresen. J. Anal. Chem.*, 364:32–40, 1999.

[115] W. Q. Cao and Y. X. Duan. Optical fiber evanescent wave sensor for oxygen deficiency detection. *Sens. Act. B - Chem.*, 119:363–369, 2006.

[116] C. A. Browne, D. H. Tarrant, M. S. Olteanu, J. W. Mullens, and E. L. Chronister. Intrinsic sol-gel clad fiber-optic sensors with time-resolved detection. *Anal. Chem.*, 68:2289–2295, 1996.

[117] E. Alvarado-Mendez, R. Rojas-Laguna, J. A. Andrade-Lucio, D. Hernandez-Cruz, R. A. Lessard, and J. G. Avina-Cervantes. Design and characterization of pH sensor based on sol-gel silica layer on plastic optical fiber. *Sens. Act. B - Chem.*, 106:518–522, 2005.

[118] O. B. Miled, D. Grosso, C. Sanchez, and J. Livage. An optical fibre pH sensor based on dye doped mesostructured silica. *J. Phys. Chem. Solids*, 65:1751–1755, 2004.

[119] B. D. Gupta and N. K. Sharma. Fabrication and characterization of U-shaped fiber-optic pH probes. *Sens. Act. B - Chem.*, 82:89–93, 2002.

[120] P. A. S. Jorge, P. Caldas, C. C. Rosa, A. G. Oliva, and J. L. Santos. Optical fiber probes for fluorescence based oxygen sensing. *Sens. Act. B - Chem.*, 103:290–299, 2004.

[121] S. Tao, L. Xu, and J. C. Fanguy. Optical fiber ammonia sensing probes using reagent immobilized porous silica coating as transducers. *Sens. Act. B - Chem.*, 115:158–163, 2006.

[122] S. Tao, C. B. Winstead, J. P. Singh, and R. Jindal. Porous solgel fiber as a transducer for highly sensitive chemical sensing. *Opt. Lett.*, 27:1382–1384, 2002.

[123] J. E. Debs, H. Ebendorff-Heidepriem, J. S. Quinton, and T. M. Monro. A fundamental study into the surface functionalization of soft glass microstructured optical fibers via silane coupling agents. *J. Lightwave Technol.*, 27:576–582, 2009.

[124] G. Emiliyanov, J. B. Jensen, O. Bang, P. E. Hoiby, L. H. Pedersen, E. M. Kjaer, and L. Lindvold. Localized biosensing with Topas microstructured polymer optical fiber. *Opt. Lett.*, 32:460–462, 2007.

[125] A. Francois, H. Ebendorff-Heidepriem, and T. M. Monro. Comparison of surface functionalization processes for optical fibre biosensing applications. *Proc. SPIE*, 7503:75030U, 2009.

[126] S. Sumida, S. Okazaki, S. Asakura, H. Nakagawa, H. Murayama, and T. Hasegawa. Distributed hydrogen determination with fiber-optic sensor. *Sens. Act. B - Chem.*, 108:508–514, 2005.

[127] P. A. Wallace, M. Campbell, Y. Yang, A. S. Holmes-Smith, and M. Uttamlal. A distributed optical fibre fluorosensor for pH measurement. *J. Lumin.*, 72-74: 1017–1019, 1997.

[128] A. Rogers. Distributed optical-fibre sensing. *Meas. Sci. Technol.*, 10:R75–R99, 1999.

[129] W. C. Michie, G. Thursby, D. Walsh, B. Culshaw, and M. Konstantaki. Distributed sensing of physical and chemical parameters for structural monitoring. *IEE Colloquium on Optical Techniques for SMART Structures and Structural Monitoring*, pages 3/1–3/9, 1997.

[130] W. C. Michie, B. Culshaw, I. McKenzie, M. Konstantakis, N. B. Graham, C. Moran, F. Santos, E. Bergqvist, and B. Carlstrom. Distributed sensor for water and pH measurements using fiber optics and swellable polymeric systems. *Opt. Lett.*, 20:103–105, 1995.

[131] B. Culshaw, C. Michie, P. Gardiner, and A. McGown. Smart structures and applications in civil engineering. *Proc. IEEE*, 84:78–86, 1996.

[132] N. Singh, S. C. Jain, A. K. Aggarwal, M. L. Singla, and M. Singh. A simple fiber optic technique for in-situ corrosion sensing in structures. *Proc. SPIE*, 3993: 201–203, 2000.

[133] P. L. Fuhr and D. R. Huston. Corrosion detection in reinforced concrete roadways and bridges via embedded fiber optic sensors. *Smart Mater. Struct.*, 7:217–228, 1998.

[134] P. Rutherford, R. Ikegami, J. Shrader, D. Sherrer, N. Zabaronick, J. Zeakes, K. Murphy, and R. Claus. Aluminum alloy clad fiber optic corrosion sensor. *Proc. SPIE*, 3042:248–259, 1997.

[135] M. Benounis, N. Jaffrezic-Renault, G. Stremsdoerfer, and R. Kherrat. Elaboration and standardization of an optical fibre corrosion sensor based on an electroless deposit of copper. *Sens. Act. B - Chem.*, 90:90–97, 2003.

[136] M. Benounis and N. Jaffrezic-Renault. Elaboration of an optical fibre corrosion sensor for aircraft applications. *Sens. Act. B - Chem.*, 100:1–8, 2004.

[137] X. M. Li, W. M. Chen, Z. Q. Huang, S. L. Huang, and K. D. Bennett. Fiber optic corrosion sensor fabricated by electrochemical method. *Proc. SPIE*, 3330:126–133, 1998.

[138] S. Dong, Y. Liao, and Q. Tian. Sensing of corrosion on aluminum surfaces by use of metallic optical fiber. *Appl. Optics*, 44:6334–6337, 2005.

[139] X. M. Li, W. M. Chen, Y. Zhu, S. L. Huang, and K. D. Bennett. Monitoring the corrosion of steel in reinforced concrete using optical waveguide methods. *Proc. SPIE*, 3986:172–179, 2000.

[140] S. Abderrahmane, A. Himour, R. Kherrat, E. Chailleux, N. Jaffrezic-Renault, and G. Stremsdoerfer. An optical fibre corrosion sensor with an electroless deposit of Ni-P. *Sens. Act. B - Chem.*, 75:1–4, 2001.

[141] S. Dong, Y. Liao, and Q. Tian. Intensity-based optical fiber sensor for monitoring corrosion of aluminum alloys. *Appl. Optics*, 44:5773–5777, 2005.

[142] J. L. Elster, A. Trego, C. Catterall, J. Averett, M. E. Jones, M. K. Evans, and B. Fielder. Flight demonstration of fiber optic sensors. *Proc. SPIE*, 5050:34–42, 2003.

[143] J. A. Greene, M. E. Jones, T. A. Bailey, and I. M. Perez. Optical fiber corrosion sensors for aging aircraft. *Proc. SPIE*, 3399:28–33, 1998.

[144] J. L. Elster, J. A. Greene, M. E. Jones, T. A. Bailey, S. M. Lenahan, W. H. Velander, R. Van Tassell, W. Hodges, and I. M. Perez. Optical fiber-based chemical sensors for detection of corrosion precursors and by-products. *Proc. SPIE*, 3540: 251–257, 1999.

[145] K. R. Cooper, J. Elster, M. Jones, and R. G. Kelly. Optical fiber-based corrosion sensor systems for health monitoring of aging aircraft. *IEEE Autotestcon Proceedings. IEEE Systems Readiness Technology Conference.*, pages 847–856, 2001.

[146] L. A. Saarl and W. Rudolf Seltz. Immobilized morin as fluoresence sensor for determination of aluminum (III). *Anal. Chem.*, 55:667–670, 1983.

[147] S. Szunerits and D. R. Walt. Aluminum surface corrosion and the mechanism of inhibitors using pH and metal ion selective imaging fiber bundles. *Anal. Chem.*, 74:886–894, 2002.

[148] M. Ahmad and R. Narayanaswamy. Optical fibre Al(III) sensor based on solid surface fluorescence measurement. *Sens. Act. B - Chem.*, 81:259–266, 2002.

[149] W. Henry. Evanescent field devices: a comparison between tapered optical fibres and polished or D-fibres. *Opt. Quant. Electron.*, 26:S261–S272, 1994.

[150] P. Lucas, M. R. Riley, C. Boussard-Pledel, and B. Bureau. Advances in chalcogenide fiber evanescent wave biochemical sensing. *Anal. Biochem.*, 351:1–10, 2006.

[151] C. M. B. Cordeiro, M. A. R. Franco, G. Chesini, E. C. S. Barretto, R. Lwin, C. H. Brito Cruz, and M. C. J. Large. Microstructured-core optical fibre for evanescent sensing applications. *Opt. Express*, 14:13056–13066, 2006.

[152] L. Rindorf, P. E. Hoiby, J. B. Jensen, L. H. Pedersen, O. Bang, and O. Geschke. Towards biochips using microstructured optical fiber sensors. *Anal. Bioanal. Chem.*, 385:1370–1375, 2006.

[153] R. E. Bailey, A. M. Smith, and S. Nie. Quantum dots in biology and medicine. *Physica E*, 25:1–12, 2004.

[154] M. Nagel, A. Marchewka, and H. Kurz. Low-index discontinuity terahertz waveguides. *Opt. Express*, 14:9944–9954, 2006.

[155] G. S. Wiederhecker, C. M. B. Cordeiro, F. Couny, F. Benabid, S. A. Maier, J. C. Knight, C. H. B. Cruz, and H. L. Fragnito. Field enhancement within an optical fibre with a subwavelength air core. *Nat. Photonics*, 1:115–118, 2007.

[156] S. C. Warren-Smith, S Afshar V., and T. M. Monro. Highly efficient fluorescence sensing using microstructured optical fibres: side-access and thin-layer configurations. *Proc. SPIE*, 7004:70041X, 2008.

[157] T. M. Monro, Y. Ruan, H. Ebendorff-Heidepriem, T. Foo, P. Hoffmann, and R. C. Moore. Antibody immobilization within glass microstructured fibers: a route to sensitive and selective biosensors. *Proc. SPIE*, 7004:70046Q, 2008.

[158] W. Zakowicz and M. Janowicz. Spontaneous emission in the presence of a dielectric cylinder. *Phys. Rev. A*, 62:013820–1–17, 2000.

[159] J. Mertz. Radiative absorption, fluorescence, and scattering of a classical dipole near a lossless interface: a unified description. *J. Opt. Soc. Am. B*, 17:1906–1913, 2000.

[160] W. Lukosz and R. E. Kunz. Light emission by magnetic and electric dipoles close to a plane interface. I. Total radiated power. *J. Opt. Soc. Am.*, 67:1607–1615, 1977.

[161] X. Brokmann, L. Coolen, J.-P. Hermier, and M. Dahan. Emission properties of single CdSe/ZnS quantum dots close to a dielectric interface. *Chem. Phys.*, 318: 91–98, 2005.

[162] R. W. C. Vance and F. Ladouceur. One-photon electrodynamics in optical fiber with fluorophore systems. I. One-photon correspondance principle for electomagnetic field propagation in matter. *J. Opt. Soc. Am. B*, 24:928–941, 2007.

[163] R. W. C. Vance and F. Ladouceur. One-photon electrodynamics in optical fiber with fluorophore systems. II. One-polariton propagation in matter and fibers from the one-photon correspondance principle. *J. Opt. Soc. Am. B*, 24:942–958, 2007.

[164] R. W. C. Vance and F. Ladouceur. One-photon electrodynamics in optical fiber with fluorophore systems. III. One-polariton propagation in fluorophore-driven fibers. *J. Opt. Soc. Am. B*, 24:1369–1382, 2007.

[165] G. Smith and T. A. King. *Optics and Photonics: an introduction*. Wiley, 2004.

[166] R. Tricker. *Optoelectronics and Fiber Optic Technology*. Newnes, 2002.

[167] A. C. S. van Heel. A new method of transporting optical images without aberrations. *Nature*, 173:39, 1954.

[168] J. MacChesney. MCVD: Its origin and subsequent development. *IEEE Journal of Selected Topics in Quantum Electronics*, 6:1305–1306, 2000.

[169] P. Kaiser, E. A. J. Marcatili, and S. E. Miller. A new optical fiber. *Bell Syst. Tech. J.*, 52:265–269, 1973.

[170] Schott Glass Co. Accessed 6^{th} September 2010, http://www.schott.com/advanced_optics/english/our_products/materials/optical_glass.html.

[171] H. Ebendorff-Heidepriem and T. M. Monro. Extrusion of complex preforms for microstructured optical fibers. *Opt. Express*, 15:15086–15092, 2007.

[172] M. A. Foster, A. C. Turner, M. Lipson, and A. L. Gaeta. Nonlinear optics in photonic nanowires. *Opt. Express*, 16:1300–1320, 2008.

[173] Y. Ruan, E. P. Schartner, H. Ebendorff-Heidepriem, P. Hoffmann, and T. M. Monro. Detection of quantum-dot labeled proteins using soft glass microstructured optical fibers. *Opt. Express*, 15:17819–17826, 2007.

[174] J. Y. Y. Leong, P. Petropoulos, J. H. V. Price, H. Ebendorff-Heidepriem, S. Asimakis, R. C. Moore, K. E. Frampton, V. Finazzi, X. Feng, T. M. Monro, and D. J. Richardson. High-nonlinearity dispersion-shifted lead silicate holey fibers for efficient 1 μm pumped supercontinuum generation. *J. Lightwave Technol.*, 24: 183–190, 2006.

[175] E. C. Magi, L. B. Fu, H. C. Nguyen, M. R. Lamont, D. I. Yeom, and B. J. Eggleton. Enhanced Kerr nonlinearity in sub-wavelength diameter As_2Se_3 chalcogenide fiber tapers. *Opt. Express*, 15:10324–10329, 2007.

[176] G. Brambilla, V. Finazzi, and D. J. Richardson. Ultra-low-loss optical fiber nanotapers. *Opt. Express*, 12:2258–2263, 2004.

[177] G. Brambilla, F. Xu, and X. Feng. Fabrication of optical fibre nanowires and their optical and mechanical characterisation. *Electron. Lett.*, 42:517–519, 2006.

[178] A. Karagiannis, A. N. Hrymak, and J. Vlachopoulos. Three-dimensional nonisothermal extrusion flows. *Rheol. Acta*, 28:121–133, 1989.

[179] P. R. Stoddart, P. J. Cadusch, J. B. Pearce, D. Vukovic, C. R. Nagarajah, and D. J. Booth. Fibre optic distributed temperature sensor with an integrated background correction function. *Meas. Sci. Technol.*, 16:1299–1304, 2005.

[180] E. I. Sinchenko, W. Gibbs, and P. R. Stoddart. Fluorescence-based distributed chemical sensing for structural health monitoring. *Proc. SPIE*, 7268:72681K, 2008.

[181] R. S. Becker. *Theory and Interpretation of Fluorescence and Phosphorescence*. Wiley Interscience, 1969.

[182] S. R. Taylor and B. D. Chambers. The high throughput assessment of aluminium alloy corrosion using fluorometric methods. Part I - Development of a fluorometric method to quantify aluminium ion concentration. *Corros. Sci.*, 49:1584–1596, 2007.

[183] T. Kataoka, M. Mori, T. M. Nakanishi, S. Matsumoto, and A. Uchiumi. Highly sensitive analytical method for aluminum movement in soybean root through lumogallion staining. *J. Plant. Res.*, 110:305–309, 1997.

[184] H. Hoshino, K. Nakano, and T. Yotsuyanagi. 2,2'-Dihydroxyazobenzene derivatives as reagents for trace-metal determination by ion-pair reversed-phase high-performance liquid-chromatography with spectrophotometric detection. *Analyst*, 115:133–137, 1990.

[185] E. Kaneki, A. Ishida, Y. Deguchi, and T. Yotsuyanagi. A new confined spot test with hydrophobic filter paper and its application to the visual fluorometric determination of trace aluminum with 2,2'-dihydroxyazobenzene. *Chem. Lett.*, 23: 1615–1618, 1994.

[186] E. Kaneko, H. Hoshino, T. Yotsuyanagi, N. Gunji, M. Sato, T. Kikuta, and M. Yuasa. Determination of aluminum in the human serum of a dialysis patient by ion-pair reversed-phase partition high-performance liquid-chromatography. *Anal. Chem.*, 63:2219–2222, 1991.

[187] A. Ishida, E. Kaneko, and T. Yotsuyanagi. Highly sensitive visual fluorometry of aluminium at ppb level with ring-like solid phase of poly(vinyl alcohol). *Chem. Lett.*, 28:217–218, 1999.

[188] H. Hoshino and T. Yotsuyangi. Highly selective determination of trace metal ions with 2,2'-dihydroxyazobenzene by ion-pair reversed-phase partition HPLC-spectrophotometric system. *Chem. Lett.*, 13:1445–1448, 1984.

[189] H. Mizuguchi, H. Yasuda, E. Kaneko, and T. Yotsuyanagi. Drop based visual fluorometry of aluminium at ppb level with 2,2'-dihydroxyazobenzene by using octadecylsilanized silica thin layer. *Chem. Lett.*, 26:895–896, 1997.

[190] S. R. Taylor and B. D. Chambers. The high throughput assessment of aluminium alloy corrosion using fluorometric methods. Part II - A combinatorial study of corrosion inhibitors and synergistic combinations. *Corros. Sci.*, 49:1597–1609, 2007.

[191] M. P. Sibi and Z. Zong. Determination of corrosion on aluminum alloy under protective coatings using fluorescent probes. *Prog. Org. Coat.*, 47:8–15, 2003.

[192] G. R. Haugen, L. L. Steinmetz, T. B. Hirschfeld, and S. M. Klainer. Laser-induced fluorometric-determination of aluminium by the lumogallion complex. *Appl. Spectros.*, 35:568–571, 1981.

[193] D. J. Hydes and P. S. Liss. Fluorimetric method for the determination of low concentrations of dissolved aluminium in natural water. *Analyst*, 101:922–931, 1976.

[194] V. V. N. Ravi Kishore, A. Aziz, K. L. Narasimhan, N. Periasamy, P. S. Meenakshi, and S. Wategaonkar. On the assignment of the absorption bands in the optical spectrum of Alq_3. *Synthetic Met.*, 126:199–205, 2002.

[195] P. R. Haddad, P. W. Alexander, and L. E. Smythe. The effect of HNO_3, HCl and HBr on the fluorescence of the aluminium complex of 1-(2-pyridylazo)-2-naphthol and an improved fluorometric procedure for determination of aluminium. *Talanta*, 21:123–130, 1974.

[196] T. C. R. dos Santos, R. Q. Aucelio, and R. C. Campos. Spectrofluorimetric method for the determination of aluminum with alizarin red PS. *Microchim. Acta*, 142: 63–66, 2003.

[197] G. Albendin, M. P. Manuel-Vez, C. Moreno, and M. Garcia-Vargas. Reverse flow-injection manifold for spectrofluorimetric determination of aluminum in drinking water. *Talanta*, 60:425–431, 2003.

[198] W. Huiqin and Y. Zhibin. Synthesis of 2,4-dihydroxybenzaldehyde-isonicotinylhydrazone and its fluorescence reaction with aluminium. *Microchem. J.*, 55:340–347, 1997.

[199] E. P. Schartner, R. T. White, S. C. Warren-Smith, and T. M. Monro. Practical sensitive fluorescence sensing with microstructured fibres. *Proc. SPIE*, 7503: 75035X, 2009.

[200] Schott Glass Co. *Schott Technical Information. TIE-36: Fluorescence of optical glass.* Accessed 19th July 2010. http://www.schott.com/advanced_optics/english/download/schott_tie-36_fluorescence_of_optical_glass_v2.pdf.

[201] S. Tejedor, C. Davis, G. McAdam, D. Cannon, and B. Cumming. Doped porous polymers on optical fibres for fluorescence based detection of aluminium ions. *Australian Conference on Optical Fibre Technology*, 2009.

[202] C. Vargel. *Corrosion of Aluminium.* Elsevier Science, 2004.

[203] M. J. Steel, T. P. White, C. M. de Sterke, R. C. McPhedran, and L. C. Botten. Symmetry and degeneracy in microstructured optical fibers. *Opt. Lett.*, 26:488–490, 2001.

[204] J. A. Buck. *Fundamentals of Optical Fibers.* John Wiley & Sons, 2004.

[205] M. Lehtonen, G. Genty, and H. Ludvigsen. Tapered microstructured fibers for efficient coupling to optical waveguides: a numerical study. *Appl. Phys. B - Lasers O.*, 81:295–300, 2005.

[206] Y. L. Hoo, W. Jin, J Ju, and H. L. Ho. Loss analysis of single-mode fiber/photonic-crystal fiber splice. *Microw. Opt. Techn. Let.*, 40:378–380, 2004.

[207] A. Cardama and E. T. Kornhauser. Modal analysis of coupling problems in optical fibers. *IEEE T. Microw. Theory*, 23:162–169, 1975.

[208] J. S. Cook, W. L. Mammel, and R. J. Grow. Effect of misalignments on coupling efficiency of single-mode optical fiber butt joints. *Bell Syst. Tech. J.*, 52:1439–1448, 1973.

[209] D. Marcuse. Loss analysis of single-mode fiber splices. *Bell Syst. Tech. J.*, 56: 703–718, 1977.

[210] R. L. Gallawa, A. Kumar, and A. Weisshaar. Fibre splice loss: a simple method of calculation. *Opt. Quantum Electron.*, 26:S162–S174, 1994.

[211] C. Vassallo. On a rigorous calculation of the efficiency for coupling light power into optical-waveguides. *IEEE J. Quantum Elect.*, 13:165–173, 1977.

[212] G. Kweon and I. Park. Splicing losses between dissimilar optical waveguides. *J. Lightwave Technol.*, 17:690–703, 1999.

[213] G. I. Kweon, I. S. Park, and J. I. Shim. A computational method of determining reflectance at abrupt waveguide interfaces. *J. Lightwave Technol.*, 14:2436–2443, 1996.

[214] T. Conese, Barbarossa G., and M. N. Armenise. Accurate loss analysis of single-mode fiber/ D-fiber splice by vectorial finite-element method. *IEEE Photonic. Tech. L.*, 7:523 – 525, 1995.

[215] C. Vassallo. *Optical Waveguide Concepts.* Elsevier, 1991.

[216] M. Mostafavi, T. Itoh, and R. Mittra. Excitation of an optical fiber by a Gaussian-beam. *Appl. Optics*, 14:2190–2193, 1975.

[217] D. Marcuse. Excitation of dominant mode of a round fiber by a Gaussian beam. *Bell Syst. Tech. J.*, 49:1695–1703, 1970.

[218] K. Okamoto. *Fundamentals of Optical Waveguides.* Academic Press, 2000.

[219] *MATLAB version 7.6.0.324. The MathWorks Inc., 2008.*

[220] P. Viale, S. Fevrier, F. Gerome, and H. Vilard. Confinement loss computations in photonic crystal fibres using a novel perfectly matched layer design. *Proceedings of the COMSOL Multiphysics User's Conference, Paris*, 2005.

[221] L. G. Cohen, D. Marcuse, and W. L. Mammel. Radiating leaky-mode losses in single-mode lightguides with depressed-index claddings. *IEEE T. Microw. Theory*, 30:1455–1460, 1982.

[222] D. Marcuse. Influence of curvature on the losses of doubly clad fibers. *Appl. Optics*, 21:4208–4213, 1982.

[223] M. Maeda and S. Yamada. Leaky modes on W-fibers: mode structure and attenuation. *Appl. Optics*, 16:2198–2203, 1977.

[224] M. Koshiba and K. Saitoh. Simple evaluation of confinement losses in holey fibers. *Opt. Commun.*, 253:95–98, 2005.

[225] E. Kreyszig. *Advanced Engineering Mathematics (8^{th} edition)*. John Wiley & Sons Inc., 1999.